INFORMATION TO USERS

This manuscript has been reproduced from the microfilm master. UMI films the text directly from the original or copy submitted. Thus, some thesis and dissertation copies are in typewriter face, while others may be from any type of computer printer.

The quality of this reproduction is dependent upon the quality of the copy submitted. Broken or indistinct print, colored or poor quality illustrations and photographs, print bleedthrough, substandard margins, and improper alignment can adversely affect reproduction.

In the unlikely event that the author did not send UMI a complete manuscript and there are missing pages, these will be noted. Also, if unauthorized copyright material had to be removed, a note will indicate the deletion.

Oversize materials (e.g., maps, drawings, charts) are reproduced by sectioning the original, beginning at the upper left-hand corner and continuing from left to right in equal sections with small overlaps.

Photographs included in the original manuscript have been reproduced xerographically in this copy. Higher quality 6" x 9" black and white photographic prints are available for any photographs or illustrations appearing in this copy for an additional charge. Contact UMI directly to order.

ProQuest Information and Learning
300 North Zeeb Road, Ann Arbor, MI 48106-1346 USA
800-521-0600

UMI®

POLYMER MELT FORMATION AND DENSIFICATION IN ROTATIONAL MOLDING

By

MARIANNA KONTOPOULOU, M. Eng.

A Thesis

Submitted to the School of Graduate Studies

in Partial Fulfillment of the Requirements

for the Degree

Doctor of Philosophy

McMaster University

POLYMER MELT FORMATION AND DENSIFICATION IN ROTATIONAL MOLDING

Dedicated to the loving memory of my father, Antonios Kontopoulos

Στη μνήμη του πατέρα μου, Αντώνη Κοντόπουλου

DOCTOR OF PHILOSOPHY (1999) McMaster University
(Chemical Engineering) Hamilton, Ontario

TITLE: Polymer Melt Formation and Densification in Rotational Molding

AUTHOR: Marianna Kontopoulou, M Eng. (McMaster University)

SUPERVISOR: Professor J. Vlachopoulos

NUMBER OF PAGES: xx, 228

ABSTRACT

The creation of a homogeneous polymer melt from powder particles, which involves particle coalescence followed by the formation and dissolution of bubbles, is a situation encountered in processes such as rotational molding and powder coating. The present work focuses on the study of the transformation of a loosely packed, low density powder compact, to a fully densified polymer part, when processed at temperatures above the melting (or glass transition) point of the polymer. The purpose of this work is to study the appearance of air pockets, or bubbles, which are trapped during the melting-sintering of the polymer particles, to elucidate the mechanisms involved in their formation and subsequent dissolution and to propose models which are suitable for the description of the overall densification of the powder compact.

A comparative study of the processing characteristics and properties offered by various polymers has been undertaken. During this work, the problem of the presence of excessive bubbles has been encountered mainly in polymers with high amorphous contents and low crystallinities. Rheological characterization suggested that these types of polymers typically exhibit weak viscosity dependence on temperature and higher melt elasticities.

The formation of bubbles and their subsequent dissolution have been studied experimentally. Various types of polymers have been examined, in an

effort to identify the important material parameters affecting bubble formation and to elucidate the mechanisms involved.

The evolution of density as a function of time during sinter-melting was measured experimentally, using a heating oven. The results revealed that the overall process consists of two stages: Particle coalescence, which depends on viscosity, surface tension and powder properties, occurs during the first stage, during which air pockets, which eventually become bubbles, are entrapped inside the melt. The second stage involves the shrinkage and eventual disappearance of the bubbles.

The experimental results were compared to models commonly used in the ceramics, glass and metals processing literature for the densification of particulate compacts. Application of models based solely on viscosity and surface tension phenomena, can describe satisfactorily the process until the point where closed pores (bubbles) form.

The latter stage of bubble dissolution has been addressed by modeling the dissolution of a single spherical bubble in an infinite polymer melt under isothermal conditions. The bubble dissolution model has been successfully applied to provide predictions of density as a function of time for the late stages of densification.

ACKNOWLEDGEMENTS

I would like to express my thanks and appreciation to my supervisor Dr. J. Vlachopoulos for entrusting me with this project, for his constant support and for giving me numerous opportunities for scientific advancement and personal improvement. I am also grateful to my Ph.D. committee members, Drs. Andrew Hrymak and Shiping Zhu for their valuable advice and discussions, but most importantly for their support and encouragement, which are greatly appreciated.

Financial support provided for this work by the following organizations is gratefully acknowledged: The Ontario Government, NSERC of Canada, Imperial Oil, the School of Graduate Studies and the Department of Chemical Engineering of McMaster University. The particle coalescence experiments and some material characterization have been performed by Ms. Elizabeth Takács. Materials were supplied by Imperial Oil, Borealis A/S, Equistar (formerly Quantum), Dow Chemical and Miles Canada. A clamshell rotational molding machine by FSP machinery was used for the rotational molding experiments.

I am also grateful to Dr. H.H. Winter of University of Massachusetts, Amherst, for kindly allowing us to use the IRIS® software, to Dr. B. Monrabal of Polymer Char, Spain for performing CRYSTAF analysis on the polymer samples and Dr. J. Soares of the University of Waterloo for helpful advice regarding CRYSTAF analysis.

Thanks to all people of the CAPPA-D group. Elizabeth Takács and Dr. Céline Bellehumeur for their help and collaboration, but most importantly for their friendship throughout the years, Farhad Sharif for many interesting discussions and my husband, Vasileios Sidiropoulos for his support and valuable help. Thank you to everyone in the Chemical Engineering Department for being so kind to me and for providing an enriching experience.

TABLE OF CONTENTS

LIST OF FIGURES

LIST OF TABLES

Chapter 1

INTRODUCTION

1.1. The rotational molding process

Rotational molding, also known as rotocasting or rotomolding is a method for producing hollow plastic articles. The rotational molding process is comprised of four essential steps, illustrated in Figure 1.1:

1. The mold is charged with fine plastic powder (usually over 35 mesh or below 500 microns), under ambient temperature and pressure.
2. The charged mold is closed and placed inside an oven, where it is heated and simultaneously rotated around two axes, in planes at right angles to each other. During this stage the resin melts, fuses and takes the shape of the mold.
3. After all the powder has formed a homogeneous layer on the walls of the mold cavity, the mold is cooled slowly, usually by a combination of air and water.
4. The mold is removed from the cooling chamber, opened and the finished part is removed. The mold is charged with powder for the next cycle.

Rotational molding offers several advantages over other polymer processes, such as the possibility of molding extremely large hollow containers, excellent thickness uniformity, virtually stress- free parts with no weld lines and inexpensive equipment. The disadvantages are high material costs because of the

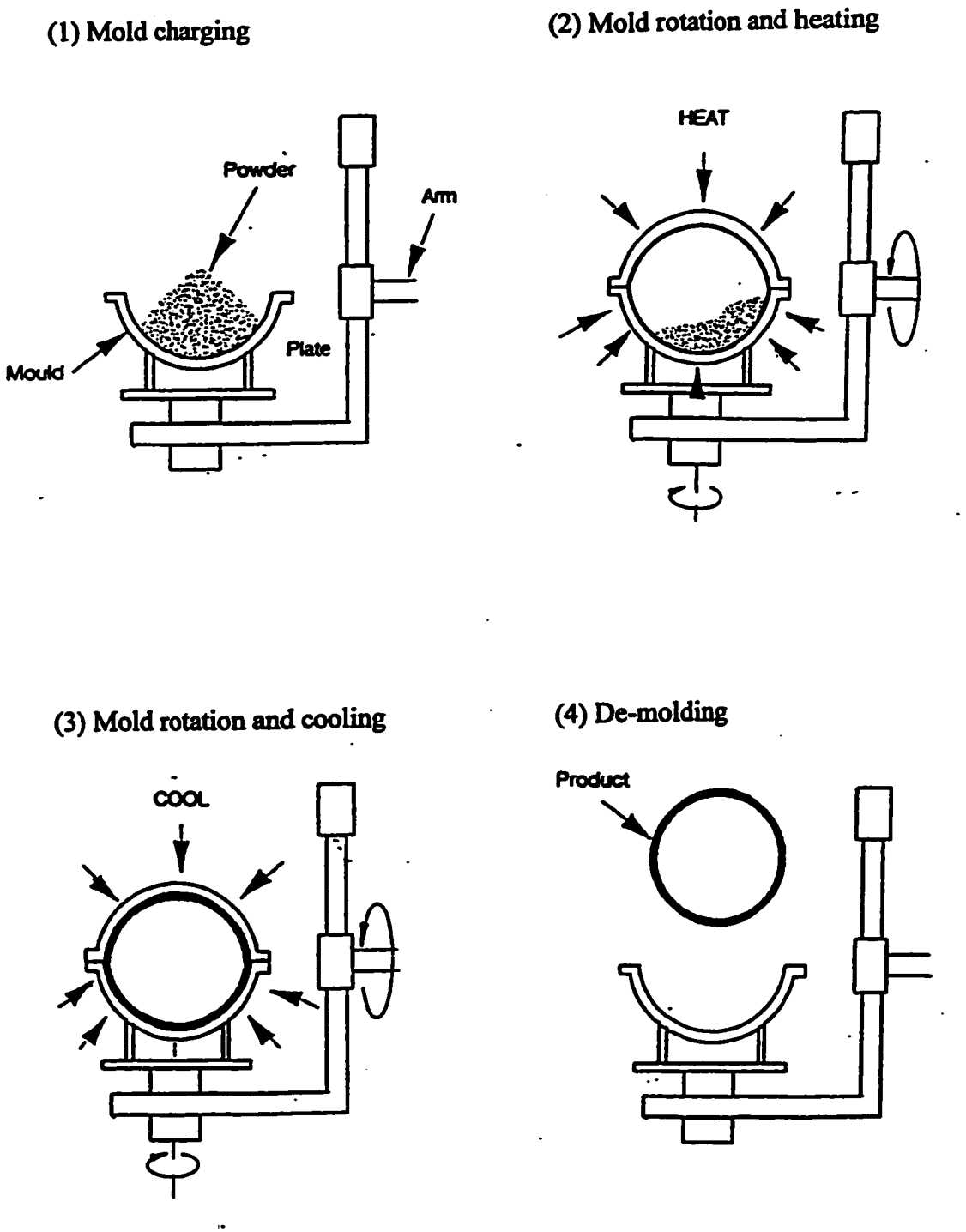

Figure 1.1: Stages of the rotational molding process (Crawford, 1992)

need of resin pulverization, limited choice of thermoplastics suitable for the process, significantly longer cycle times and subsequently low production rates, as well as lack of automation.

The relatively low investment costs for molds and machinery have made rotational molding competitive to blow molding and thermoforming or even injection molding, when small quantities of large parts are required.

In spite of its apparent simplicity, the complex flow patterns of polymer powder and sinter-melting phenomena inherent in the process, have traditionally limited fundamental understanding, contrary to other competitive processes such as thermoforming and blow molding. However a significant amount of research, which has been conducted since the mid-eighties has shed considerable light on various aspects, such as heat transfer phenomena during the heating and cooling cycles, sintering of the polymer powder particles, warpage and shrinkage phenomena, presence of bubbles in rotomolded parts and dependence of part properties on processing conditions. The improved understanding resulting from this research has led to better process control, optimization of properties of rotomolded parts, reductions of the molding cycle times through pressurization and introduction of several resins with improved properties in the market.

1.2. Polymer powder technology processes

The uniqueness of rotational molding and the ensuing difficulties in the fundamental understanding and modeling of the process emerge from the fact that contrary to the more common polymer processing methods, such as extrusion,

injection molding and blow molding, there is no mechanical shearing involved in the transformation of the polymer into a shapable homogeneous form.

Instead, rotational molding is a technique which features a heating and coalescence step that transforms a particulate porous mass into a homogeneous, porosity free one. As such, it can be classified together with other processes, such as powder coating, sintering of a powder, compression molding (when no forced shear flow occurs) and ram extrusion, as a polymer powder technology process (Rosenzweig and Narkis, 1995).

The term polymer powder technology is used to describe several powder processing techniques in which no forced relative motion between coalescing polymeric particles takes place, i.e. no machine-induced shear is involved. A typical polymer powder technology process includes the following steps: powder deposition (or compaction), powder heating (normally by either conduction or forced convection), particle coalescence and densification (driven by surface tension forces) and cooling. Particulate polymers are commonly used as a raw material by these polymer processing techniques.

The limitations of these no-shear coalescence processes arise from the fact that they cause the particle boundaries to remain noticeable even in a solid, fully sintered product, thus revealing its "powder origin". Therefore in powder technology processes mixing is limited roughly to the scale of a single particle. Contrary to processes involving high shear rates, it is almost impossible to get good mixing in no-shear coalescence processes.

1.3. Sintering, or densification of powder compacts

As described above, the powder technology processes involve a heating and coalescence step that transforms a particulate porous mass into a homogeneous, porosity free part. Solid particles, when in contact with each other at elevated temperatures, tend to decrease their total surface area by coalescence. This process is called sintering and is usually accompanied by a decrease in the total volume of the particulate bed. The main factor opposing particle coalescence is the materials' resistance to flow, expressed by its viscosity.

The sintering process proceeds in two distinct stages, first by developing interfaces and bridges between adjacent particles with little change in density, followed by a stage of densification in which the inter-particles cavities are eliminated. The initial coalescence stage is usually considered to be terminated when the neck growth ratio reaches a value of 0.5 (Tadmor and Gogos, 1979).

There has often been some controversy in the rotational molding literature about the split of the sintering process into the two stages described above, which has commonly lead to the term "sintering" used for the initial development of neck between particles and the term "densification" used for the subsequent stage of pore closing (Rao and Throne, 1972, Throne, 1995). However, in accordance to the materials science literature, it is deemed as more correct to use the term sintering for the entire process of the formation of a homogeneous, porosity free melt from the coalescence of solid particles. Moreover, often in the literature concerning sintering of glass (Scherer, 1977, Orgaz-Orgaz, 1988), the term

"densification" is used interchangeably with the word "sintering", as it involves the transformation of a loose particulate compact with low density to a final product of high density. This latter terminology will be followed throughout the present work, as well.

It should be noted that the rate of the sintering process is greatly affected by the local temperature. Hence the overall heat transfer problem within the particulate system is superimposed on the sintering process.

An added complication encountered in rotational molding is the presence of air pockets, or bubbles which form inside the polymer melt as a result of the entrapment of air between the coalescing particles and must be removed completely in order to obtain optimum part properties.

Although it is commonly recognized that sintering of polymeric powders is a fundamental phenomenon for the rotomolding process, it has been totally neglected or empirically correlated in the vast majority of modeling efforts. A significant step towards the development of suitable models which can describe effectively the sintering process has been made by Bellehumeur et al (1996, 1998) and Bellehumeur (1997). However, this work has been restricted to the simple two-dimensional modeling of two coalescing particles and therefore presents limitations in handling the real three dimensional problem and in predicting the shrinkage of the particulate compacts involved in powder densification.

1.4. Research objectives and thesis outline

The present work focuses on the study of the sinter-melting of powder compacts, with sintering meaning the whole process of density increase (or densification) involving the transformation of a loosely packed powder compact, with a bulk density of around $0.3 g/cm^3$, to a fully densified polymer part with a density of $0.9 g/cm^3$. The purpose of this work is to study the appearance of air pockets, or bubbles, which are trapped during the sinter-melting of the polymer particles and to elucidate the mechanisms involved in their formation and subsequent dissolution. The ultimate goal is to identify the parameters involved in the overall densification process and to propose models which are suitable for the description of its various stages.

This thesis comprises of six chapters, including the introduction. Chapter 2 presents a literature review on sintering and rotational molding. Chapter 3 summarizes the experimental methods and materials used in this study. A comparative study of the processing characteristics of various polymers in rotational molding is presented in Chapter 4. Chapter 4 also deals with the problem of the presence of bubbles in rotomolded parts. A detailed experimental study on the parameters affecting the formation of bubbles and on the mechanism of densification in polymer melts has been undertaken in Chapter 5. The experimental densification data have been compared to various analytical densification models and the important parameters affecting the process have been identified. The dissolution of bubbles, which is considered as the final stage

of the densification of the polymer melt has been treated in Chapter 6 and a relevant model has been proposed. The conclusions, contributions and suggestions for future work are compiled in chapter 7.

Chapter 2

LITERATURE REVIEW

2.1. A typical rotational molding cycle

The duration of the rotomolding cycle and the properties of the rotomolded parts are greatly affected by processing parameters, such as oven temperature, heating time, cooling rate, rotation speed and the ratio of rotational speeds between primary and secondary axes, usually denoted as the rotation ratio. Crawford and Nugent (1992(a)) found that the impact strength of the molded parts is highly correlated with the inside air temperature in the mold. Based on this finding they suggested that measurements of the internal air temperature can provide a means of characterization of the rotational molding cycle. They developed a control system (ROTOLOG^{TM}), which uses temperature measurements taken from inside the mold, as it rotates (Crawford and Nugent, 1992(b)). Using these measurements they were able to identify the stages of the process. Their findings were later confirmed by visual observations, done in a uniaxially rotating machine equiped with a pyrex glass window (Bisaria et al., 1994, Kontopoulou, 1995) . Rigorous analytical and numerical models developed by Gogos et al. (1998, 1999) were in agreement with experimental data presented

by Nugent, 1990). A typical internal air temperature profile, shown in Figure 2.1, can be described as follows (Nugent and Crawford, 1992, Kontopoulou, 1995):

1. Induction: In the beginning of the cycle there is only powder inside the mold. The temperature rises steadily and the powder tumbles freely, being heated through conduction and radiation, up to point A.

2. Adherence: From point A to B, the powder particles adhere to the mold and melt in layers. The rate of temperature rise is reduced, due to the energy absorption during melting.

3. Sintering: The powder particles, after having reached their melting temperature, coalesce and form a porous network. If the oven were to be removed during this stage, the resulting molding would consist of partially molten powder, connected loosely to form a porous part. The sintering stage lasts up until point C, which is the point where the boundaries between the powder particles have disappeared and a transparent polymer melt has formed. During this stage pockets of air are trapped in the melt, forming bubbles.

4. Fusion-removal of bubbles: Between C and D the density of the melt pool increases and the bubbles that formed in the previous stage decrease in size. The inner surface of the part becomes smooth. Heating continues until the maximum desired temperature (point D) has been reached. Crawford and Nugent (1992(a)) demonstrated experimentally that the peak temperature is directly related to the mechanical performance of the products and is vital for deciding the optimum processing conditions.

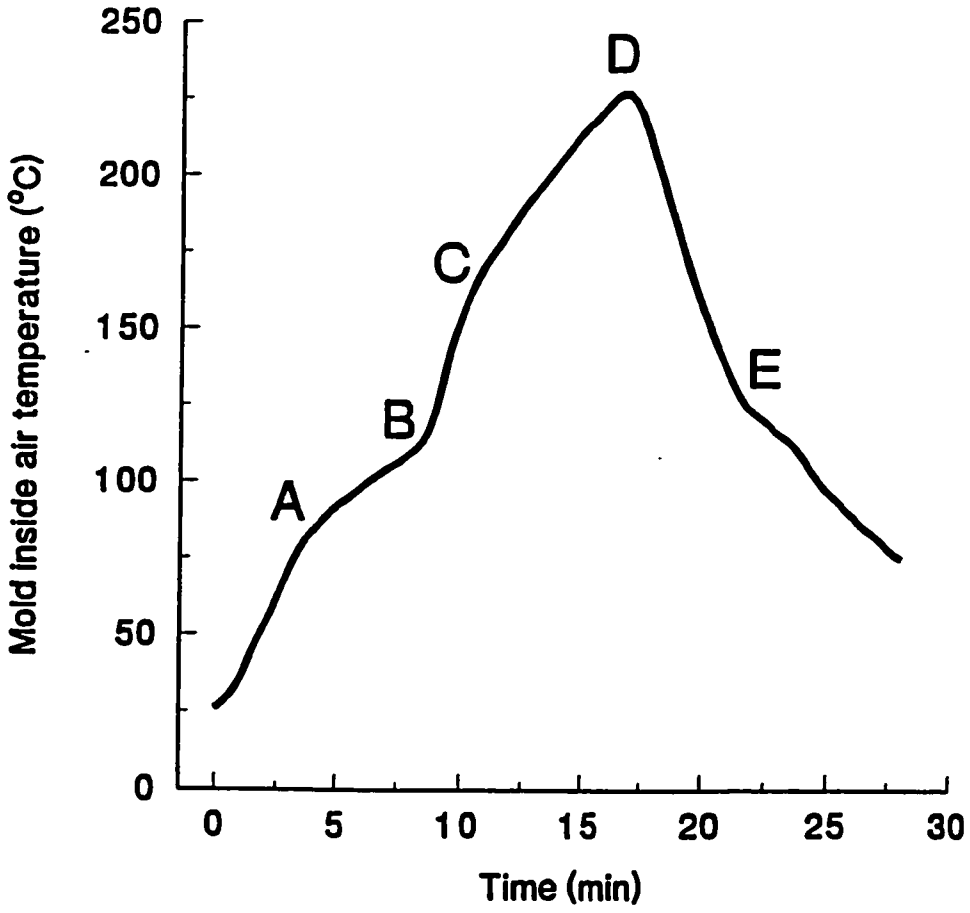

Figure 2.1: Typical mold internal air temperature during a rotational molding cycle

5. Cooling and melt crystallization: After point D the melt temperature decreases steadily, until it reaches point E, where solidification takes place. The rate of decrease of temperature depends on the method of cooling (quiescent air < forced air < water spray) and part thickness.

In rotational molding, which is virtually shear and pressure free, the polymer tends to melt freely, since there are no external forces applied. The formation of a homogeneous polymer melt, which forms from powder particles in such a manner, is also encountered in other polymer processing methods, such as powder coating (Richart,1995), laser induced sintering (Nelson et al., 1993) and solid state processing of polymers which involves sintering of previously compacted powder preforms (Jog, 1993, Narkis, 1995).

2.2. Sintering

Sintering is usually defined as the formation of a homogeneous melt from the coalescence of solid particles under the action of surface tension, with or without the application of external pressure (Thummler and Thomma, 1967), as illustrated in Figure 2.2. The term sintering has been also used to describe the coalescence of polymer particles, which usually takes place at temperatures above the melting point for semi-crystalline materials, or above the glass transition temperature for amorphous materials. The sintering process has been studied extensively for ceramic materials and metals, but its application in polymer processing has also attracted some interest. Polymer sintering is a very important stage in many industrial processes such as the fabrication of particulate

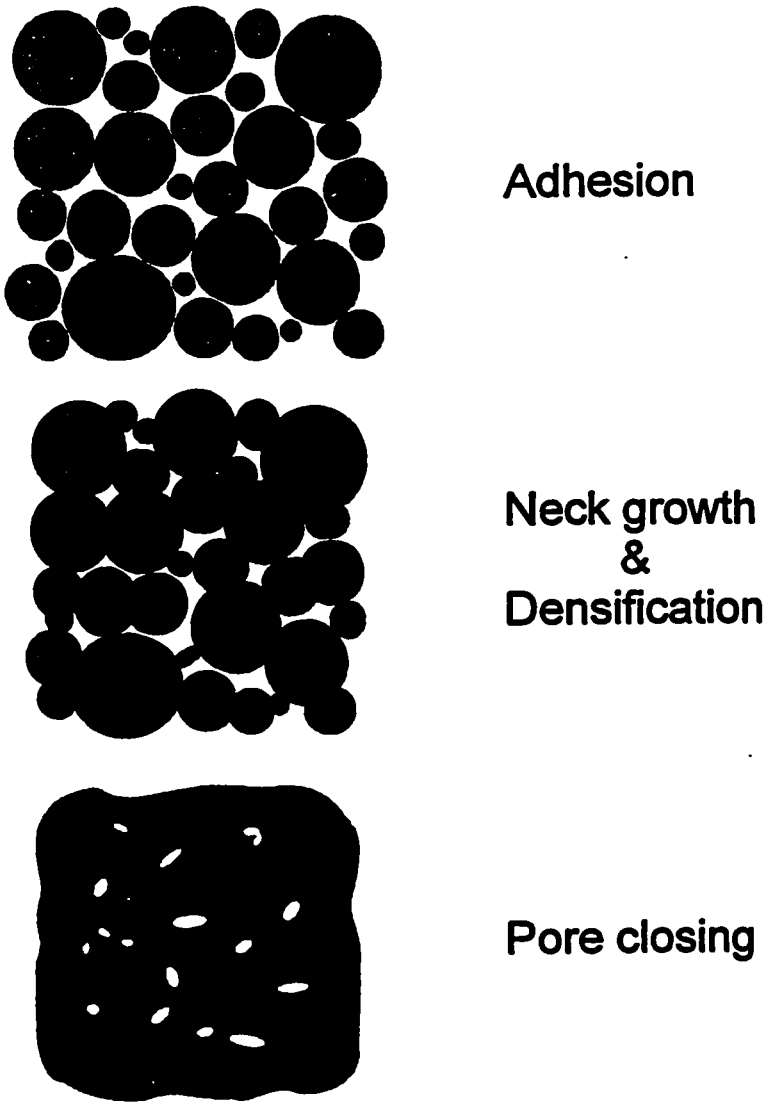

Figure 2.2: Schematic view of coalescence of particles (Bellehumeur, 1997)

preforms, powder coating, dispersion coating, cold compression molding and rotational molding.

The concept of viscous sintering was first developed by Frenkel (1945). He derived an expression for the rate of coalescence of adjacent spheres under the action of surface tension. The thermodynamic basis for this derivation is that a system left to itself will lower its free energy, by decreasing its total surface.

The validity of the model is limited to the Newtonian behavior of two identical spherical particles at the early stages of coalescence, when the particle diameters remain relatively constant.

$$\frac{y}{\alpha} = \left(\frac{3}{2} \frac{t\sigma}{\eta\alpha} \right)^{1/2} \tag{2-1}$$

where y and α denote the radius of the interface between the two spheres and the radius of the sphere respectively, σ the surface tension, η the (zero shear) viscosity and t the time (see also Figure 2.3). Applying the correction proposed by Eshelby (1949), the Frenkel expression, for isothermal conditions, takes the form (Frenkel/Eshelby model):

$$\frac{y}{\alpha} = \left(\frac{t\sigma}{\eta\alpha} \right)^{1/2} \tag{2-2}$$

The above models imply that the growth of the "neck" or "web" between the two particles is proportional to the square root of time. The Frenkel relationship has been confirmed experimentally by Kuczynski (1949) for glass spheres.

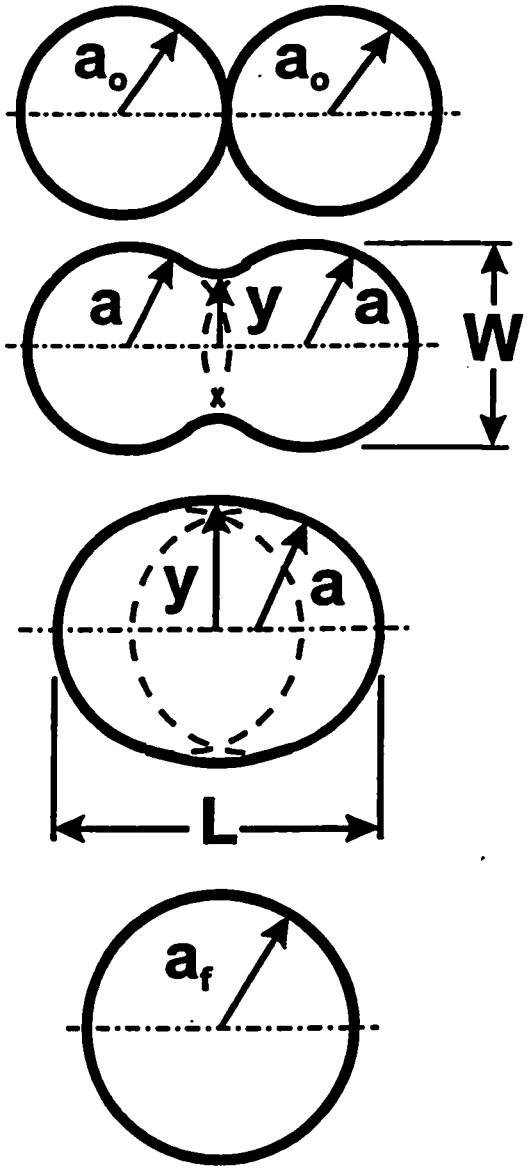

Figure 2.3: Schematic sintering sequence for two particles, where α, α_o, α_f, y, L and W are the particle radius, initial particle radius, final particle radius, neck radius, length and width of the coalescing particles (Bellehumeur, 1997)

A noteworthy effort on modeling the coalescence of two particles is that of Hopper (1984), who proposed an exact analytical solution of the Navier-Stokes equations for two dimensional viscous flow driven by capillary forces acting on a free-surface. Subsequently he analyzed the capillary flow for two cylinders having an inverse ellipse at their cross section and presented a sintering model, which can be solved analytically. Hopper's theory is limited to two-dimensional and Newtonian flow problems.

The fact that Newtonian viscous flow is applicable in the sintering of amorphous and semi-crystalline polymers has been confirmed in experimental work by various researchers, such as Rosenzweig and Narkis (1981) and Hornsby and Maxwell (1992). However, several authors, such as Kuczynski et al. (1970), Lontz (1964) and Mazur and Plazek (1994) have suggested that the Newtonian viscous flow mechanism may not adequately represent sintering of polymers. The above researchers adopted various approaches in trying to develop appropriate models. Kuczynski et al. (1970) using polymethyl methacrylate (PMMA) spheres proposed the use of a shear dependent viscosity in Frenkel's model. Lontz (1964) suggested that sintering by viscous flow can be restrained by the elastic character of the polymer and hence some relaxation constant is needed to account for the actual mechanism. Mazur and Plazek (1994) observed experimentally the sintering of acrylic resins and compared their results with analytical and numerical solutions for Newtonian sintering. They found that the sintering rate is underestimated by the Newtonian models and concluded that quasi-elastic

deformation controls the early stage of sintering. They visualized the particle coalescence process as a "miniature creep experiment involving a complicated geometry and a stress which is intrinsic (rather than applied)". They proposed a viscoelastic sintering model treating the elastic and viscous flows as mutually independent contributions (Mazur, 1995). The Mazur model predictions follow qualitatively the trends shown in experiments with acrylic resins, however the predicted sintering rates are significantly faster than the values found experimentally.

Various numerical solutions of two dimensional and axisymmetric sintering systems have been presented (Jagota and Dawson, 1988(a) (b), 1990, Jagota and Scherer, 1993, Martinez-Herrera and Derby, 1994, Van de Vorst, 1994). Van de Vorst (1994) obtained numerical results for the coalescence of two cylinders which were in excellent agreement with Hopper's model predictions. He also treated the sintering of various two-dimensional packings of cylinders and studied numerically the closing of pores.

2.2.1. Sintering in rotational molding

Polymer sintering is of particular interest in rotational molding. It is viewed as the fundamental and controlling mechanism for the process, because it commands a significant part of the heating time and has a profound influence on properties of the final part such as presence of bubbles, thickness uniformity and part quality (porosity and density). Polymer sintering relevant to rotational molding has been studied extensively by Bellehumeur et al. (1996) and

Bellehumeur (1997), who conducted an experimental study using rotational molding grade polyethylenes. They presented a simplified scheme according to which the coalescence of two powder particles can be described by treating them as spheres. They compared Frenkel's model to experimental data obtained for the coalescence of two polymer powder particles and found that it is valid only in the early stages of the process. However Hopper's model proved to describe successfully their experimental data. Bellehumeur et al. also discussed the effect of viscosity and particle geometry on the sintering rates.

Pokluda et al. (1997) modified the Frenkel/Eshelby model to account for the variation of the particle radius with time and they found good agreement of their model with experimental data obtained by using rotational molding grade polyethylenes. Their predictions compared well with Hopper's model predictions and numerical results presented by Jagota and Dawson (1988(a)).

Bellehumeur et al. (1998) attempted to explain experimental results which indicated that the purely Newtonian models could not describe well the sintering behavior of polyolefins with high melt elasticities (Vlachopoulos et al., 1996). They used the convected Maxwell constitutive equation to introduce viscoelastic behavior in the Pokluda et al. (1997) model and concluded that sintering rates are slower for the more elastic polymers.

2.2.2. Densification of powder compacts

In reality the formation of a homogeneous polymer melt from molten powder particles involves particle coalescence and densification of a powder

compact, rather than the simple two dimensional sintering of particles described above. The problem then consists in describing the shrinkage of the compact and the evolution of its density with time, as the compact sinters.

Considerable research has been done to describe various aspects of the densification process in glass powders, colloidal particles and polymeric gels. A comprehensive review has been presented by Orgaz-Orgaz (1988). Research has focused in establishing the driving force, mechanisms of densification and the kinetics of the processes that lead to particle coalescence and porosity elimination.

Scherer and Bachman (1977) studied experimentally the densification rates of soot preforms made by flame hydrolysis, siliga gel and glass. Several experimental efforts have been made to study the viscous sintering of gels under conventional and applied load sintering (Orgaz-Orgaz, 1988). Densification rates of dust particles deposited on recovery boilers have been measured experimentally by Techakijkajorn et al. (1999). They fitted their data by using a model based on volume diffusion as the controlling mechanism.

Vick and Kander (1997, 1998(a),(b)) studied the compaction and sintering of powdered polycarbonate. Kandis and Bergman (1997) examined experimentally the non-isothermal sintering of amorphous bisphenol-A polycarbonate powders by growing solid shapes under highly non-isothermal conditions. They built a non-isothermal mathematical model, using a semi-empirical densification model derived by Nelson et al. (1993) for the same

material.

Several mathematical models for the prediction of shrinkage and densification kinetics as a function of viscosity, particle size etc. have been proposed. Most of these theoretical models have been based on Frenkel's approach of equating the rate of energy gain from the reduction of surface area, to the energy dissipation in viscous flow (Scherer, 1977, 1979, 1984, Scherer and Garino, 1985). Numerical simulations of the sintering of particle packings have been presented as well (Jagota et al., 1990, Jagota and Scherer, 1995).

The first effort to generalize Frenkel's model was done by Exner and Petzow (1975), who attempted to predict shrinkage by calculating the rate of approach of the centers of two spheres during the early stages of sintering. They pointed out that asymmetric neck growth and formation of new compacts during sintering makes the quantitative description of the shrinkage of irregularly packed particles from models based on two particles quite doubtful and that their approach provides a satisfactory description only for the early stages of sintering.

Another effort to translate Frenkel's model into densification terms has been presented by Scherer (1984), who considered the microstructure of a cell consisting of packed spheres. Starting from Frenkel's equation, Scherer derived an expression for the shrinkage of the cell. Although it has been reported that this model is in good agreement with several experimental data (Scherer, 1984, Orgaz-Orgaz, 1988), this agreement must be viewed as fortuitous since the derivation was based on Frenkel's model, which is valid only at the early stages

of sintering.

Subsequently Scherer adopted a different approach and published several papers on the densification of compacts (Scherer, 1977, 1979, 1984, Scherer and Garino, 1985). In an effort to describe the early and intermediate stages of sintering of low density glass compacts with open pores, he developed the open pores model (Scherer, 1977), which considers the shrinkage of a three dimensional cubic array of interconnected cylinders. The model consists of a cubic array formed by intersecting cylinders. The choice of a cubic cell is arbitrary, however its advantage is that it has a very simple geometry. Moreover, it has been shown that the cell shape has a marginal effect on the model predictions (Scherer, 1991). The geometrical parameters necessary for the model application can be estimated if the initial bulk density and particle size of the compact are known. To calculate the rate of sintering of the model structure Scherer (1977) applied Frenkel's energy balance and obtained an analytical relationship between density and time, which is valid for the sintering of a free, unconstrained body.

The underlying assumption in all derivations descrived above is that the pore size distribution is uniform throughout the compact. Scherer suggested that if a pore size distribution is present, the densification rate will vary from point to point, resulting in the development of stresses. He calculated the stresses caused by local variations for a compact with a bimodal pore-size distribution and extended his model to handle this situation (Scherer, 1984).

Scherer and Garino (1985) attempted to describe the densification rate of a porous glass layer on a rigid substrate. When such a layer sinters on a rigid substrate, tensile stresses develop, which are expected to retard its densification. The authors presented an analysis that predicts the sintering rate of the layer and the magnitude of the developing stresses. They assumed that shrinkage is normal to the substrate and that there is no warping of the substrate. Scherer and Garino (1985) presented two distinct approaches: First, by using a continuum model, they calculated the strain rates by using the cylindrical array microstructural model and obtained predictions for the sintering kinetics and for the magnitude of the tensile stress in the layer. During sintering, shrinkage was not permitted in the plane of the substrate, thus it was assumed that no deformation occurs in the plane of the substrate and that the layer densifies by contracting in the direction normal to the plane.

The possibility of anisotropy in the microstructure of the sintering layer, which may develop during sintering and can result in pore orientation was taken into account by the second approach (Scherer and Garino, 1985), which represents the sintering layer by tubes whose axes are normal to the substrate. The latter model describes the densification of a layer which is allowed to contract only in one direction, normal to the substrate.

The open pores models break down when the pores become trapped in each cell, in the late sintering stage, which occurs when the density of the compact relative to the theoretical solid density is $\rho/\rho_s=0.942$ (Scherer, 1977).

Beyond this point, the array consists of closed pores and Scherer's analysis is no longer appropriate.

Pore closing – The closed pores model

The first model for pore closing was developed by Kuczynski and Zaplatynskyj (1956), who conducted sintering experiments in glass. They applied Frenkel's theory (Frenkel, 1945) according to the expression:

$$R_o - R = \frac{\sigma t}{2\eta} \qquad (2\text{-}3)$$

where R_o and R are the original radius of the cavity and the cavity radius at time t respectively.

Throne (1979) suggested that the filling of voids by capillary action can be calculated using a differential form of the equation developed by Frenkel for the densification of glass.

Mackenzie and Shuttleworth (1949) have proposed a model, commonly termed as MS model, or closed pores model, whose applicability for the late stages of metal densification has gained wide recognition. According to this model, densification results from the shrinkage of uniform spherical pores in a viscous matrix. The flow field of an individual spherical pore can be calculated analytically because of the simple geometrical deformation. It is also assumed that the pores are equally sized spheres and that densification is uniform throughout the compact. After applying Frenkel's energy balance Mackenzie and Shuttleworth (1949) derived an equation for the sintering time necessary to reach

a particular density of the compact.

The underlying mechanism involved in all the models described above is surface tension driven flow, opposed by viscosity. The MS model, which is appropriate for relative densities above ρ/ρ_s=0.942, is often combined with one of Scherer's open pores model, to describe the overall densification rates of a powder compact (Orgaz-Orgaz, 1988, Scherer and Garino, 1985).

2.2.3. Densification and the problem of bubble formation in rotational molding

In an initial attempt to describe the bubble formation problem relevant to rotational molding, Rao and Throne (1972) drew extensively from the theories of metal sintering. They suggested that the formation of a homogeneous melt from powder particles is a two step process. During the first stage, denoted as sintering, the powder particles stick, or fuse, together at their points of contact. Interfaces and bridges develop between adjacent particles, until the mass becomes a porous three-dimensional network. During this stage there is little change in the density of the mass. The next stage is denoted as densification and begins once the relative web neck to particle radius ratio approaches 0.5. The porous character of the mass begins to change as the network begins to collapse into the void spaces, which become bubbles. Throne (1995) maintained that the primary mechanism for expressing the entrained air is by lattice stucture collapse into the melt and not by capillary action. Subsequently the bubbles are either pushed ahead of the coalescing front to the free surface, if the melting is sufficiently slow, or become

encapsulated and remain in the polymer after it is quenched, which is the usual case for rotomolding.

Throne (1979) noted that the Frenkel forces, responsible for filling the voids can also be affected by the viscoelasticity of the melt, because the viscoelastic forces can slow down the densification process in the same way that they can slow down the particle coalescence.

Progelhof et al. (1982) studied powder densification, by using a flat plate simulator. They physically observed the densification process by heating polyethylene powder inside a glass ring. They observed that as heating progresses, the solid/melt interface moves upwards and the free surface of the powder drops, until the powder has completely melted. They observed two phenomena: surface leveling and formation of voids, or bubbles in the molded part. The formation of voids, according to Progelhof et al. (1982), is a result of a "bound inclusion of the space between individual particles".

Kelly (undated) who conducted his work using a variety of microscope techniques, observed that the powder mass, during heating, can be divided into three zones shown in Figure 2.4: Zone 1, which is closer to the mold surface, consists of molten polymer. Heat is transferred from zone 1 to the rest of the powder (zones 2 and 3). As the melting front (edge of the molten polymer) advances into zone 2, the powder particles soften, stick together and start to melt. During this process, the air between the particles will either escape into zone 3, or

get trapped, forming bubbles. Kelly stressed the importance of good quality powder for the production of a bubble free part.

Crawford and Scott (1987), in a detailed study of the phenomena occurring during bubble formation and removal, visualized a different mechanism than that of a three dimensional network suggested by Rao and Throne. They described the melting and collapse of the powder as the combination of two bulk movements "firstly the progression of the melt front through the powder mass to the free surface and then the collapsing of powder particles into the melt. Air is trapped during the latter process" (Figure 2.5). The trapped air from neighbouring particles forms irregular shapes initially, but due to capillary forces eventually the shape becomes spherical. Spence and Crawford (Spence, 1994, Crawford and Spence, 1996, Spence and Crawford, 1996) presented an extensive study on the processing variables affecting the formation and removal of bubbles. They studied the effects of viscosity, powder characteristics, processing conditions, moisture, mold material and mold release agents.

Recently Liu (1996) and Liu et al. (1996) reported some bulk sintering data of LDPE and LLDPE rotational molding grade powders and studied the effect of viscosity and temperature on the bulk sintering rates.

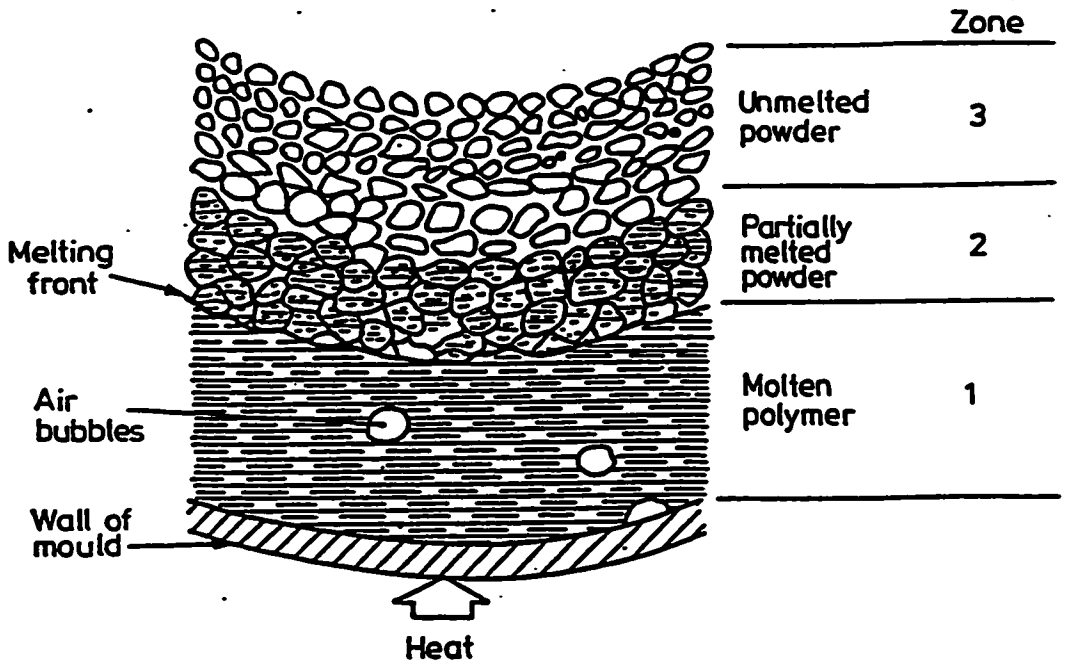

Figure 2.4: Heating zones in the powder mass (Kelly, undated)

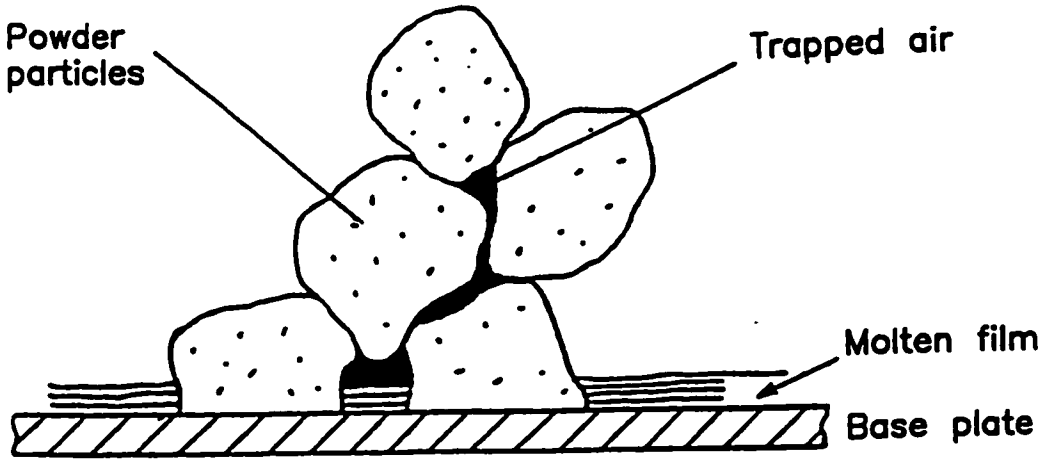

Figure 2.5: Bubble formation in a melting powder (Spence, 1994)

2.3. Bubble removal

The presence of bubbles in viscous materials is often encountered in metal and glass processing and there is a great deal of literature addressing this aspect. Greene and Gaffney (1959) used a specially designed apparatus to study oxygen dissolution in molten glass. They modelled the process by solving a Fickian type equation and treated the moving boundary as a Stefan type problem. Doremus (1960) through a comparison of theory with experiment computed diffusion coefficients of oxygen in molten glass and commented on the possible mechanisms for the diffusion process. The models concerning bubble growth and dissolution in glass melts have been reviewed by Kramer (1985).

The diffusion controlled dissolution of air bubbles in water has been studied by Epstein and Plesset (1950). They discussed the effect of surface tension and derived suitable analytical solutions. Readey and Cooper (1966) and Cable and Evans (1967) have treated the problem of molecular diffusion of gas bubbles with the inclusion of moving boundary and radial convective transport effects.

Other studies (Street, 1968, Fogler and Goddard, 1970, Zana and Leal, 1975, Pearson and Middleman, 1977, Papanastasiou et al. 1984) have covered the aspect of bubble growth and collapse in viscous or viscoelastic fluids. These papers are mostly concerned with the formation and removal of cavitation bubbles in polymeric solutions of relatively low viscosities and usually at high Reynolds numbers. In these cases, bubble dynamics are mainly controlled by pressure

differences and fluid velocities. The bubble growth or collapse mechanism is modeled by solving the coupled continuity and momentum equations, without taking diffusion into account. Zana and Leal (1975) modeled the dissolution of a bubble in a viscoelastic fluid rigorously, by solving the continuity, momentum and diffusion equations.

2.3.1. Bubbles in polymer melts

Bubble formation and removal is not a situation encountered frequently in common polymer processing methods, so there is very limited literature covering the aspect of bubble removal from polymer melts. A great deal of work has been done though, on the opposite problem of bubble growth in polymer melts during the foaming process. Han and Yoo (1981) and Arefmanesh and Advani (1991, 1995) in their work on bubble growth in polymeric foams showed that the important phenomena occurring during bubble growth are mass, momentum and energy transfer between the bubble and the fluid surrounding it. Arefmanesh and Advani used the Upper Convected Maxwell constitutive model to account for the viscoelastic character of the polymer melt surrounding the bubble. Ramesh et al. (1991) verified Arefmanesh and Advani's theoretical predictions, by comparing them to experimental data.

Bubble removal has also been studied in the context of rotational molding by several researchers (Progelhof et al. 1982, Kelly, undated, Crawford and Scott, 1987). Progelhof et al. (1982) reported a slow movement of the voids towards the free surface. On the contrary, Kelly (undated) suggested that bubbles remain

stationary and that the oxygen in the air bubble begins to physically dissolve in the polymer, as the temperature of the melt increases. The oxygen is the first gas to dissolve, because it has twice the solubility of nitrogen in polyethylene. The depletion of oxygen results in the reduction of the bubble diameter, which in turn results in the increase of the pressure inside the bubble, as dictated by the laws of surface tension. The increase in pressure forces nitrogen to dissolve in the polymer, further reducing the bubble diameter.

Crawford and Scott (1987), in a detailed study of the phenomena occurring during bubble formation and removal, proved Kelly's suggestion that bubbles remain virtually stationary in the melt due to the high viscosity of the melt by performing a force analysis on the bubble. They concluded that the viscosity of the molten polyethylene is so large that the buoyancy forces acting on the bubble are insignificant and they further confirmed this with photographic evidence.

Spence and Crawford (Spence, 1994, Crawford and Spence, 1996, Spence and Crawford, 1996) studied experimentally bubble removal. They observed that mold pressurization during the rotomolding cycle is an efficient method to remove bubbles from rotomolded parts, but an in-depth understanding of this phenomenon is still lacking. Crawford and his co-workers (Crawford and Scott, 1987, Spence, 1994, Xu and Crawford, 1993) proposed that the mechanism for bubble removal is governed by the diffusion of gas through the polymer melt. They developed a model for the diffusion of bubbles, based on a similar approach

as that of Greene and Gaffney (1959). Crawford and Scott (1987) and Xu and Crawford (1993) subsequently proposed several simplifications to this model.

Although these models seem to describe qualitatively the removal of bubbles from polyethylene melts, they rely on the estimation of physical constants by curve fitting. In addition surface tension does not appear in the equations and the effect of melt viscosity has not been considered.

2.4. Modeling efforts in rotational molding

Modeling of the rotational molding process is a complicated matter, associated with unsteady state conditions and various heat transfer phenomena, such as convection, conduction and radiation. A series of stages, such as heating of powder, melting, heating of polymer melt and cooling, must be considered. Co-existence of powder, partially molten powder and molten polymer, complicates further the modeling of heat transfer.

The powder kinematics during the initial induction stage have been studied by Pantani et al. (1996). McCarthy et al. (1996) and Khakhar et al. (1997) discussed the flow and mixing of granular materials in rotating containers.

Among the first attempts which have been made to develop a model describing the kinematics and heat transfer involved in rotational molding the most important are those by Rao and Throne (1972) and Throne (1976, 1979). Rao and Throne (1972) made several assumptions with respect to mold geometry, powder flow and heat transfer mechanisms involved. Throne (1972) presented an analysis of the factors influencing cooling rates in rotational molding.

The problem of lack of experimental data on the actual rotational molding process has been addressed by the work done at the Queen's University of Belfast by Crawford and his group during the eighties (Crawford and Scott, 1985, Scott, 1986, Crawford and Nugent, 1989, Nugent, 1990).

Crawford and Scott (1985) were the first to consider a series of distinct regions in a typical time/temperature profile. These regions were identified as: induction, melting, dissolution of bubbles and cooling. Crawford and Nugent (1989) and Nugent (1990) developed a model for the process by addressing all of the aspects encountered in rotational molding, such as rotation, heat transfer and powder densification. Further refinements of the heat transfer simulation were attempted by Sun and Crawford (1993(a),(b)), who considered internal heating and cooling and Xu and Crawford (1994), who considered the temperature change of the air inside the mold during the molding cycle.

Bawiskar and White (1995) presented a heat transfer study which lead to a simple analytical expression for the calculation of the melt front thickness. Gogos et al. (1998) presented a detailed theoretical model of the process and identified the key dimensionless groups affecting the process cycle time. They employed differential and lumped parameter numerical models, as well as a simple closed form estimate for the time required for complete powder deposition. Subsequently they extended their model to include the cooling stage and studied part shrinkage effects (Gogos et al. 1999). Furthermore Olson et al. (1998) discussed the application of finite element models in rotational molding.

At present, one commercial numerical simulation of the rotational molding process is available (Xu and Crawford, 1997). However, it has the same limitations as all heat transfer models developed to predict the molding cycle: it is limited to simple mold geometry. Moreover, in all the models presented in the literature for rotational molding or any other process involving polymer sintering, the sintering process is either neglected or determined empirically (Nelson et al. 1995, Kandis and Bergman, 1997).

2.5. Materials used in rotational molding

In earlier applications of rotational molding liquid plastisol was principally used. However the introduction of powdered resins lead the rotational molding industry to a significant growth rate (Throne, 1979, Crawford, 1992). Some alternatives to powder, mainly in the form of micropellets have been developed recently (Gala Industries, 1995, Takács et al, 1996, Mack and Voigt, 1999).

A material should exhibit certain fundamental characteristics in order to be suitable for rotational molding. Some of the basic requirements are the following: sufficient melt flow properties to coat the surface area of the mold evenly, thermal stability to withstand elevated temperatures for prolonged periods of time and suitable powder heat transfer characteristics. The wetting characteristics of the polymer/mold system are also an important consideration. In order for the polymer to wet the surface of the mold, the critical surface energy (surface tension) of the molten polymer must be less than the critical surface energy of the

metal (Spence, 1994). This is true for the polymer/metal systems usually encountered in rotational molding, so that the wetting and spreading of the molten polymer inside the mold does not pose a problem (Spence, 1994).

Economic considerations are also very important and may result in the exclusion of several materials, which could otherwise be suitable for the process.

Today a large percentage of the total tonnage of plastics used in rotomolding consists of polyethylene (Crawford, 1992). This is mainly because the powder flow, melt flow, thermal stability and impact properties of polyethylene are ideally suited for the process. Table 2.1 shows the percentage of the consumption of rotomolding resins in the North American market (Mooney, 1995). Linear-Low-Density polyethylene commands the largest portion (over 70%) of the polyethylene market share (Mooney, 1999).

Table 2.1: Consumption of rotomolding resins in the North American market, in 1994 (Mooney, 1995). Total consumption estimated at 799 million lbs.

Material	% of North American market
Polyethylene	85.3
PVC	13.2
Nylon	0.5
Polycarbonate	0.4
Polypropylene	0.3
Fluropolymers	0.1
Others	0.2

Impact strength, or toughness is very important in materials selection and it is a major requirement for rotomolded products. Polyethylene and especially LLDPE meets these requirements and is used extensively in the process (Crawford, 1992, Kliene, 1992, Beall, 1998). Cross-linked polyethylene can provide even better low temperature impact strength while offering improved environmental stress cracking resistance (Crawford, 1992, Loti and Howerter, 1999).

Because of the inherent low strength and stiffness of polyethylene, other materials have been introduced, such as polypropylene, nylon and polycarbonate. Polypropylene homopolymer offers a desirable range of properties, but it has serious drawbacks, being prone to thermal degradation and having low impact strength, especially in low temperatures. It has therefore found limited use in rotational molding as moldings are too brittle, although they have good rigidity and surface finish. In recent years some rotomolding grade rubber toughened polypropylenes have been introduced in the market. There are mainly two types of rubber toughened polypropylene (Quantum, undated): Polypropylene Impact Copolymers (PPIC) and polypropylene block copolymers, sometimes termed as thermoplastic olefins (TPO). These resins offer excellent environmental stress cracking resistance, high stiffness, high heat distortion temperatures and scratch resistance, while having improved toughness compared to the homopolymer (Kontopoulou, 1996, Kontopoulou et al., 1997, Dodge, 1999). Chemical storage

tanks, tanks which can withstand autoclave sterilization and metal pipe linings are some of the areas of application for these PP copolymers.

Polyamide (nylon) resins, which are available as type 6, 11 and 12 provide excellent chemical, abrasion and environmental stress cracking resistance, toughness, stiffness and they can be used in elevated temperatures for a long period of time (Petrucelli, 1992). Application areas include fuel and chemical storage tanks, hydraulic oil reservoirs, cyclones, heat resistance containers and air ducts. Nylons are also used for multi-layer rotational molding (Anon, 1993). Useful combinations of Nylons with other materials include polyethylenes (except from cross-linked PE), fluoropolymers and ethylene acrylic acid copolymers.

Polycarbonate is an engineering plastic, which offers transparency, excellent toughness, high heat resistance and dimensional stability (Anon, 1980). In comparison to polyethylene, polycarbonate is more expensive, but offers important advantages, such as higher heat distortion temperature, clarity, three to four times higher impact strength and reduced warpage (Long, 1989). Consumption has been limited so far, but it has been used for items as light globes, housings, snowmobile engine covers and display signs (Foster, 1970, Nugent, 1990).

Flexible parts can be obtained by using polyethylene copolymers, such as ethylene-vinyl-acetate (EVA) and ethylene-butyl-acrylate (EBA). EVAs and EBAs are typically soft, flexible materials. They are more transparent and have higher cold temperature impact strength than the other PEs. Typical applications

include soft, squeezable toys, traffic cones, energy-absorbing barricade covers and bumpers for boats and bumper cars (Anon, 1976, Nugent, 1990, Beall, 1998).

Apart from the materials mentioned above, there have been some efforts to introduce rubber toughened polymers, such as High Impact Polystyrene (HIPS) (Anon, 1967, 1968(a)) and Acrylonitrile-Butadiene-Styrene (ABS) (Anon, 1968(b), Tanaka, 1974, White et al., undated, Strong and Kinghorn, 1998) in the rotational molding market, but with limited success.

Rotational molding of liquid reactive plastic systems, such as liquid nylon block copolymer (NYRIM) and polyurethanes has also gained some interest (Harkin-Jones and Crawford, 1996(a),(b), Rabinovitz and Rigbi, 1985). Liquid plastic systems offer a number of advantages, such as reduced cycle times, excellent reproducibility of surface detail due to the low viscosity of the liquids relative to the melts and a great range of material properties

Rotational molding of thermosetting syntactic foams has been considered in the past (Narkis and al., 1982), but a significant recent development is the introduction of polyethylene foams suitable for rotational molding (Liu and Tsai, 1998, Liu et al., 1998).

Recently a new class of very narrow molecular weight distribution polyethylenes, made by metallocene catalysts have been made available to the rotomolding market (Fatnes, 1999, Loti and Howerter, 1999). The new catalysts can facilitate the molecular design of the polymer molecules, in order to achieve specific desirable characteristics.

2.6. Material properties relevant to rotational molding

The parameters which influence the process of rotational molding fall mainly in two categories: powder properties and polymer properties, which include melt properties.

2.6.1. Powder properties

Rotational molding uses polymer resins in powder form. There does not exist a single size of powder particles, but rather a size distribution, ranging from the finest (less than 150 microns) to approximately 500 microns. The properties of the powder can have an important effect on processing and on final part properties.

Particle size distribution is very important. In general coarser particles lead to increased cycle times and inferior surface finish. Fine particles enhance heat transfer and their presence results in good surface finish (Kliene, 1992). On the other hand they tend to fluidize excessively and can cause bridging, because the finer particles can melt before the rest of the powder and prevent other particles from entering sections of the mold such as corners and ribs. Too many fine particles can also cause agglomeration, due to build-up of static. This results in flow and melting problems. It is generally accepted in the rotational molding industry that powders having nominal –35 +100 mesh size (corresponding to a particle size range between 150 and 500 μm) offer the best compromise in particle properties and required grinding energy (Throne, 1995).

Particle shape is also important and it affects heat transfer and flow characteristics of the powder. The presence of 'tails' results in bridging, favors the formation of voids and bubbles and results in poor part properties. It is has been proposed that the most desirable particle shape is cubic, with rounded corners (Rao and Throne, 1972, Throne and Sohn, 1989(a)).

Throne and Sohn (1989(a)) and Kliene (1992) reviewed the available methods for the characterization of powder properties. These include dry flow tests, bulk density tests and particle size distribution tests. Microscopic examination of the powder shape can also be useful. The calculation of the Hausner ratio as a measure of the packing tendency of the powder has also been applied (Bisaria et al., 1994), mainly because of its sensitivity to the shape and size of particles and because of its insensitivity to relative humidity .

2.6.2. Polymer properties

The most significant properties affecting rotational molding are viscosity, usually expressed as melt flow index, density and molecular weight distribution. Thermal properties, such as melting point, heat of melting and breadth of melting range are also expected to play an important role.

Density of a polymer is a measure of how close the long molecular chains are packed. Density is very important in distinguishing between polyethylene resins, while it does not play a significant role for other resins, like polypropylene. Increasing density (which implies higher crystallinity) results in increased stiffness, tensile strength, hardness, heat deflection and chemical resistance. High

density can also be disadvantageous, because it leads to reduction in impact strength and environmental stress cracking resistance (ESCR) and to increased shrinkage (Crawford, 1992).

The role of viscosity is of great importance. Since rotational molding is a very low shear process, the flow characteristics of the melt have a great influence on the final part porosity and on the duration of the molding cycle. Low viscosity is necessary to ensure adequate particle coalescence and good surface finish. Although the most popular criterion for evaluating the moldability of a polymer in general is the melt flow index (MFI), the most suitable one for rotational molding should be the zero shear viscosity (Bisaria et al., 1994, Vlachopoulos et al., 1996). A higher MFI resin offers impoved flow properties, good surface finish and will require shorter cycle times. On the other hand, impact strength, ESCR, weatherability, chemical resistance and tensile strength are compromised. Low MFI results in poor surface finish and excessive bubbles.

The molecular structure, expressed by the molecular weight distribution (MWD) is also important. A narrow MWD leads to better processability, better mechanical properties and lower warpage and it is generally desirable for rotomolding. A broad MWD offers the advantage of improved ESCR at the expense of processability (Crawford, 1992).

Measurements of thermal properties, such as melting point, heat of fusion, heat capacity, crystallinity and thermal conductivity of various materials have been reported (Nugent, 1990, Xu, 1994, Kontopoulou, 1995). The effect of

melting point, heat of fusion, heat capacity and thermal conductivity on the "powder-end" time and on total cycle times has been studied by Gogos et al. (1998) and Gogos et al. (1999) respectively.

2.7. Final part properties

Quality control is a very important consideration for rotomolded parts. Properties like impact strength, tensile strength, ESCR, chemical resistance, heat deflection temperature, etc. are of great importance and there are several standard methods available for their assessment.

Throne and Sohn (1989(b)) performed a series of tests on rotationally molded polyethylene samples and compared their properties with those of injection molded parts. They observed that the rotationally molded parts exhibited higher porosity and showed greater strengths and moduli, but lower elongations and impact strengths. Scott (1986) studied the effect of cycle times and oven temperatures on the properties of the final parts. Crawford and Nugent (1992(a)) demonstrated that the impact strength of polyethylene parts is correlated to the maximum inside air temperature achieved during the cycle. Increasing the maximum inside air temperature contributes to better fusion of the part, thus resulting in an increase in impact strength up to a point, but beyond this point overcurring can result in significant reduction of impact strength. Based on this observation, Crawford et al. (1991) and Crawford and Nugent (1992b) predicted optimum process conditions for various polyethylenes.

Oliveira et al (1996) in an effort to explain the effect of processing conditions on mechanical properties, presented a detailed study of the morphology of rotationally molded polyethylene.

The effect of cooling on the properties of the final part has been studied by Sun and Crawford (1993 (b)). Cooling rate has been found to affect warpage, shrinkage, residual stresses and mechanical properties (Chen et al., 1990). Increasing quench rate resulted in increased elongation at break and impact strength, but also to increased warpage. The problems of warpage and shrinkage of polyethylene parts have been addressed by Chen et al. (1990).

Finally Nagy and White (1996) and Cramez et al. (1998) investigated the effect of pigmentation on the mechanical properties, warpage, shrinkage and microstructure of rotomolded polyethylene parts.

Chapter 3

EXPERIMENTAL: MATERIALS, EQUIPMENT AND PROCEDURES

3.1. Materials

Semi-crystalline and amorphous thermoplastic polymers used in this work included various LLDPEs (PE-1 – PE-6), polypropylene (PP) and polypropylene copolymers (PP/PE), ethylene-butyl-acrylate (EBA) and ethylene-vinyl-acetate (EVA) copolymers, an ultra low density polyethylene (polyolefin plastomer or POP) and polycarbonate (PC). All the materials listed in Table 3.1 are rotational molding grade resins supplied in powder form.

3.2. Equipment and procedures

3.2.1. Evaluation of powder properties

Bulk density (ASTM D 1895)

The bulk density of a powder is the weight of powder that is held in a given volume without being packed. The measuring apparatus consisted of a cylindrical cup of 100 ± 0.5 cm^3 capacity and a funnel having a 9.5 mm diameter opening at the bottom and mounted at a height of 38 mm above the cup. A 100 g powder sample was poured into the funnel, which had the bottom closed with a flat strip. The bottom of the funnel was opened quickly and the material was

allowed to flow freely into the cup. The excess of material was removed from the top of the cup with a ruler and the material in the cup was weighed. The bulk density was calculated as the weight in grams of 1 cm^3 of the material.

Table 3.1: Material properties

Resin	Trade Name	Supplier	MFI or MFR[1] (g/10 min)	Density (kg/m^3)
PE-1	Escorene LL-8461	Exxon Chemical	3.3	939
PE-2	Escorene LL-8361	Exxon Chemical	5.2	932
PE-3	Escorene LL-8556	Exxon Chemical	6.5	935
PE-4	Affinity DSQ 1504	Dow Chemical	3.5	949
PE-5	Affinity DSQ 1506	Dow Chemical	5	945
PE-6	XUS 59900.29L	Dow Chemical	15	935
PE-7	Borecene ME 8167	Borealis A/S	3.2	938
PP	Test Resin	Exxon Chemical	35	900
PP/PE-1	SC13 55RM	Borealis A/S	13	900
PP/PE-2	Test Resin	Exxon Chemical	20	900
PP/PE-3	Petrothene MT4390HU	Equistar Chemicals[2]	20	900
PP/PE-4	Petrothene TR121	Equistar Chemicals[2]	11	900
EBA	NCPE 8019	Borealis A/S	7.5	924
EVA-1	MU 763-00	Equistar Chemicals[2]	11	927
EVA-2	MU 760-00	Equistar Chemicals[2]	23	941
POP	SM 8250/XU 59400.00	Dow Chemical	30	885
PC	Makrolon 5303	Miles	11	1200

[1] MFI (for PEs) evaluated at 190°C – MFR at 230°C for PPs and 300°C for PC

[2] Formerly Quantum

Pourability (ASTM D 1895)

The funnel used for the bulk density, described above, was used for the pourability test, as well. A sample of the powder weighing in grams 100 times its density after molding was used. The sample was worked on a paper until there was no tendency for it to pack or cake. The powder was poured into the funnel, which had the bottom closed. The bottom of the funnel was opened quickly and with the aid of a stopwatch the time for all the powder to flow out of the funnel was recorded. The time for the sample of powder to flow through the funnel gives a measure of the "ease of flow", i.e. the pourability.

Sieving procedure

The powders received from the suppliers have a wide particle size distribution, which may vary from one polymer to another. In order to obtain powder particles of similar size for the needs of the experiments, a ROTAP sieving machine was used. A set of 7 sieves of mesh sizes ranging from 500 microns (mesh No. 35) to 75 microns (mesh No. 200) were available. Sieving was done by shaking 100-200 grams of powder through the stack of sieves for 20 minutes.

3.2.2. Thermal properties

Differential Scanning Calorimetry (ASTM D 3417)

The melting points, heats of fusion and crystallinities of the semi-crystalline polymers, were determined by DSC (DuPont model TA2100). The instrument was calibrated with a standard reference material (Sapphire) at a

heating rate of 10°C/min. 5 - 10 mg of powder were placed into hermetic pans, which were loaded into the instrument cell. The cell was purged with nitrogen. The samples were first held isothermally at a starting temperature of 30°C for 5 min. Afterwards they were heated at a rate of 10°C/min and the heating curve was recorded. The area under the fusion endotherm peak, which corresponds to the heat of fusion, was calculated.

Two types of melting temperatures were determined from the recorded curves: The extrapolated onset temperature and the melting peak temperature.

The crystallinity of the polymers was calculated from the ratio of the calculated enthalpy (heat) of fusion and the enthalpy of fusion of a completely crystalline sample (Richardson, 1984):

$$\% \text{ crystallinity} = (H_f / H_{f,c}) \times 100 \qquad (3\text{-}1)$$

where H_f the enthalpy of fusion of the sample, in J/g and $H_{f,c}$ the enthalpy of fusion of a 100% crystalline sample of the same polymer, in J/g

The values of the enthalpies of fusion of completely crystalline isotactic polypropylene and polyethylene samples are 163 J/g and 293 J/g respectively (Mark, 1990). The theoretical value of the enthalpy of fusion of a completely crystalline mixture of polypropylene and polyethylene was calculated using a weighted average of the above two values.

Thermogravimetric analysis (TGA)

Thermogravimetric analysis (TGA) was performed in selected polymer samples using a NETZSCH STA-409 Simultaneous Thermal Analyzer, under

atmospheric air.

In thermogravimetric analysis, the mass of a substance as a function of time and temperature is used to assess the thermal stability and degradation of polymers. The test is conducted by heating the sample to the desired conditions and recording the mass of the sample as a function of temperature or time (Mathot, 1994). Weight losses occur when volatiles absorbed by the polymer are driven off and at higher temperatures when degradation of the polymer occurs, leading to the formation of volatile products. Thus this technique can be used both to examine the state of the material (i.e. presence and quantity of volatiles and/or water) and to investigate the process of degradation. The purpose of this test was to examine the possibility of degradation, existence of residual monomer vapors in the polymers or gas generation when the polymers were exposed to conditions similar to the experimental conditions used for the bubble formation and dissolution experiments.

Two types of tests were conducted. The first test was isothermal at 190°C and its purpose was to determine the time needed for the onset of degradation. The second test was non-isothermal and determined the temperature at which degradation of the polymer samples occurred.

Crystallization Analysis Fractionation

The PP/PE copolymers were analyzed by Crystallization Analysis Fractionation (Monrabal, 1994, 1996), which is a technique similar to Temperature Rise Elution Fractionation to evaluate the copolymer content

distribution and measure the amorphous content in the polymers. A CRYSTAF instrument, model 100, developed by Polymer Char in Spain was used. The tests were conducted by Polymer Char. A 0.1% by weight solution of the polypropylenes in trichlorobenzene was used for the test. The polymers were dissolved at 170°C for 60 minutes and then cooled quickly to 90°C. From there, crystallization proceeded at a rate of 0.1°C/min until the temperature reached 30°C. In CRYSTAF the analysis is carried out by monitoring the polymer solution concentration during crystallization by temperature reduction. Samples of the solution are filtered and analyzed by a concentration detector.

A typical CRYSTAF trace, for an LLDPE containing short chain branching, is shown in Figure 3.1 (Monrabal, 1994). The first data points, taken at temperatures well above crystallization, provide a constant concentration equal to the initial polymer solution concentration (zone 1 in Figure 3.1). As temperature goes down, the most crystalline fractions, composed of molecules with zero or very few branches precipitate first, resulting in a steep decrease in the solution concentration (zone 2 in Figure 3.1). This is followed by precipitation of fractions of increasing branch content as temperature continues to decrease (zone 3). The last data point, corresponding to the lowest temperature of the crystallization cycle, represents the fraction that has not crystallized and remains soluble. The first derivative of the cumulative curve corresponds to the comonomer content distribution, or short chain branching distribution.

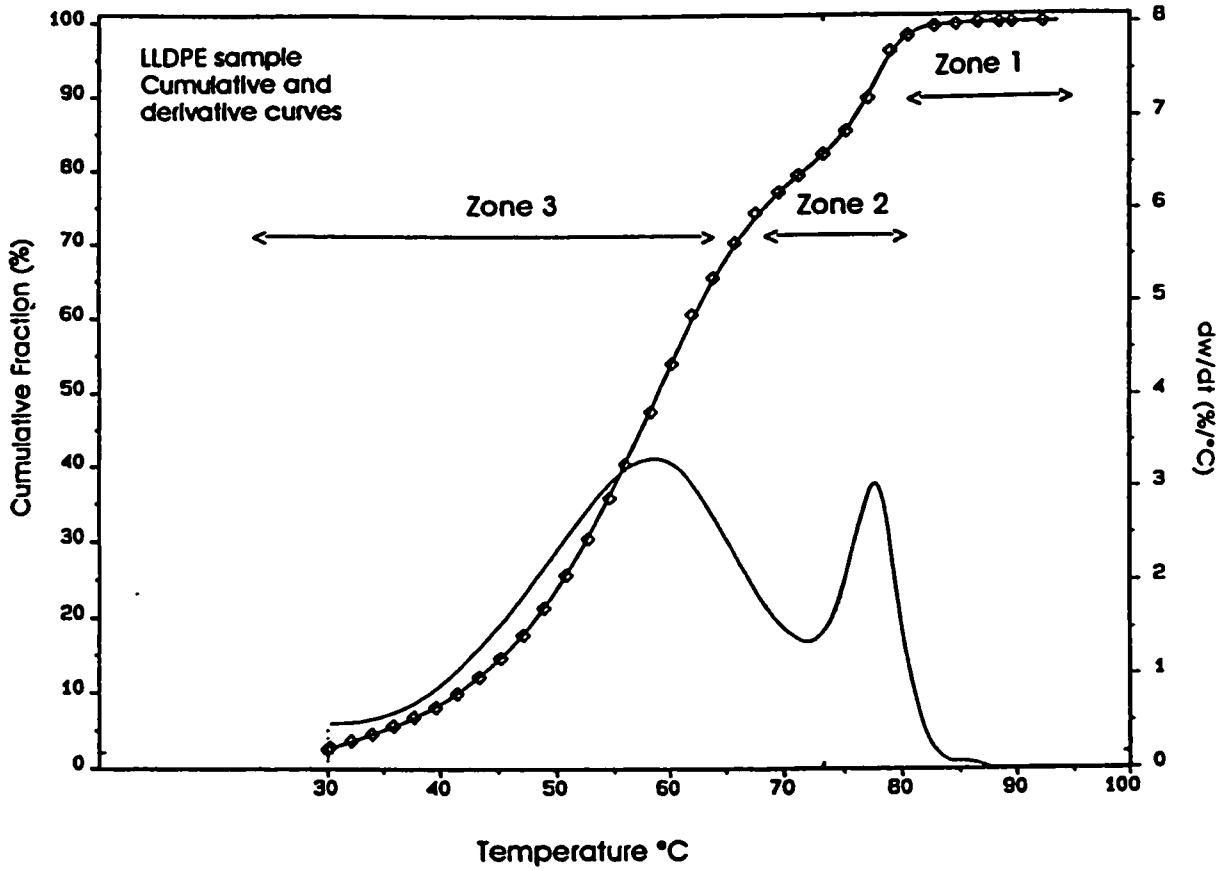

Figure 3.1: Typical CRYSTAF trace for LLDPE containing short chain branching (Monrabal, 1994)

3.2.3. Rheological properties

Dynamic measurements

In dynamic (oscillatory) measurements the stress response of a viscoelastic material to a sinusoidally varying strain is monitored as a function of time. Dynamic measurements are useful for the study of the viscoelasticity of the materials. They are also useful for obtaining values of (dynamic) viscosity for shear rates higher than those reached by simple shear viscosity measurements.

A Rheometrics (model ARES) rotational rheometer equipped with a parallel plate measuring system was used for the dynamic measurements. The gap between the parallel plates varied from 0.5 to 1 mm. Strain rates during the dynamic experiments ranged from 5% to 15%. Measurements of dynamic modulus versus strain rate were done to ensure that this range was within the linear viscoelasticity region. The dynamic viscosity was recorded as a function of the frequency, ω (in rad/s). The zero shear viscosity was determined from the dynamic viscosity measurement by applying the Cross model (Macosko, 1994):

$$\frac{\eta - \eta_\infty}{\eta_o - \eta_\infty} = \frac{1}{1 + \left(\lambda^2 \left| II_{2D} \right| \right)^{(1-n)/2}} \qquad (3\text{-}2)$$

where η is the shear viscosity, η_∞ the high shear rate Newtonian limit, η_o the zero shear viscosity, λ the characteristic time, which is specific for each resin, n the shear thinning parameter and $(II_{2D})^{1/2} = \dot{\gamma}$

The Cross model, equation (3-2) can be simplified to give:

$$\eta = \frac{\eta_o}{1 + \left(\lambda \dot{\gamma}\right)^{(1-n)}} \qquad (3\text{-}3)$$

The storage modulus, G′ and the loss modulus, G″ were measured as a function of frequency at different temperatures. The storage modulus is associated with the elastic character of the material, while the loss modulus is associated with the viscous character of the material. Thus the measurements of storage and loss modulus can give valuable information about the viscoelastic properties of the materials.

Master curves were constructed in order to cover the largest possible range of frequencies. The shift factor, used to shift the curves, thus superimposing them, is calculated by using the WLF equation (Ferry, 1980):

$$\log a_T = \frac{-C_1(T-T^*)}{C_2+(T-T^*)} \tag{3-4}$$

where T* is the glass transition temperature, or a reference temperature and T is the actual temperature of the measurement.

By performing measurements at a sufficiently wide range of temperatures and using the time-temperature superposition, it has been possible to construct master curves, which cover several decades of frequency. This was accomplished with the aid of a specialized software named IRIS© (Baumgartel et al., 1994).

3.2.4. Rotational molding apparatus

Clamshell rotational molding machine

A clamshell rotomolding machine, model M20, manufactured by FSP machinery was used for the molding experiments. In this type of machine, shown in Figure 3.2 heating and cooling take place inside the same chamber (inside the

Figure 3.2: Picture of FSP Clamshell rotational molding machine (model M20)

clamshell). The heating cycle is conducted first by heating the oven by hot air. After the cure is complete, the burner is extinguished and a circulating air fan is used to cool the product. In the cooling cycle a bypass duct allows the surrounding air to be ducted into the oven chamber to provide the cooling air. Later in the cooling cycle, water spray can be introduced into the oven to cool the mold.

A cubic mold made of steel, with dimensions 9.5x9.5x10 cm^3 was used. The shot weight was 140 g, which produced parts with approximately 3 mm wall thickness. The mold surface was coated with a silicon based mold release (Dura Kote by Chemtrend). A mold rotation ratio of 4:1 was used, corresponding to main axis rotation of 4 rpm and secondary axis rotation of 1 rpm. Polycarbonate powders were dried in a vacuum oven for one day prior to the experiment, because they are very hygroscopic.

A range of different oven temperature / heating time combinations were applied, depending on the type of materials used, in order to determine the effect of processing conditions on mechanical properties. The controllable parameters were the maximum oven temperature and the residence time at the maximum oven temperature. The oven temperatures varied from 260 to 330°C. In most cases, the oven was programmed to maintain the maximum temperature for several prescribed periods of time, ranging from 1 to 4 minutes. This was done with the purpose of prolonging the residence time of the polymer inside the oven without raising the temperature excessively, which would result in degradation of

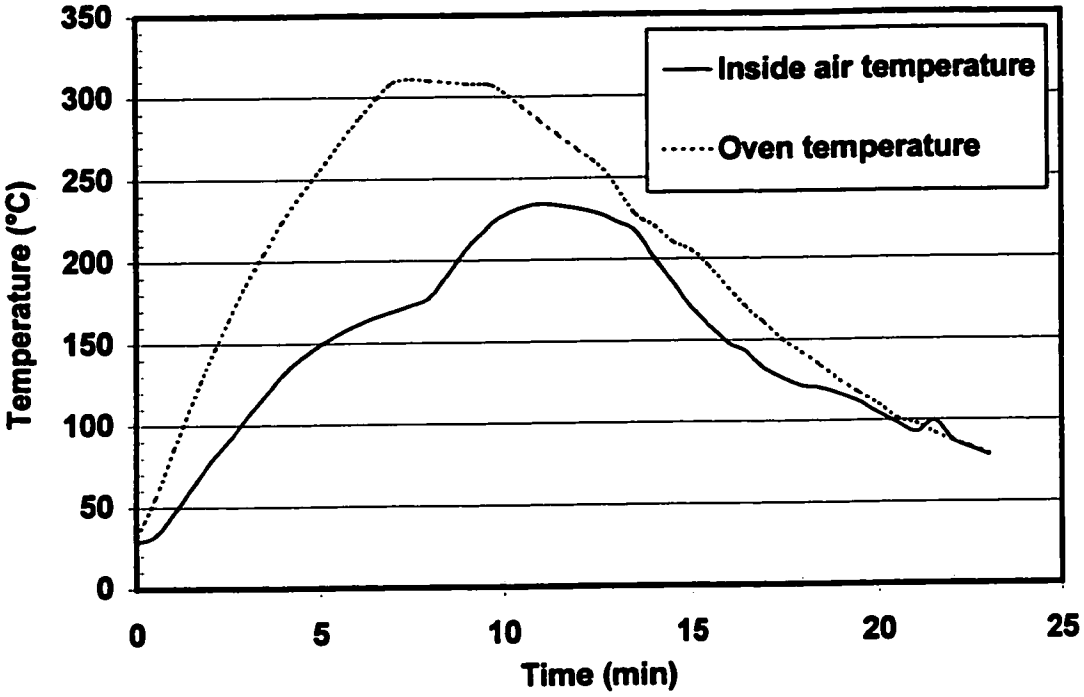

Figure 3.3 (c): Oven temperature and inside the mold air temperature profile for oven temperature set-point 310°C and residence time at peak oven temperature 3 min.

3.2.5. Rotomolded part characterization

Dart impact tests (A.R.M. standard)

This test determines the energy required to cause failure of plastic samples by a free falling dart. A 3 m high dart drop tester, equipped with a 10 lb. (4.536 kg) dart was used. An air circulating freezer with adjustable thermostat was used to cool the samples at –40°C, for low temperature impact tests.

Samples having a thickness of 3 mm were prepared with the clamshell machine using the cubic mold. Flat square samples with dimensions 8.3×8.3 cm were cut off the boxes. Two boxes where prepared for each condition, which means that 8 flat samples were tested in total for each condition.

For the low temperature tests the specimens were conditioned in the freezer for 4 hours at -40°C, prior to the test.

The samples were placed on the test holder with the inner surface of the part facing downwards. The dart was raised to an initial height chosen arbitrarily or based on previous experience. Subsequently it was released and the result of pass or fail for the sample was recorded. The type of failure (brittle or ductile) was also recorded. If the first specimen failed the dropping height was lowered by 7.5 cm (0.25 ft) and the test was repeated with a new specimen. If the new specimen failed again, the height was continuously decreased, until the part passed. When the part passed the height was continuously increased by 7.5 cm until failure occurred. The procedure continued until all of the 8 specimens,

corresponding to each experimental condition, were tested. The mean failure height was calculated as:

$$h = h_o + \Delta h(A / N \pm 0.5) \qquad (3\text{-}5)$$

where h: mean failure height, *m*

h_o: shortest height at which an event occurred, *m*

Δh: increment of the change in dart height used (0.075 cm)

N: total number of events (failures or non-failures), whichever is smaller

also $A = \sum_{i=0}^{i=k} i n_i$

n_i : number of events at h_i

$h_i = h_o \pm i\,\Delta h$

h_k : maximum height at which an event occured

The negative sign is used in equation (3-5) when the events are failures and the positive sign is used when the events are non-failures.

The mean failure energy, MFE, in m.kg, was calculated as follows:

$$MFE = h \times w \qquad (3\text{-}6)$$

where w: dart weight, in kg

Tensile tests (ASTM D638M)

Tensile tests were performed on specimens cut from the rotomolded parts with a specially designed die cutter. The dimensions of the specimens were in accordance to the guidelines described in the standard test (Type M-III from ASTM D638).

A LLOYD tensiometer, equipped with a 1kN load cell was used for the tensile tests. Five test specimens were tested for each material. The width and

thickness of the specimens were measured by means of a micrometer. The speed of testing was 50 mm/min. The load versus extension curves were recorded and were transformed into stress vs. strain curves. The tensile strengths at yield and at break were calculated, by dividing the loads at yield and at break by the original minimum cross-sectional area of the specimen. The percent elongations at yield and at break and the moduli of elasticity were also calculated.

3.2.6. Bubble formation and dissolution experiments

Apparatus

Bubble formation and dissolution experiments were conducted by using a heating chamber, which consisted of a cylindrical oven with a diameter of 16 cm and a height of 11 cm. The oven was made out of an aluminum shaft with a hole cut through it. The hole had quartz covers at both ends, to allow light to be transmitted during microscopic observations. A schematic of the oven is shown in Figure 3.4. Detailed design schematics are shown in Figure 3.5. (Sloane, 1997).

Heat was supplied to the oven by a band heater. A temperature controller was used to control the oven temperature. A K-type thermocouple inserted through the oven wall measured the wall temperature, which was used as the control parameter for the oven temperature. A second K-type thermocouple measured the sample temperature through a hole drilled on the oven cover.

Experimental procedure

A sample cup holder, made of glass (D=2.5 cm, H=1 cm) was loaded with 0.7 grams of powder and placed in the center of the heating chamber. Whole

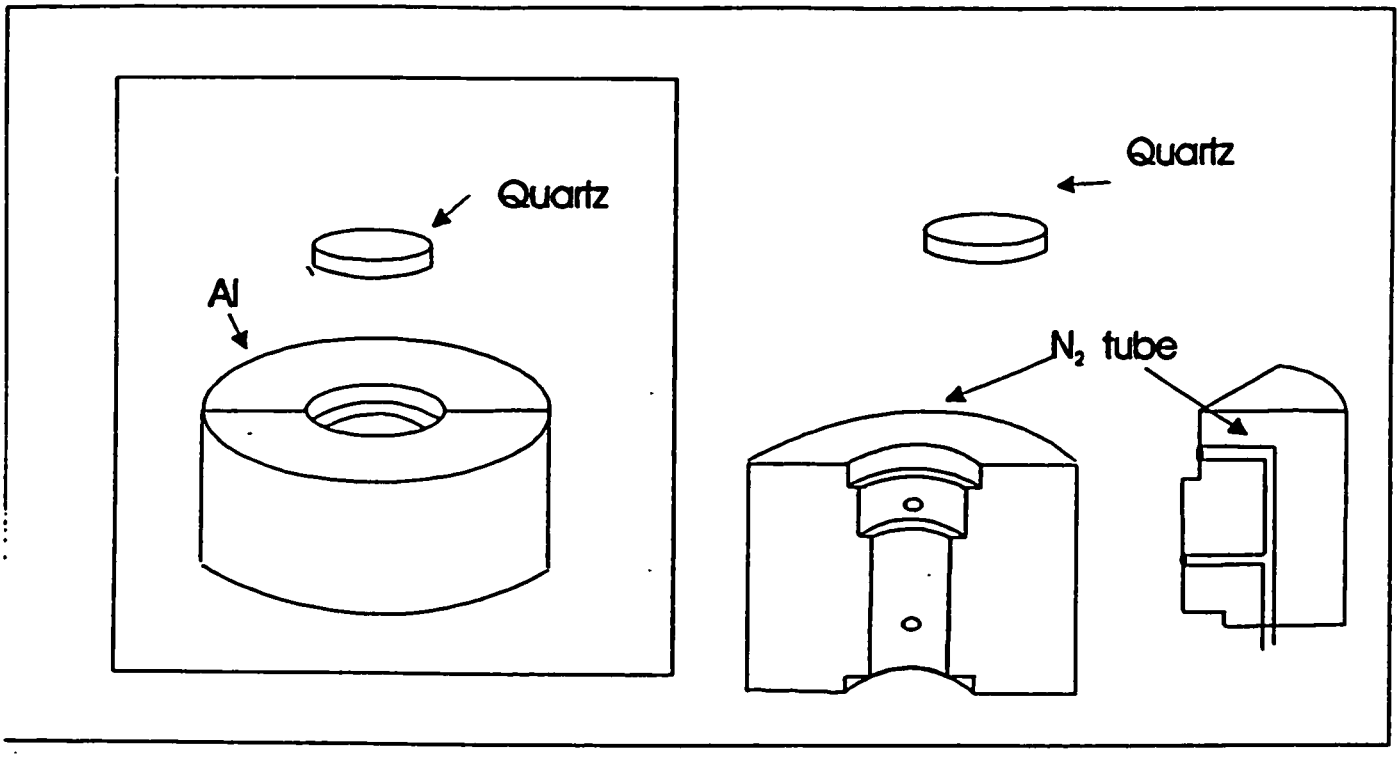

Figure 3.4: Schematic of the heating chamber, consisting of cylindrical oven and quartz sample holder (Sloane, 1997).

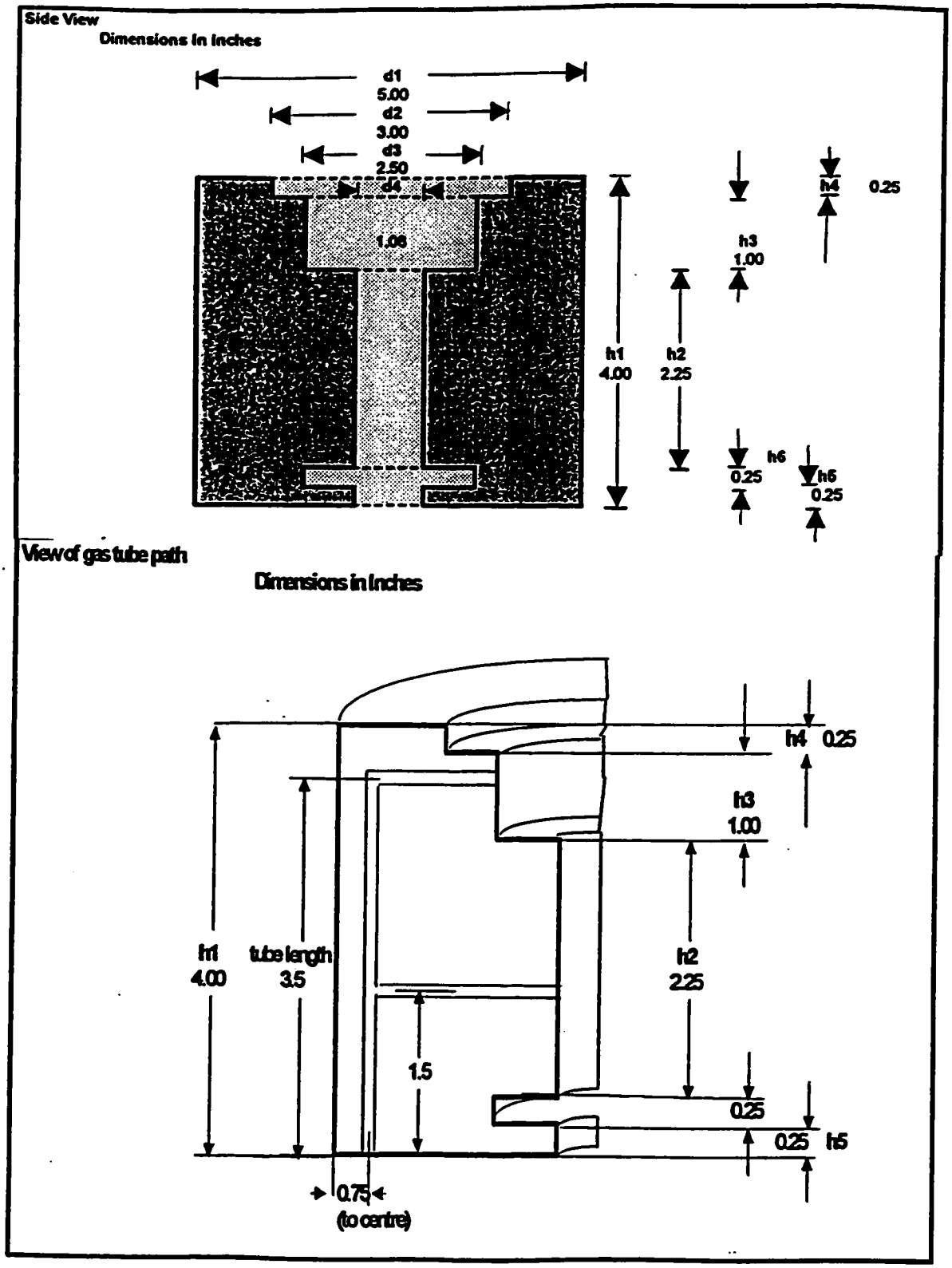

Figure 3.5: Detailed schematics of heating chamber

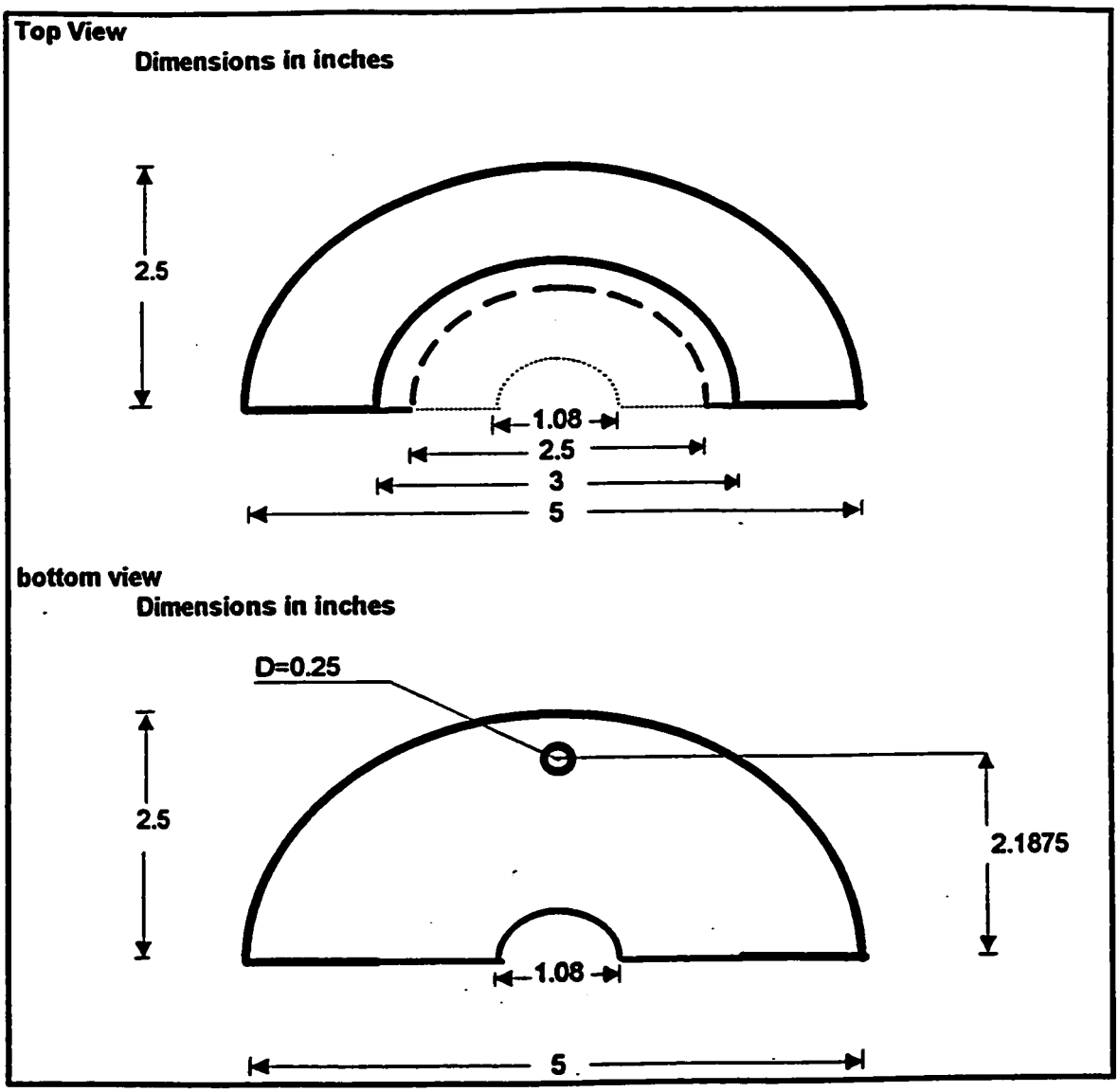

Figure 3.5 (cont'd): Detailed schematics of heating chamber

powder as received from the resin producers or sieved was used.

Two series of bubble formation experiments were done under atmospheric pressure. The purpose of the first series was to conduct experiments isothermally. The samples were placed inside the oven, which was preheated at 190°C.

However it was found that it is impossible to maintain truly isothermal conditions during the initial minutes which are crucial for the formation of bubbles, because the heating of the powder is inherently non-isothermal. The second difficulty encountered was that it was hard to compare resins with different melting points.

Therefore a second series was done under non-isothermal conditions, intended to simulate the non-steady state conditions encountered in the actual rotomolding process. The samples were placed inside the oven at room temperature and were heated subsequently, after the oven temperature set-point was fixed to 230°C. Typical oven temperature and polymer melt profiles obtained during a non-isothermal experiment are shown in Figures 3.6 – 3.8 for polyethylenes, polyethylene copolymers and polypropylenes respectively. The polymer melt temperatures shown in the graphs were recorded at the center of the sample every time. There was an unavoidable temperature variation within the sample due to the non-steady state nature of the experiment, but measurements of temperature within several positions inside the melt revealed that the maximum variation from the center of the melt to the oven wall was 3 to 4°C.

All bubble dissolution experiments were conducted isothermally at 190°C.

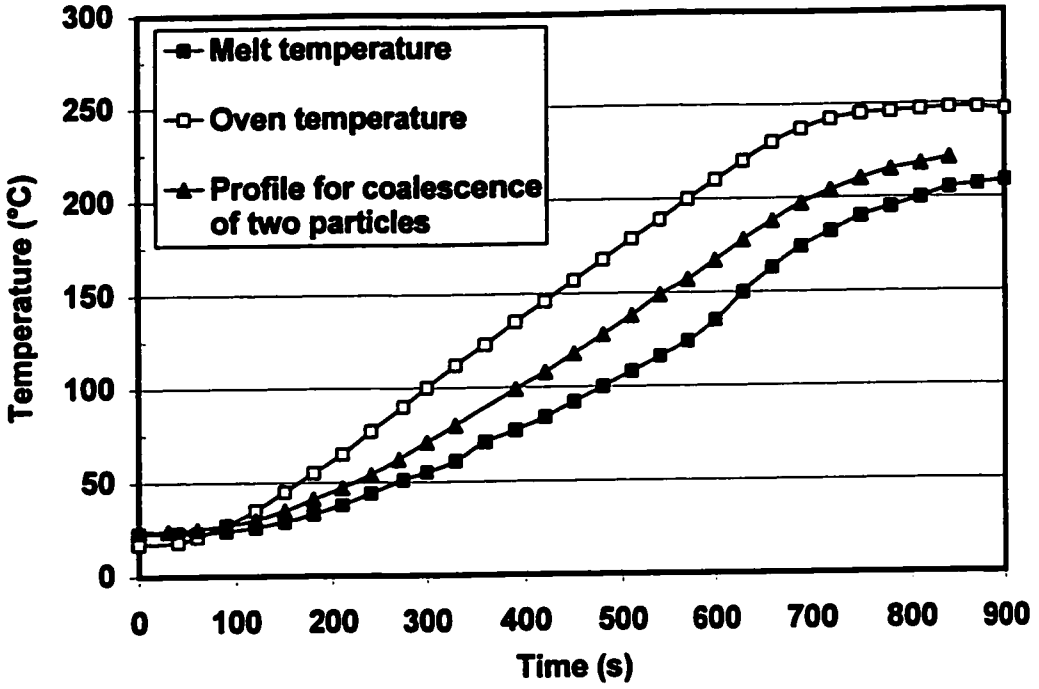

Figure 3.6: Oven and melt temperature profile for polyethylene for particle coalescence, bubble formation and densification experiments.

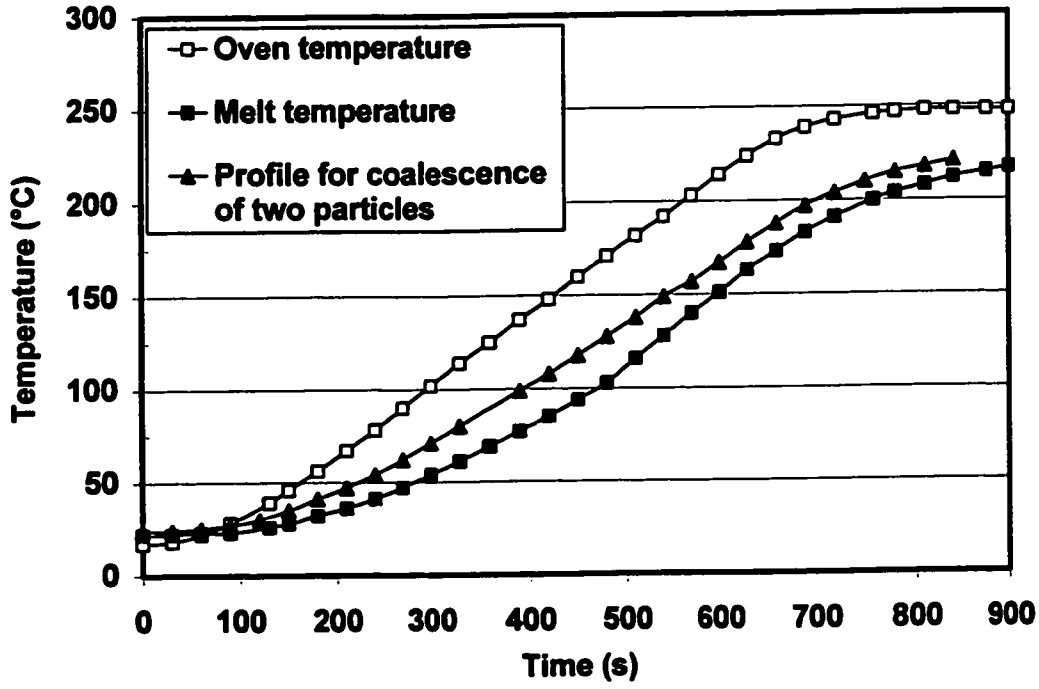

Figure 3.7: Oven and melt temperature profile for polyethylene copolymers for particle coalescence, bubble formation and densification experiments

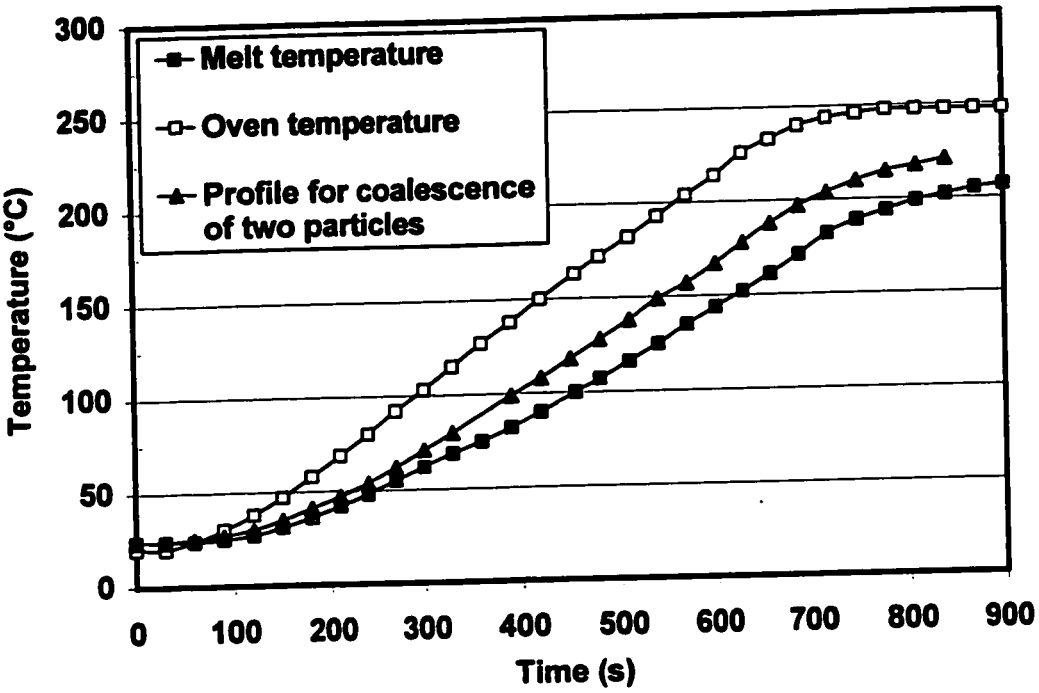

Figure 3.8: Oven and melt temperature profile for polypropylene for particle coalescence, bubble formation and densification experiments

The process of powder melting and air entrapment inside the melt was observed through an Olympus optical microscope and recorded with a Panasonic video camera. Several bubbles were observed as they formed and subsequently dissolved.

In all cases the microscope was aimed at the area in the center of the sample. A frame grabber (Data Translation), accompanied by a software package (HLImage++97) was used to obtain images for further image analysis. Bubble content and bubble size distribution, as well as the reduction of the bubble diameter with time were evaluated by image analysis using a specialized software (Sigma-Scan Pro version 3.0) (Jandel Scientific Software, 1992). The reported values of bubble content and bubble diameter were obtained as averages of three experiments. The maximum estimated error was 5%.

3.2.7. Densification experiments

Densification experiments were performed using the heating chamber described above, in order to evaluate how the density of the polymer samples changes as a function of heating time and to visualize the structure of the melt at different times throughout the densification process. In these experiments the polymer powder was heated for predetermined amounts of time. Subsequently the cup holder containing the melt was removed and quenched into water to "freeze" the structure of the sintered powder compact. The density of the solidified compact was measured as described below and thin slices were cut and observed under the microscope.

Isothermal experiments were done to allow comparison of the experimental data with theoretical models, while non-isothermal experiments intended to simulate real rotomolding behavior. Isothermal experiments were conducted at temperatures just above the melting points of the polymers, i.e. 105°C for PE copolymers, 132°C for polyethylenes and 165°C for polypropylenes. These temperatures, just above the melting points of the polymers, were chosen because under these conditions densification progressed at a relatively slow rate, which made sampling at intervals of 30 seconds adequate and allowed the sample to reach uniform temperatures before any substantial neck growth between particles took place.

The temperature profiles for the non-isothermal experiments are the same as those for bubble formation experiments, shown in Figures 3.6 through 3.8.

Average values from three experiments were reported. The error in the measurements ranged from 0.25- 4.8%.

Density measurements

Segments of dimensions 1cm x 1cm were cut around the centre of the solidified samples prepared as described above. The density of the solid samples was measured with a MD-200S electronic densimeter. This instrument operates using the Archimedes principle. The determination of the density value is based on the density of water at 4°C (1 g/cm^3). The same method was used to measure the density of some rotomolded parts as a function of oven temperature. In this case 4cm x 2cm samples were cut from the rotomolded parts. Error in the density

measurements was a consideration, but repeat measurements of the same sample revealed that the maximum error was 2.7%.

The thickness of the samples was measured using a Mitutoyo digital micrometer.

3.2.8. Particle coalescence experiments

Particle coalescence experiments using only two particles were also done for comparison with the overall bubble formation and densification behavior of the polymers. These experiments were conducted non-isothermally, using the same oven conditions as described in the bubble formation experiments. However, the sample temperature increased at a higher rate than in the bubble formation and densification experiments, because of the presence of only two particles instead of a powder compact, as shown in Figures 3.6, 3.7 and 3.8.

In order to exclude the powder size effects that can affect the sintering process, cylindrically shaped particles of diameter 0.32 mm and height 0.3 mm were prepared. The samples were prepared by compression molding, using a plate with holes of diameter 0.32 mm and height of 0.3 mm. The cylinders were cut off from the compression molded film.

The rate of coalescence was quantified with the aid of image analysis in terms of the neck radius between particles (y) and the particle radius (a), as described by Bellehumeur et al. (1996) and Bellehumeur (1997) (see also Figure 2.3). Plots of dimensionless neck growth (y/a) versus time were constructed.

Chapter 4

RELATIONS BETWEEN POLYMER PROPERTIES, ROTOMOLDING CYCLES AND PART PROPERTIES

4.1. Introduction

The majority of the research work performed until now in rotational molding has dealt with processing of polyethylene. Linear Low Density Polyethylene (LLDPE) is used extensively, because it meets the standards of impact strength (or toughness), which is a major requirement for rotomolded products. However, the rotational molding industry also needs materials offering good surface hardness, stiffness and high temperature stability, properties not achievable by polyethylene. Seeking expansion to new markets, resin producers have introduced other materials, such as rubber modified polypropylenes, polycarbonate, ethylene-vinyl-acetate (EVA) and ethylene-butyl-acrylate (EBA) copolymers, as well as various polyethylenes made by metallocene catalysts.

Although theoretically every thermoplastic with a suitable viscosity should be processable by rotational molding, it has not been possible to rotomold successfully many thermoplastic polymers in a commercial scale. The purpose of this chapter is to present a thorough investigation on the properties of various rotational molding grade polymers and how they affect their processing behavior in rotational molding.

Some important properties of the resins under consideration are summarized in Table 4.1. In Table 4.1. values of viscosity of all polymers are reported at 190°C to provide a reference for comparison between materials. The comonomer content in the PP/PE copolymers has been determined using combined ^{13}C NMR and FT-IR chemical analysis. Details of the chemical analysis are given elsewhere (Kontopoulou, 1995).

4.2. Material properties and processing of Polyethylene and Polyethylene Copolymers

4.2.1. Material properties

Resin producers often aim at the production of materials with very low crystallinity, which can produce flexible products with elastomeric properties. This is achieved by copolymerizing polyethylene with various comonomers. Vinyl – acetate and butyl – acrylate are the two most frequently used comonomers in the rotomolding industry. Recently the advent of metallocene catalysts has made possible the production of very low and ultra low density polyethylenes, by using comonomers such as hexene and octene. These materials, which also have elastomeric properties, are often termed as Polyolefin Plastomers (POP) or Polyolefin Elastomers (POE). All the polymers described above have very low crystallinities and low melting points (see also Table 4.1). DSC traces for the PE copolymers are shown in Figure 4.1. Figure 4.2 compares the DSC traces of a PE copolymer (EVA-2) and a typical rotomolding grade LLDPE (PE-2).

Table 4.1: Material properties of resins used in the current study

Resin	Conomomer content (mole%)	Zero shear viscosity (Pa-s) at 190°C	Melting point or glass transition (°C)	Heat of fusion (J/g)	% Crystallinity
PE-1	-	2658	128	142	49
PE-2	-	1830	128	122.8	43
PE-3	-	1413	127	137.4	48
PE-4	-	2722	133	160.3	55
PE-5	-	1794	130	142.5	49
PE-6	-	525	128	137.6	48
PE-7	-	2400	127	146.8	50
PP	-	503	160	95.95	59
PP/PE-1	12.4	2700	164	81.9	48
PP/PE-2	13.1	1364	163	80.9	49
PP/PE-3	14.8	1020	165	71.9	41
PP/PE-4	16	2112	164	71.8	40
EBA	17	2420	52, 99[2]	59.6	20
EVA-1	9	1969	62, 97[2]	83.9	29
EVA-2	19	714	56, 87[2]	64.4	22
POP	*	275	48.7, 88[2]	47.7	16
PC	-	68000[1]	149 (T_g)	-	-

* not reported by supplier
[1] measured at 200°C
[2] corresponding to double peaks

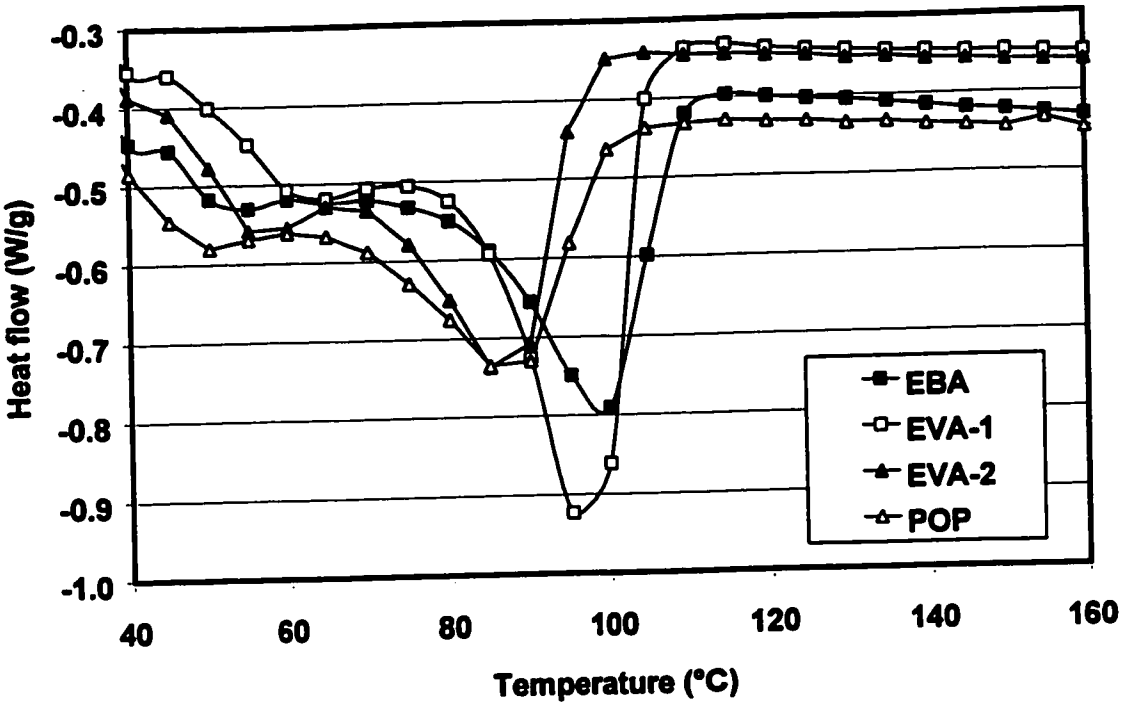

Figure 4.1: Comparison of DSC traces of PE copolymers

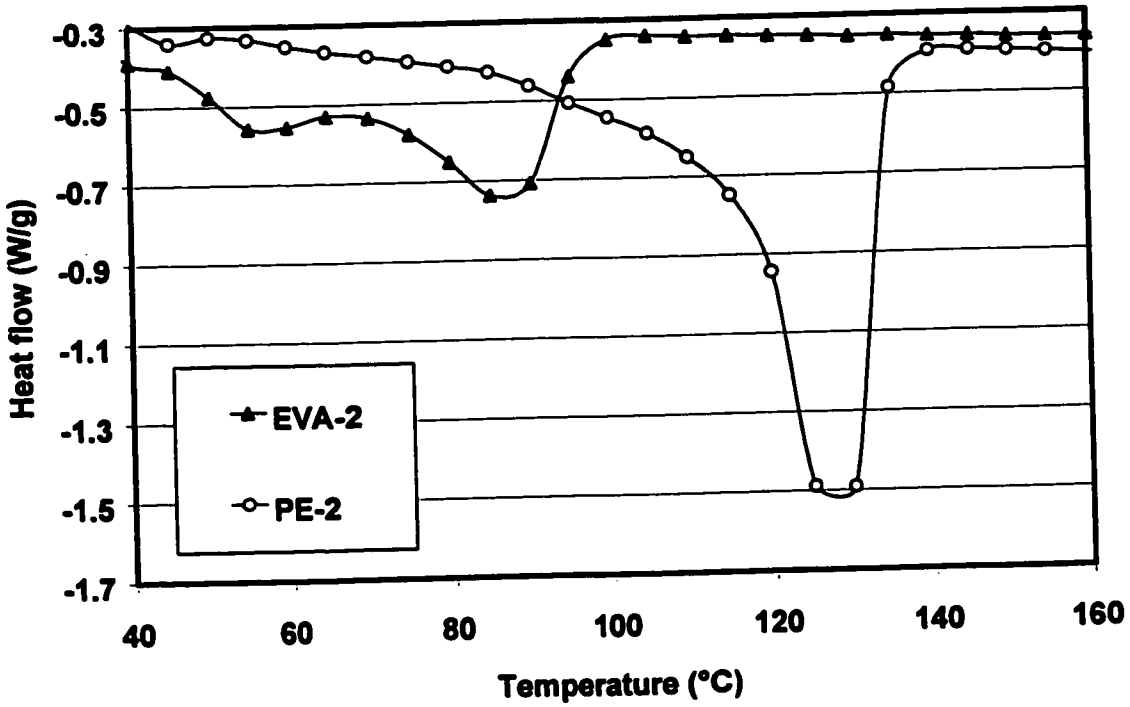

Figure 4.2: Comparison of DSC traces of polyethylene (PE-2) and polyethylene copolymer (EVA-2)

The dynamic viscosity versus shear rate curves at 170°C are shown in Figure 4.3. Generally the viscosity curves of the PE copolymers, with the exception of POP, display noticeable shear thinning characteristics. PE-2 shows little shear thinning, indicating a relatively narrow molecular weight distribution, which is common in rotational molding grade polyethylene resins. POP which is made by metallocene catalyst polymerization shows very little shear thinning, as well.

Rotational molding is a temperature and time dependent process, exhibiting complex transient and non-isothermal phenomena, in addition to its low shear character.

Therefore a meaningful rheological characterization, which would allow one to predict the processing behaviour of the polymers, should take into account temperature changes. This can be achieved by temperature based methods, such as measuring the viscosity as a function of shear rates at different temperatures and extrapolating to find the zero shear viscosity. It was found that the viscosity of PE copolymers decreases slowly as temperature increases, starting from very high values (Figure 4.4). By contrast, the viscosity of PE-2 assumes relatively low values immediately upon reaching the melting point at approximately 130°C. A notable exception from the copolymers is the POP resin, whose viscosity decreases rapidly as temperature increases.

Dynamic oscillatory measurements covering a wide spectrum of frequencies, can give very useful information about the viscoelastic behavior of

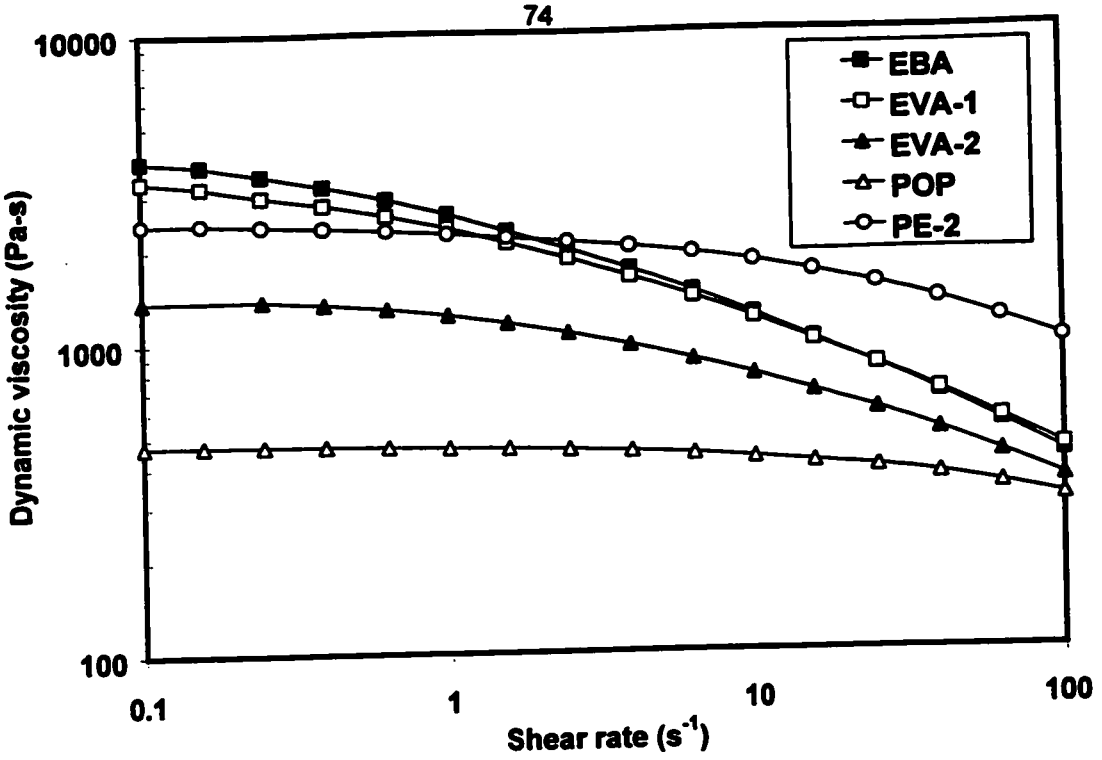

Figure 4.3: Comparison of dynamic viscosity curves for PE and PE copolymers at 170°C

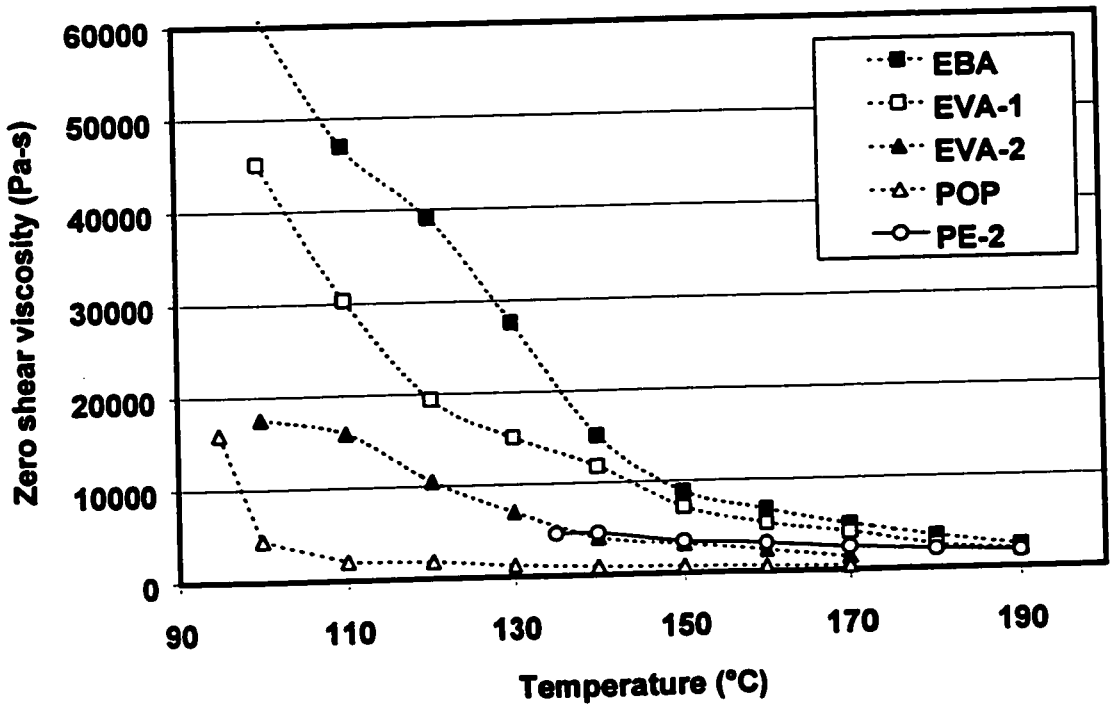

Figure 4.4: Viscosity versus temperature curves for PE and PE copolymers

the polymer, which is related to its molecular structure. Since it is useful to capture the behavior at as low frequencies as possible (corresponding to low shear rates, according to the Cox-Merz rule) which are relevant to rotational molding, it is desirable to cover a large range of frequencies when performing the dynamic oscillatory measurements. If the equipment resolution is not enough to achieve sufficiently low frequencies, time-temperature superposition can be used. In this method, measurements are performed at different temperatures and the resulting curves are superimposed, to yield a master curve, which covers a large range of frequencies. The shift factor, used to shift the curves, thus superimposing them, is calculated by using the WLF equation (Ferry, 1980):

$$\log a_T = \frac{-C_1(T-T^*)}{C_2+(T-T^*)} \tag{4-1}$$

where T* is the glass transition temperature, or another reference temperature, α_T is the temperature shift factor and C_1, C_2 are constants determined by curve-fitting (Baumgärtel et al., 1994).

By performing measurements at a range of temperatures and using time-temperature superposition, master curves have been constructed, covering several decades of frequency. Measurements were performed for all the PE copolymers at temperatures ranging from 95 to 190°C and for PE at temperatures between 130 to 190°C. Time-temperature superposition was done using specialized software named IRIS© (Baumgärtel et al., 1994). Master curves obtained for the PE copolymers at a reference temperature of 170°C are shown in Figure 4.5 (a),(b).

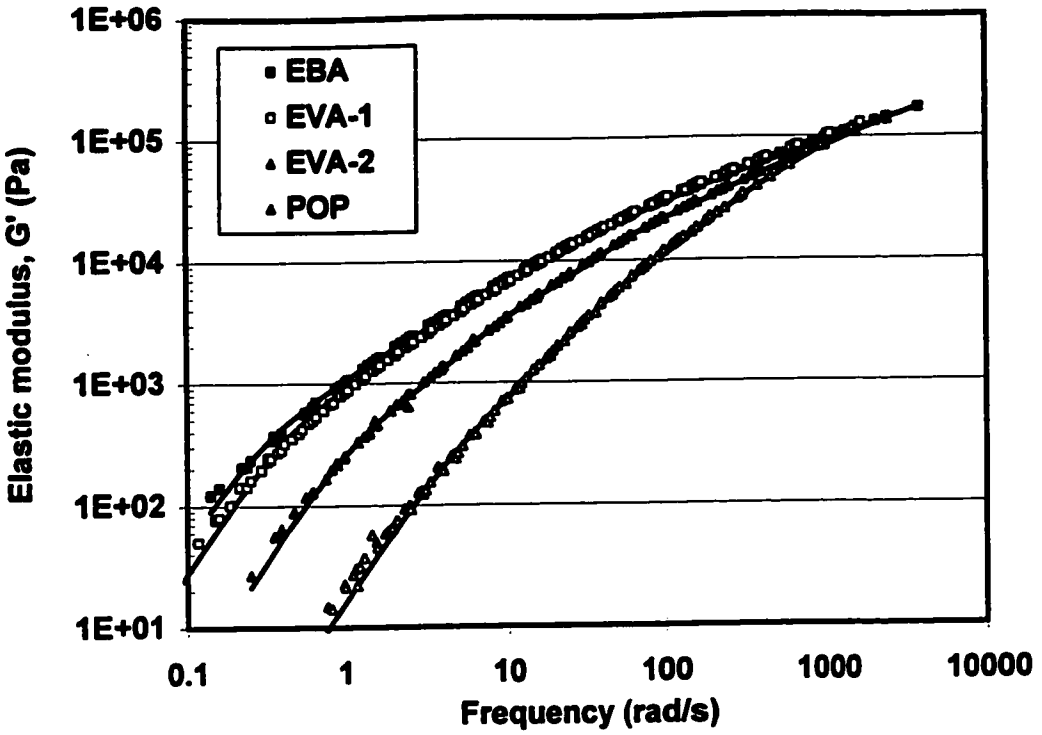

Figure 4.5 (a): Comparison of elastic modulus master curves for PE copolymers (T_{ref}=170°C). Solid lines indicate fit by series of Maxwell relaxation modes.

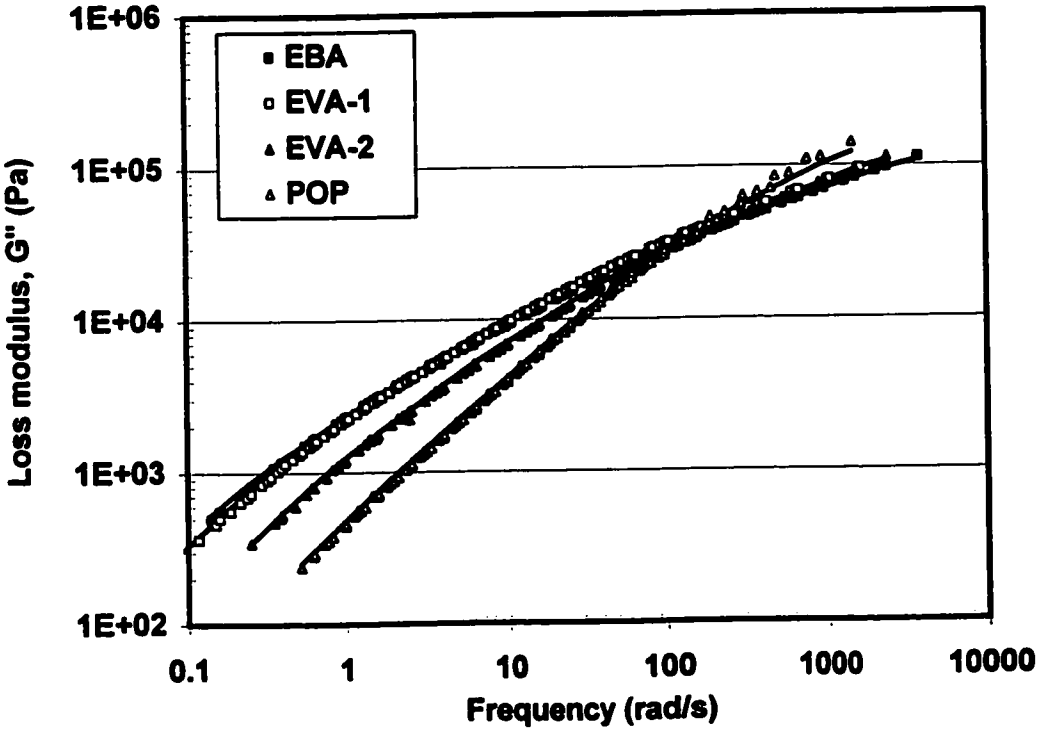

Figure 4.5 (b): Comparison of loss modulus master curves for PE copolymers (T_{ref}=170°C). Solid lines indicate fit by series of Maxwell relaxation modes.

The master curve for a typical polyethylene (PE-2) at a reference temperature of 170°C is shown in Figure 4.6. A comparison of the elastic modulus (G′) curves of the PE copolymers shows that in general they cover a wider frequency range than the respective PE curve, with the exception of the POP resin. A comparison of the ratio tanδ = G″/G′ is shown in Figure 4.7. For the PE copolymers, tanδ is generally lower, indicating a higher contribution of the elastic response to the total rheological response of the polymers. POP has the highest tanδ values.

The data shown in Figures 4.5 and 4.6 can be used to calculate the discrete relaxation spectra of the polymers under consideration. The relaxation time distribution was calculated by fitting simultaneously both storage and loss moduli data to a series of Maxwell-type relaxation modes (Ferry, 1980, Baumgärtel and Winter, 1989), to yield a discrete relaxation time spectrum in the form of a discrete relaxation strength, g_i and discrete relaxation time, λ_i:

$$G'(\omega) = \sum_{i=1}^{N} g_i \frac{(\omega \lambda_i)^2}{1 + (\omega \lambda_i)^2} \qquad (4\text{-}2)$$

$$G''(\omega) = \sum_{i=1}^{N} g_i \frac{(\omega \lambda_i)}{1 + (\omega \lambda_i)^2}$$

The spectrum calculation was accomplished using non-linear regression analysis. The relative deviation between experimental data and values predicted by the model was minimized:

$$\sum_{n=1}^{N} \left(\frac{\Delta G'}{G'}\right)_n^2 + \left(\frac{\Delta G''}{G''}\right)_n^2 = \text{MIN} \qquad (4\text{-}3)$$

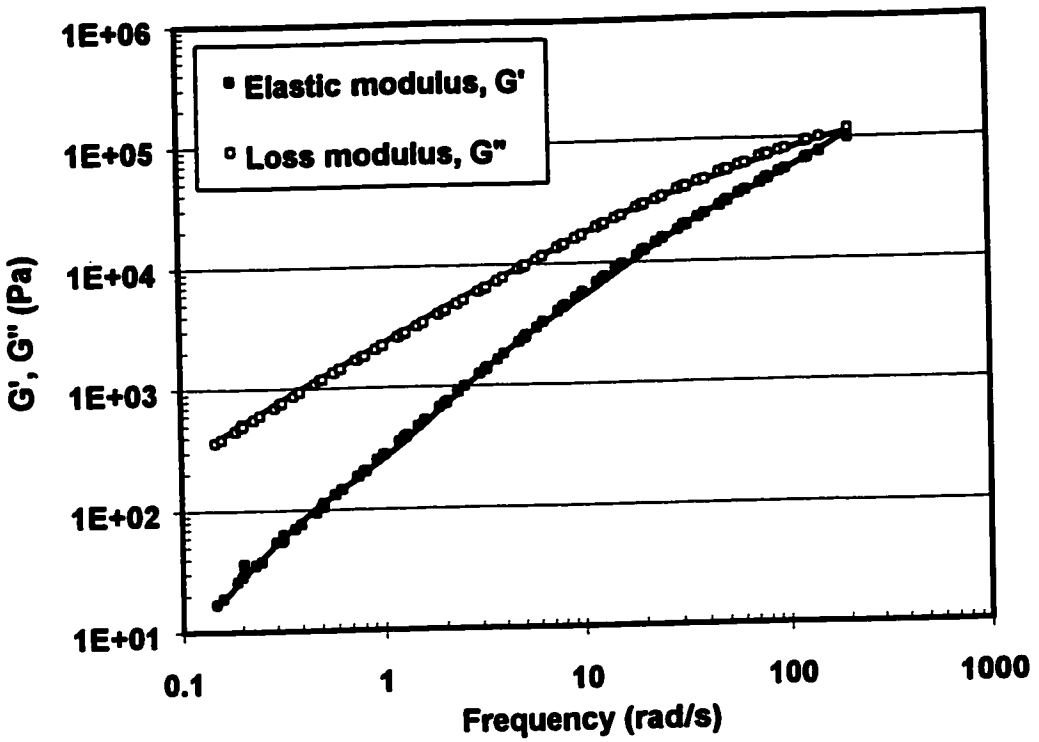

Figure 4.6: Elastic and loss modulus master curves for PE-2 (T_{ref}=170°C). Solid lines indicate fit by series of Maxwell relaxation modes.

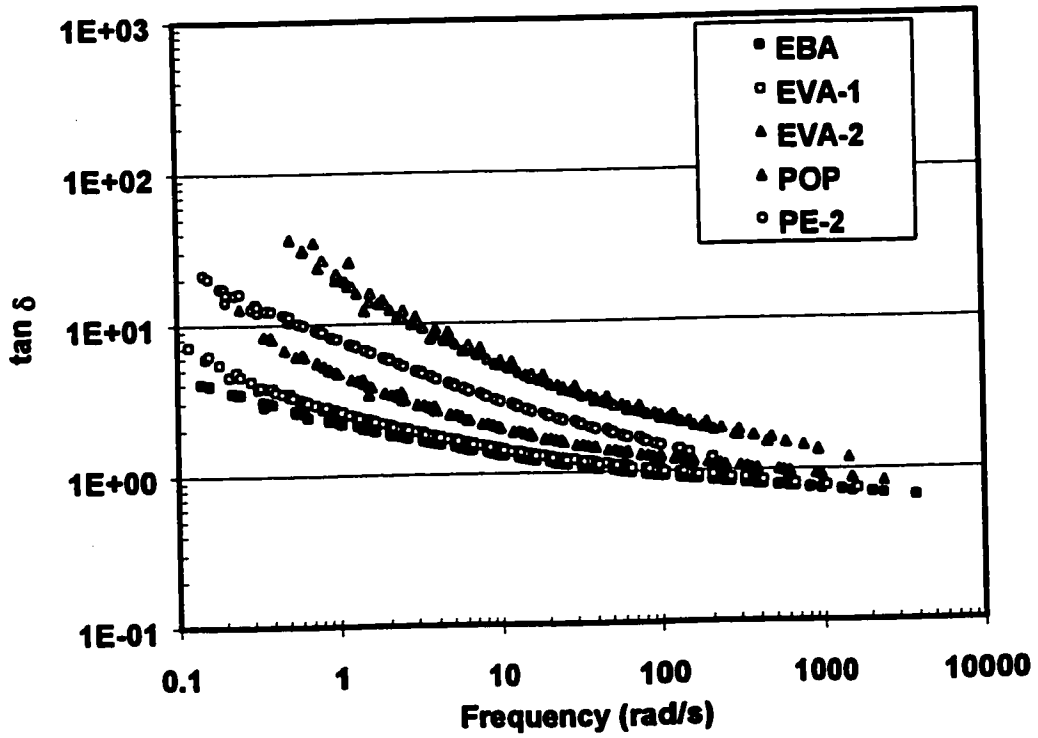

Figure 4.7: Comparison of tan δ for PE and PE copolymers (T_{ref}=170°C)

The fits obtained by this method are shown together with the experimental data in Figures 4.5 and 4.6.

The discrete relaxation spectra for all the materials, obtained by the method described above, are displayed in Figure 4.8. The discrete relaxation spectrum has similar shape as the continuous relaxation spectrum (Baumgärtel and Winter, 1992). The results shown in Figure 4.8 revealed that overall the relaxation spectra of the PE copolymers, with the exception of POP are significantly wider than the PE spectrum. A convenient way to characterize the breadth of the relaxation time spectrum is by using the concept of the relaxation spectrum index (RSI) (Wasserman, 1997). The first and second moments of the relaxation time distribution (RTD) are:

$$\lambda_I = \frac{\sum_i g_i}{\sum_i (g_i / \lambda_i)} \text{ and } \lambda_{II} = \frac{\sum_i g_i \lambda_i}{\sum_i g_i} \tag{4-4}$$

Then the RSI is defined as the ratio:

$$RSI = \lambda_{II} / \lambda_I \tag{4-5}$$

The RSI has been found to be a sensitive indicator of differences in molecular structure, especially where these differences affect the breadth of the relaxation spectrum (Wasserman, 1997). Another desirable characteristic of the RSI factor is that, although all the quantities reported above depend on temperature, RSI is relatively insensitive to temperature differences, meaning that it can be used as a means of comparison, even if measurements are available at different temperatures. This is shown in Table 4.2, which summarizes the values

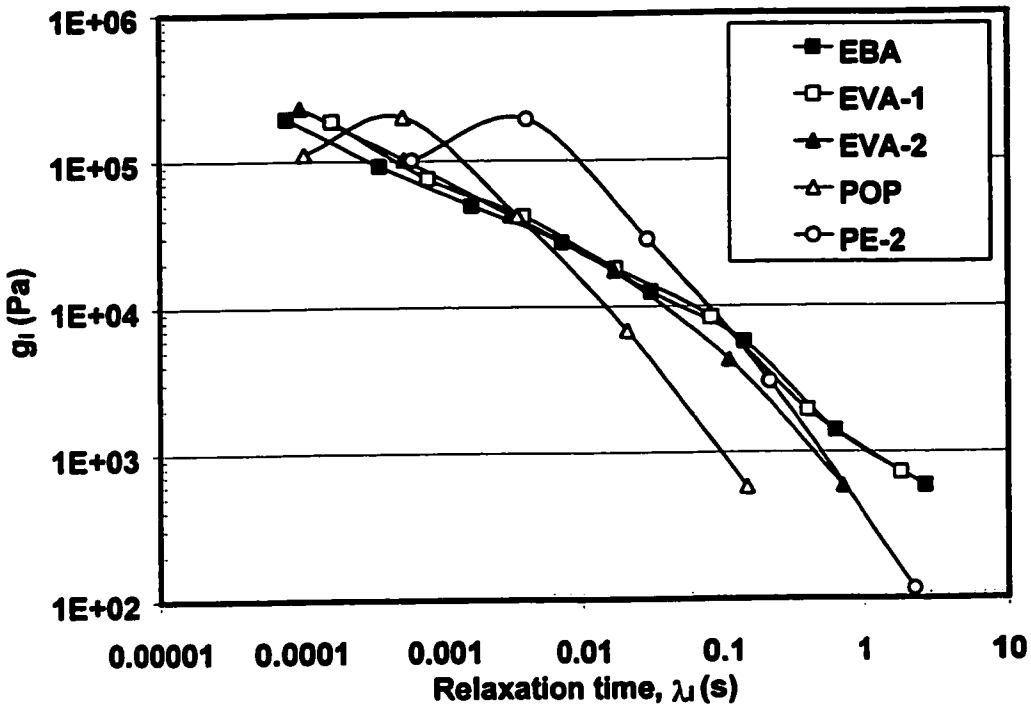

Figure 4.8: Comparison of discrete relaxation spectra for PE and PE copolymers (T_{ref}=170°C)

of RSI for the materials under consideration. The higher the value of RSI, the wider the relaxation spectrum. Wide relaxation spectra have been associated to broad molecular weight distribution (Kazatchkov et al., 1999), blends (Lacroix et al., 1997), presence of chain branching (Wasserman, 1997) and polymers consisting of molecules with long side groups (Ferry, 1980). The longest relaxation times (or terminal region relaxations) are strongly dependent on the large scale chain architecture and therefore govern the flow properties of the melt (Graessley, 1984). Thus wide relaxation spectra, associated with long terminal relaxation times can imply that long times are needed for polymer chains to disentangle and flow, thus potentially affecting the sintering process (Bellehumeur et al., 1998).

Table 4.2. Relaxation Spetrum Index for PE and PE copolymers

Material	RSI (100°C)	RSI (170°C)
EBA	74.6	74.6
EVA-1	37.9	37.8
EVA-2	21.7	22.3
POP	4.31	5.41
PE-2	3.78[1]	5.36

[1] reference temperature 135°C

It can be also observed that, although the POP elastomeric resin made by metallocene catalyst has similar thermal properties as the rest of the PE copolymers, its viscoelastic character resembles closely the behavior of the

polyethylene resin. The RSI factor for the POP resin is similar to that of PE-2. It is known from the resin supplier that this resin has a narrow MWD and comonomer content, therefore it can be suggested that the observed viscoelastic behaviour may be due to the homogeneous molecular structure.

4.2.2. Rotomolding cycles

A comparison of the inside air temperature profiles of PE-2 and EVA-2 recorded in the uniaxial rotational molding machine can be seen in Figure 4.9. These polymers were compared because they have very similar viscosity values at a range between 130 and 190°C (Figure 4.4). The heating cycle was interrupted when it was determined visually that all bubbles had been removed from the polymer melt. The temperature profiles reflect the different melting characteristics of the two polymers, indicating that the EVA-2 powder particles started to melt and adhere on the mold considerably earlier. However longer processing time was required in order for all the bubbles to be removed. It is speculated that the presence of more bubbles, which need long heating times to dissolve is associated to the high viscosities of the EVA-2 melt at temperatures just above its melting point. Similar observations have been made for the rest of the PE copolymers (EVA-1 and EBA), for which bubble removal was problematic and long cycle times were required. These resins have several similar characteristics: low melting points and low crystallinities (Figure 4.1), high viscosities at temperatures above the melting point (Figure 4.4), high melt elasticities (Figure 4.7) and broad relaxation spectra (Table 4.2).

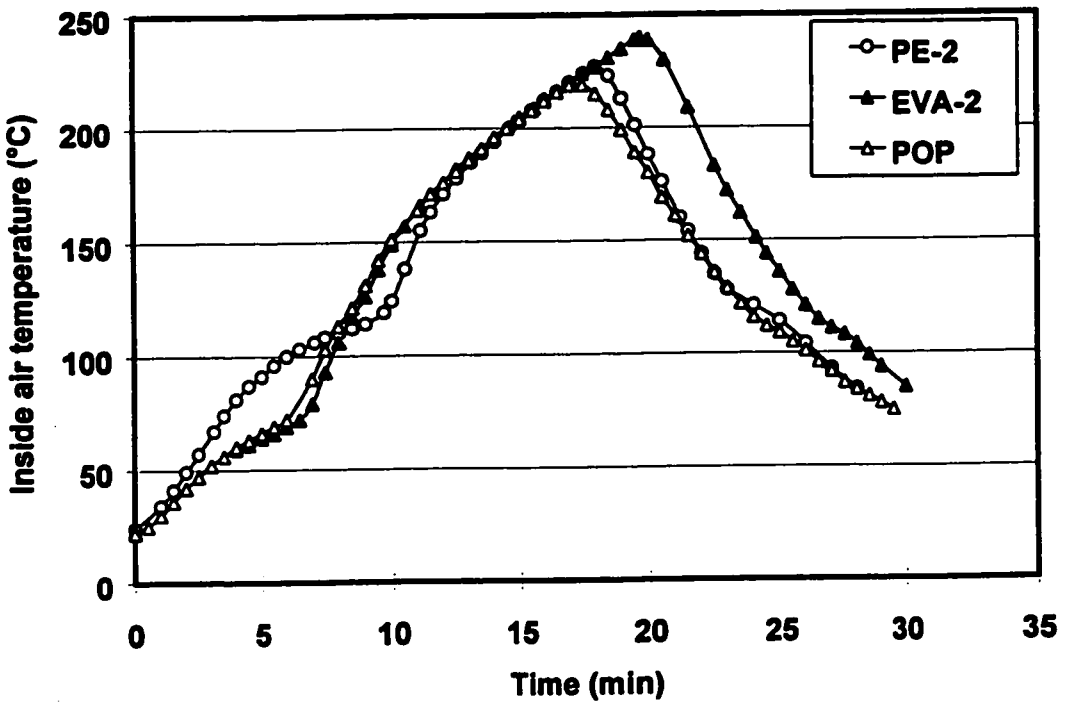

Figure 4.9: Comparison of inside air temperature profile for PE and PE copolymers in the uniaxial rotational molding machine

The temperature profile of the POP resin resembles that of EVA-2 in the beginning, because of the similar thermal properties (Figure 4.1), but the bubbles disappear sooner and the duration of the cycle is significantly shorter (Figure 4.9). It must be noted that for the POP resin, viscosity assumes a low value immediately upon melting (Figure 4.4) and the melt elasticity and RSI are low (Figure 4.7 and Table 4.2).

4.3. Material properties and processing of polypropylenes

4.3.1. Material properties

The introduction of ethylene comonomer to the polypropylene matrix alters its properties in several ways (Kontopoulou, 1995, Kontopoulou et al., 1997). As the ethylene content increases, the crystallinity of the polymer compared to a polypropylene homopolymer generally decreases (Table 4.1). A second crystallizable phase, attributed to polyethylene crystallization, appears in the DSC trace of a typical PP/PE copolymer as a minor second peak (Figure 4.10).

Crystallization Analysis Fractionation (CRYSTAF), which is a technique similar to Temperature Rise Elution Fractionation Analysis (TREF), was used to detect the presence of a non-crystallizable amorphous phase. The crystallization of a solution of polypropylene in trichlorobenzene was followed as the solution was cooled slowly, as explained in Chapter 3. In CRYSTAF the analysis is carried out by monitoring the polymer solution concentration during

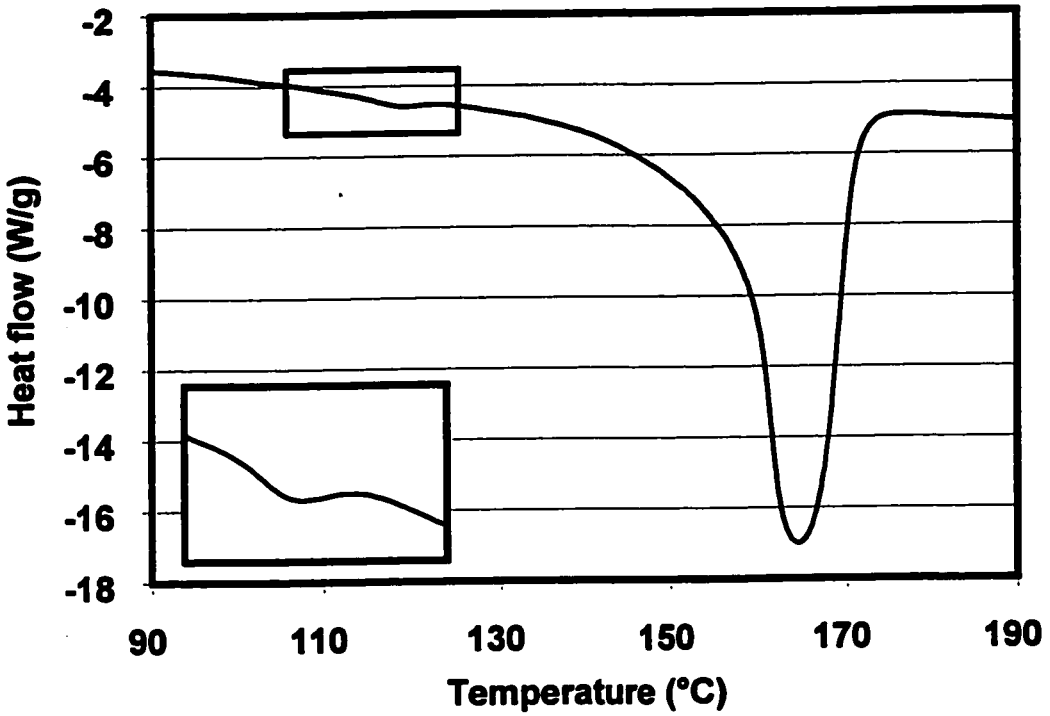

Figure 4.10: DSC trace for a typical PP/PE copolymer (PP/PE-1) (Kontopoulou, 1995)

crystallization by temperature reduction (Monrabal, 1994, 1996). A typical trace for a PP/PE copolymer obtained by CRYSTAF is shown in Figure 4.11. The concentration of the solution (represented by the cumulative fraction curve in Figure 4.11) is monitored as a function of temperature: As the temperature goes down, the more crystalline fractions precipitate first, resulting in a steep decrease in the solution concentration. The last data point of the cumulative curve, corresponding to the lowest temperature of the crystallization cycle, represents the amorphous (rubbery) fraction that has not crystallized and remains soluble (Monrabal, 1994).

The first derivative of the cumulative curve, dw/dT, has been also calculated in Figure 4.11. The curve of dw/dt versus temperature denotes copolymer content distribution: The larger the standard deviation of the distribution, the wider the copolymer content distribution (Monrabal, 1998).

Table 4.3 lists the results obtained by CRYSTAF for all four PP/PE copolymers. PP/PE-3 and PP/PE-4 appear to contain a higher amorphous fraction (represented by the % soluble fraction).

Table 4.3: Results of CRYSTAF analysis for PP/PE copolymers

Resin	Crystallization peak temperature (°C)	Soluble Fraction (%)	Standard deviation of distribution (°C)
PP/PE-1	79	16.7	15.4
PP/PE-2	78.8	16.6	15.2
PP/PE-3	77.8	20	17
PP/PE-4	78.1	18.7	17.2

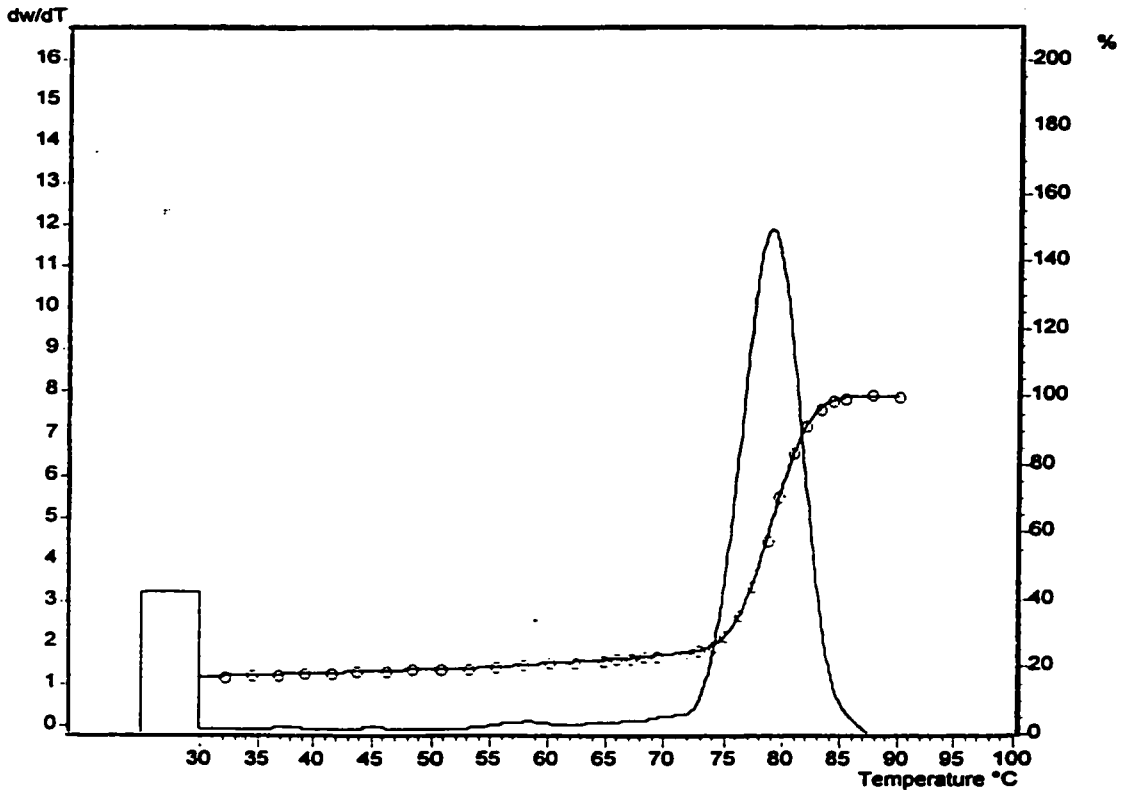

Figure 4.11: CRYSTAF trace for PP copolymer (PP/PE-1)

Figure 4.12 summarizes the dynamic viscosity versus shear rate curves for all the polypropylene resins at 190°C. The temperature dependence of the zero shear viscosity is shown in Figure 4.13.

It has been reported in previous work (Kontopoulou, 1995, Kontopoulou et al. 1997, Bellehumeur et al. 1998) that the viscoelastic properties of the polypropylene copolymers depend on the ethylene content and measurements of stress relaxation after cessation of steady state flow were used to demonstrate this. In this work dynamic oscillatory measurements using time-temperature superposition as described in the previous section were performed. A comparison of the master curves obtained at a reference temperature of 180°C for the PP/PE copolymers revealed that the storage modulus of PP/PE-3 and PP/PE-4, which have higher polyethylene contents is characterized by a shoulder in the low frequency region (Figure 4.14a). The respective master curves of the loss moduli are shown in Figure 4.14(b). The lower values of the ratio $\tan\delta = G''/G'$ for the PP/PE-3 and PP/PE-4 melts at low frequencies are an indication of higher contribution of the elastic response to the total rheological response of the polymers (Figure 4.15).

Increases in the low frequency moduli of block copolymers have also been reported elsewhere (Gouinlock and Porter, 1977, Chung and Lin, 1978) and have been attributed to micro-phase separation. In addition, Carreau et al. (1994) and Lacroix et al. (1997) have attributed the observed increase in elasticity of blends in the terminal zone to the deformability of the suspended droplets under a strain

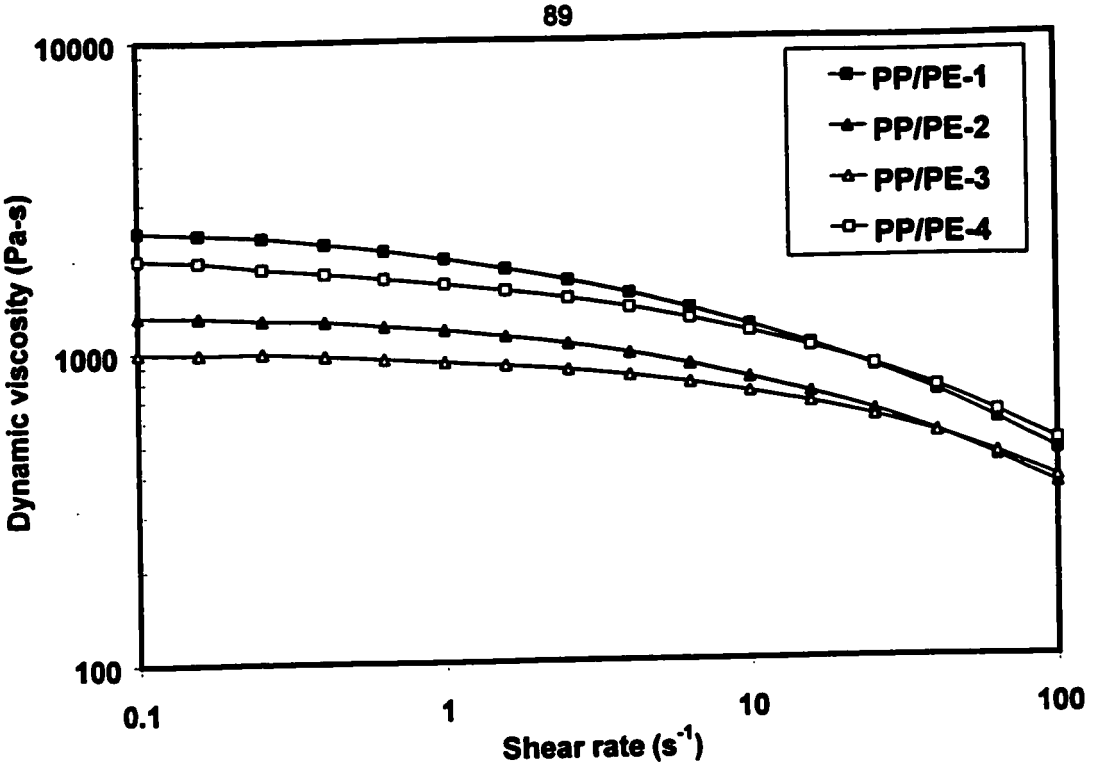

Figure 4.12: Comparison of dynamic viscosity curves for PP/PE copolymers at 190°C

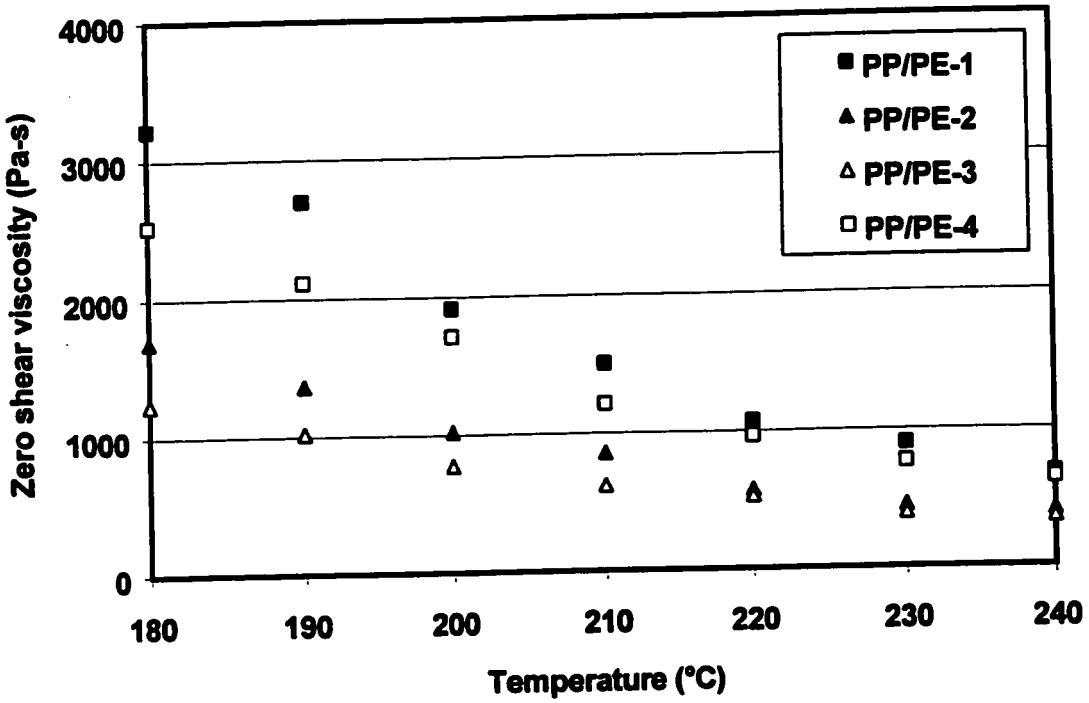

Figure 4.13: Viscosity versus temperature curves for PP/PE copolymers

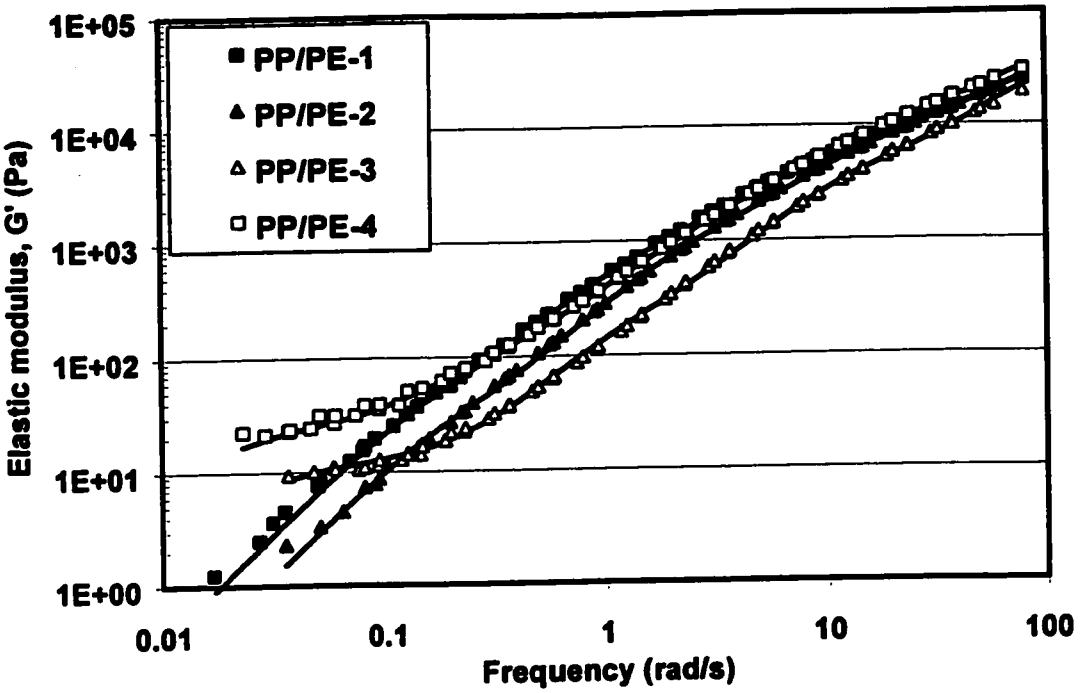

Figure 4.14 (a): Comparison of elastic modulus master curves for PP/PE copolymers (T_{ref}=180°C). Solid lines indicate fit by series of Maxwell relaxation modes.

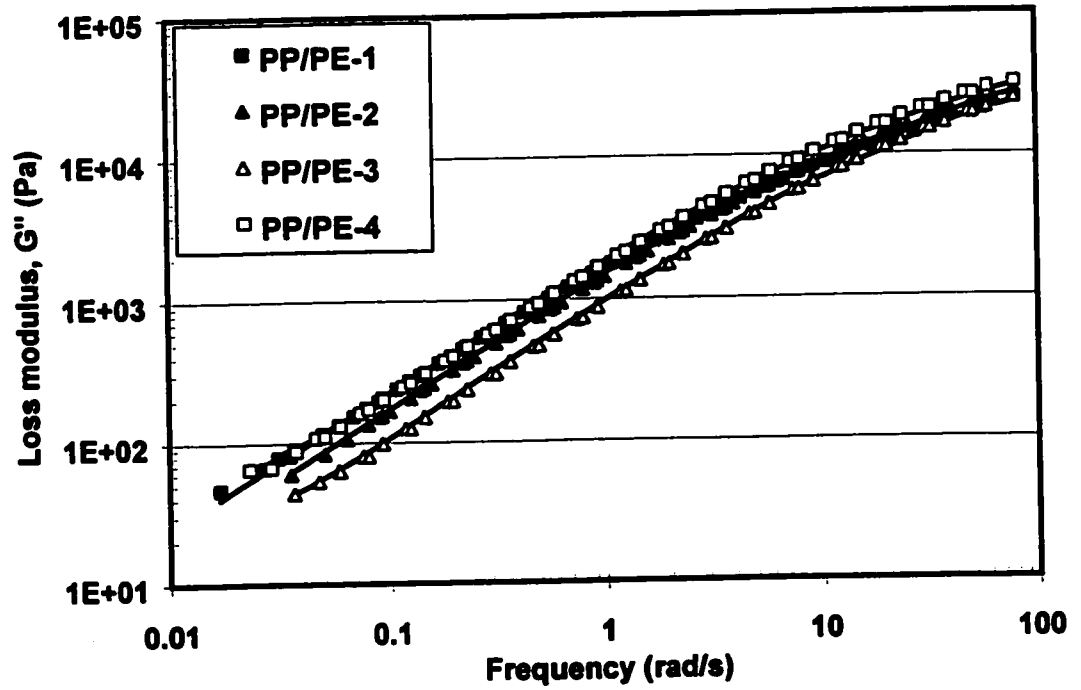

Figure 4.14 (b): Comparison of loss modulus master curves for PP/PE copolymers (T_{ref}=180°C). Solid lines indicate fit by series of Maxwell relaxation modes.

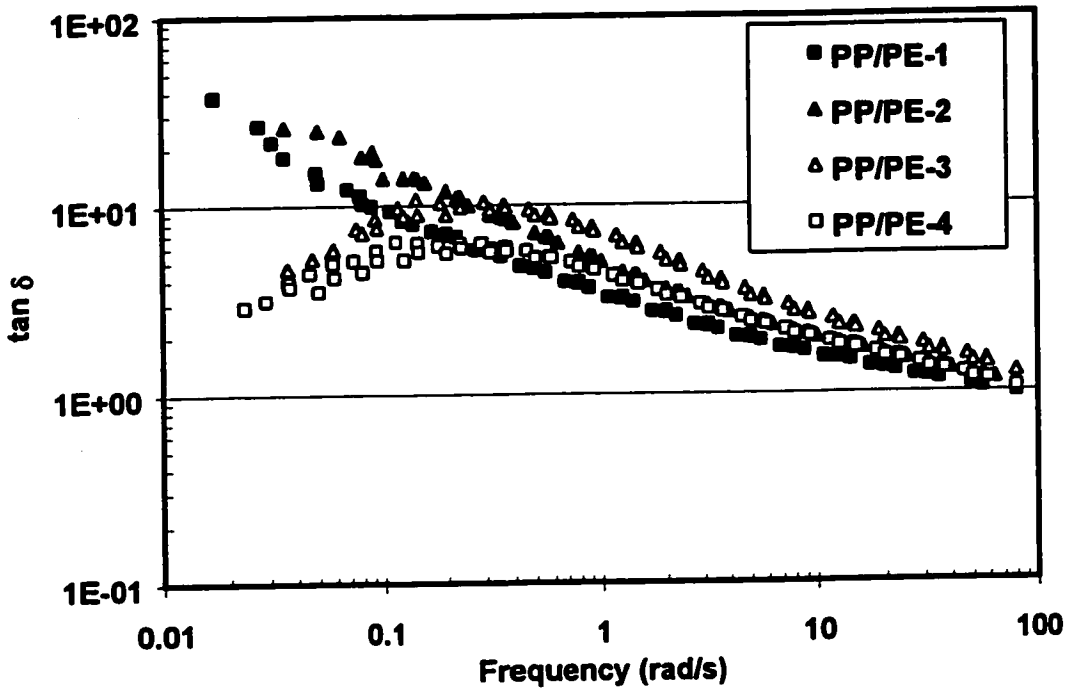

Figure 4.15: Comparison of tan δ for PP/PE copolymers (T_{ref}=180°C)

in the flow field. According to them, in order to observe such effects, the measurements have to be carried out at sufficiently low frequencies, for which the oscillation period is long enough to observe the relaxation of the deformable droplets.

Increases in melt elasticity of polypropylenes have been also associated to the presence of ultra-high molecular weight components, which are otherwise undetected by methods such as GPC and low angle laser light scattering (LALLS) (Sugimoto et al., 1999).

Based on the above analysis it can be concluded that the observed melt elasticity enhancement in PP/PE copolymers (Figures 4.14, 4.15) may be due to the appearance of a significant rubbery dispersed phase in the polypropylene matrix as PE content increases, or to the presence of ultra-high molecular weight comonents. Thus it is suggested that dynamic measurements of the polypropylene copolymers can reveal some useful information about the structure of the polymers without having to resort to time consuming and expensive chemical analysis techniques.

The values of g_i and λ_i used to fit the dynamic and loss modulus data (Figures 4.14(a) and (b)) are summarized in Figure 4.16. The fact that the response of resins PP/PE-3 and PP/PE-4 is characterized by longer relaxation times can be seen from their discrete relaxation spectra, shown in Figure 4.16, which vanish at longer times.

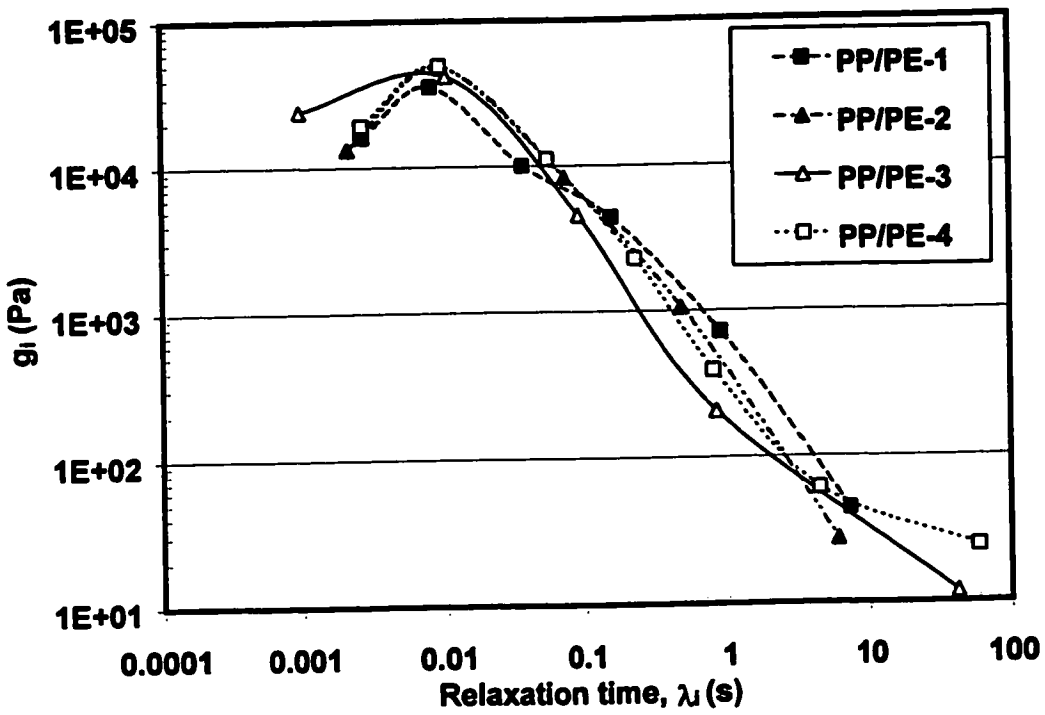

Figure 4.16: Comparison of discrete relaxation spectra for PP/PE copolymers (T_{ref} = 180°C)

4.3.2. Rotomolding cycles

Polypropylene copolymers became more difficult to process as PE content increased, because they produced parts with uneven surfaces and high bubble contents. This observations, done in the clamshell rotational molding machine are consistent with previous results reported by using the uniaxial rotational molding machine (Kontopoulou, 1995, Kontopoulou et al., 1997).

In order to clarify these findings PP/PE copolymers with similar viscosities and different PE contents have been compared, in order to exclude the viscosity effect. This will be demonstrated by an example: PP/PE-2 and PP/PE-3 have the same MFR. PP/PE-3 has slightly lower zero shear viscosity value (Table 4.1 and Figure 4.13) and higher PE content. Rotomolding experiments showed that PP/PE-2 needs lower oven temperature and processing time than PP/PE-3. Bubbles are completely removed from parts formed by PP/PE-2, while long heating times are needed to remove bubbles from parts made by PP/PE-3. Density measurements performed in rotomolded parts are shown in Figure 4.17. The evolution of density with time for PP/PE-3 is delayed considerably when compared to PP/PE-2, due to the presence of excessive bubbles in parts made by PP/PE-3. Figure 4.18 shows an underfused PP/PE-3 sample containing bubbles.

The surface of the parts rotomolded by PP/PE-2 leveled off sooner too, as demonstrated in Table 4.4 by the standard deviation of thickness, which is a measure of the surface non-uniformity, as a function of oven temperature.

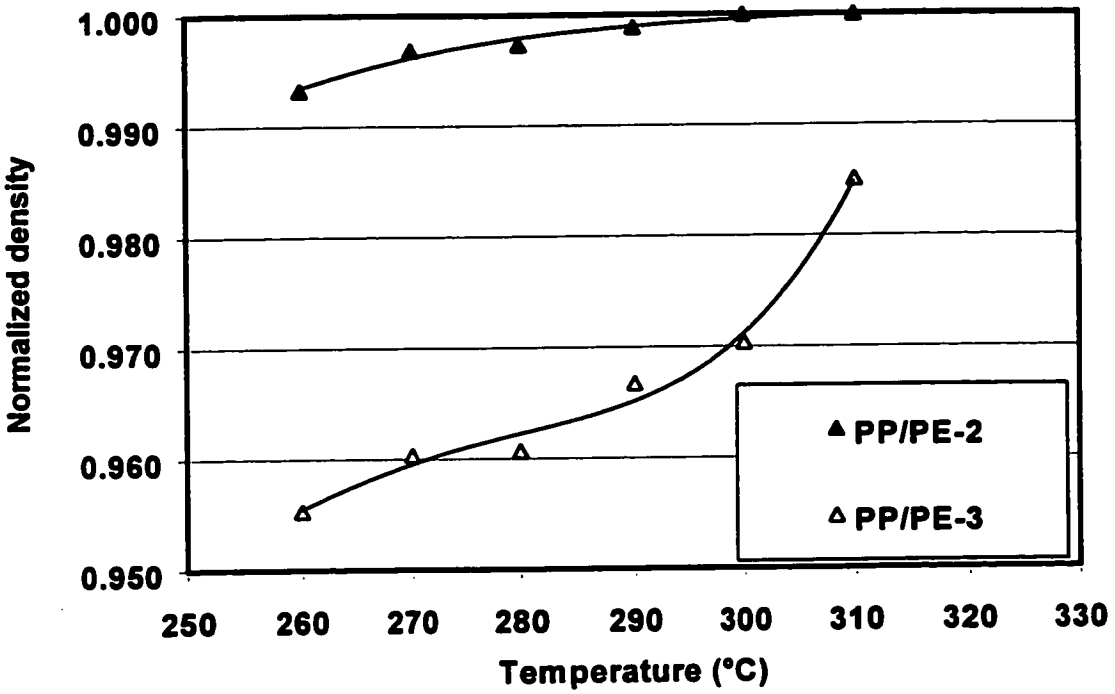

Figure 4.17: Density evolution of rotomolded PP parts as a function of oven temperature

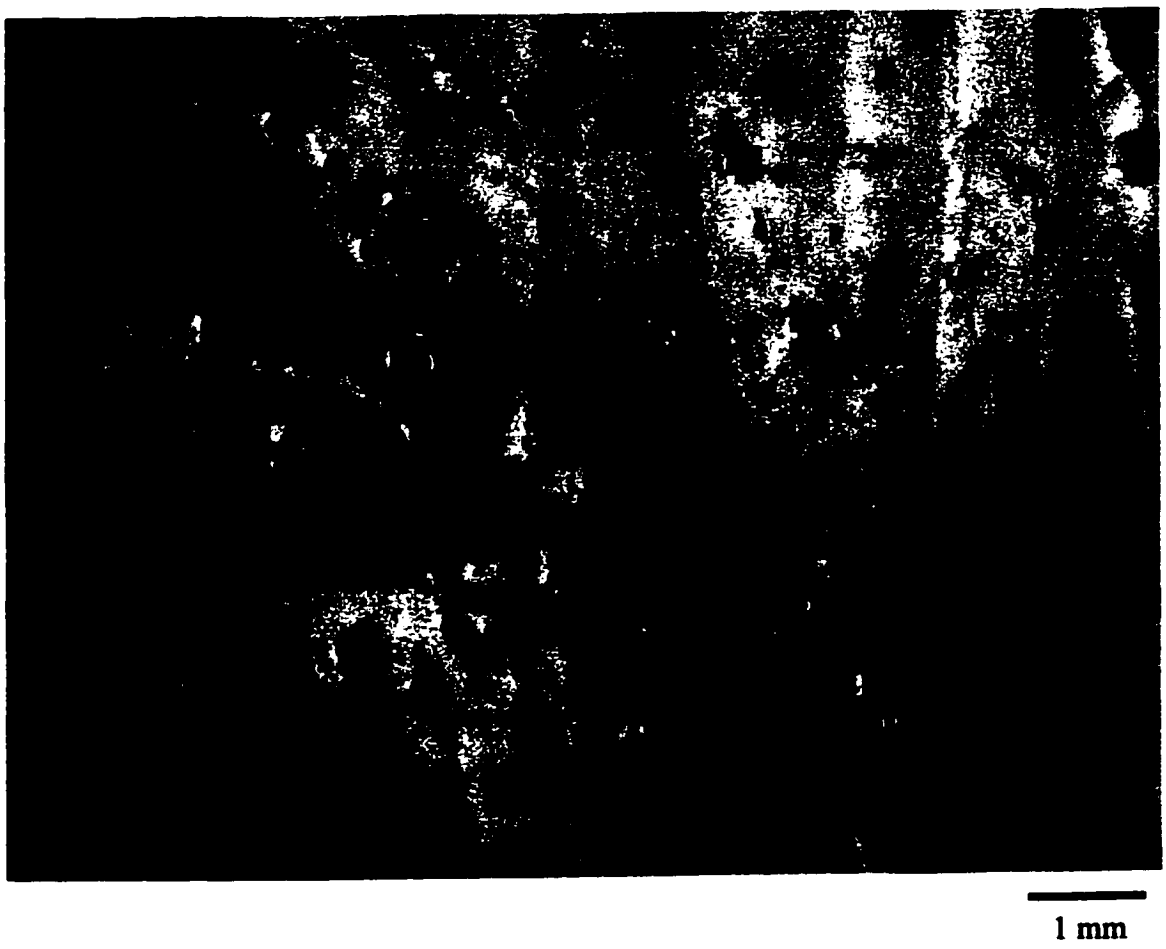

Figure 4.18: Optical microphotograph of underfused PP/PE-3 sample containing bubbles

Table 4.4: Standard deviation of thickness of PP parts as a function of oven temperature

Oven Temperature Set Point (°C)	Standard deviation of thickness (mm) PP/PE-2	PP/PE-3
270	0.187	0.331
280	0.211	0.348
290	0.184	0.302
300	0.211	0.218
310	0.204	0.220

4.4. Material properties and processing of polyethylenes made by conventional (Ziegler-Natta) and single-site (metallocene) catalysts

4.4.1. Material properties

Polyethylene resins made with metallocene catalysts have been recently introduced in the rotational molding market (Anon, 1997). These polyethylenes, with very narrow molecular weight distribution, have been reported to offer significantly faster sintering rates and reduced cycle times, when compared to conventional polyethylenes of similar MFI (Fatnes, 1999).

PE-7, which is a polyethylene with MFI=3.2 made by metallocene catalysts using a slurry-loop process, has been compared with PE-1 (MFI=3.3) and PE-2 (MFI=5.2). The thermal properties of PE-7 are almost identical with PE-1 (Figure 4.19). PE-2 on the other hand displays lower heat of fusion, which translates to lower crystallinity. Viscosity versus shear rate data (Figure 4.20)

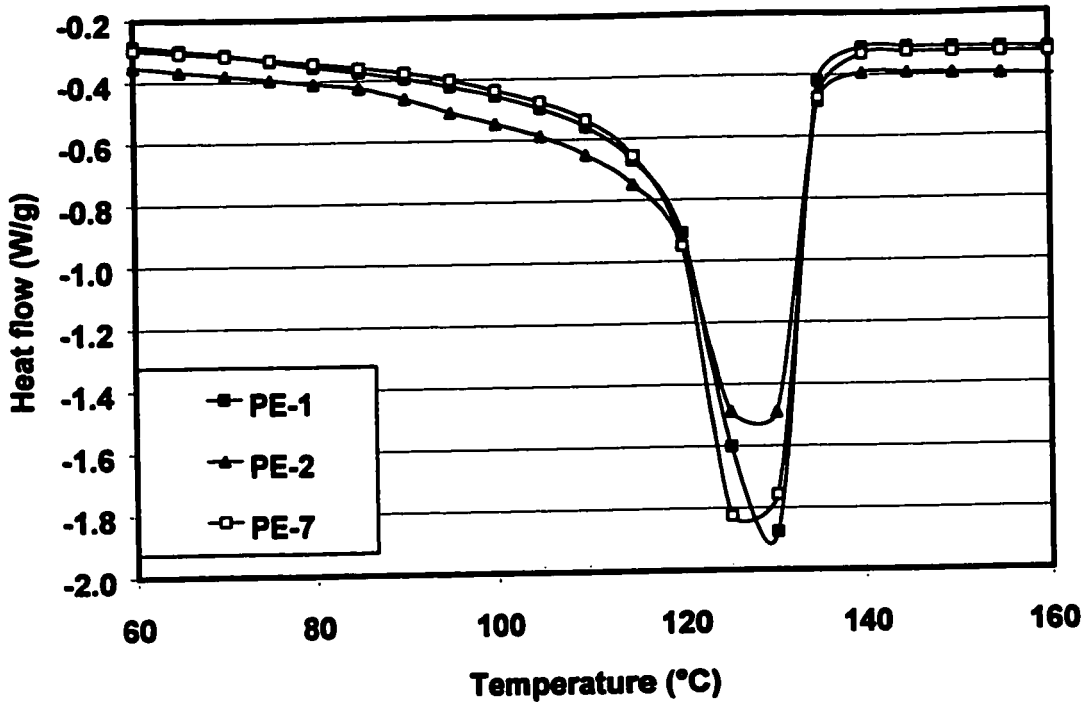

Figure 4.19: Comparison of DSC traces of conventional (PE-1 and PE-2) and metallocene polyethylenes (PE-7)

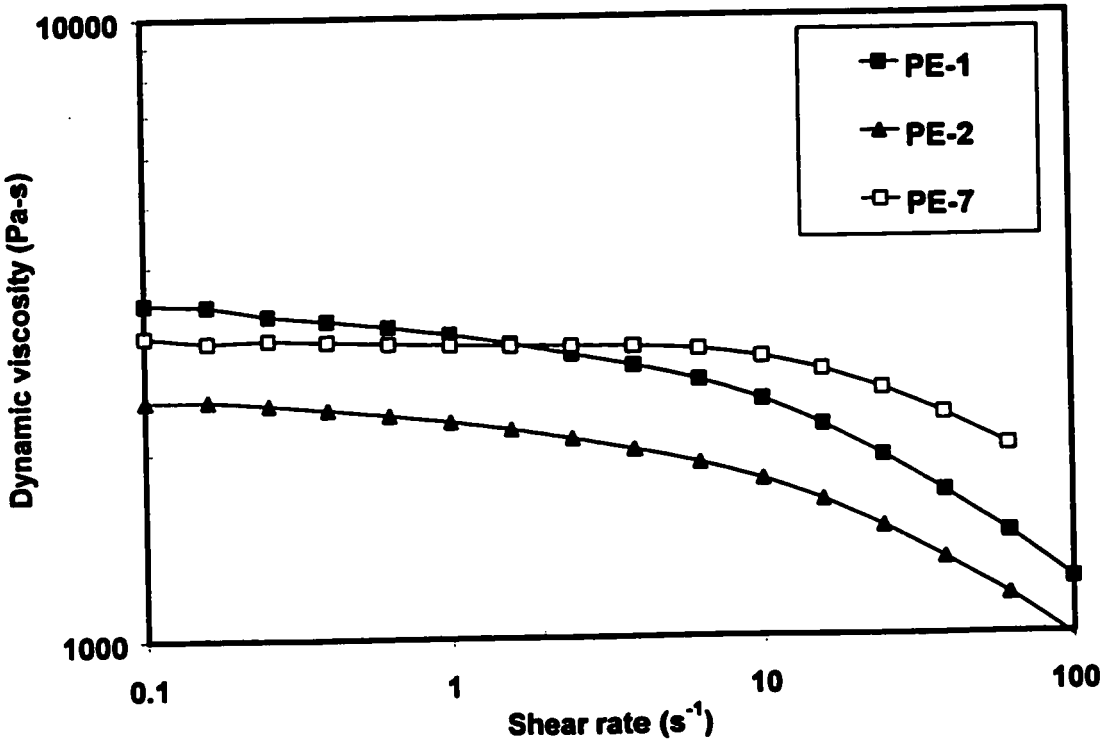

Figure 4.20: Comparison of dynamic viscosity curves for conventional and metallocene polyethylenes at 170°C

revealed that PE-7 exhibits less shear thinning than PE-1 and PE-2 and this can be attributed to its narrow molecular weight distribution. Although PE-7 is reported to have a melt flow index value of 3.2, it can be seen from the viscosity curves at 170°C that it has a somewhat lower zero shear viscosity than PE-1 which has MFI=3.3. Figures 4.21(a) and (b) respectively show a comparison of the elastic and loss moduli for the three polyethylenes and values of tanδ are summarized in Figure 4.22. From the data in Figures 4.21 and 4.22 it can be concluded that the melt elasticity of PE-7 is lower than that of both conventional polyethylenes.

4.4.2. Rotomolding cycles

A comparison of the inside air temperature profiles of polyethylenes made by conventional Ziegler-Natta (PE-1 and PE-2) and metallocene (PE-7) polyethylenes recorded in the uniaxial rotational molding machine can be seen in Figure 4.23. The heating cycle was interrupted when all bubbles had been removed from the polymer melt.

Although it has been reported that the cycle times for the metallocene based polyethylenes are significantly reduced, when compared to conventional polyethylenes of similar MFI (Fatnes, 1999), this has not been confirmed in the current work. The cycle time required to completely remove the bubbles was comparable to the cycle time for the conventional PE-1 with similar viscosity (Figure 4.23) and the shape of the temperature profiles is almost identical. However, it seems that the literature claims about faster coalescence rates of the metallocene polyethylenes have some merit, as will be discussed in Chapter 5.

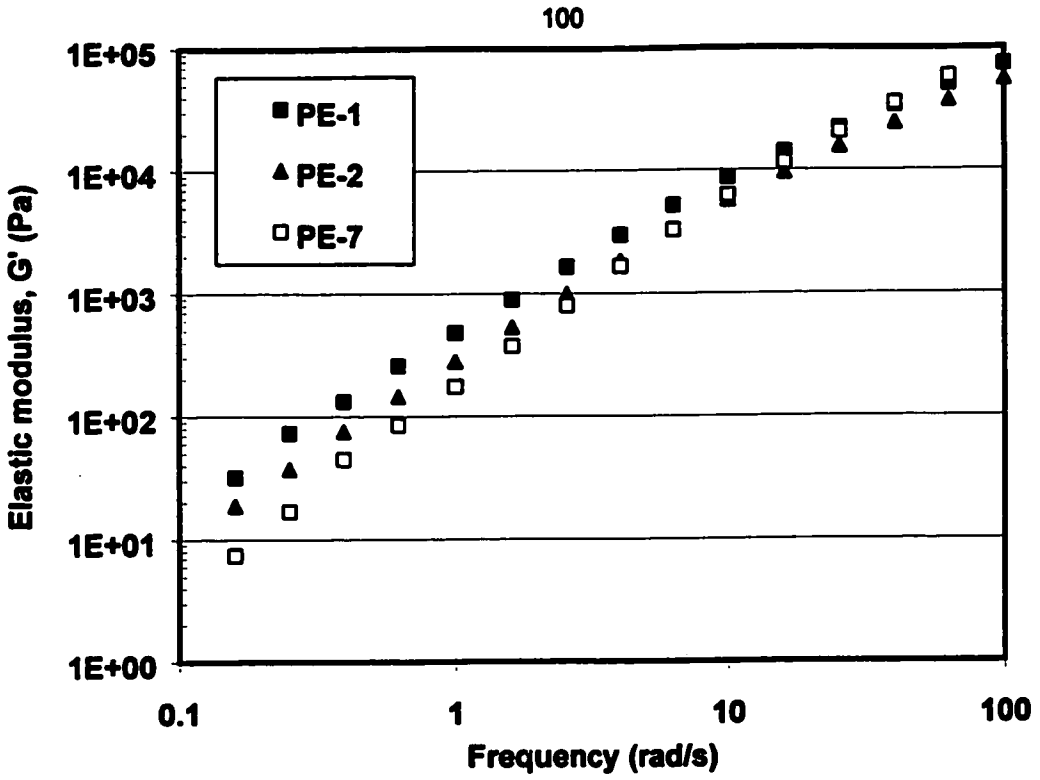

Figure 4.21(a): Comparison of elastic modulus for conventional and metallocene polyethylenes at 170°C

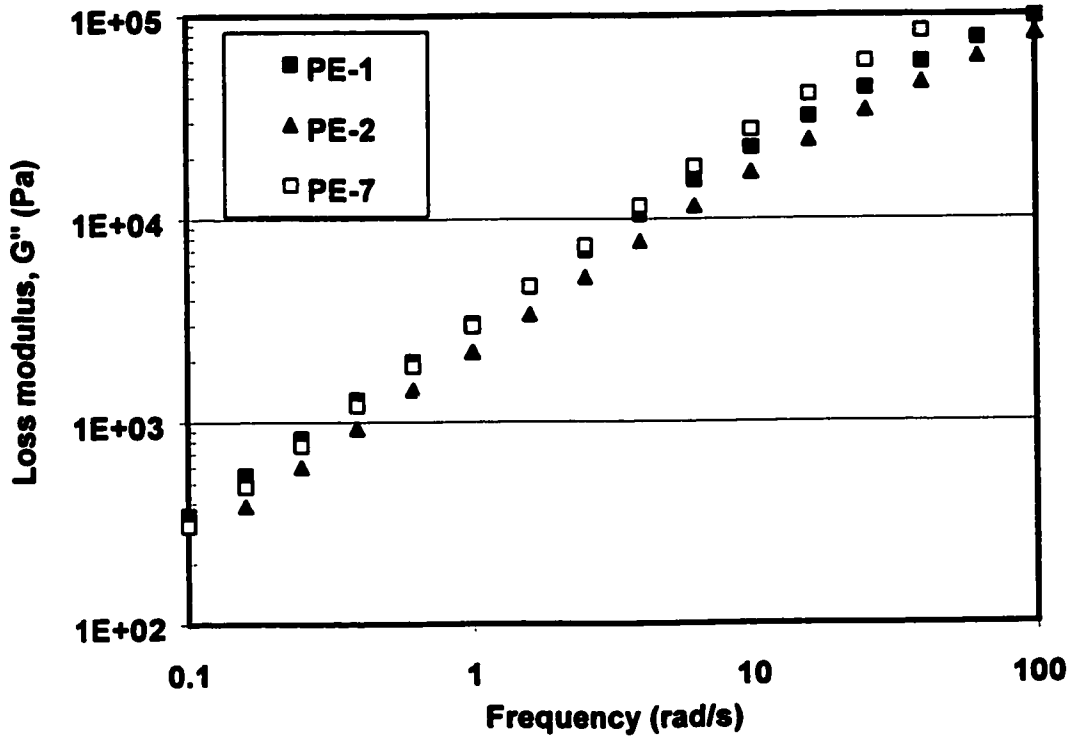

Figure 4.21(b): Comparison of loss modulus for conventional and metallocene polyethylenes at 170°C

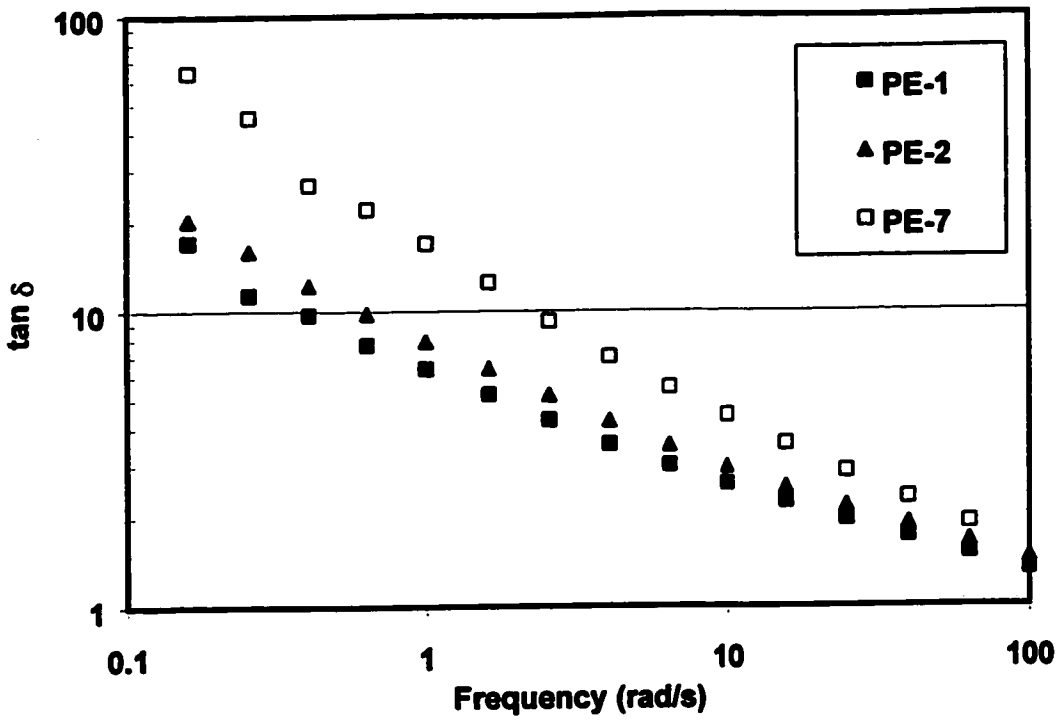

Figure 4.22: Comparison of tanδ for conventional and metallocene polyethylenes, 170°C

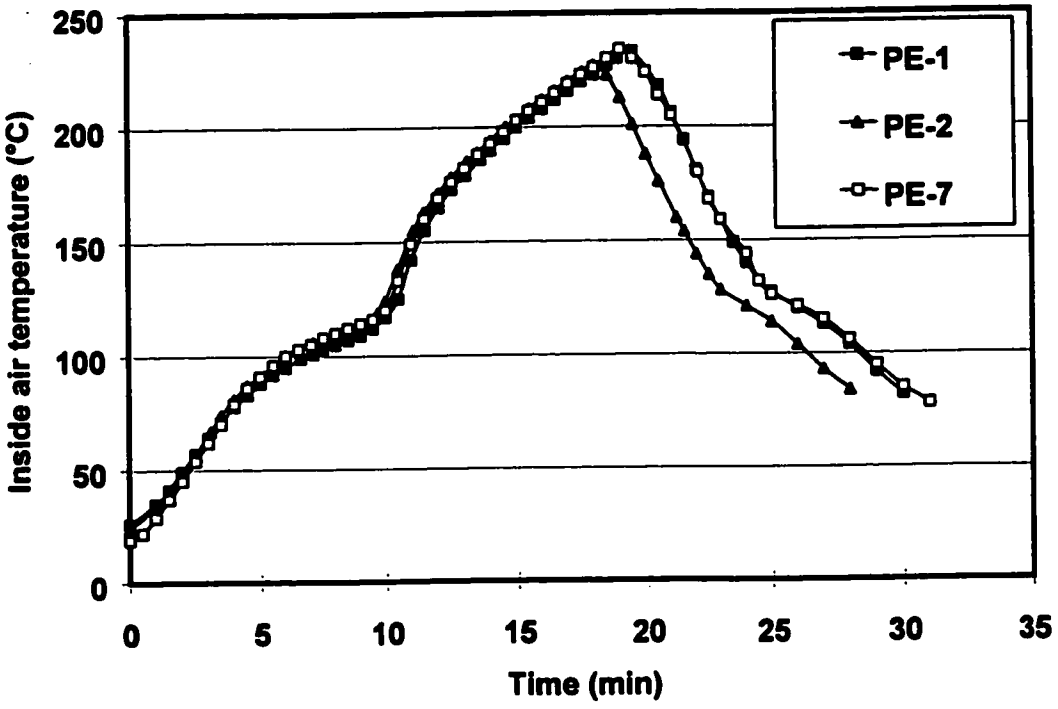

Figure 4.23: Comparison of inside air temperature profiles of conventional (PE-1, PE-2) and metallocene (PE-7) polyethylenes in the uniaxial rotational molding machine.

4.5. Material properties and processing of polycarbonate

Completely amorphous polymers, such as polycarbonate, do not have a melting point, which is a well defined transition from powder to melt, but rather softening occurs over a range of temperatures. Only at 40 - 50°C above the glass transition temperature can typical amorphous polymers be considered as processable melts in rotomolding, because viscosity values remain high, even above the glass transition temperature. This can be seen particularly well in Figure 4.24 which compares the viscosity of PC with two semi-crystalline rotational molding resins. A dramatic decrease in viscosity of PC is observed above 200°C, but the viscosity values are still very high compared to the typical PE and PP viscosities.

High viscosities in the beginning of the cycle affect seriously PC processability. The effective particle coalescence occurs only at the late stage of the heating cycle, due to very high viscosities (Bellehumeur, 1997, Kontopoulou et al., 1998). At this point, most particles have already adhered to each other and air has been entrapped forming bubbles, which are almost impossible to remove completely.

4.6. Rotomolded part properties and structure

Optimum values of impact strength were determined for the different polymers by using several combinations of oven temperatures and residence times in the clamshell rotational molding machine, as explained in section 3.2.4 of Chapter 3. Values of mean failure energies of different types of polymers as a

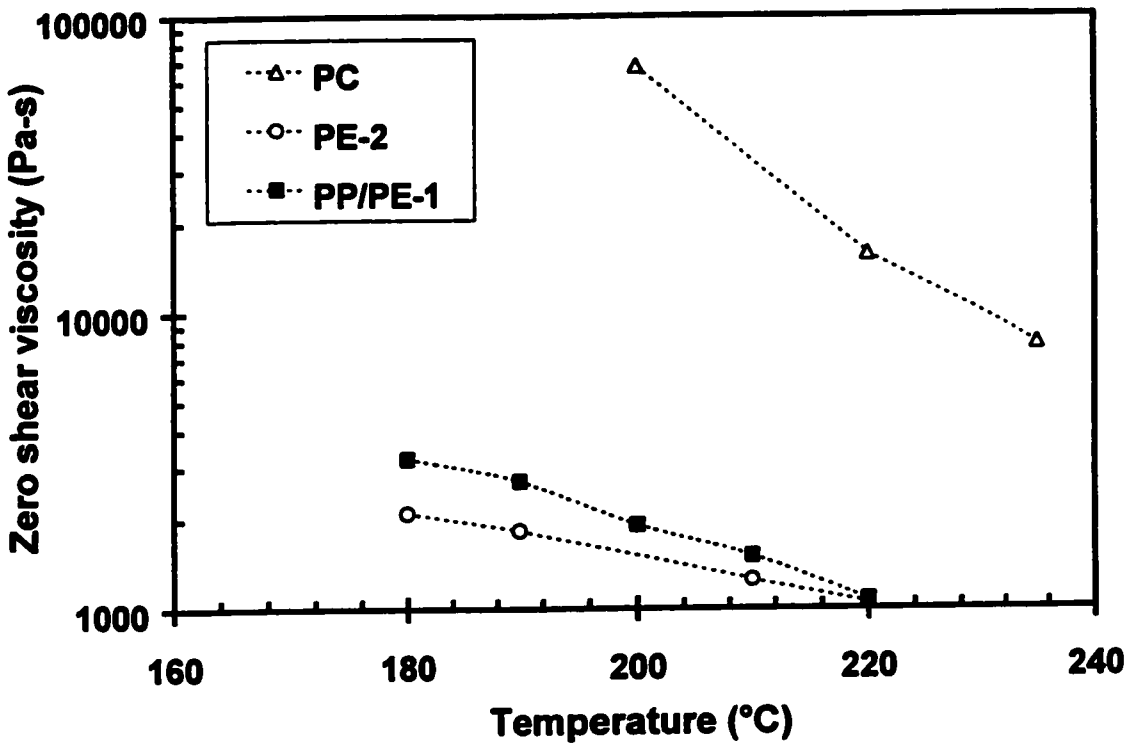

Figure 4.24: Viscosity versus temperature dependence for PC, PE and PP/PE

function of residence time at the peak oven temperature are compared in Figure 4.25. The recorded values correspond to low temperature (-40°C) impact tests, with the exception polypropylene. Polypropylene did not have any measurable impact strength at low temperature, thus the reported values were obtained at room temperature. The general trend observed in Figure 4.25 is that as residence time increases, impact strength improves and reaches an optimum value, because parts are more properly fused. However if the polymer remains inside the oven for too long, degradation occurs, which results in a reduction in impact properties. This is consistent with previous observations by Crawford and Nugent (1992(a)). The optimum processing conditions, corresponding to the highest values of impact strength were determined from the data in Figure 4.25 and tensile tests were performed on specimens rotomolded at the optimum processing conditions. Typical tensile curves are shown in Figure 4.26 and values of the most important tensile properties are summarized in Table 4.5.

Polyethylene offers better toughness and polypropylene better stiffness. Polycarbonate produces transparent products, with high heat resistance, dimensional stability and excellent impact properties, coupled with good tensile properties. However PC degrades easily and this has detrimental effects in its impact strength (Figure 4.25). Drying of polycarbonate prior to processing and preheating of the mold was necessary to obtain parts with satisfactory qualities.

From the above results, it can be seen that the introduction of comonomers results in the modification of the properties of the original polymer by improving

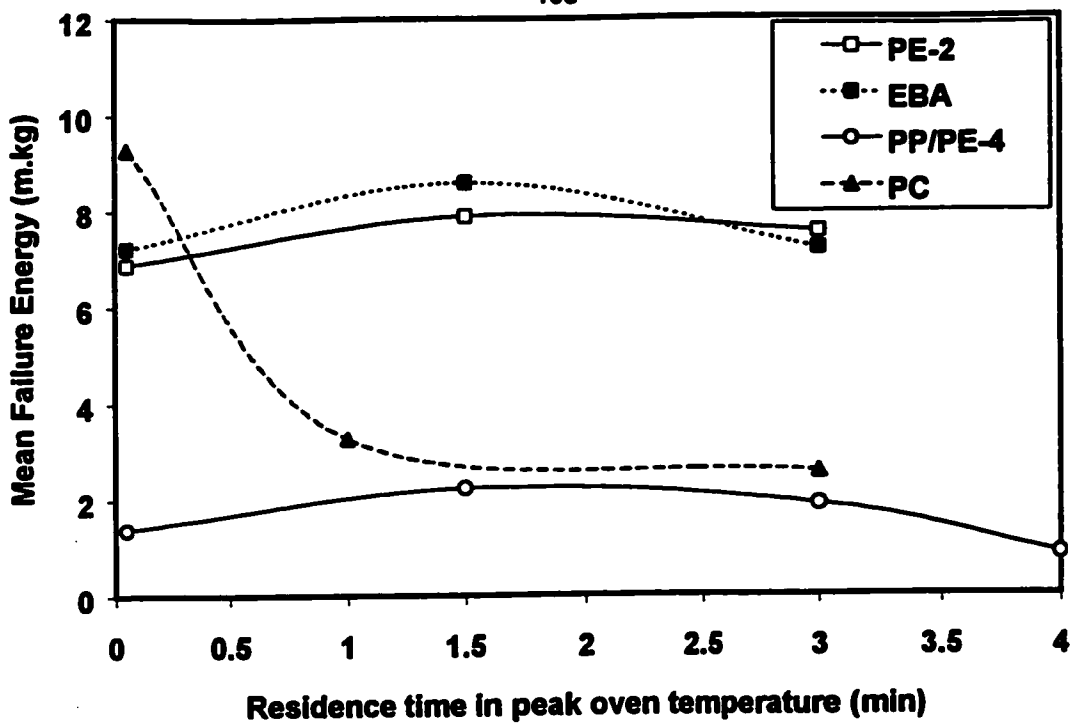

Figure 4.25: Comparison of impact strength of various rotomolding grade polymers as a function of residence time at peak oven temperature (values for PP correspond to room temperature). Max. oven temperature: 310°C for PE, EBA, PP/PE; 340°C for PC

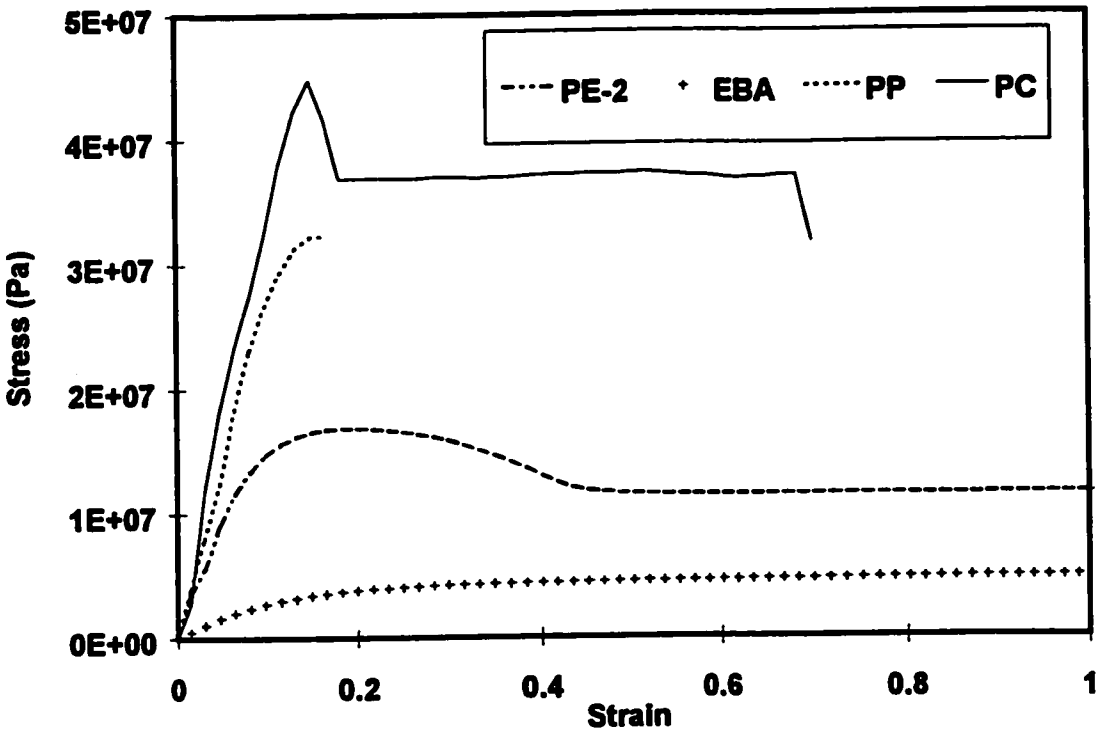

Figure 4.26: Comparison of tensile curves of various rotomolding grade polymers

impact properties and reducing tensile strength. The introduction of a comonomer, such as butyl-acrylate or vinyl-acetate in polyethylene, results in flexible parts, which have slightly higher impact strength and significantly lower tensile strength than PE. The modification in properties is due to the disruption of the crystalline structure of PE when a comonomer is introduced. This is demonstrated by images of fractured surfaces of LL-2 and EBA obtained by SEM, shown in Figures 4.27 and 4.28.

Table 4.5: Comparison of tensile properties of rotomolding resins

Resin	Tensile strength (MPa)	% Elongation at yield	% Elongation at break
PE-2	24	19.6	1271.5
EBA	10.3	38.9	998
PP	31.8	14.6	14.6
PP/PE-1	24.7	12.6	19.3
PP/PE-2	25.6	12.2	23
PP/PE-3	18.1	13.6	35.4
PC	47.6	14.7	47.8

Rotomolded parts made by polypropylene homopolymer (PP) offer higher tensile strength than PE (Figure 4.26, Table 4.5), but they are very brittle. The PP and PP/PE-1 resins did not exhibit any measurable impact strength. The effect of increasing PE content in the impact strength of PP/PE copolymers can be seen in Figure 4.29. Introduction of ethylene comonomer increases elongation at break (Figure 4.30), consistently with the observed improvement in impact strength.

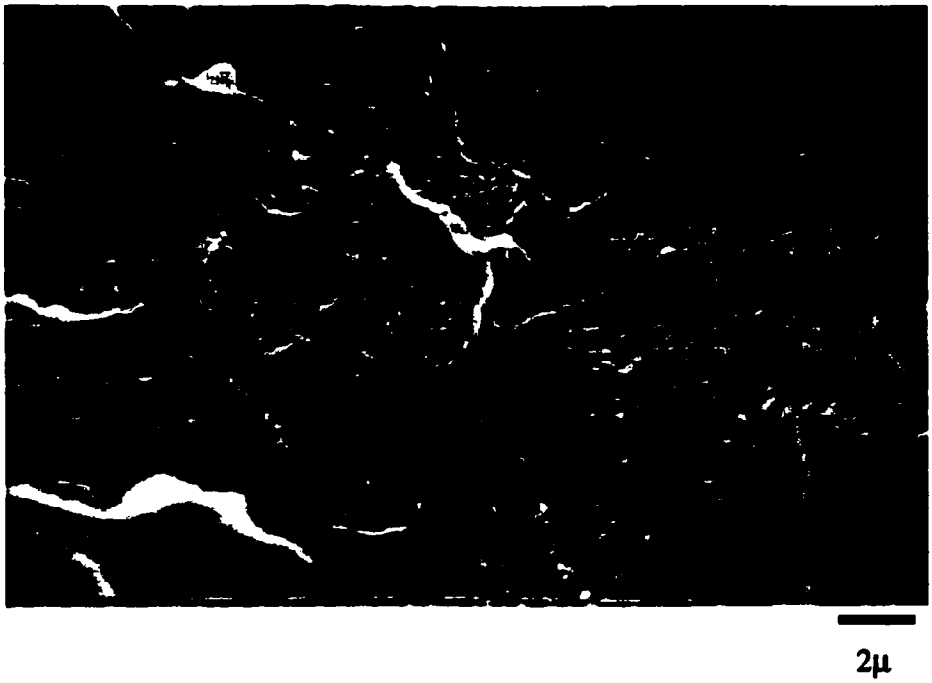

Figure 4.27: SEM microphotograph of fractured surface of rotomolded polyethylene (PE-2)

Figure 4.28: SEM microphotograph of fractured surface of rotomolded EBA

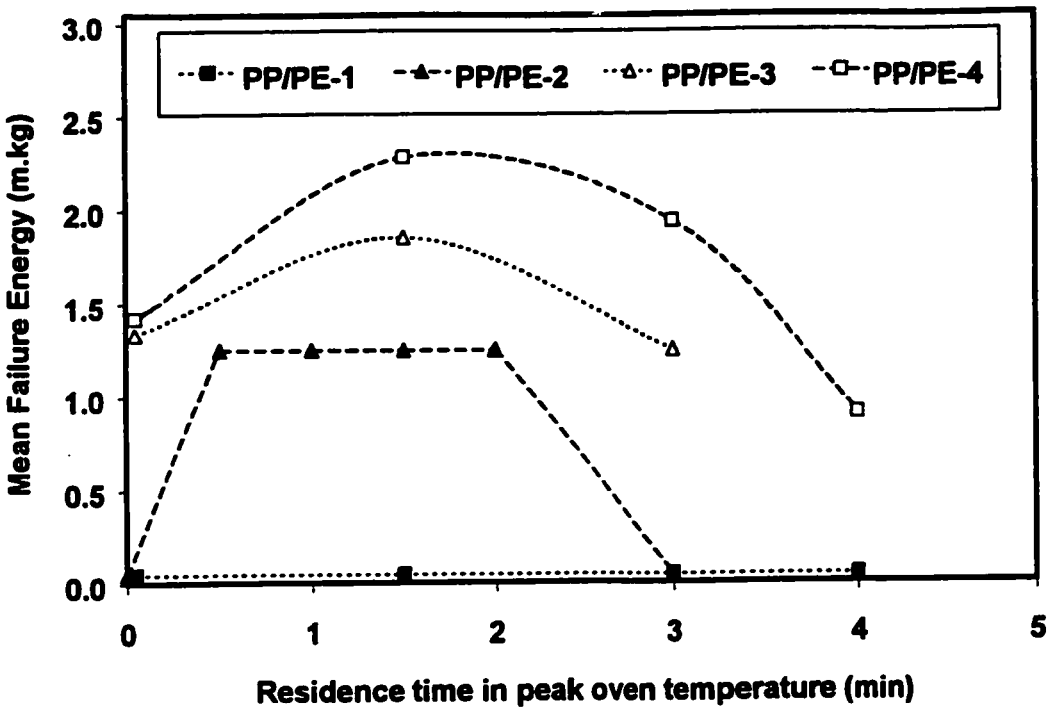

Figure 4.29: Comparison of impact strength at room temperature of polypropylene copolymers as a function of residence time at the peak oven temperature

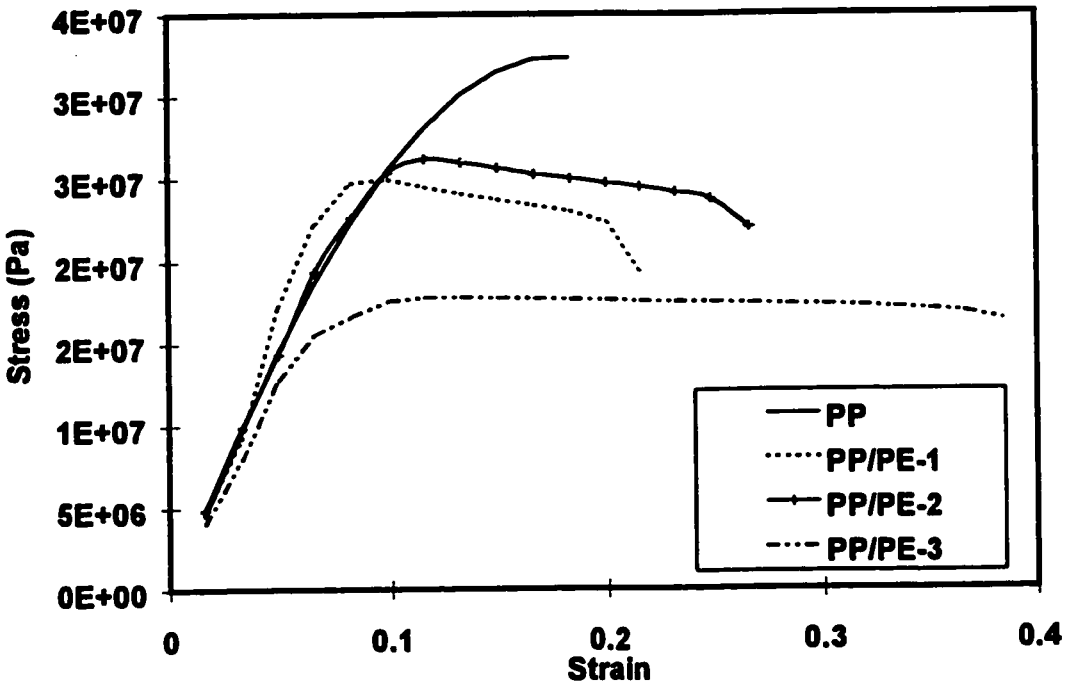

Figure 4.30: Comparison of tensile curves of polypropylene copolymers

On the other hand tensile strength is reduced. Microphotographs of the fractured surfaces taken using SEM microscopy (Figures 4.31 and 4.32) revealed that as PE content increases, the particles of the dispersed ethylene phase become smaller and the fractured surface shows more ductility.

4.7. Effect of bubbles in rotomolded parts

A common problem encountered during processing some of the polymers described above was the presence of bubbles. The presence of bubbles is inherent in rotational molding. Their effect on the rotomolded part properties is discussed in this section.

Figures 4.33 (a) through (d) show the evolution of bubble content in rotomolded parts made from two LLDPE resins, PE-2 and PE-5, as a function of oven temperature. In general, as the oven temperature increases, the number of bubbles decrease. However, PE-2 has a slightly lower peak melting point than PE-5 (Table 4.1). In addition, the extrapolated onset melting temperature, denoting the temperature when the polymer first starts to melt as measured from the DSC curve, is 120°C for PE-2 and 125°C for PE-5. This means that melting and subsequently the formation of bubbles occur at higher temperatures, thus requiring longer overall processing time. Figure 4.34 displays the evolution of density of the rotomolded parts with time at the same processing conditions as the ones shown in Figures 4.33 (a)-(d). For both resins density increases with time as bubbles dissolve, but the overall process is delayed for PE-5, due to the higher melting point. These results indicate that density values of rotomolded parts can

Figure 4.31: SEM microphotograph of fractured surface of rotomolded polypropylene (PP/PE-1, 12.4% PE)

Figure 4.32: SEM microphotograph of fractured surface of rotomolded polypropylene

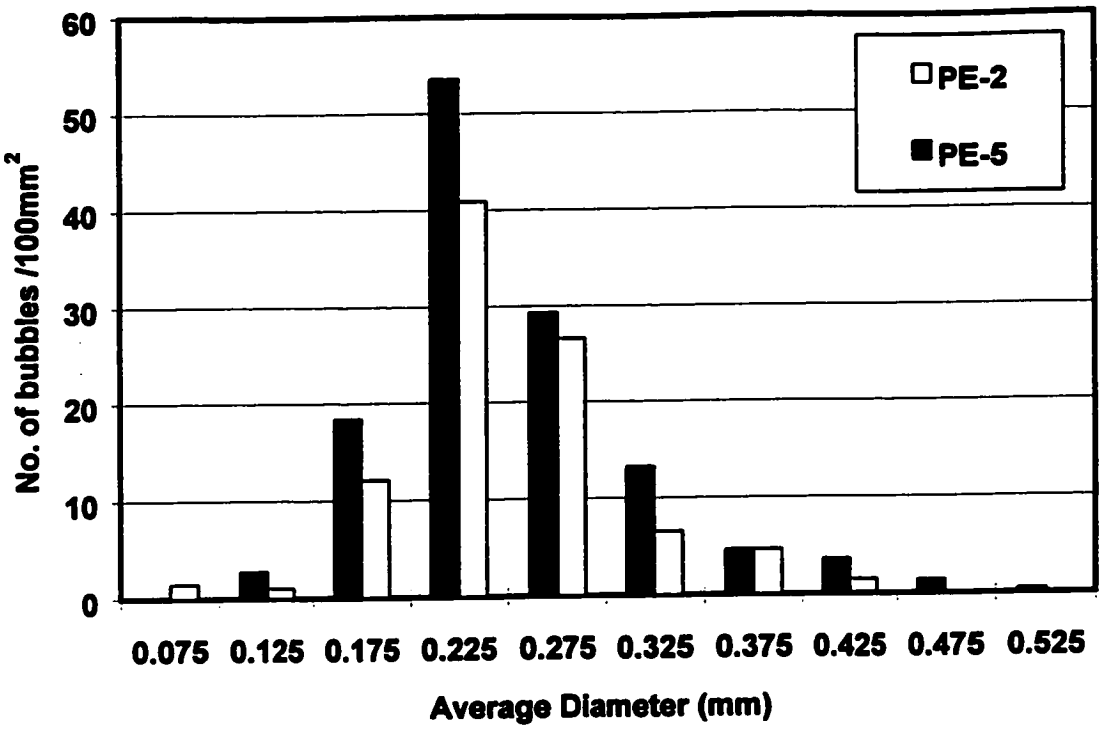

Figure 4.33 (a): Bubble content distribution in rotomolded parts. Oven set-point 260°C

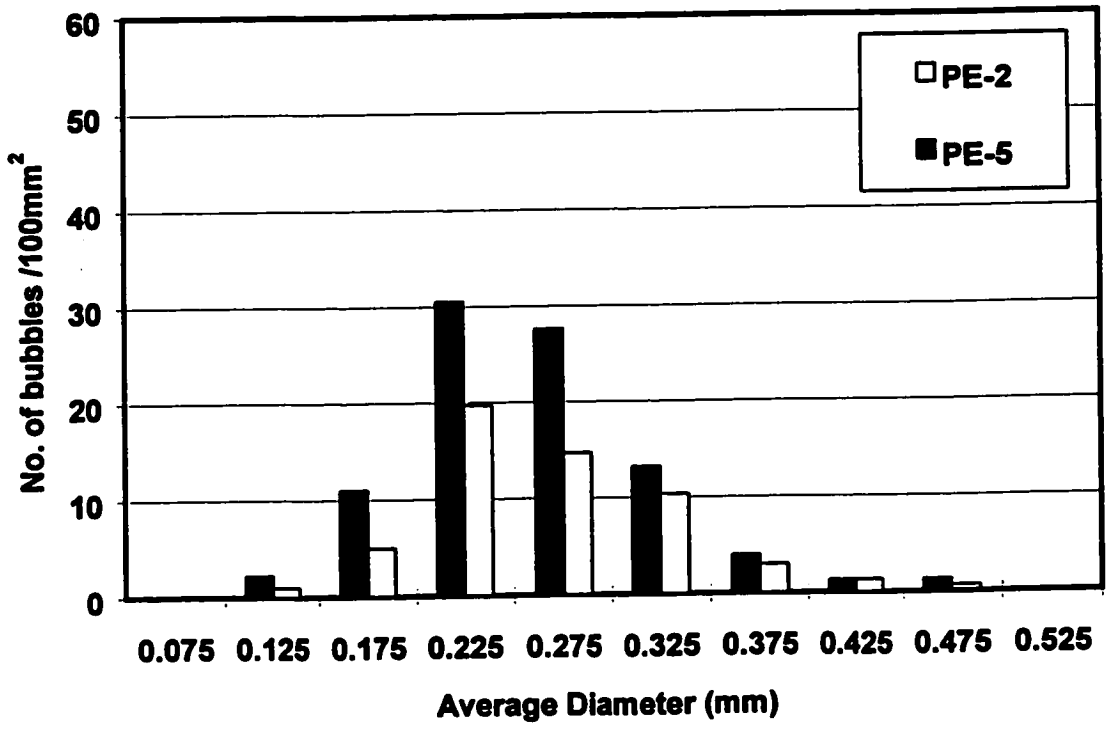

Figure 4.33 (b): Bubble content distribution in rotomolded parts. Oven set-point 270°C

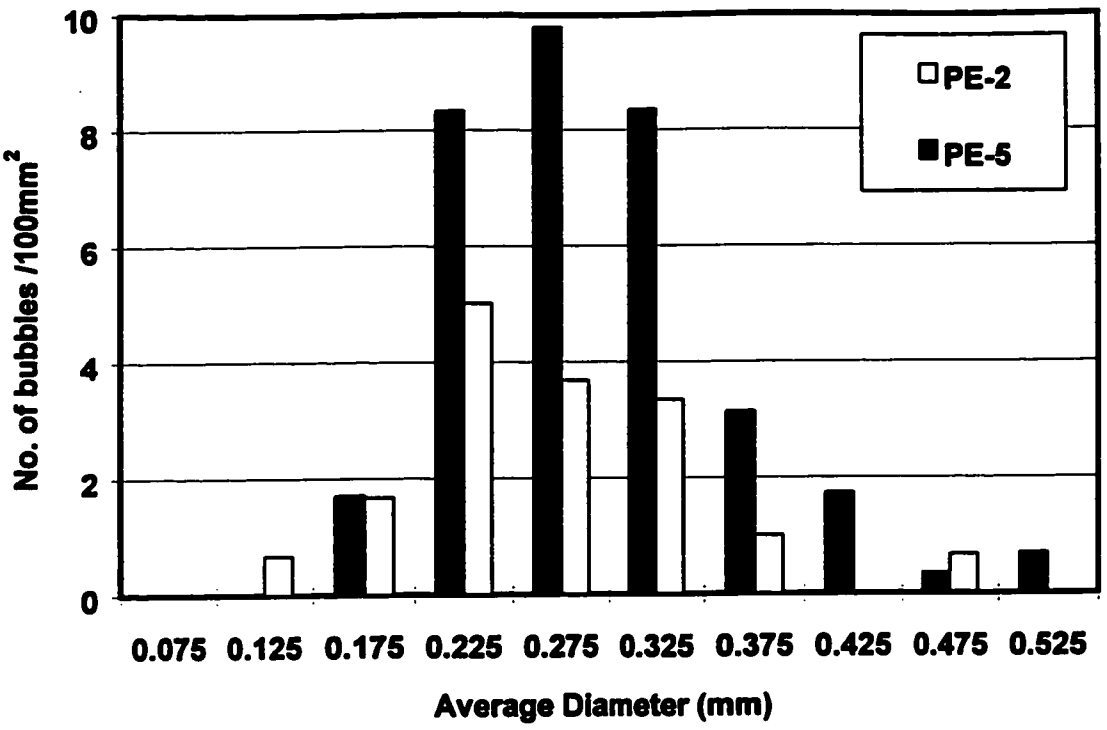

Figure 4.33 (c): Bubble content distribution in rotomolded parts. Oven set-point 280°C

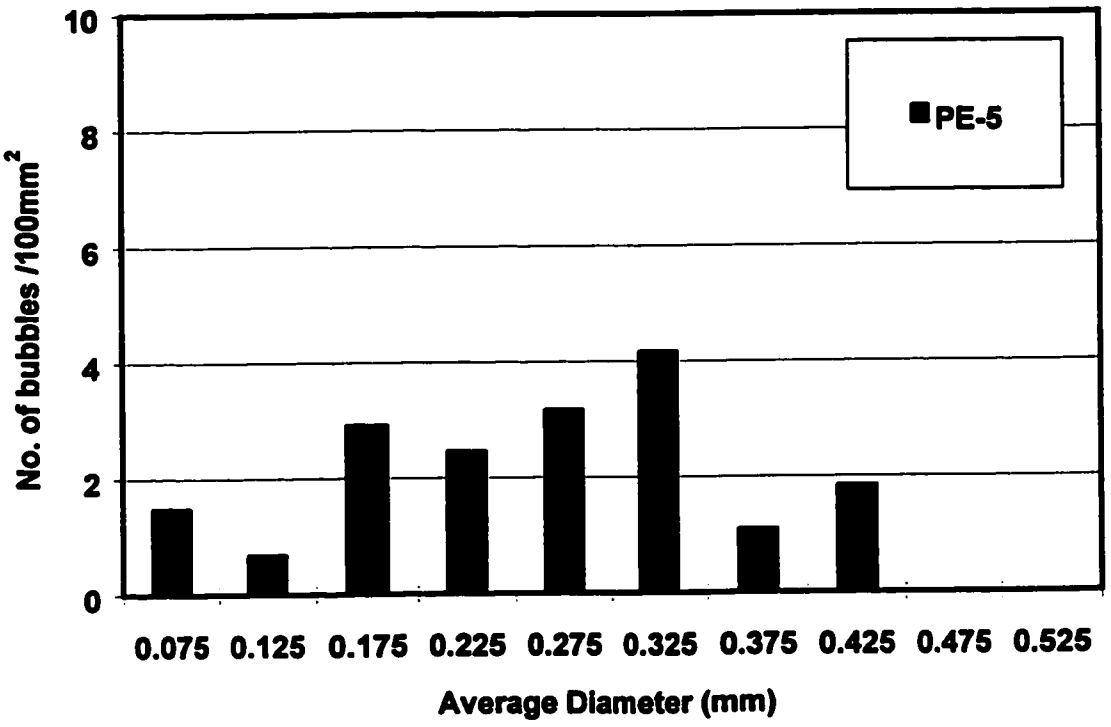

Figure 4.33 (d): Bubble content distribution in rotomolded parts. Oven set-point 290°C

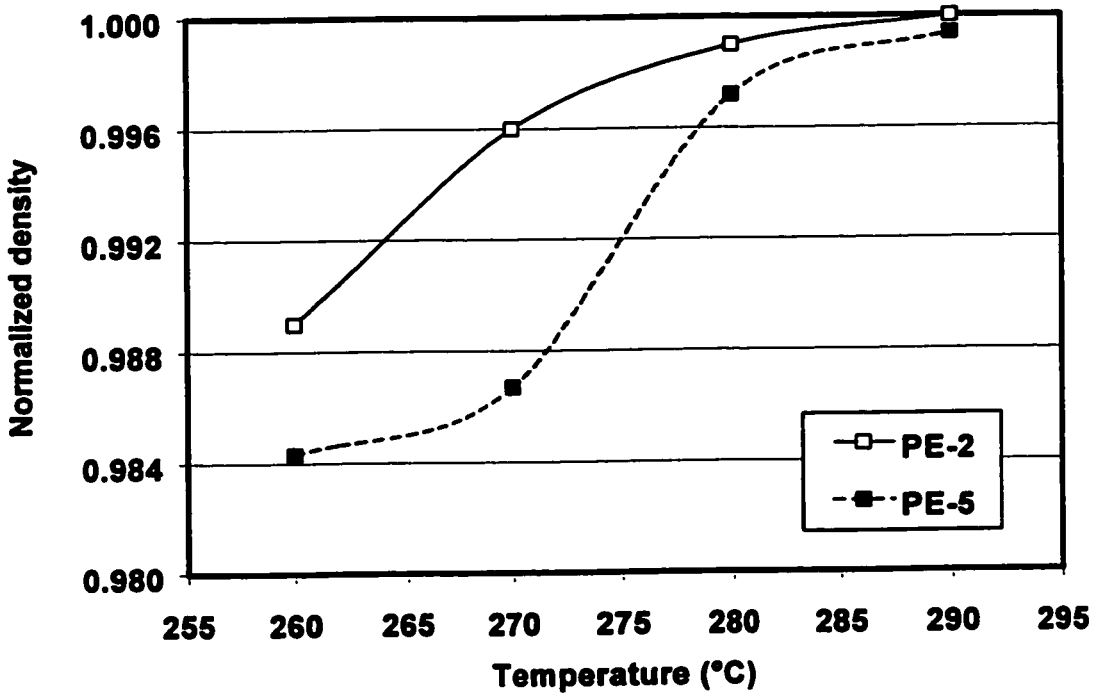

Figure 4.34: Density evolution of rotomolded PE parts as a function of oven temperature

provide an accurate representation of bubble content, without having to resort to time consuming image analysis techniques.

Table 4.6 shows how the impact strength, expressed as Mean Failure Energy (MFE) evolves as a function of oven temperature and residence time in the peak oven temperature for the two resins. The presence of bubbles affects the impact strength of PE-5, which needs a longer processing time to achieve its maximum impact strength. Bubbles also affect tensile properties, because they can cause weak points on the tensile specimens.

Table 4.6: Mean Failure Energy as a function of oven temperature and residence time inside the oven at the maximum oven temperature

Oven Temperature Set Point (°C)	Residence time (min)	MFE (m.kg)	
		PE-2	PE-5
290	0	6.3	5.2
300	1.5	7.9	7.7
310	3	7.6	8.2

4.8. Conclusions

A wide selection of polymers are available to rotomolders nowadays, offering a variety of properties. It was found that polyethylene based polymers offer better toughness, while polypropylenes offer better stiffness. Introduction of comonomers significantly alters the properties of the original polymers, usually by improving impact and reducing tensile properties. Polycarbonate offers the best combination of mechanical properties, at the expense of processing ease.

The presence of bubbles in rotomolded parts is a problem which appears especially when materials other than polyethylenes are used. Bubbles can potentially affect the mechanical properties and aesthetics of the final product. In the cases presented above, the occurrence of excessive bubbles which are hard to remove is mostly encountered in polymers with high amorphous contents (corresponding to low crystallinities). Rheological characterization suggested that these types of polymers may exhibit weak viscosity dependence on temperature and higher melt elasticities. A more detailed analysis of the phenomena controlling the appearance and removal of bubbles will be undertaken in the following chapters.

Chapter 5

BUBBLE FORMATION AND DENSIFICATION OF POLYMER MELTS

5.1. Introduction

The formation of a homogeneous polymer melt from powder particles is encountered in several polymer processing methods, such as rotational molding and powder coating. In rotational molding for example, which is virtually shear and pressure free, the polymer tends to melt freely, since there are no external forces applied. Air pockets or bubbles are trapped during melting, thus delaying the formation of a homogeneous melt. The presence of bubbles in rotomolded parts can potentially affect the mechanical properties and aesthetics of the final product, as discussed in Chapter 4.

In order to predict the physical properties of a powder compact, which transforms gradually into a homogeneous polymer melt and to make possible the modeling of the overall densification process it is imperative to conduct a fundamental study on all the stages beginning from the powder state until the formation of a homogeneous polymer melt. Since there is a lack of published research covering densification in polymers, one commonly has to resort to literature relevant to ceramics, metals and glass processing. This chapter examines the applicability of several models to phenomena encountered in

polymer melts. An experimental study, using polymers with diverse properties, has been undertaken to identify the important parameters and evaluate their effect in the densification process. The experimental findings were subsequently compared to available models in an effort to gain an in-depth understanding of the mechanisms involved in the process.

In the present work the term polymer densification is used interchangeably with the term sintering to describe the whole process of particle coalescence, formation and dissolution of bubbles which results in the transformation of a porous powder compact to a fully densified plastic part.

5.2. Experimental studies on bubble formation and densification of polymeric powders

The vast majority of the densification models discussed in the literature review have been developed to model the sintering behavior of glass gels, metals and ceramics. The present study will attempt to elucidate the mechanism of densification of polymeric powders, which coalesce at temperatures above their melting point and to evaluate the applicability of several models, based on comparisons with experimental data.

The increase of density, as the powder compact gradually transforms into a polymer melt, essentially depends on the size and number of air pockets, or bubbles which form when the powder melts. It is therefore important to conduct first an investigation on the bubble formation process and the parameters involved. These studies were conducted by using the heating chamber and the

procedure described in the experimental section (section 3.2.6.).

The density of the polymer samples as a function of heating time has been measured and has been complemented with visual observations of the structure of the material throughout the densification process. The procedure has been outlined in section 3.2.7. The results obtained from the bubble formation and densification experiments have been compared with results from coalescence experiments of two particles, in order to relate the fundamental phemonenon of the coalescence of two particles to the entire densification process.

5.2.1. Effect of powder properties on bubble formation

Powder particle size and more importantly particle shape affect significantly the formation of bubbles. Due to the grinding procedure, smaller particles tend to have more irregularities and tails thus trapping more, but smaller air pockets. On the other hand, sieving and retaining the coarser fractions in the powder resulted in the formation of fewer but larger bubbles, as demonstrated in Figure 5.1 and Table 5.1. Figure 5.2 summarizes the air content inside the melt as a function of particle size. In addition powders with smaller particle size tend to melt earlier in the cycle and to sinter faster (Bellehumeur et al., 1996) thus reducing the required heating time. These findings are of considerable interest, because they suggest that the use of micropellets instead of powder can prove very beneficial: the micropelletization technology (Gala Industries, 1995, Takács et al., 1996) can provide particles of relatively small size (diameter between 0.5-0.7 mm, compared to 3 mm for regular polymer pellets), but with very regular

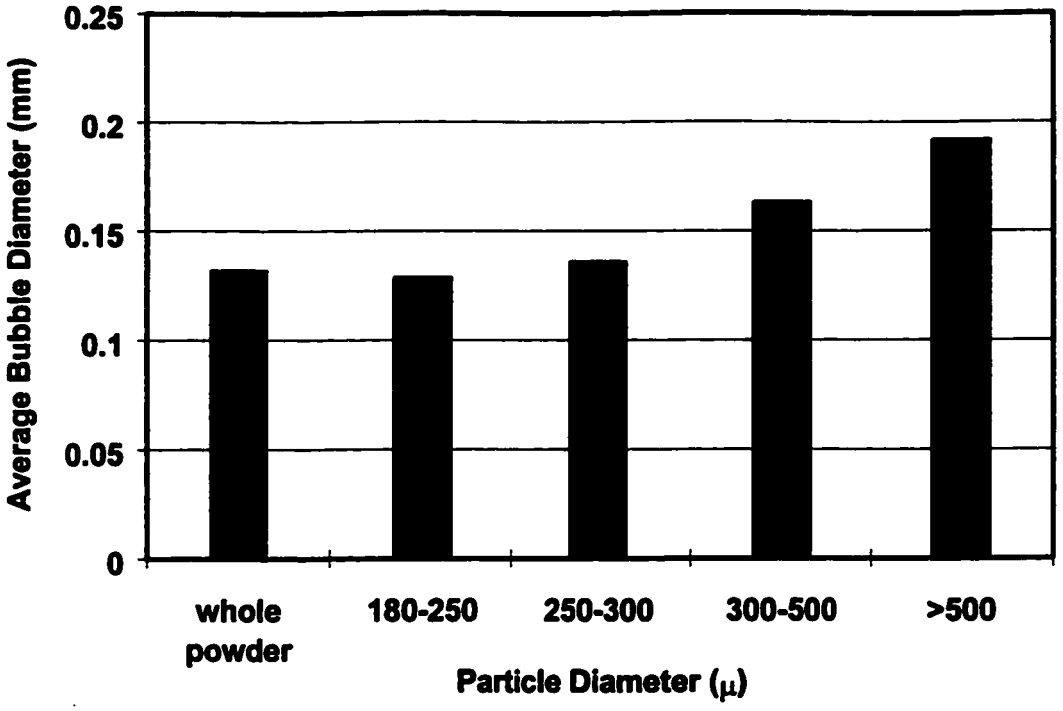

Figure 5.1: Average bubble diameter as a function of powder size for PE-2

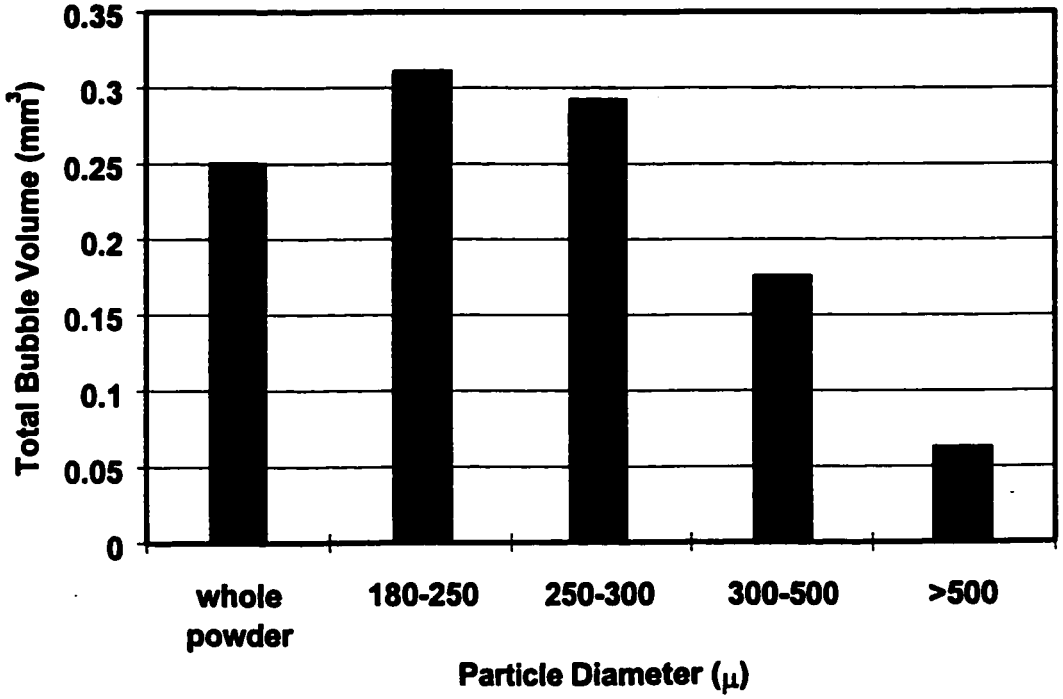

Figure 5.2: Air content as a function of particle size for PE-2 (sample size 30 mm^3)

shapes, so that good heat transfer and sintering characteristics can be maintained, while the problem of entrapment of excessive bubbles due to the poor packing of the powder can be avoided.

Table 5.1: Average bubble diameter and air content in polyethylene melts as a function of particle size

Resin	Bubble diameter (mm)	% Air content in melt
PE-2 (whole powder)	0.14 ± 0.061	1
PE-2 (average particle size > 500 μ)	0.2 ± 0.100	0.3
PE-2 (average particle size = 400 μ)	0.16 ± 0.087	0.7
PE-2 (average particle size = 275 μ)	0.14 ± 0.062	1.15
PE-2 (average particle size = 210 μ)	0.13 ± 0.058	1.22

The importance of powder quality can be also demonstrated by the following example: A series of experiments conducted with resins PE-1 to PE-3, which were supplied by the same resin producer, showed that the bubble content in the PE-3 melt was unexpectedly high (Figure 5.3), although the contrary was expected because PE-3 had the lowest viscosity. However it was found that the quality of the powder was very poor, containing large amounts of irregularly shaped particles with tails (Figure 5.4). A good means to quantify the quality of the powder in terms of its shape is the dry flow test (see description in section 3.2.1.). Typically particles containing "tails", or other irregularities, tend to bridge when poured through the test funnel, thus resulting in high values of pourability

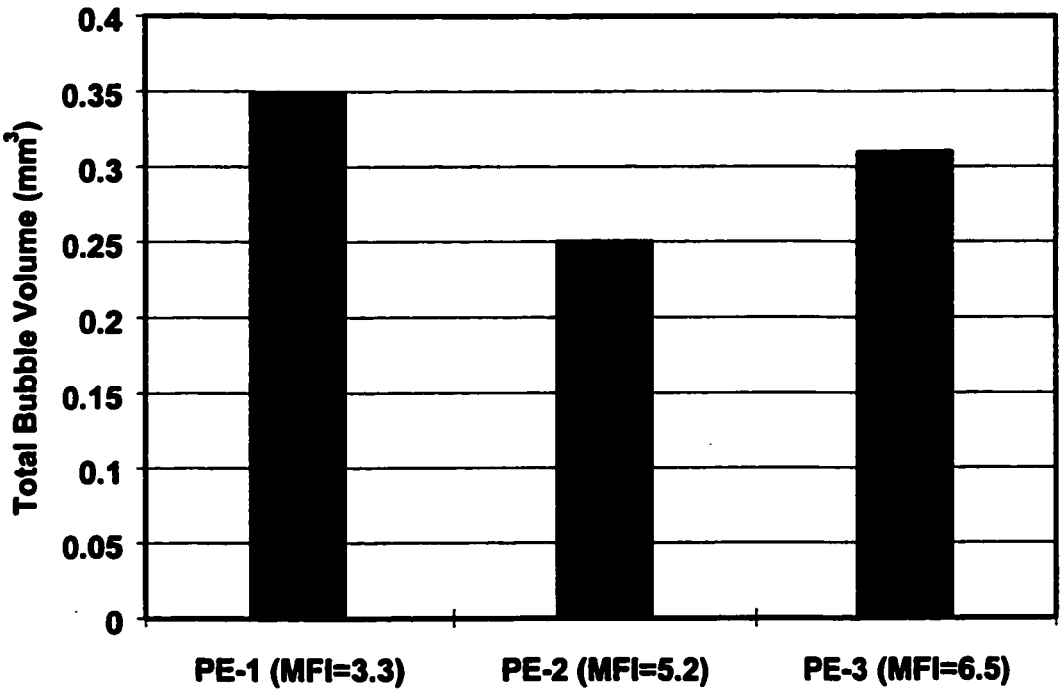

Figure 5.3: Comparison of air content for PE-1, PE-2 and PE-3 (sample size 25 mm^3)

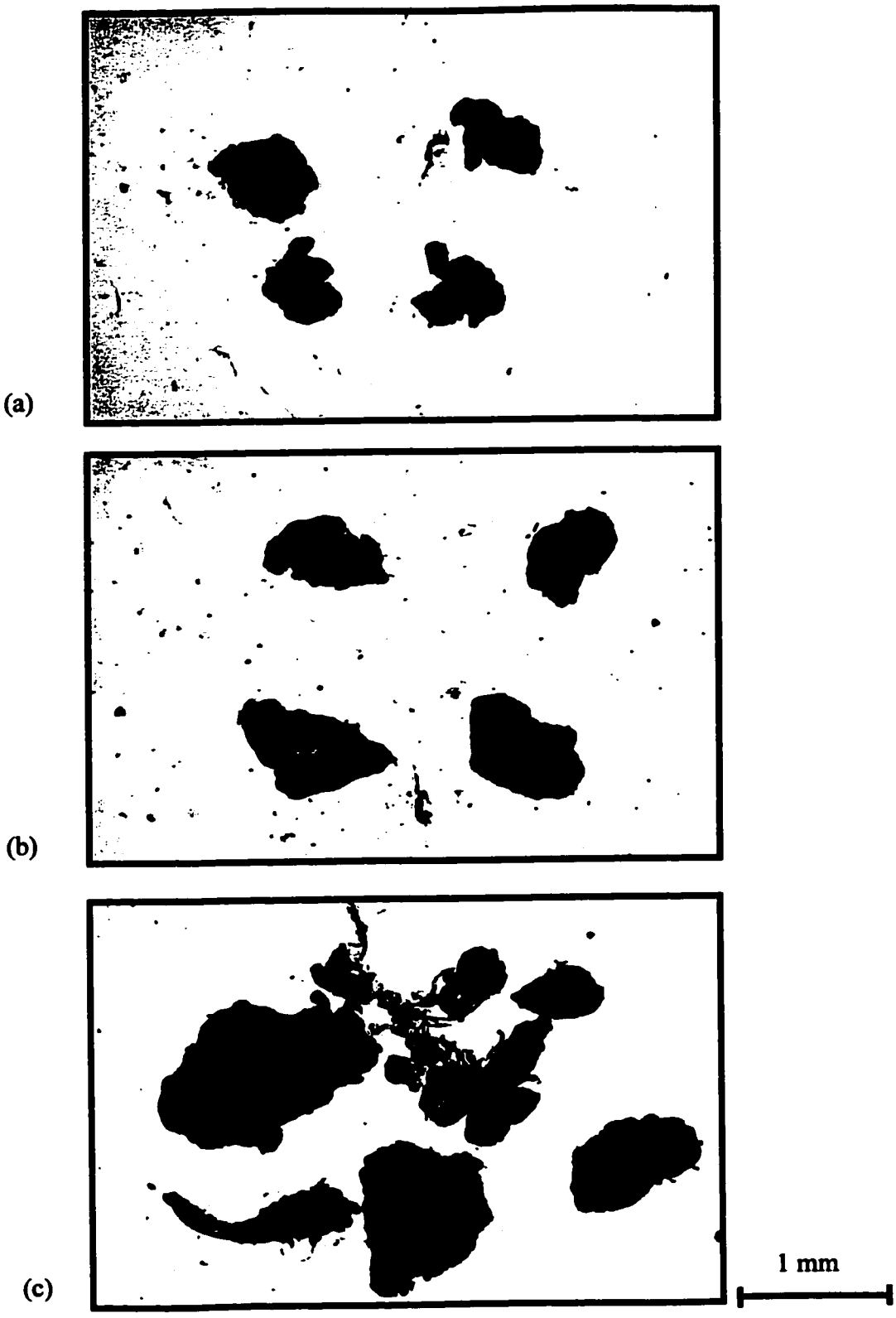

Figure 5.4: Images of powder particles (a) PE-1, (b) PE-2 and (c) PE-3

factor. Table 5.2, which summarizes the pourability of resins PE-1 through PE-3, shows that PE-3 displayed the highest value of pourability. Table 5.2 also shows that the pourability factor attains higher values, as we move towards finer powder with more irregular shape.

The average particle size and particle size distribution of the rotomolding grade powders, as supplied by the producers varies considerably, depending on the grinding procedure. To eliminate the effect powder size has on the process, the powder used in all the experiments described in the rest of the chapter has been obtained by sieving the whole powder and retaining the fraction between 300 and 500 microns (corresponding to sizes between 50 mesh and 30 mesh).

Table 5.2: Pourabilities of polyethylene powders

Material	Pourability (seconds / 100 g)
PE-1	40
PE-2	28
PE-3	44
PE-2 (300 – 500 μ)	28
PE-2 (250 – 300 μ)	29
PE-2 (180 – 210 μ)	38.8
PE-2 (< 180 μ)	70

5.2.2. Sintering and bubble formation in polyethylenes

The importance of viscosity in polymer sintering has been demonstrated by Bellehumeur et al. (1996) and Bellehumeur (1997), who conducted sintering experiments using two particles and demonstrated that the rate of neck growth

between the two particles is significantly reduced when viscosity increases. Their conclusions imply that a single layer of molten powder particles will sinter sooner as viscosity is decreased and pore closing will occur faster.

In reality rotational molding involves the sintering of a powder compact instead of a single layer, so in this work experiments were conducted by using polyethylene powder compacts and observing their melting and densification behaviour. According to Figure 5.5, which shows the progression of density as a function of time for three polyethylenes with different viscosities at 132°C, slower overall densification rates are observed as viscosity increases (or MFI decreases). This can be attributed to lower coalescence rates, as reported by Bellehumeur et al. (1996) and Bellehumeur (1997).

Non-isothermal conditions, simulating an actual rotational molding heating cycle were applied in an effort to elucidate the mechanism of bubble formation and densification. The temperature profile used in experiments involving polyethylene powders has been shown in Figure 3.6.

Visual observations made during experiments conducted by using three polyethylene resins with different viscosities (PE-4 – PE-6), revealed that the higher the viscosity, the longer the time required for particles to coalesce, lose their identity and form a homogeneous melt (Figure 5.6). These pictures can be compared to curves of two sintering particles obtained under similar oven conditions, Figure 5.7. From Figure 5.7 it can be observed that not only the rate of neck growth, y/a, is higher as viscosity decreases, but also the movement of the

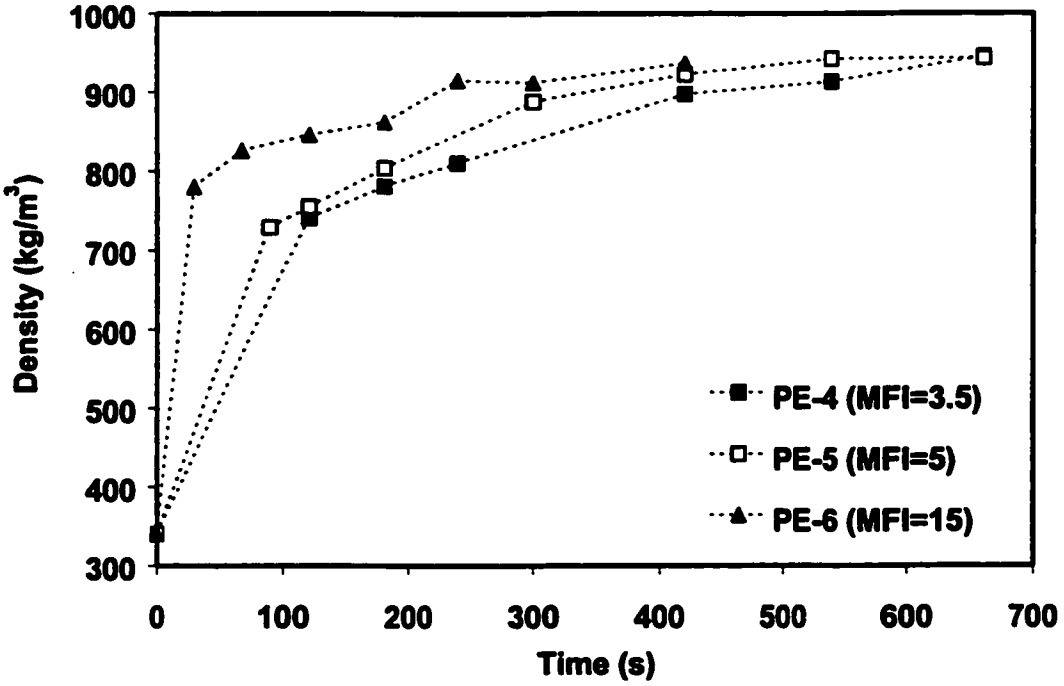

Figure 5.5: Experimental densification curves at 132°C, of polyethylenes with different MFI

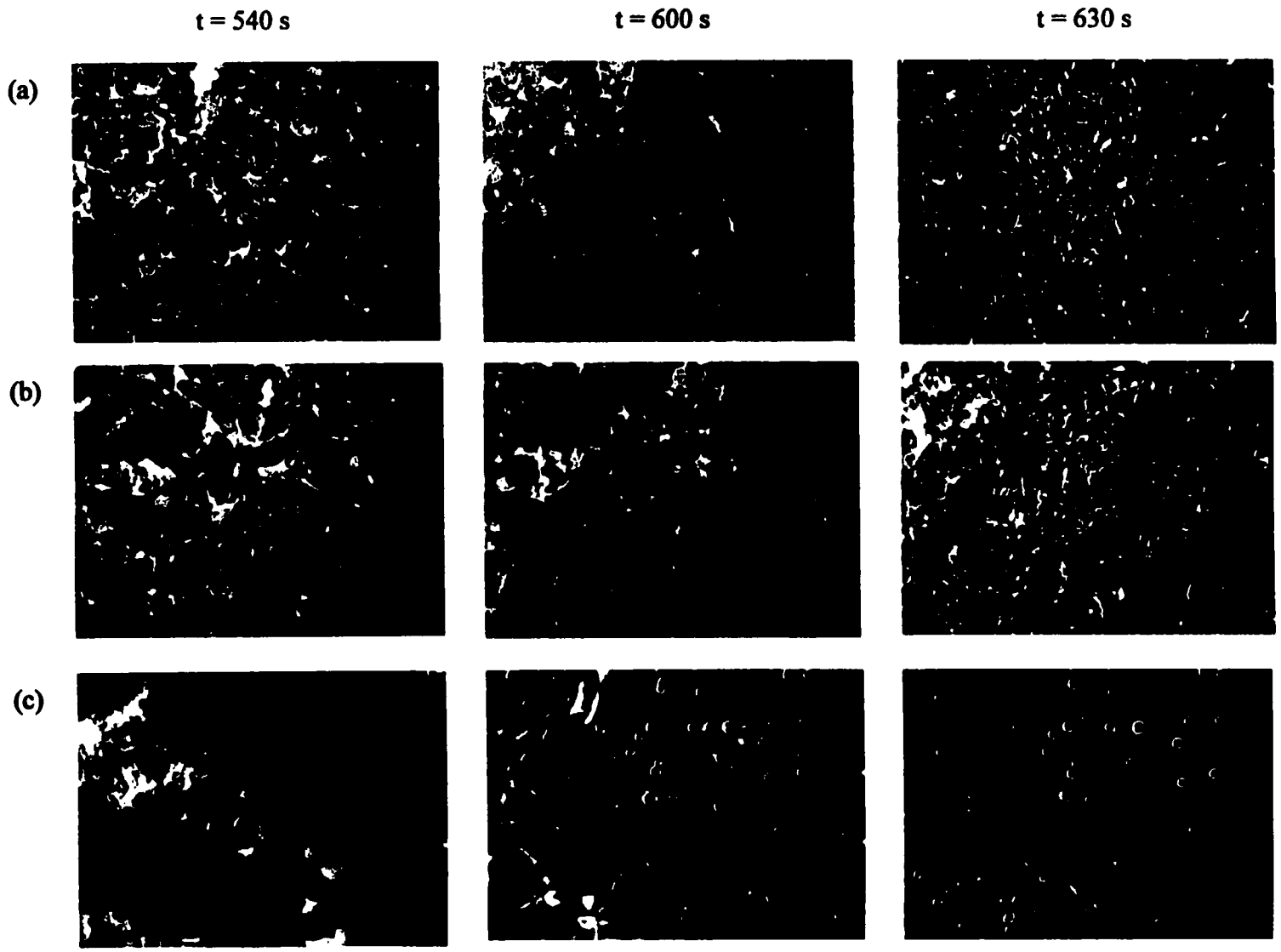

Figure 5.6: Optical microscope images of bubble formation inside heated chamber (top view) a) PE-4 b) PE-5 c) PE-6

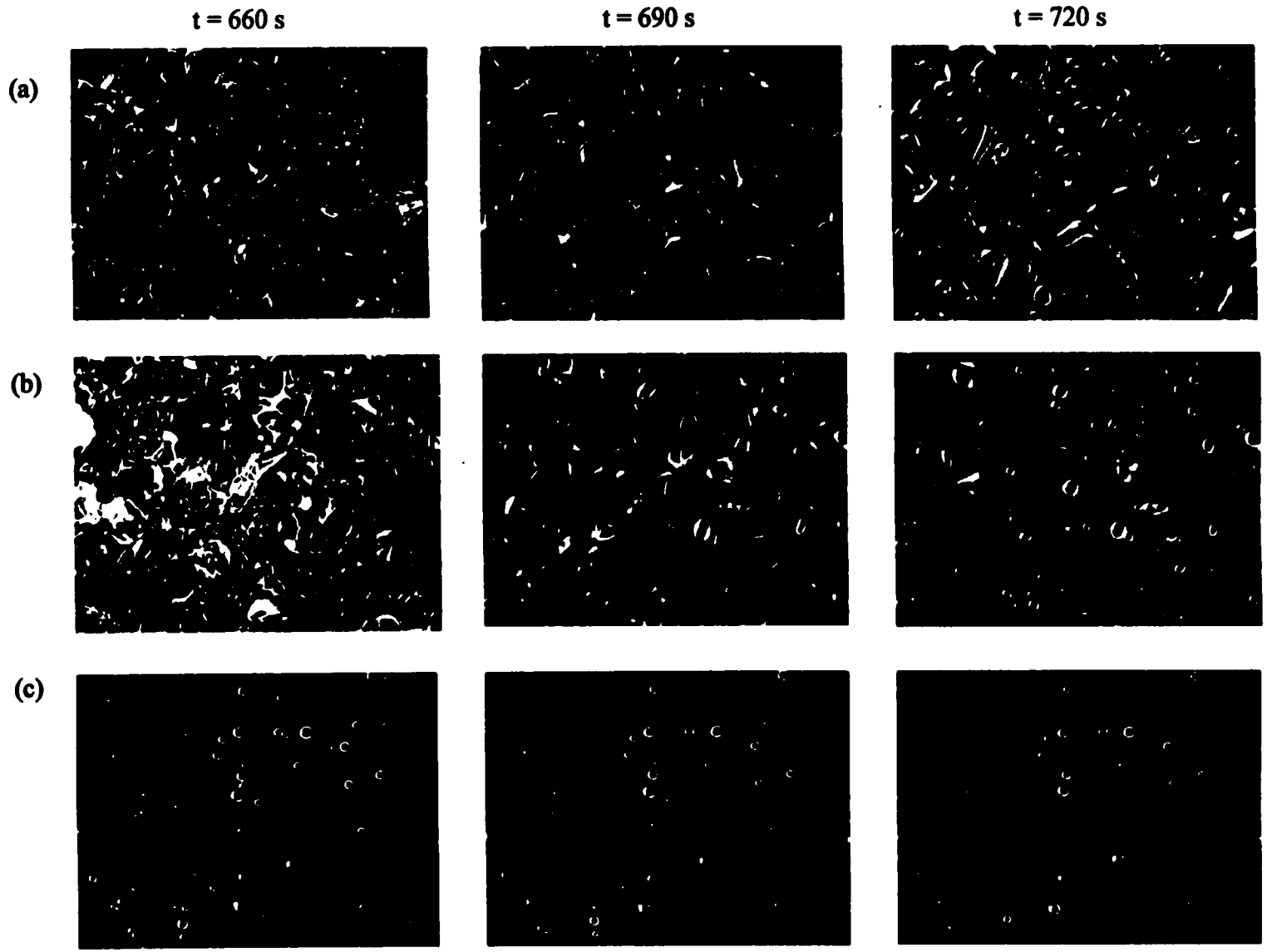

Figure 5.6 (cont'd): Optical microscope images of bubble formation inside heated chamber (top view) a) PE-4 b) PE-5 c) PE-6

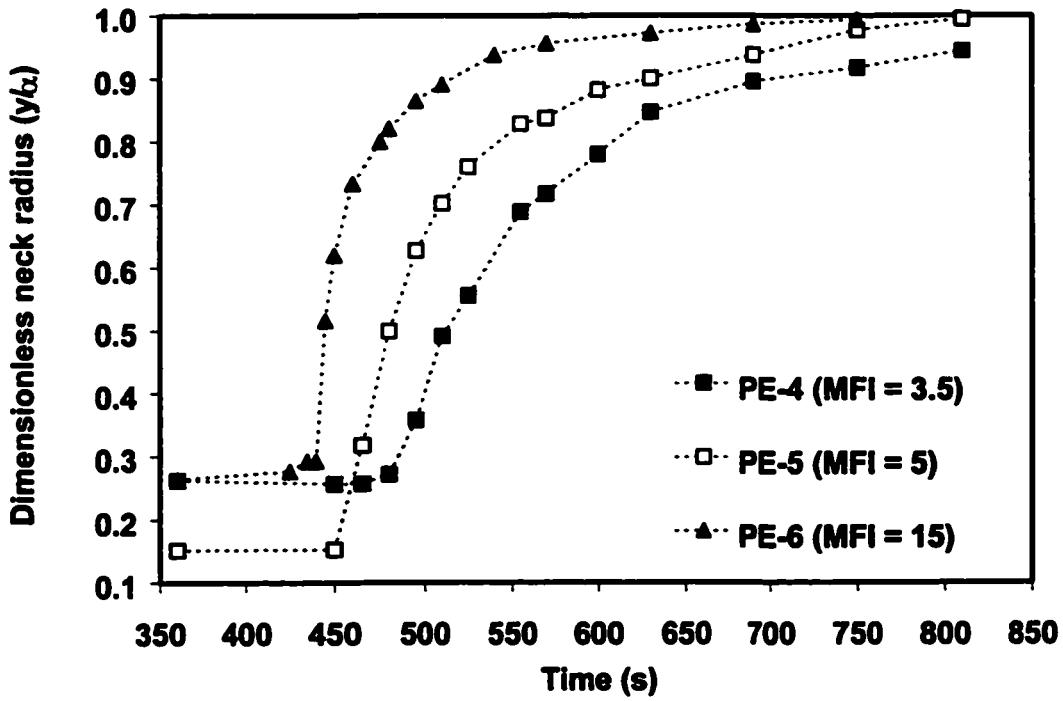

Figure 5.7: Sintering of two particles for polyethylenes with different MFI

melt begins sooner. The fact that the melt movement begins earlier is also obvious from the images shown in Figure 5.6. It is speculated that for higher MFI materials the value of viscosity becomes sufficiently low earlier in the heating cycle. It can be concluded that the benefit of using lower viscosity materials is twofold: the rate of particle coalescence itself is faster and the whole process begins earlier in the cycle, thus resulting in substantial savings in heating time.

It was also revealed that as viscosity increases more and/or larger bubbles form inside the polymer melt, as shown in Figure 5.8. Figure 5.9 demonstrates the overall air content inside the polymer melt as a function of viscosity. The average bubble size and the overall air content are summarized in Table 5.3.

The above results imply that there is a correlation between the coalescence process of two particles and the bubble formation and overall densification of the polymer compacts: Faster coalescence rates can be associated to the formation of less bubbles and to faster overall densification. Therefore, it can be suggested that experiments of coalescence of two particles can be used as an efficient screening tool for distinction between materials and for the prediction of their sintering behavior relative to each other.

It must be noted that the benefits of using low viscosity resins, which were described above, are counteracted by reduced mechanical properties as viscosity increases, because of the ensuing decrease in molecular weight (Crawford, 1992). Therefore it is customary to the rotomolding industry to use materials with a

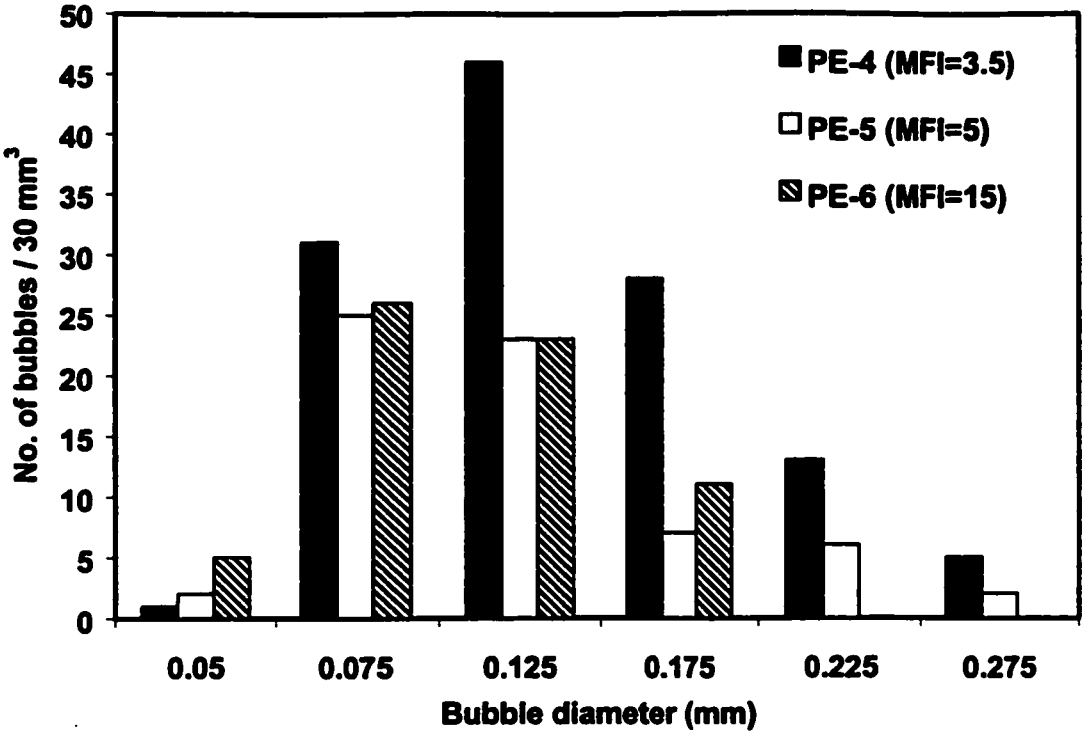

Figure 5.8: Size distribution of bubbles formed inside the polymer melt for polyethylenes with different MFI

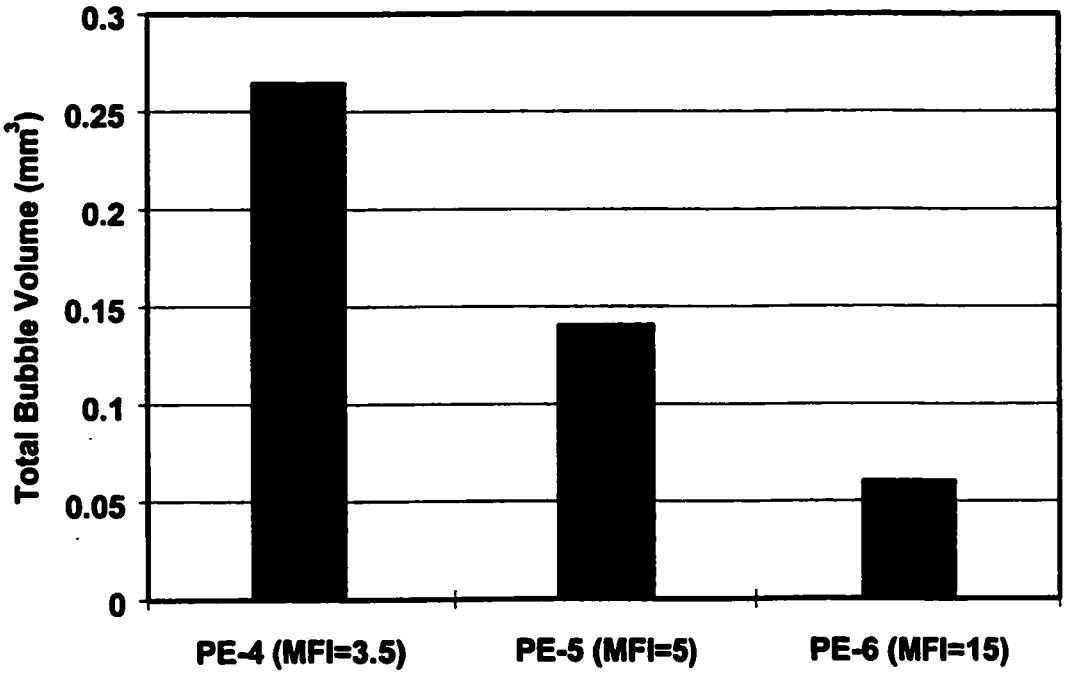

Figure 5.9: Air content inside the melt for polyethylenes with different MFI (sample volume 30 mm^3)

maximum MFI = 5. Materials with lower viscosities are used whenever the mold design specifically requires materials with superior flow properties.

Table 5.3: Average bubble diameter and air content in polyethylene melts, as a function of viscosity

Resin	Bubble diameter (mm)	% Air content in melt
PE-4 (MFI=3.5)	0.14 ± 0.055	0.93
PE-5 (MFI=5)	0.14 ± 0.071	0.5
PE-6 (MFI=15)	0.11 ± 0.039	0.21

Images of the densification process of a powder compact (PE-2) obtained with the aid of the optical microscope are presented in Figure 5.10. It must be noted that in the images of Figure 5.10 the loose powder lying above the molten layers has been removed upon taking the sample out of the heated chamber. Figure 5.11, which shows the progression of density combined with the thickness of the sintered powder compact suggests that melting-sintering is happening gradually as layer after layer of powder particles adhere. In the images taken during the early stages (Figure 5.10), two layers can be distinguished: A completely sintered homogeneous bottom layer and a top layer consisting of partially adhered particles. A sketch of the proposed mechanism is shown in Figure 5.12. If the sintering rate is sufficiently high, the void spaces between particles are expected to close and air is pushed away as each layer sinters before the next layer starts to melt. It is thus suggested that when viscosity is high, as the polymer melts layer by layer, there is not enough time for one layer to sinter

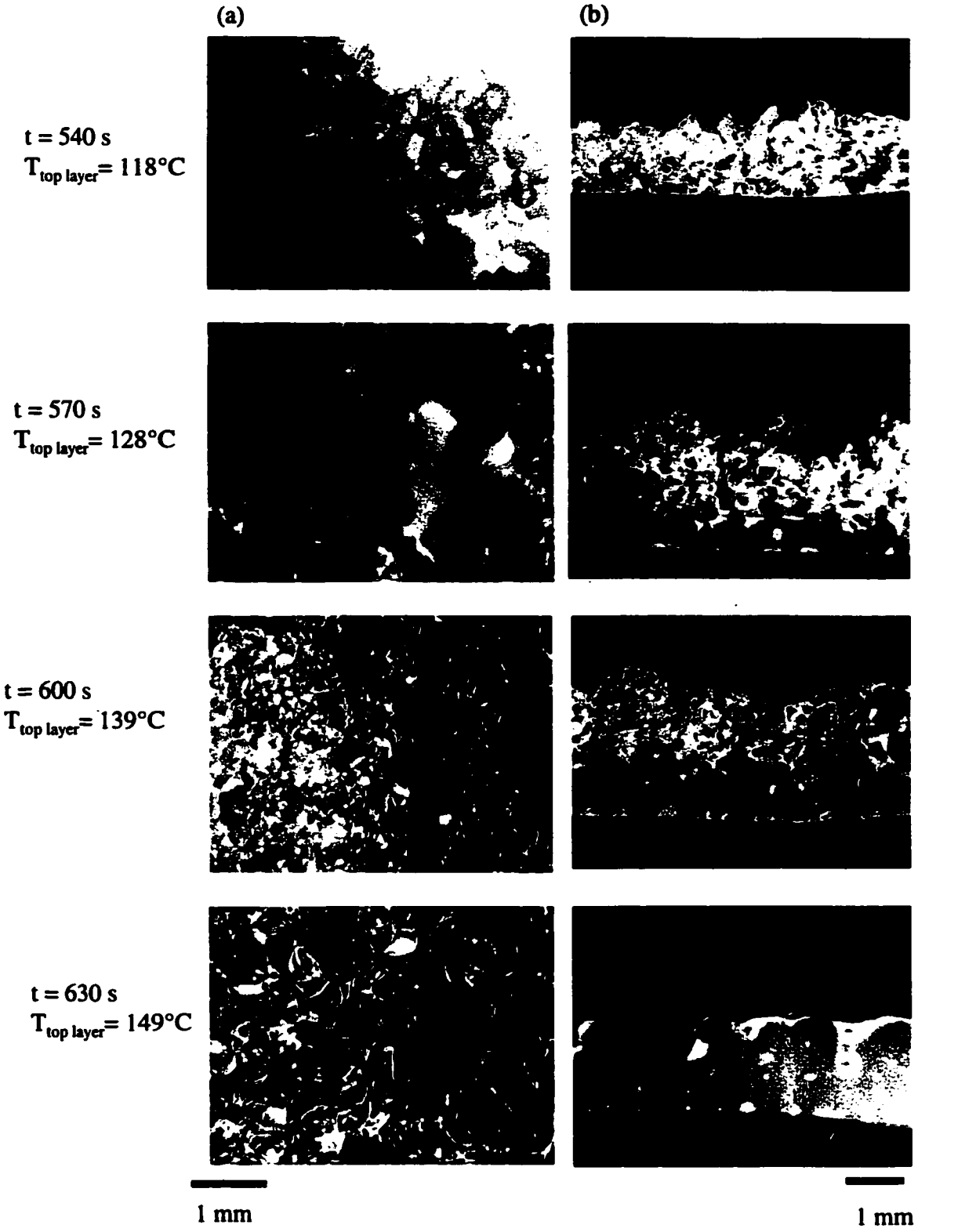

Figure 5.10: Optical microscope images of sintering of a polyethylene (PE-2) powder compact inside heating chamber a) top view b) side view

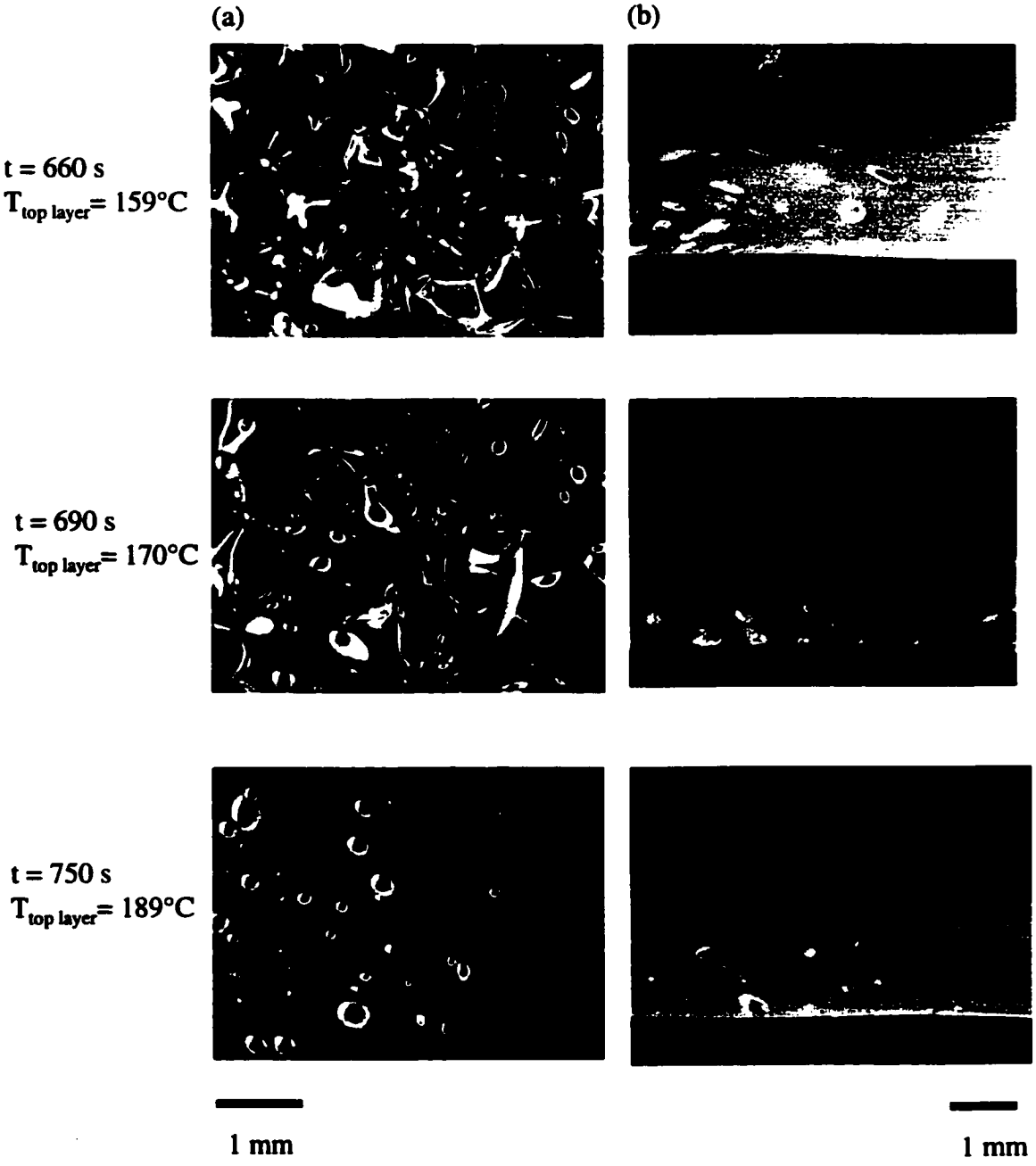

Figure 5.10 (cont'd): Optical microscope images of sintering of a polyethylene (PE-2) powder compact inside heating chamber a) top view b) side view

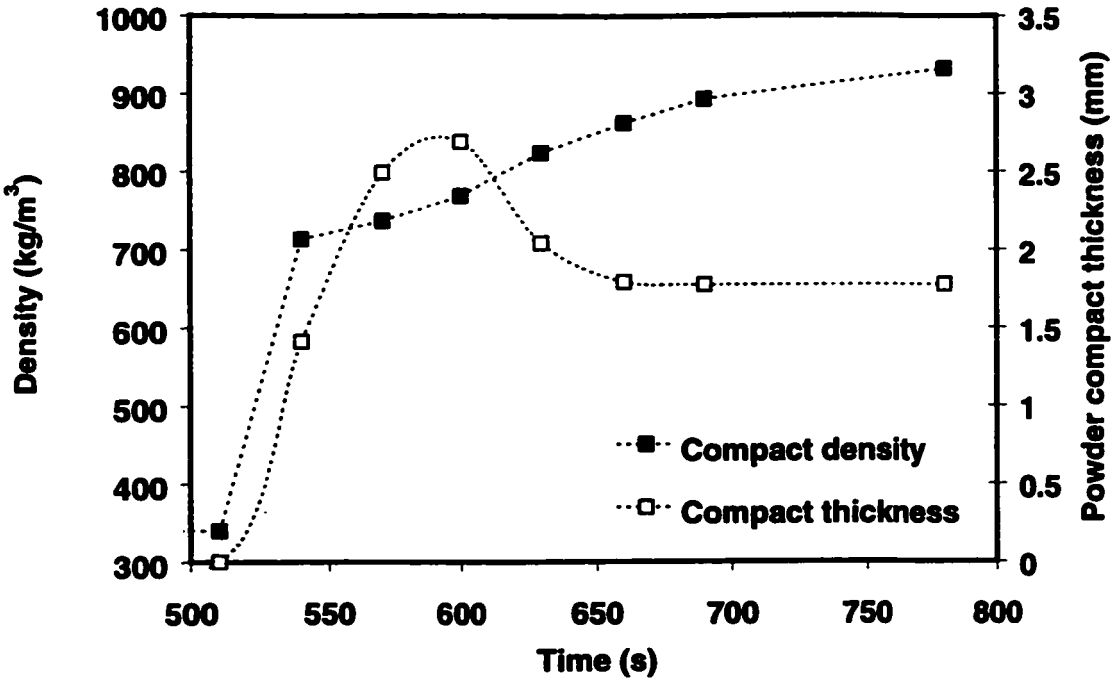

Figure 5.11: Variation of compact density and thickness as a function of time for PE-2

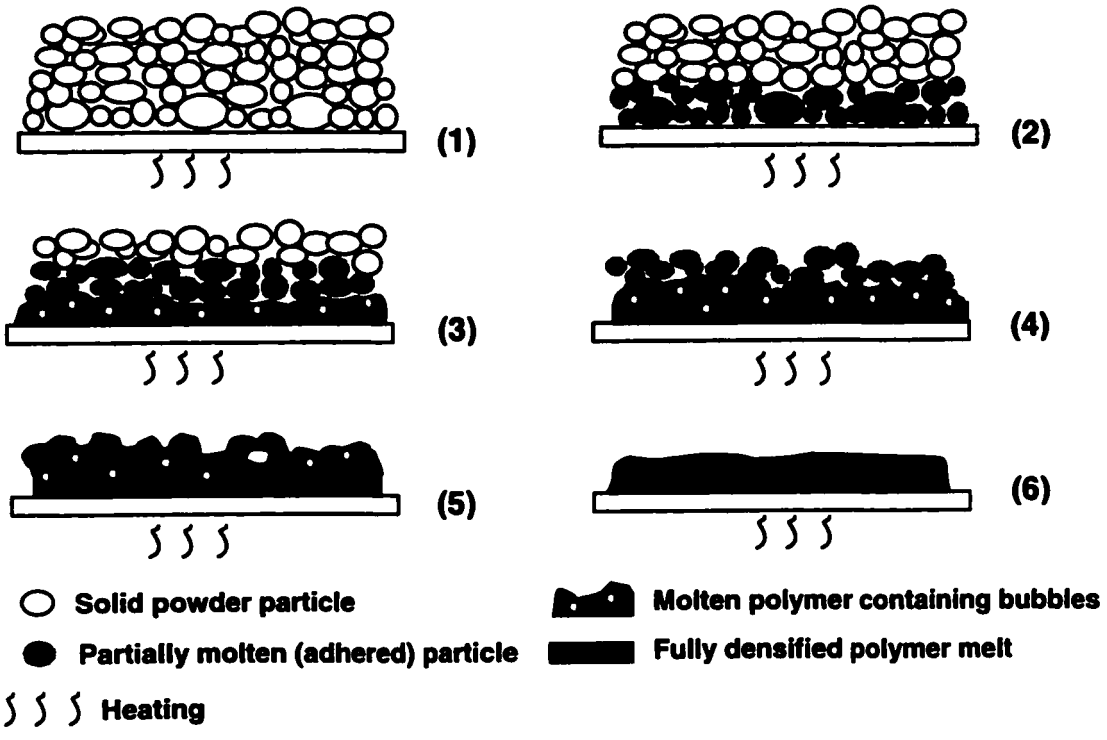

Figure 5.12: Schematic of densification of powder compact of semi-crystalline polymer

completely and for pore closing to be complete before the next layer melts. This results in the entrapment of air and subsequently the formation of more and/or larger bubbles inside the polymer melt.

5.2.3. Sintering and bubble formation in low-crystallinity polyethylene copolymers

Polymers with very low crystallinity, such as ethylene based copolymers which produce flexible products, melt very early in the heating cycle. Viscosity decreases slowly as temperature increases, starting from very high values, as demonstrated previously in Chapter 4, Figure 4.4. Particle coalescence experiments under non-isothermal conditions (temperature profile shown in Figure 3.7), demonstrated that the rate of neck growth is low in the beginning, due to the high viscosities, which inhibit melt flow (Figure 5.13). On the contrary the POP resin, whose viscosity decreases rapidly upon melting, displays a significantly faster rate of neck growth.

Figure 5.14 shows images obtained under the optical microscope of the top and side views of a compact consisting of EVA-2 powder particles. Figure 5.15 demonstrates the progression of density of the powder compact and the respective height of the sintered compact. A comparison with Figures 5.10 and 5.11 obtained previously for polyethylene, indicates that in the case of EVA-2 the whole powder compact adheres early and looks like a three dimensional compact which subsequently starts to shrink and decrease in height. A schematic of the process can be seen in Figure 5.16.

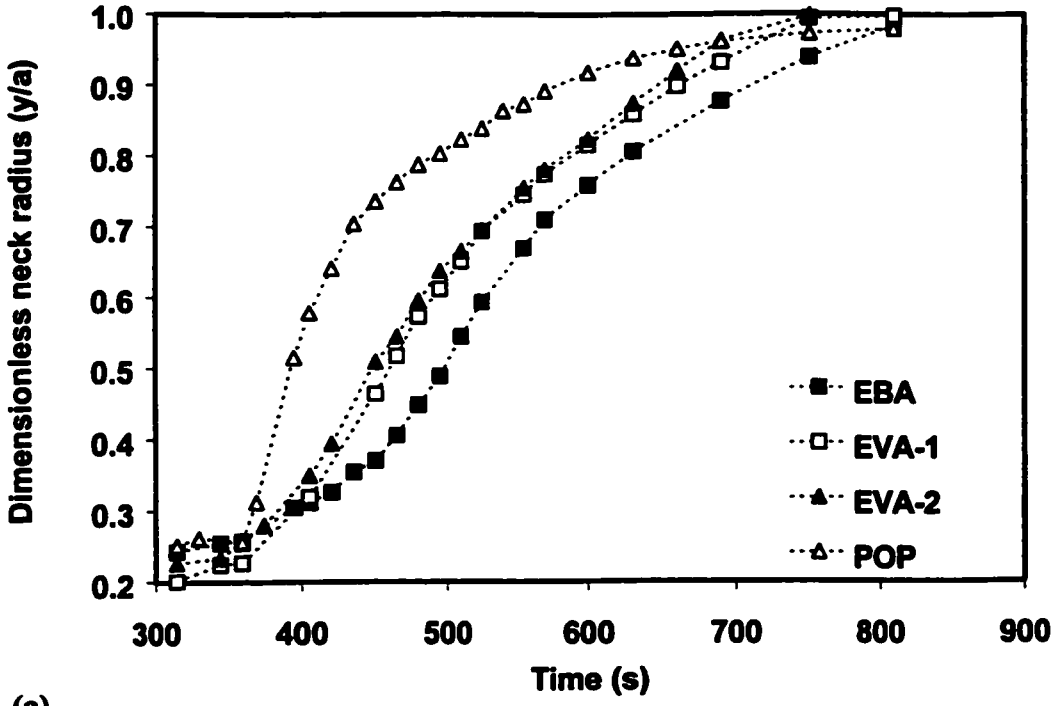

(a)

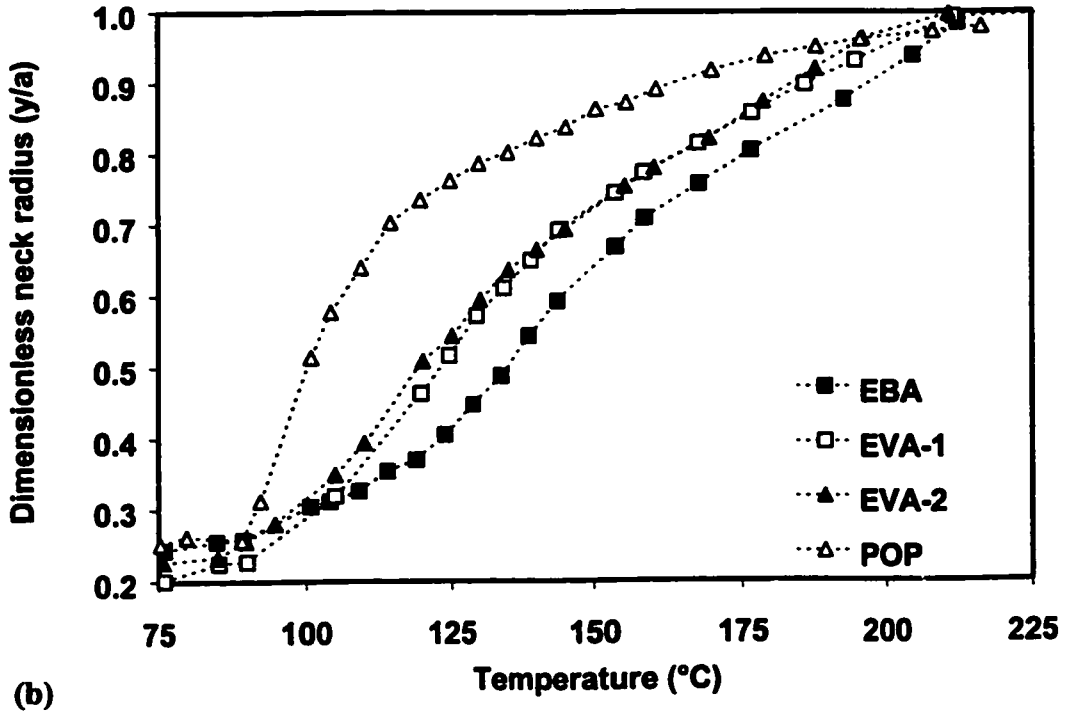

(b)

Figure 5.13: Sintering of two particles for various PE copolymers (a) neck radius vs. time, (b) neck radius vs. temperature

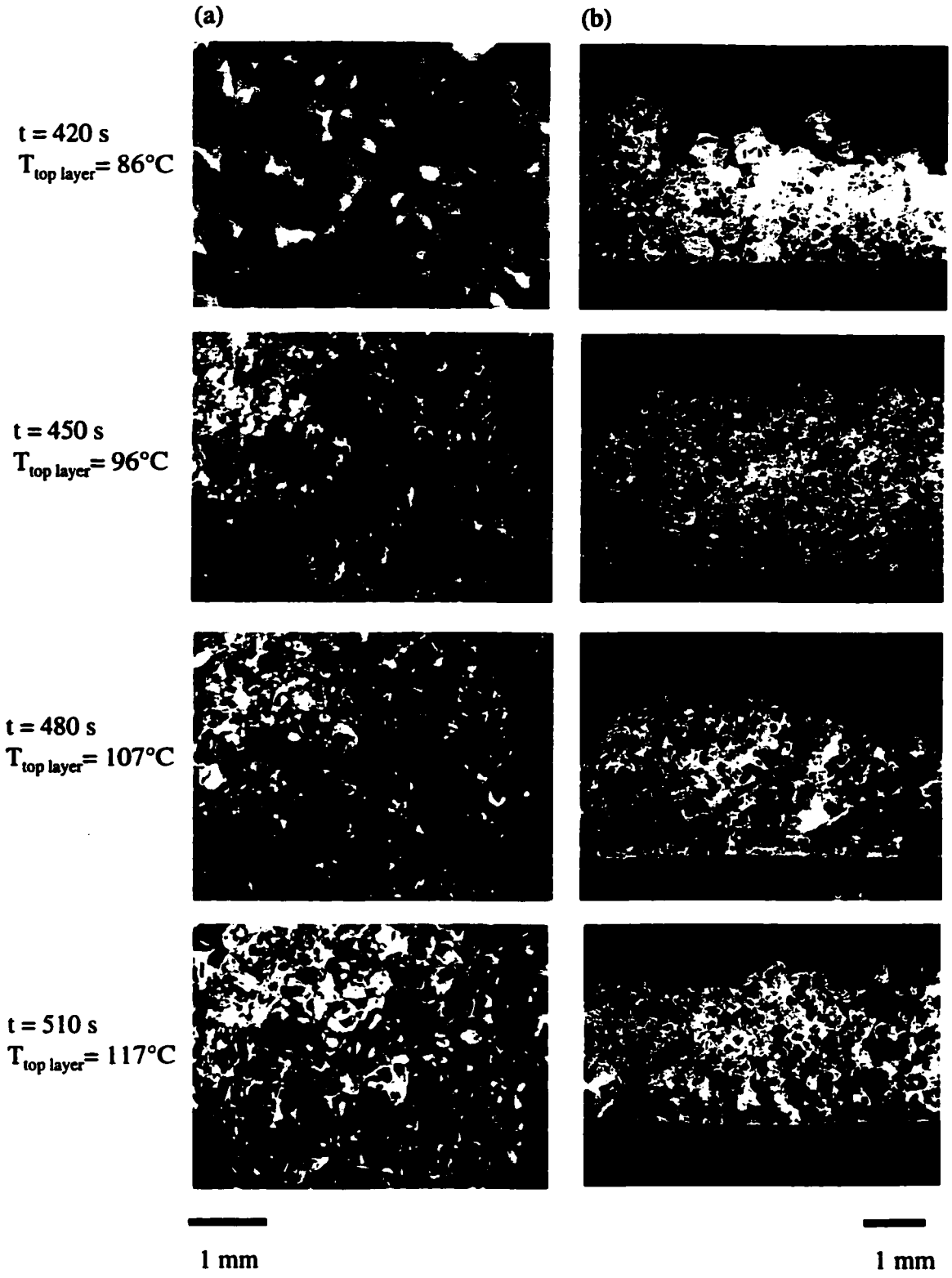

Figure 5.14: Optical microscope images of sintering of a polyethylene copolymer (EVA-2) powder compact inside heating chamber a) top view b) side view

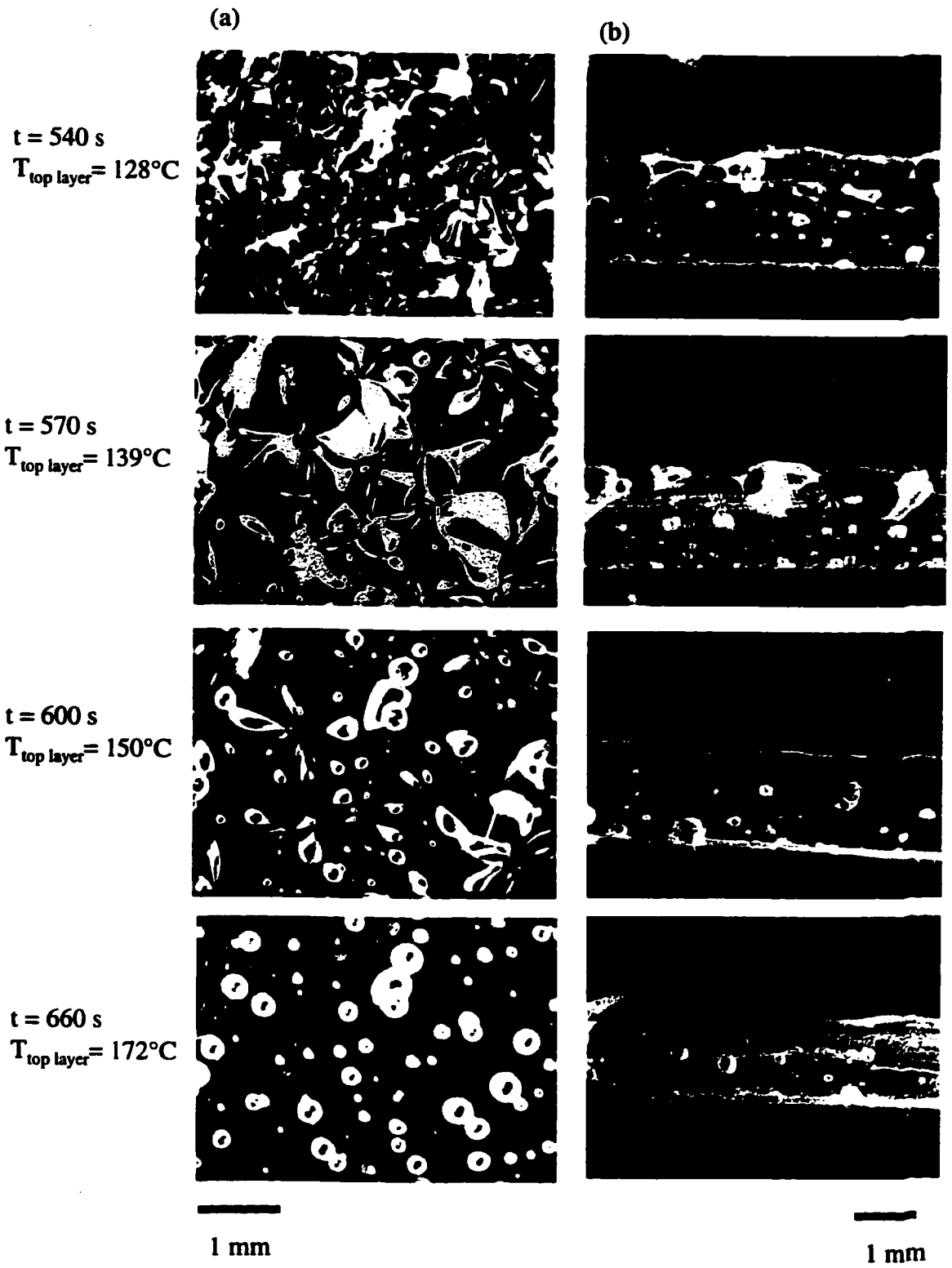

Figure 5.14 (cont'd): Optical microscope images of sintering of a polyethylene copolymer (EVA-2) powder compact inside heating chamber a) top view b) side view

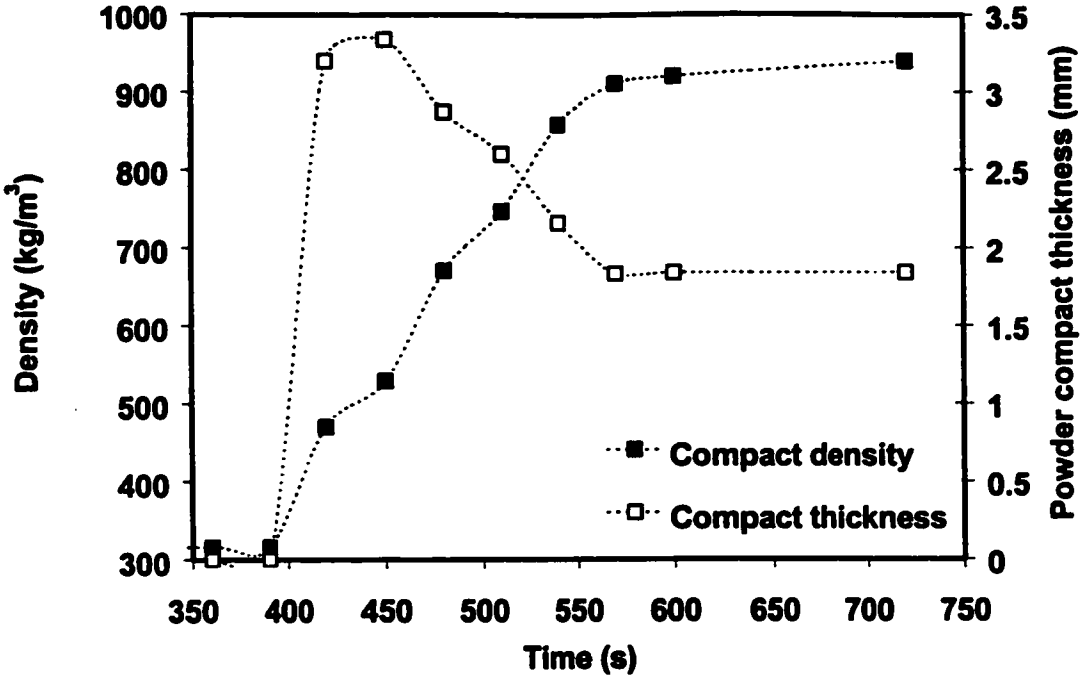

Figure 5.15: Variation of compact density and thickness as a function of time for EVA-2

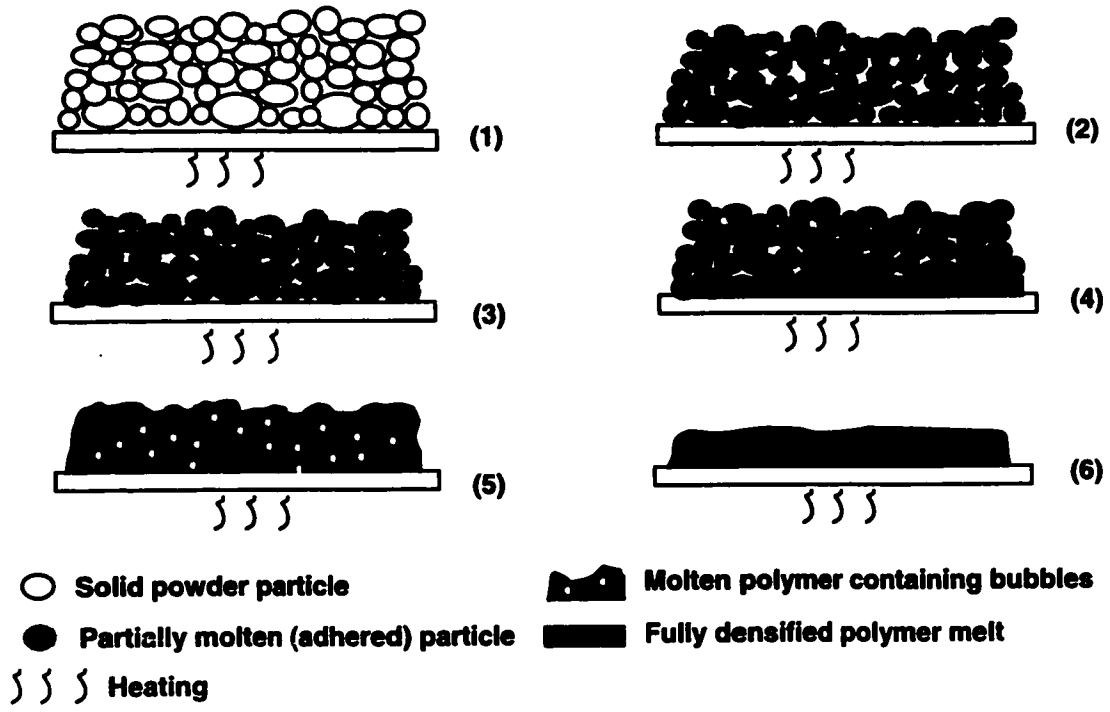

Figure 5.16: Schematic of densification of powder compact of low-crystallinity polyethylene copolymer

It can be also observed from Figure 5.15 that the shape of the densification curves of the PE copolymers is different than that of PEs, in the sense that densification occurs gradually, starting from very low values. By contrast, PE reaches relatively high density values early in the cycle (see also Figure 5.11). The point at which spherical bubbles appear in the EVA-2 melt (t ~ 600s in Figure 5.14) coincides with a change in the slope observed in Figure 5.15.

Figure 5.17 shows the bubble size distribution for three PE copolymers: EBA, EVA-1 and EVA-2. The sizes and overall bubble contents are summarized in Table 5.4. It can be seen that the numbers of bubbles in the copolymer melts are generally higher than those for polyethylenes (compare with Table 5.3), with the notable exception of the POP resin, which has a completely different behavior and will discussed in detail below. Thus the explanation for the longer processing times required during rotational molding trials presented in Chapter 4 is that more bubbles form initially in the PE copolymer melts.

Another interesting feature is that the overall air content inside the melt is constant for EBA, EVA-1 and EVA-2 and the sizes of the bubbles do not vary significantly (Table 5.4), even though their viscosities are largely different. However, when viscosity is lower the whole process begins earlier and the time needed for the overall melt densification becomes considerably shorter as melt viscosity decreases (Figure 5.18).

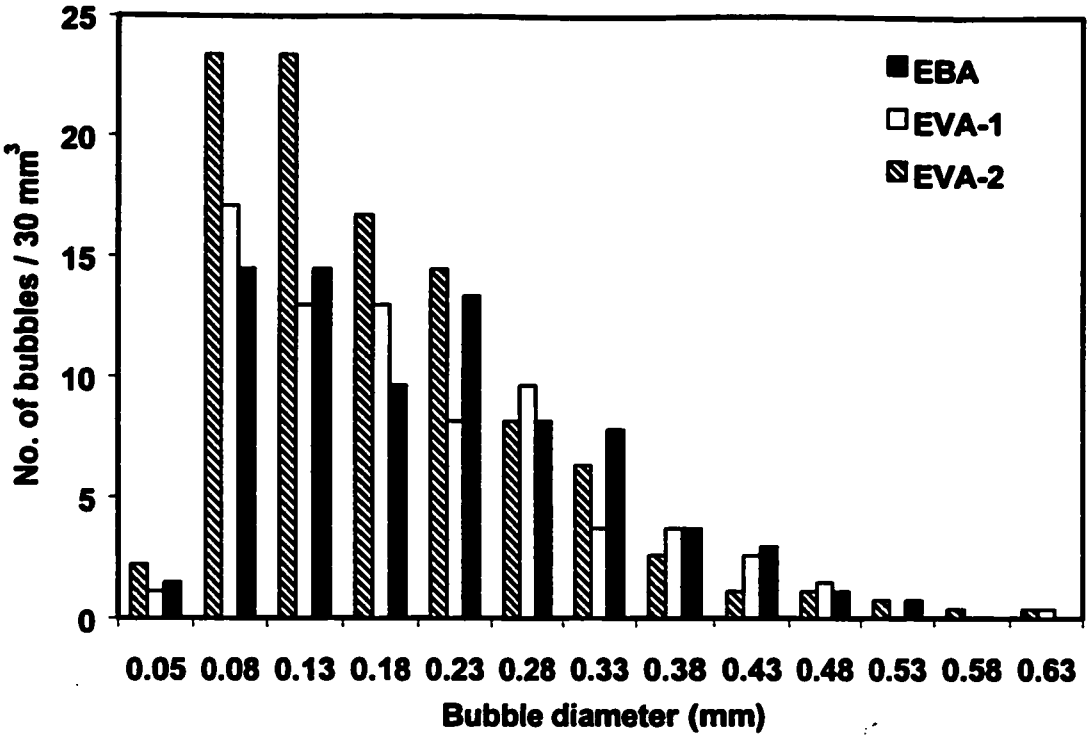

Figure 5.17: Size distribution of bubbled formed inside the melt for PE copolymers

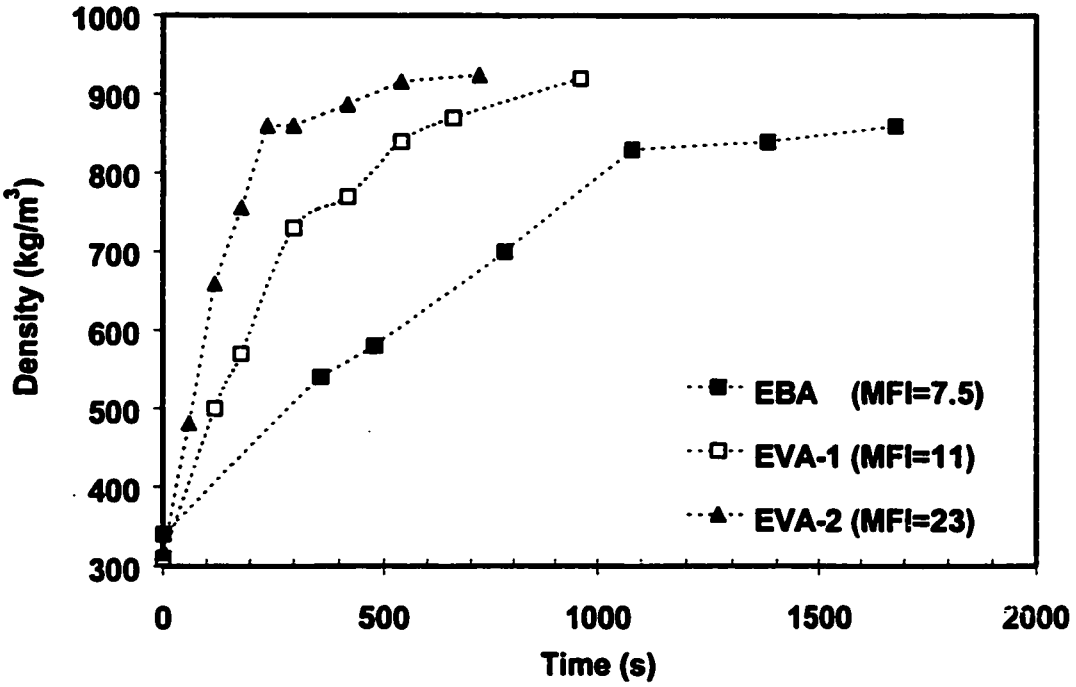

Figure 5.18: Experimental densification curves for PE copolymers (105° C)

Table 5.4: Average bubble diameter and air content in polyethylene copolymer melts

Resin	Bubble diameter (mm)	% Air content in melt
EBA	0.21 ± 0.12	2.36
EVA-1	0.195 ± 0.11	2.10
EVA-2	0.18 ± 0.10	2.40
POP	0.16 ± 0.085	0.95

Based on the above observations it is proposed that ethylene based copolymers with very low crystallinity start to melt very early in the heating cycle. Viscosity decreases slowly as temperature increases, starting from very high values. By contrast, the viscosity of typical semi-crystalline resins, such as polyethylenes, assumes relatively low values immediately upon reaching the melting point at approximately 130°C (see also Figure 4.4). Figure 5.19, compares the particle coalescence curves under non-isothermal conditions for a typical polyethylene (PE-2) and a PE copolymer (EVA-2). These polymers were chosen because their viscosities are comparable at a range from 130°C-190°C. It can be seen that the heating time required for the melting of PE particles is longer, due to the higher melting point. However, the rate of particle coalescence is significantly faster, allowing for the bottom layers to melt and sinter allowing the air to be pushed away before the subsequent layers begin to melt.

Due to their low melting point the PE copolymers polymers soften and adhere early, forming a three-dimensional network, but at temperatures just above

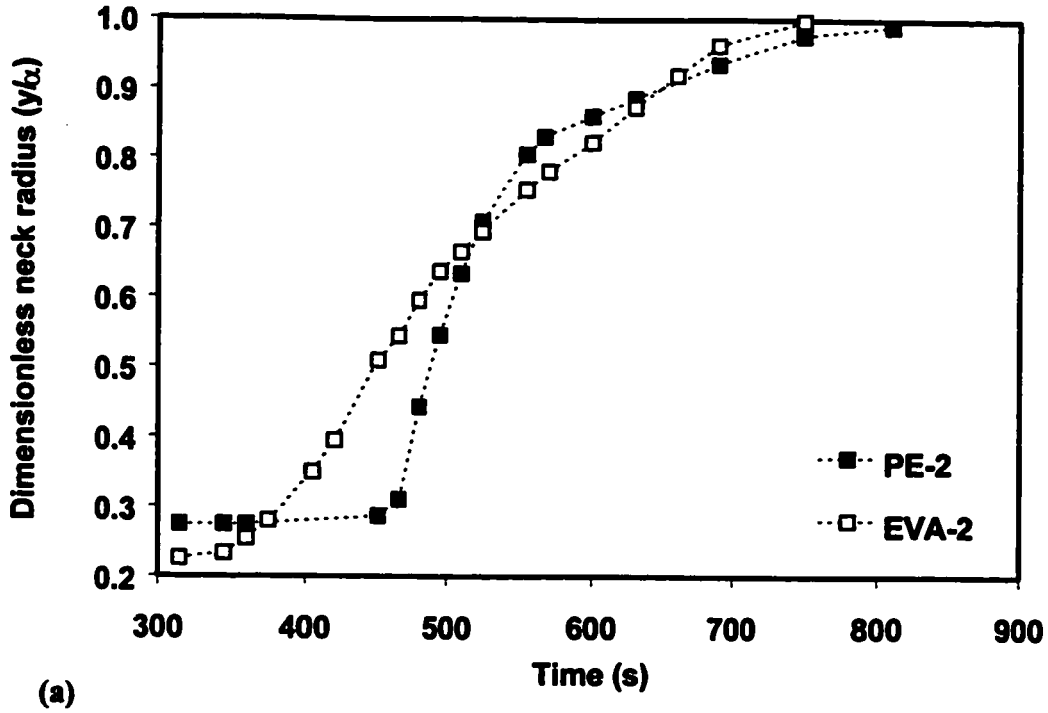

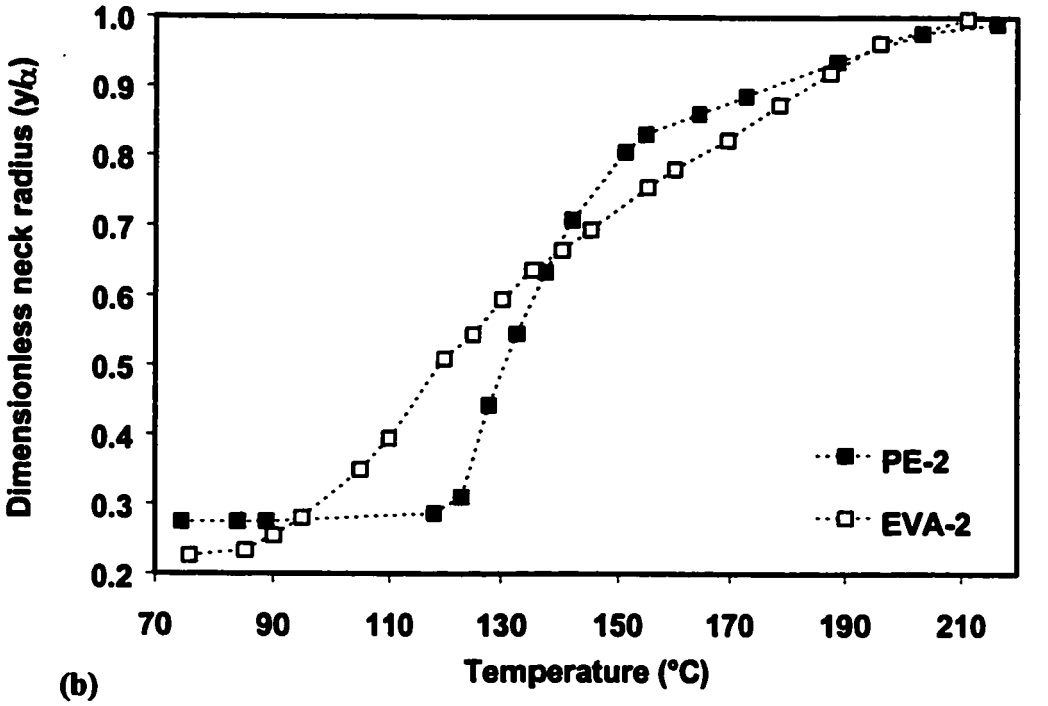

Figure 5.19: Comparison of sintering sequence of two powder particles for PE-2 and EVA-2 (a) neck radius vs. time, (b) neck radius vs. temperature. Heating rate shown in Figures 3.6 and 3.7

the melting point the rate of neck growth is very slow, due to the high viscosities. The high initial viscosities of the PE copolymers and subsequent low rates of neck growth can result in the entrapment of air and consequently the formation of large amounts of bubbles. This mechanism (see also Figure 5.16) appears to be different than the layer-by-layer scheme proposed for polyethylenes in Figure 5.12.

It seems thus that there is a competition between melting and the rate of neck growth between the particles, due to polymer flow: low melting points combined with high viscosities, which result in slow flow, favour low coalescence rates and result in the entrapment of large amounts of bubbles. It is obvious that a meaningful rheological characterization should not only be based on simple viscosity data, reported at a specific temperature or on melt flow index values as reported by the suppliers, but rather take into account the values of viscosity at the whole range of temperatures relevant to the process.

It is also worth commenting on the densification of the flexible polyolefin plastomer (POP), which has similar thermal properties as the rest of the polyethylene copolymers. The POP viscosity descreases rapidly as temperature increases, resulting to high rates of neck growth (Figure 5.13) and to the formation of significantly fewer bubbles than the rest of the PE copolymers, as shown in Table 5.4. Utilization of the POP material in rotomolding can prove very beneficial, because it can provide flexible products, with properties similar to

those of EBA and EVA, while having excellent processability, without the presence of excessive amounts of bubbles.

5.2.4. Sintering and bubble formation in polypropylenes

Processing of some polypropylenes required long cycle times, due to the presence of excessive amounts of bubbles and their slow dissolution, as described in Chapter 4.

The formation of bubbles in polypropylene melts has been investigated by comparing two groups of PP/PE copolymers with similar viscosities and various amorphous contents. Group 1 consists of PP/PE-1 (12.4% ethylene) and PP/PE-4 (16% ethylene) and group 2 consists of PP/PE-2 (13.1% ethylene) and PP/PE-3 (14.8% ethylene). In both groups, significantly more and/or larger bubbles formed in the polymers with higher ethylene content (Table 5.5). The bubble size distributions can be seen in Figure 5.20. Images of the bubble formation sequence revealed that significantly longer times were needed for PP/PE-3 and PP/PE-4 to form homogeneous melts. A comparison of the bubble formation sequence for PP/PE-1 and PP/PE-4 is shown as an example in Figure 5.21. The information obtained from the viscosity versus temperature curves, presented in Figure 4.12 could not account for the observed differences. Thermogravimetric analysis (TGA) was performed in order to investigate the possibility that the presence of bubbles is due to volatiles or degradation products during processing. It was found that the polypropylenes start to degrade at a temperature of 244°C, which is significantly higher than the temperature used in the experiments. Moreover

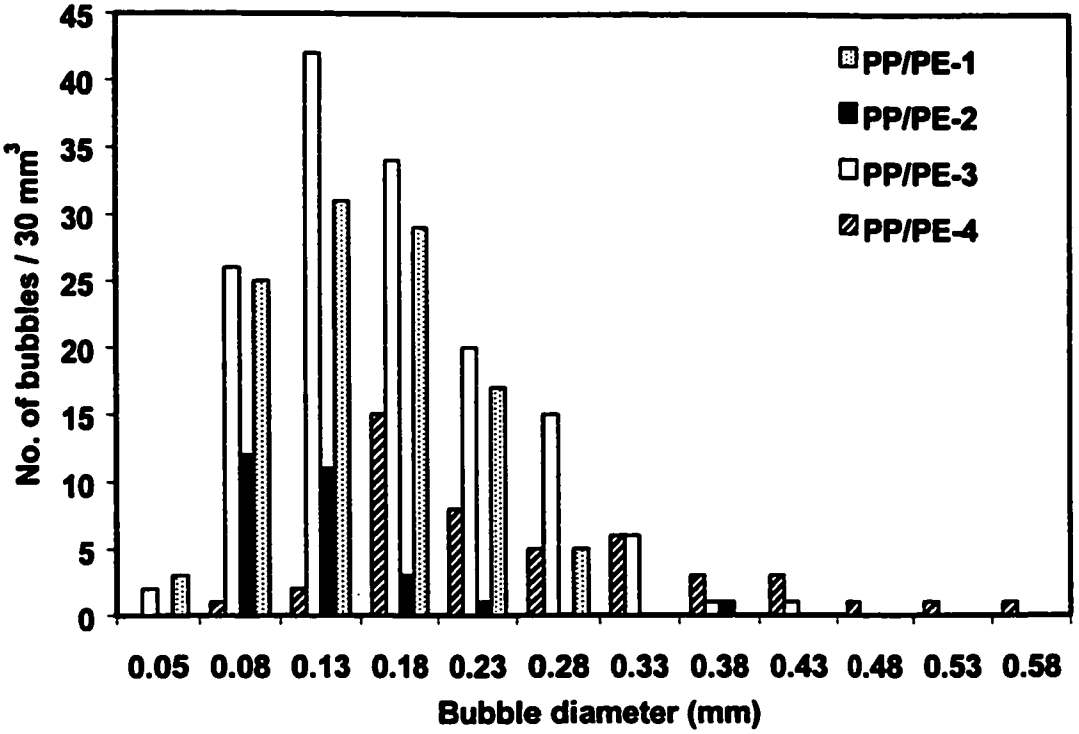

Figure 5.20: Size distribution of bubbles formed inside the melt for PP/PE copolymers

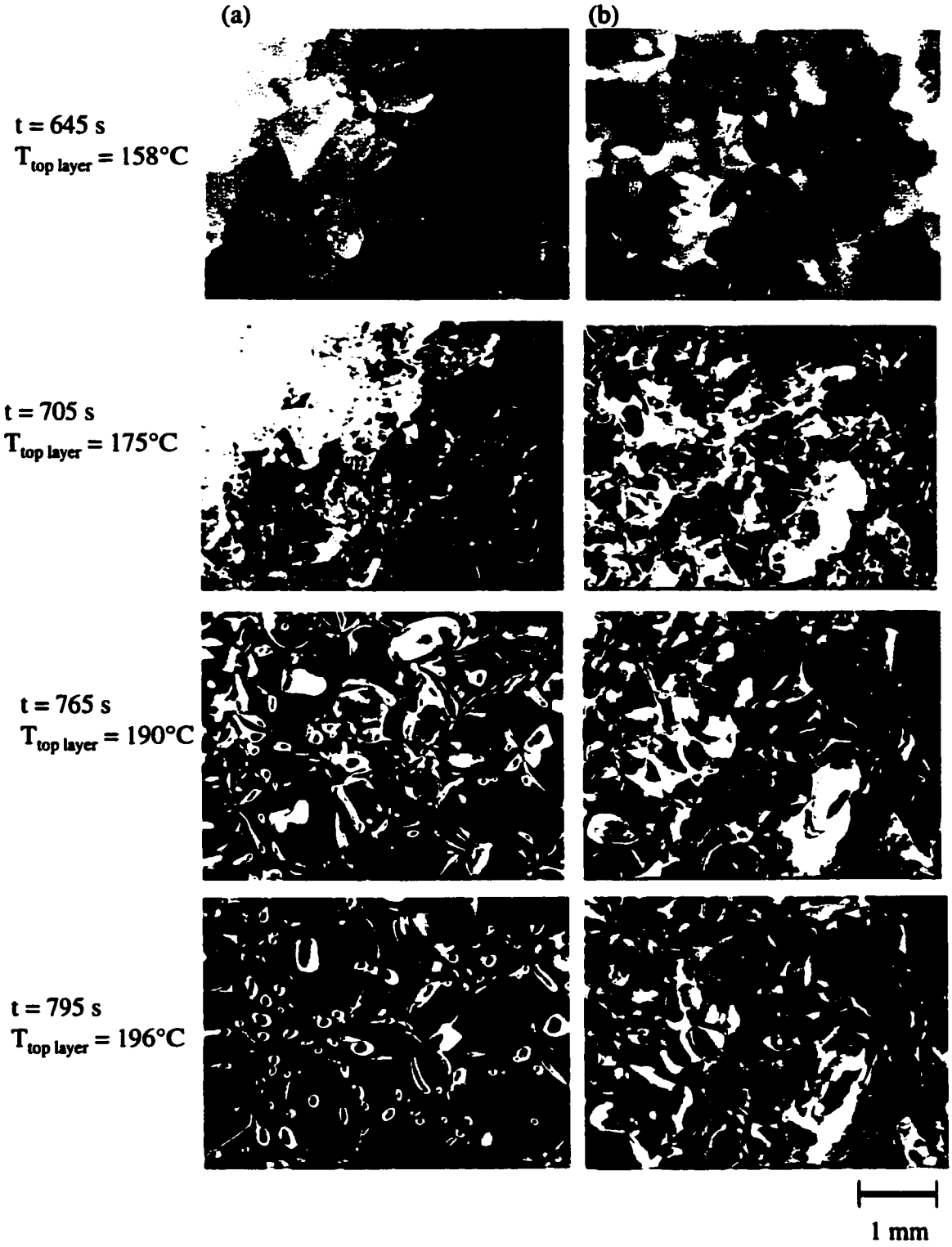

Figure 5.21: Bubble formation sequence a) PP/PE-1 b) PP/PE-4

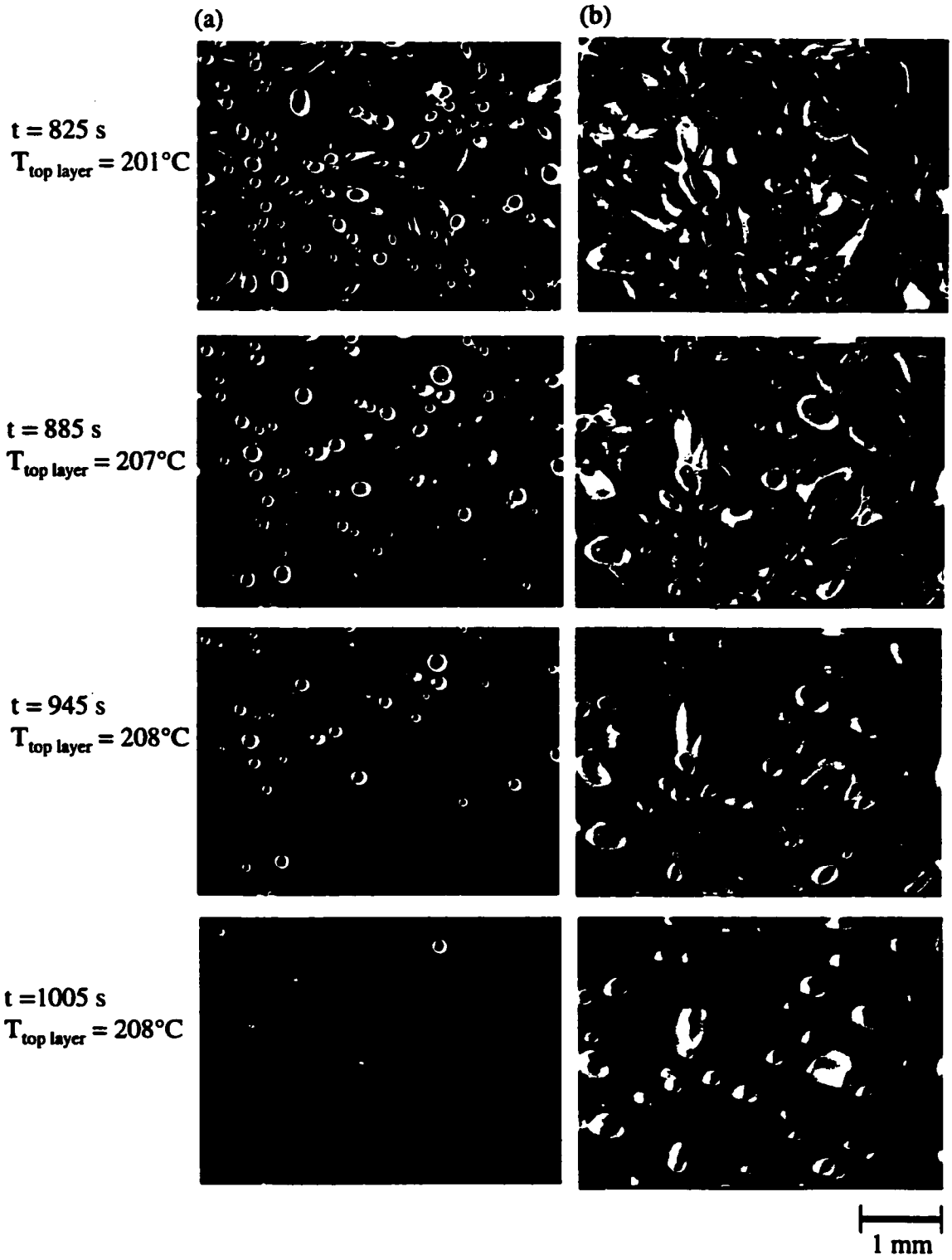

Figure 5.21 (cont'd): Bubble formation sequence a) PP/PE-1 b) PP/PE-4

experiments performed isothermally at 190°C showed that the degradation time is between 60 and 80 min, which is significantly longer than the time the experiments lasted. No indication of presence of volatiles was found either.

A comparison of the particle coalescence sequence of PP/PE-1 and PP/PE-4 showed that the coalescence of the PP/PE-4 particles was not complete at long times (Figures 5.22 and 5.23). The latter phenomenon has been associated to the elasticity of the PP/PE-4 melt (see also Figures 4.14 and 4.15) , which may result in slowing down the coalescence process (Bellehumeur et al. 1998). The result is that, as the particles melt layer by layer, there is not enough time for the pores formed in the bottom layer to close before the next layer starts to stick, thus resulting in the entrapment of pores inside the melt. This is demonstrated by images of the powder compacts of PP/PE-1 and PP/PE-4 during the early stages of densification, shown in Figure 5.24.

Table 5.5: Average bubble diameter and air content in polypropylene copolymer melts

Resin	Bubble diameter (mm)	% Air content in melt
PP/PE-1	0.15 ± 0.059	0.93
PP/PE-2	0.12 ± 0.063	0.19
PP/PE-3	0.17 ± 0.075	2.02
PP/PE-4	0.26 ± 0.11	2.30

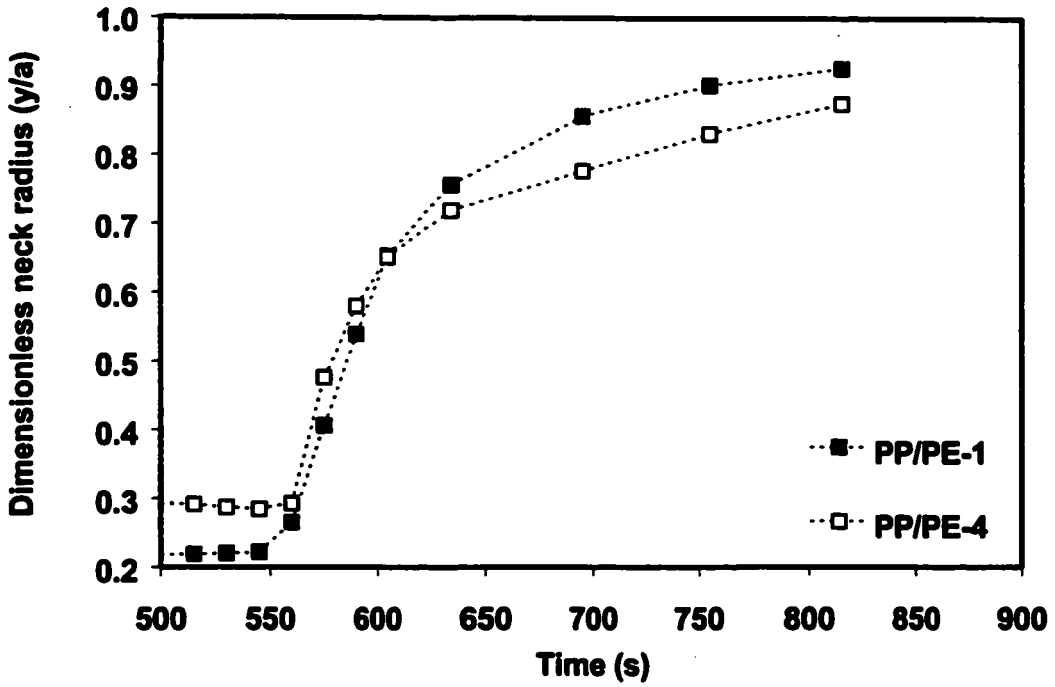

Figure 5.22: Comparison of sintering sequence of two particles for PP/PE-1 and PP/PE-4

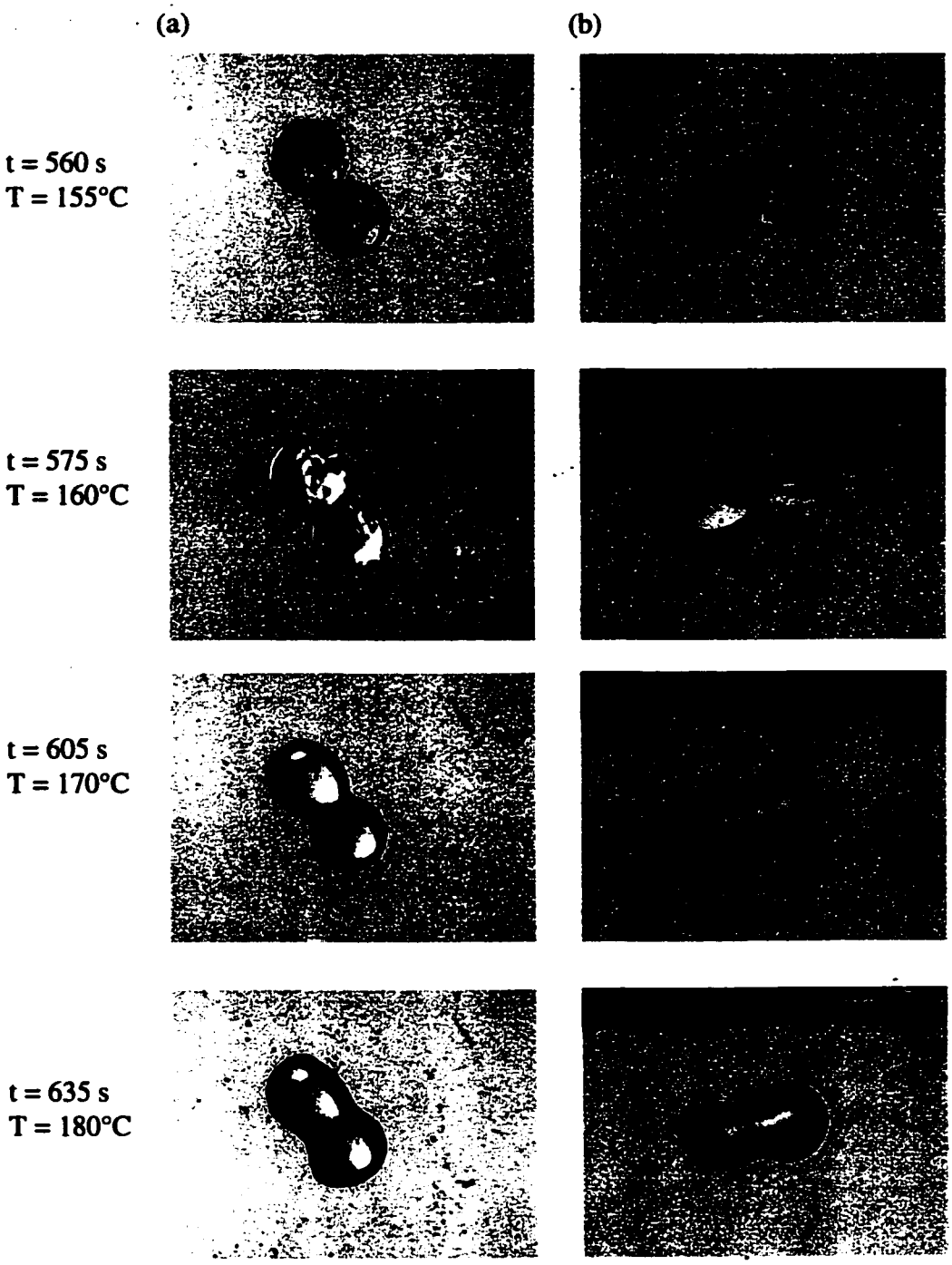

Figure 5.23: Optical microscope images of particle coalescence sequence a) PP/PE-1 b) PP/PE-4

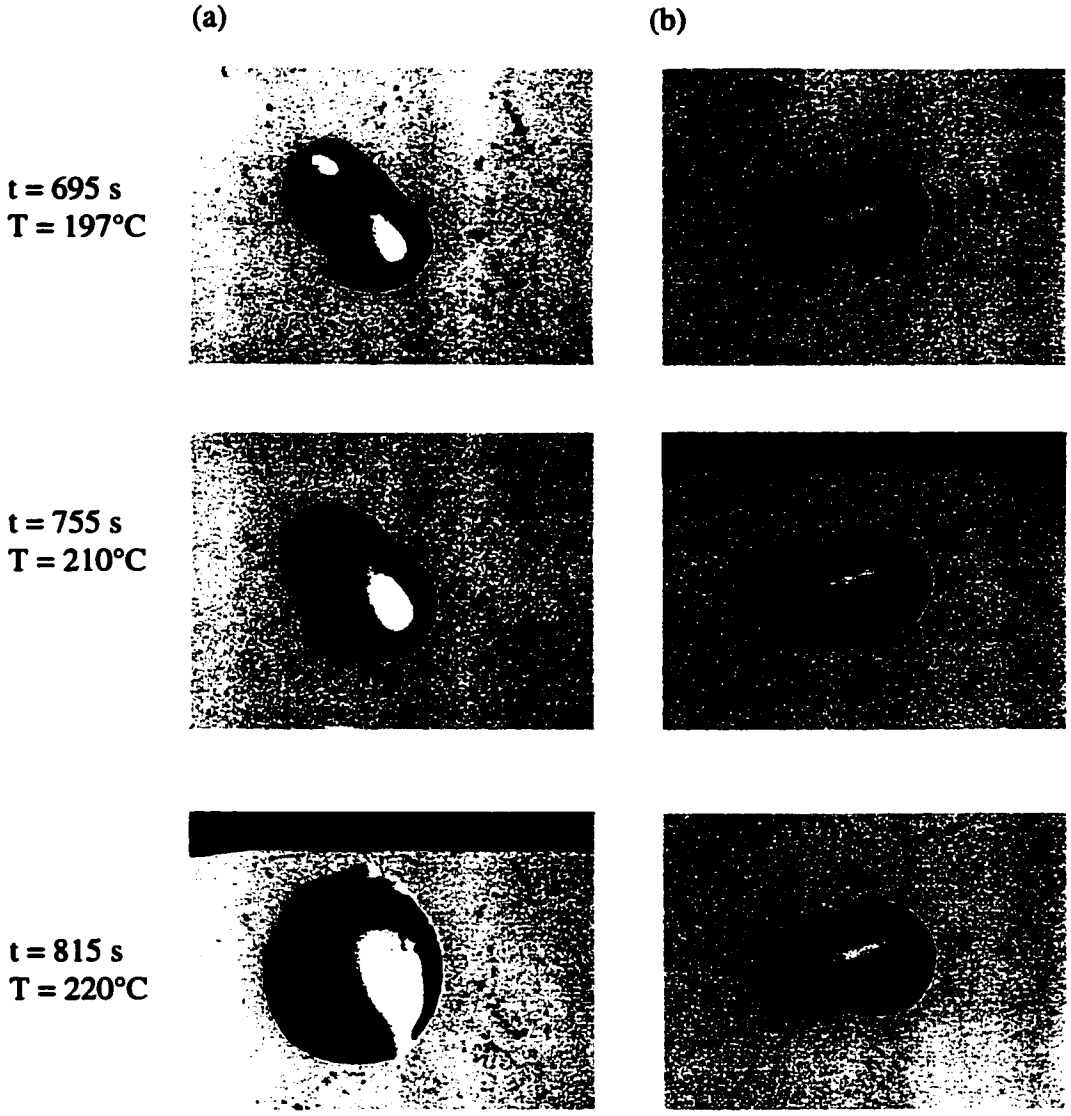

Figure 5.23 (cont'd): Optical microscope images of particle coalescence sequence a) PP/PE-1 b) PP/PE-4

(a)

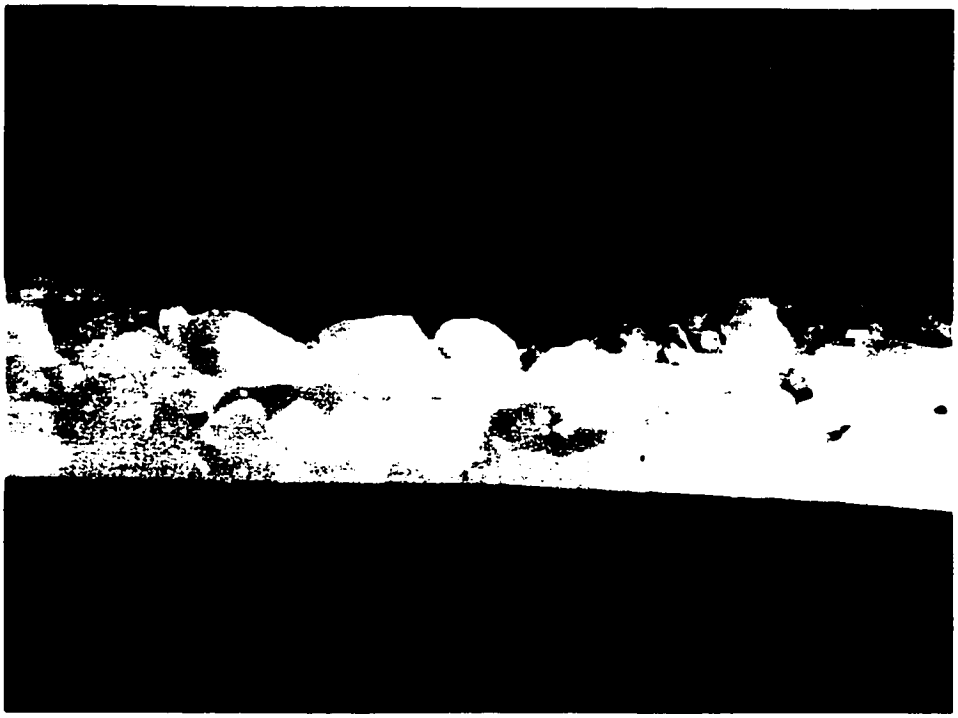

(b)

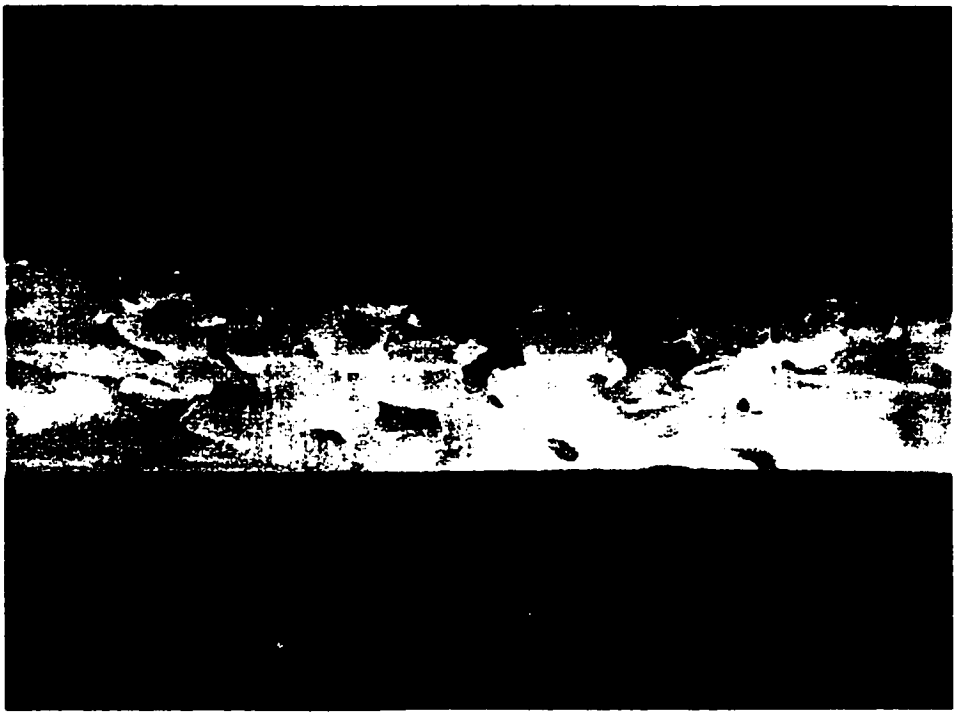

Figure 5.24: Images of powder compact during early stages of sintering a) PP/PE-1
b) PP/PE-4

5.2.5. Sintering and bubble formation in polyethylene made by metallocene catalysts

The comparison of heating cycles of polyethylenes made by conventional (PE-1, PE-2) and metallocene catalysts (PE-7), in chapter 4, section 4.4.2, showed that there were no big differences (see also Figure 4.23). However, particle coalescence and bubble formation experiments showed that the sintering and bubble formation behaviour of PE-7 (MFI=3.2) resembles more that of PE-2 (MFI=5.2) rather than that of PE-1 (MFI=3.3) (Figures 5.25 and 5.26 respectively). These results need clearly further investigation, because they contradict the observations done in the actual rotational molding cycle, but they confirm literature reports (Fatnes, 1999). The fact that the crystallinity (and thus the heat of fusion required for the melting transition of the polymer) is higher for PE-7 than PE-2 may be the reason why PE-7 needs more heating time in the actual rotational molding process, even though the sintering behaviour is similar.

5.3. Modeling of densification

From the bubble formation results analyzed above it can be concluded that viscosity and powder properties are the main factors controlling densification rates. This implies the existence of a Frenkel type mechanism, mainly surface tension driven flow opposed by viscosity. The initial bulk density of the powder, particle size and shape play also an important role in the subsequent densification rates.

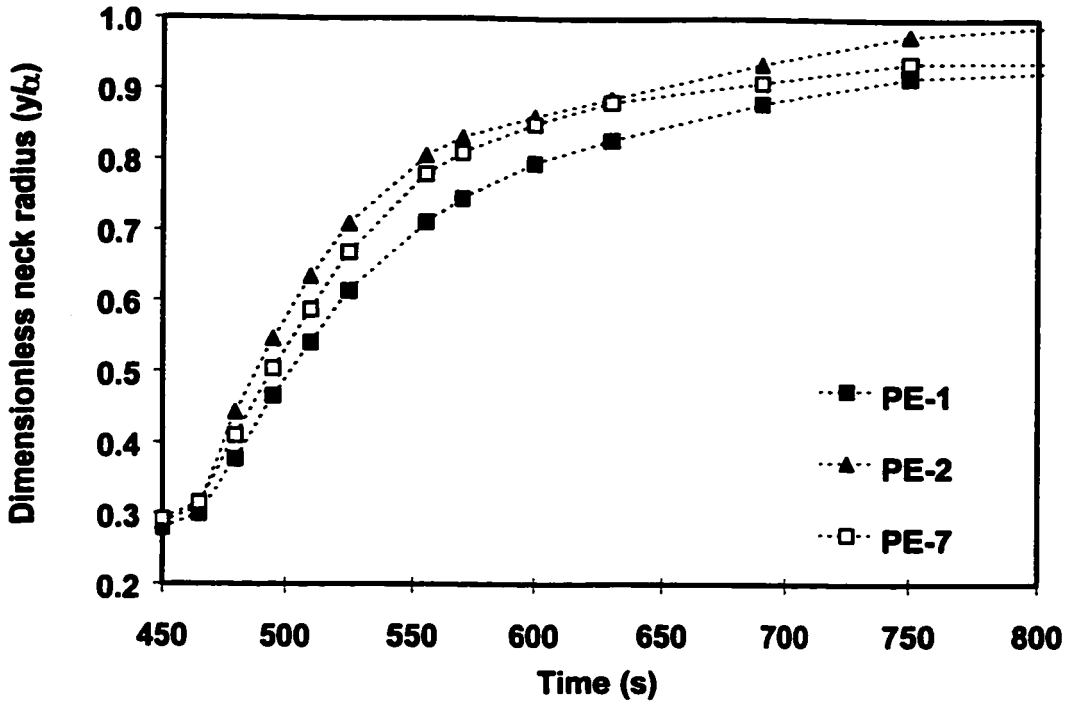

Figure 5.25: Comparison of sintering of two particles for PEs made by conventional (PE-1, PE-2) and metallocene catalysts (PE-7).

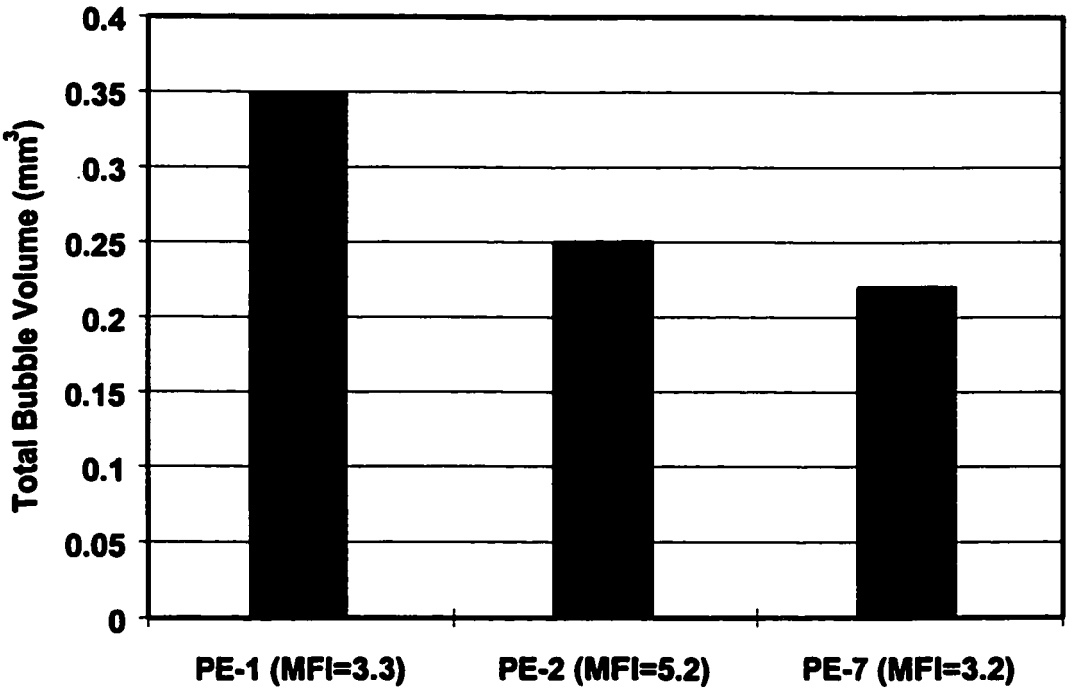

Figure 5.26: Air content inside the melt for PEs made by conventional (PE-1, PE-2) and metallocene catalysts (PE-7).

Microscopic examination of sections cut from the final parts at various times suggested that resins with low crystallinity and low melting point, such as PE copolymers densify as a three-dimensional network, as explained in section 5.2.3. Figure 5.27, which compares the densification sequence of EVA-2 with the variation in thickness of the compact, indicates that the whole powder compact adheres early in the cycle. The subsequent densification results in a reduction of the height of the compact (see also Figure 5.16). It can be hypothesized that densification of this type can be modeled by using models appropriate for the densification of three-dimensional powder compacts. This hypothesis has been tested by comparing experimental densification data, such as the ones shown in Figure 5.27, obtained for the PE copolymers under isothermal conditions, to model predictions obtained by using such models.

5.3.1. The Frenkel / Scherer model

The first model to be considered is the modification of Frenkel's equation, suggested by Scherer (1984) (Frenkel/Scherer model), based on the microstructure of a cell consisting of packed spheres (Figure 5.28). The shrinkage of a cell consisting of packed spheres has been related to its density through the following equation:

$$\frac{\Delta L}{L_o} = 1 - \left(\frac{\rho}{\rho_o}\right)^{1/3} \qquad (5\text{-}1)$$

According to Exner and Petzow (1975) shrinkage can be represented by the rate of approach of the centers of two spheres during the early stages of

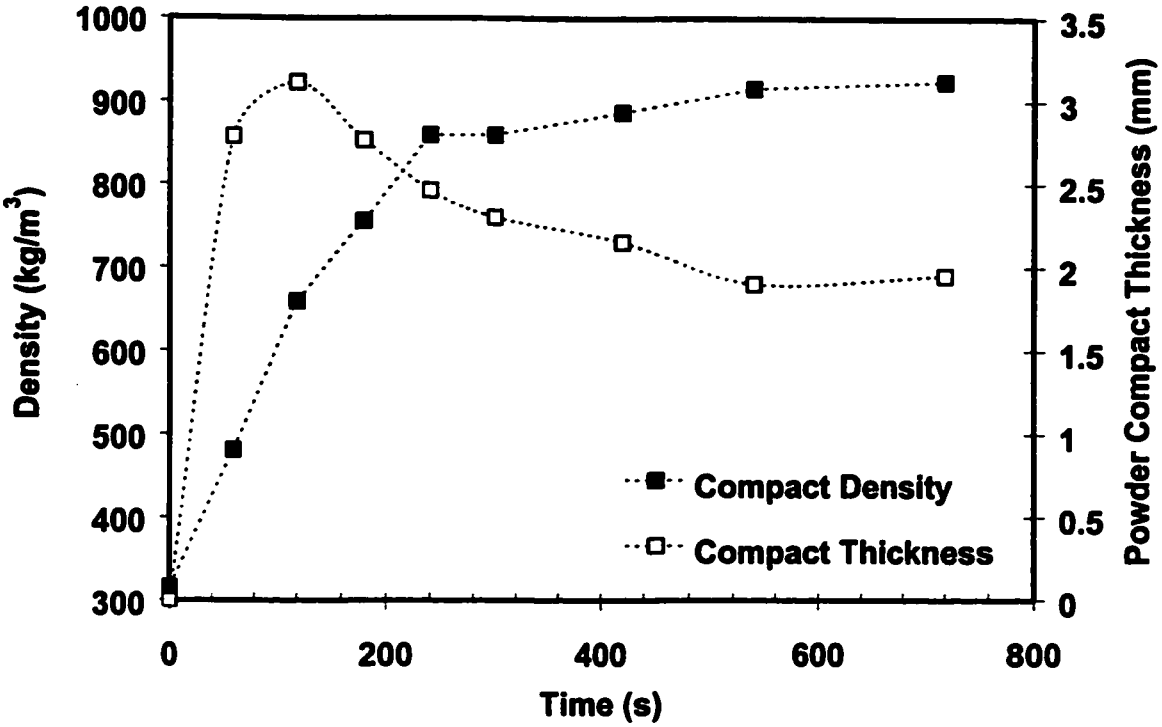

Figure 5.27: Variation of compact density and thickness as a function of time for EVA-2 (105°C)

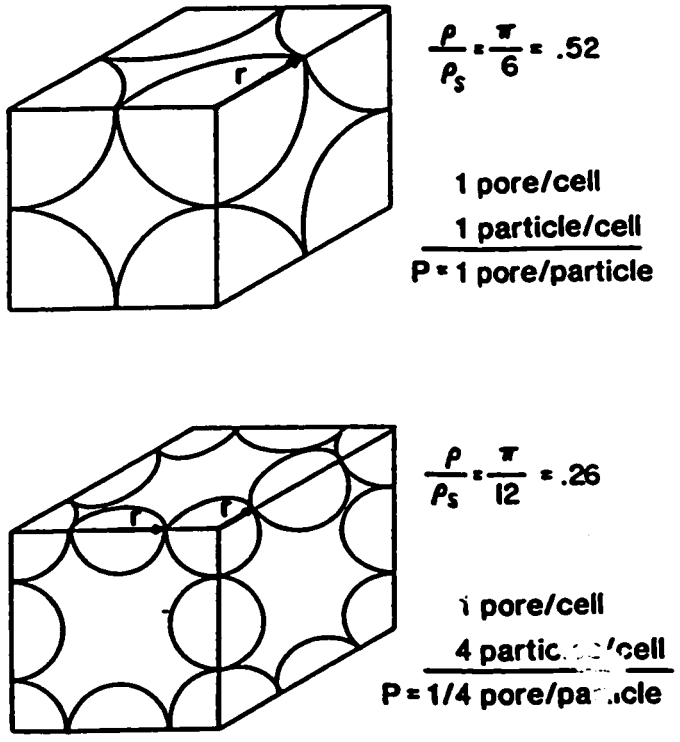

Figure 5.28: Microstructures obtained by packing spheres, showing unit cell for simple cubic packing with ρ/ρ_S=0.52 (top) and for looser packing with ρ/ρ_S=0.26 (bottom) (Scherer, 1984)

sintering by using the following expression:

$$\frac{\Delta L}{L_o} = \frac{\sigma t}{4\eta\alpha} \tag{5-2}$$

where L(t) is the distance between the centers of the spheres, $L_o = 2\alpha$ at t = 0 and $\Delta L = L_o - L(t)$.

The number of pores, n, per unit volume is :

$$n = \frac{P}{(4/3\,\pi\,\alpha^3)} \tag{5-3}$$

where P is the number of pores per particle (see also Figure 5.28). By combining the corrected by Eshelby Frenkel equation (2-2) with equations (5-1), (5-2) and (5-3), the following expression can be derived for the densification kinetics (Frenkel / Scherer model):

$$\frac{\sigma n^{1/3} t}{\eta} = 4\left[\frac{3}{4\pi}\right]^{1/3} P^{1/3}\left[1-\left(\frac{\rho_o}{\rho}\right)^{1/3}\right] \tag{5-4}$$

The factor P describing the packing characteristics can be estimated from the bulk density of the packing and the particle size (Scherer, 1984). If the relative density ρ/ρ_S of the packing is known, the number, s, of spheres of radius r contained in the cell is given by:

$$\frac{\rho}{\rho_S} = \left(\frac{\pi}{6}\right)\frac{(3s-2)}{s^3} \tag{5-5}$$

The factor P is then determined as:

$$P = \frac{1}{3s-2} \tag{5-6}$$

For example for EVA-2 with bulk density ρ=316 kg/m^3 and solid density ρ_S= 941 kg/m^3 the ratio ρ/ρ_S is equal to 0.336, which by using equations (5-5) and (5-6) gives P = 0.33.

5.3.2. The open pores models

The next models to be considered are Scherer's open pores models (Scherer, 1977, Scherer, 1984, Scherer and Garino, 1985), which describe the shrinkage of a three dimensional cubic array of interconnected cylinders (see also Figure 5.29). The radius of the cylinder comprising a unit cell of the structure (Figure 5.29 (a)) represents the average size of the particles comprising the compact and is denoted by α. The distance between the centerlines of the neighboring cylinders, which is an indication of the bulk density or "packing efficiency" of the compact is denoted by l. The density ρ of the cell is a function of $x = \alpha / l$ (Scherer 1977, 1991):

$$\frac{\rho}{\rho_S} = 3\pi x^2 - 8\sqrt{2}\, x^3 \qquad (5\text{-}7)$$

where ρ_S is the theoretical density of the solid phase. When $x = \alpha/l = 0.5$ the neighbouring cylinders touch each other and the cell contains a close pore. The density at this instant is found from equation (5-7) to be ρ/ρ_S=0.942. Furthermore, as long as the cell remains open, the pore diameter in the powder compact, d, can be estimated from:

$$\frac{\pi d^2}{4} = (l - 2\alpha)^2 \qquad (5\text{-}8)$$

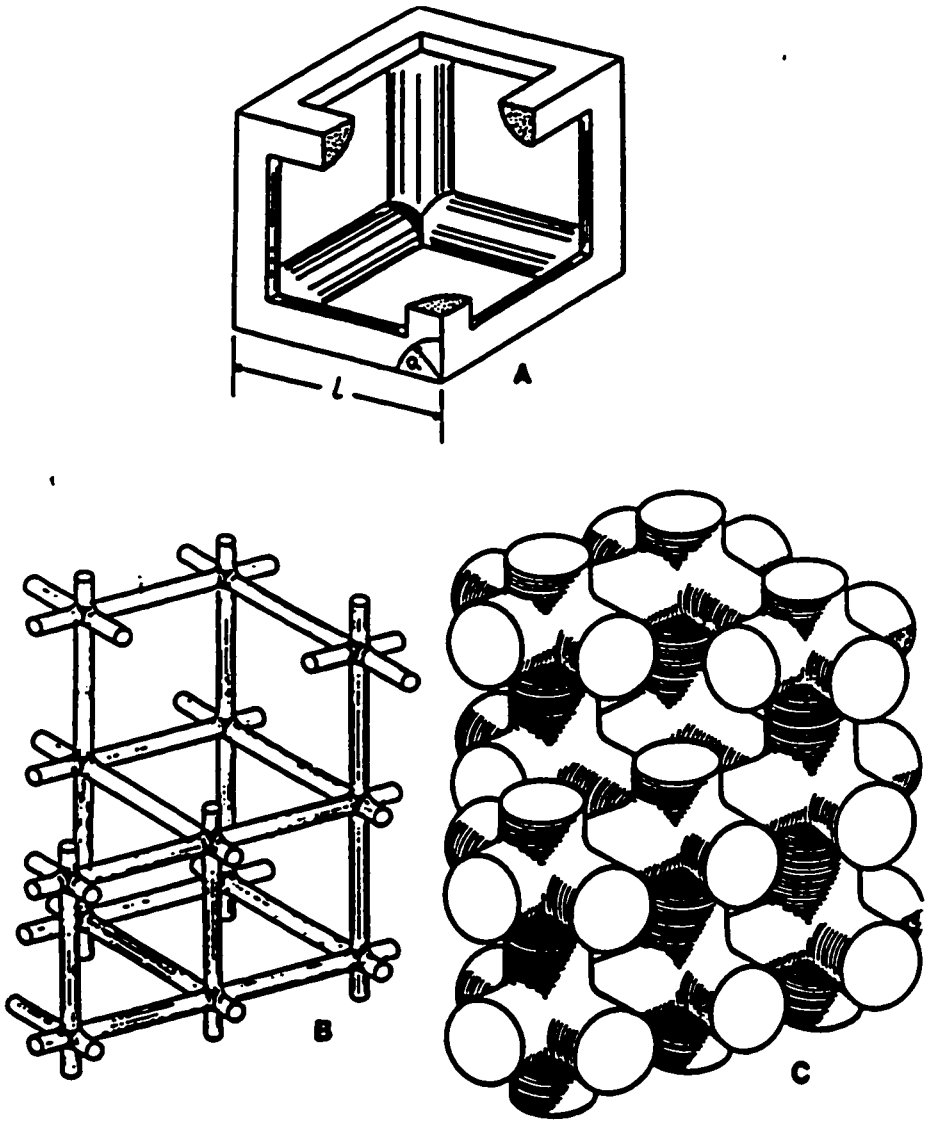

Figure 5.29: Microstructural model consisting of cylinders in cubic array: a) Unit cell showing edge length, l and cylinder radius, α, b) Model of low density microstructure (ρ/ρ_S=0.05), c) Model of microstructure wity ρ/ρ_S=0.50 (Scherer, 1977, Scherer and Garino, 1985).

Based on the concept of the cylindrical array, one can easily estimate the parameters a and l from equation (5-7) if the initial bulk density and particle size of the compact are known. Typical values of powder properties for EVA-2 and calculations of the geometric factors needed for the cylindrical array model are given in Appendix 5.A.

Scherer's model can also provide a convenient estimate of the number of closed pores which are trapped inside the compact once x=0.5 (corresponding to ρ/ρ_S=0.942). The number of closed pores / volume solid phase is (Scherer, 1977):

$$n = (1/l_o)^3(\rho_S/\rho_o) \qquad (5\text{-}9)$$

To calculate the rate of sintering of the model structure shown in Figure 5.29, Scherer (1977, 1991) applied an energy balance, equating the energy recovered by reduction in surface area to the energy dissipated in viscous flow as the cylindrical elements become shorter and thicker. He obtained an analytical relationship between density and time, which is valid for the sintering of a free, unconstrained body:

$$K(t-t_o) = \int_{x_o}^{x} \frac{2\,dx}{(3\pi - 8\sqrt{2}\,x)^{1/3}x^{2/3}} \qquad (5\text{-}10)$$

where $K= (\sigma/\eta l_o)\,(\rho_s/\rho_o)^{1/3}$ or $K = (\sigma n^{1/3}/\eta)$ and $x = a/l$. Equation (5-10) determines x as a function of time. Since ρ/ρ_S is a function only of x(t) (equation 5-7) the density of the cell can be determined as a function of time.

The shrinkage of the cylidrical array compact can also be predicted from the free strain rate, which represents the rate of deformation for an unconstrained

body. The free strain rate for the cylinder model is (Scherer 1977, 1979):

$$\dot{\gamma}_f = -\frac{(3\pi)^{1/3}}{6}\frac{\sigma}{\eta l_o}\left(\frac{\rho_s}{\rho_o}\right)^{1/3}\left[\frac{2-3cx}{x^{1/3}(1-cx)^{2/3}}\right] \qquad (5\text{-}11)$$

where $c = 8\sqrt{2}/3\pi$

The Scherer and Garino (1985) model, which takes into account the development of stresses inside the compact when the densification of the cylindrical array is only allowed in one direction has been examined, as well. If during sintering shrinkage is not permitted in the plane of the substrate, it can be assumed that no deformation occurs in the plane of the substrate and that the layer densifies by contracting in the direction normal to the plane. By using these assumptions, Scherer and Garino derived the following expression (Scherer and Garino model):

$$K(t-t_o) = \frac{6}{(3\pi)^{1/3}}\int_{x_o}^{x}\frac{\pi-2\sqrt{2}x}{\pi+2\sqrt{2}x}\frac{dx}{x^{2/3}(1-cx)^{1/3}} \qquad (5\text{-}12)$$

5.3.3. Model predictions

The predictions of all the models presented above in terms of dimensionless time $K(t-t_o)$ versus relative density ρ / ρ_S are summarized in Table 5.6. Data of density versus real time can be obtained by evaluating the appropriate value of K, which is unique for every material and depends solely on material and powder properties. Appendix 5.A. demonstrates a sample calculation of K for EVA-2.

Figure 5.30 shows a comparison of the experimental data obtained for all PE copolymers at a temperature of 105°C, expressed in terms of the dimensionless variables $K(t-t_o)$ and ρ / ρ_S with the predictions of the models. The points corresponding to the two EVA resins in Figure 5.30 show similar trends, indicating that the mechanism of densification is identical. The data for EBA deviate from the other two, displaying a delayed rate.

Table 5.6: Predictions of relative density versus dimensionless time according to the Frenkel/Scherer, Scherer and Scherer and Garino models

Frenkel / Scherer Equation (5-4)		**Scherer Equation (5-10)**		**Scherer & Garino Equation (5-12)**	
$K(t-t_o)$	ρ/ρ_S	$K(t-t_o)$	ρ/ρ_S	$K(t-t_o)$	ρ/ρ_S
0	0.336	0	0.336	0	0.336
0.114	0.412	0.084	0.412	0.163	0.412
0.146	0.438	0.110	0.438	0.213	0.438
0.176	0.464	0.136	0.464	0.261	0.464
0.204	0.491	0.162	0.491	0.308	0.491
0.230	0.517	0.187	0.517	0.352	0.517
0.254	0.543	0.212	0.543	0.395	0.543
0.352	0.669	0.330	0.669	0.590	0.669
0.422	0.784	0.441	0.784	0.755	0.784
0.470	0.878	0.547	0.878	0.897	0.878
0.499	0.942	0.651	0.942	1.022	0.942

$K = (\sigma/\eta l_o)\,(\rho_s/\rho_o)^{1/3}$

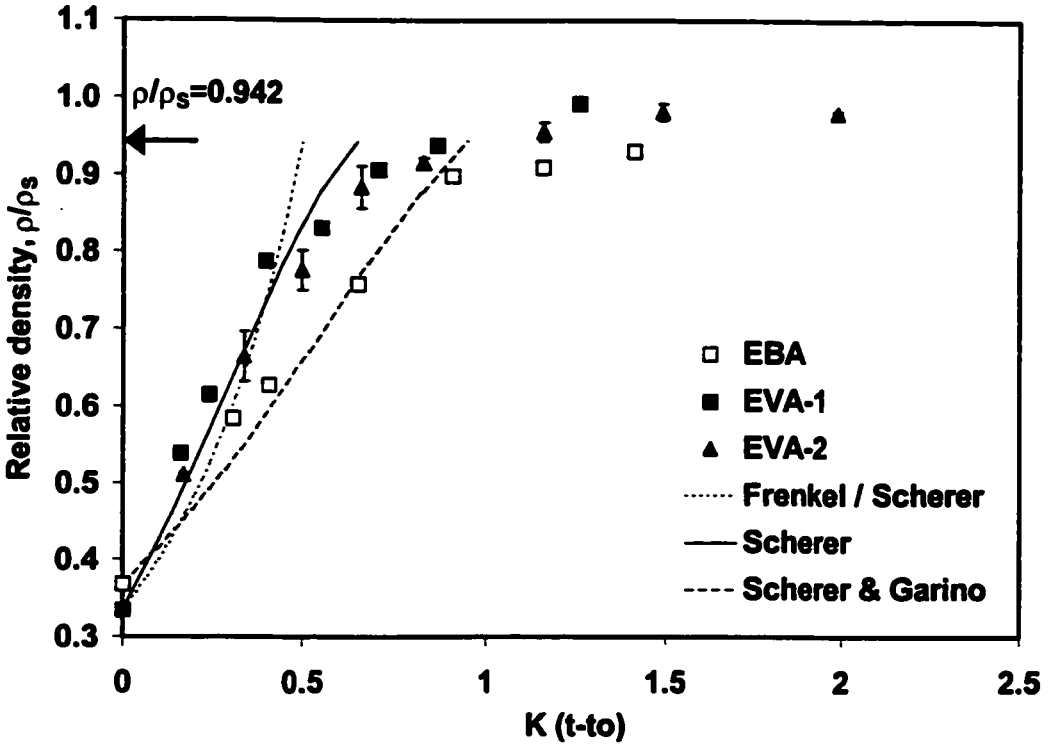

Figure 5.30: Comparison of model predictions with experimental data for PE copolymers in dimensionless variables (experimental data at 105°C). K=0.00084, 0.001312, 0.002762 for EBA, EVA-1 and EVA-2 respectively.

As expected the modified Frenkel / Scherer model can only predict the initial stages of densification. Scherer's model for the densification of an unconstrained body is more successful in describing the data for the two EVAs, while the Scherer and Garino model, equation (5-12) describes the EBA data adequately. An explanation for this difference may be that because of the very high viscosities of the EBA melt, stresses develop inside the compact during sintering. The development of stresses is taken into account only by the Scherer and Garino model.

According to Scherer's theory, based on geometrical considerations, all models are appropriate until the point where closed pores form, which occurs when $\rho/\rho_s = 0.942$. However in Figure 5.30 it can be observed that the experimental data begin to deviate from the model predictions somewhat earlier than this point, indicating that the models break down earlier in reality. This may be attributed to two reasons: the mechanistic cylindrical array model breaks down at the advanced stages of densification and the powder compact in reality contains a distribution of pore sizes, while the model considers that all the pores are monodispersed.

In spite of their simplicity, application of Scherer's models can give an insight on how various parameters, such as viscosity, surface tension and initial particle size can affect the densification process. Figure 5.31 demonstrates how the densification curves vary as a function of the parameter K (where $K = (\sigma/\eta l_o)(\rho_s/\rho_o)^{1/3}$ or $K = (\sigma n^{1/3}/\eta)$). The parameter K is a function of surface tension,

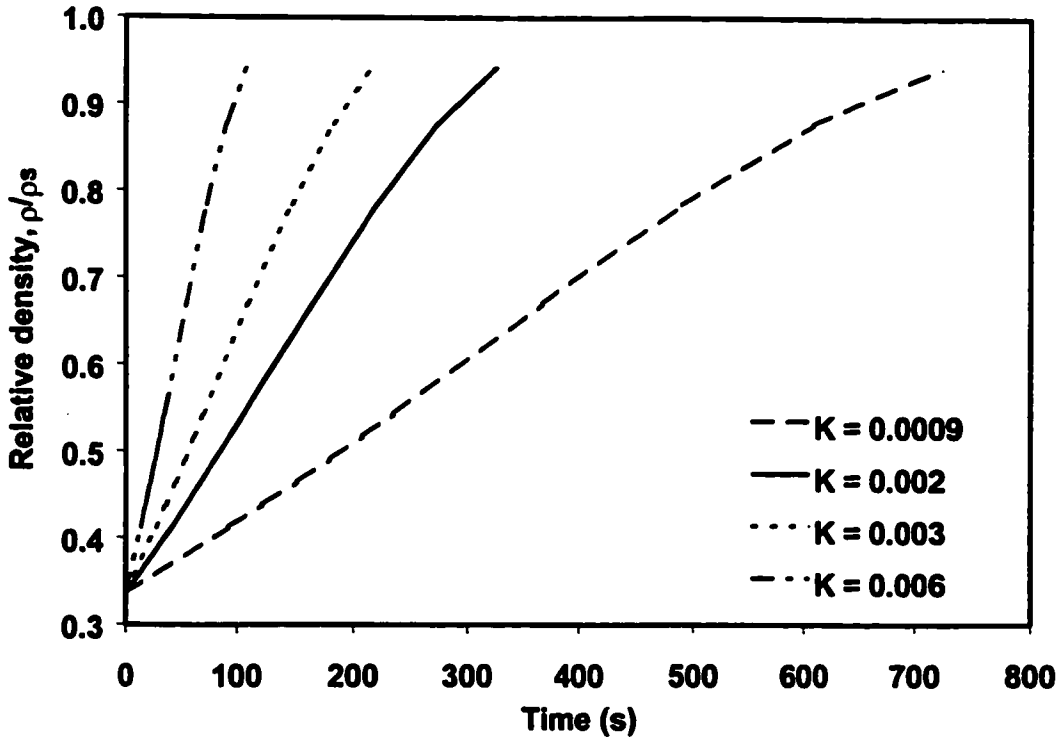

Figure 5.31: Effect of the parameter K on the densification curves predicted by Scherer's model

viscosity and initial bulk density. Figures 5.32, 5.33 and 5.34 show how viscosity, surface tension and initial particle size respectively affect the densification times. The results demonstrate that densification rates can be enhanced by choosing low viscosity resins, by increasing the surface tension of the materials, possibly through the addition of additives, or by reducing particle size.

Particle shape is also an important consideration, as discussed in section 5.2.1. Irregular particle shapes, which are encountered usually as particle size is reduced, can lead to poor "packing" of the powder, expressed by low bulk density values. A significant increase in the values of bulk density is achieved when micropellets are used. Typical values of bulk density for micropellets are around 500 kg/m^3 (Takács et al., 1996) as opposed to 300-350 kg/m^3 for powders. The benefits of higher bulk density values in the densification process, which can be achieved by micropellets, can be seen in Figure 5.35.

Unfortunately, none of the open pores model which describes the densification of a powder compact, can describe adequately data obtained for polyethylene or polypropylene (Figure 5.36). Appropriate values of physical properties of PE-5 and PP/PE-1 used for the model predictions are listed in Table 5.A in the Appendix. It is speculated that this is due to the fact that these polymers sinter layer by layer, rather than as three-dimensional compacts, as discussed in section 5.2.2. Figure 5.37, which demonstrates the variation of the compact height with time as densification progresses, under isothermal conditions, shows that the

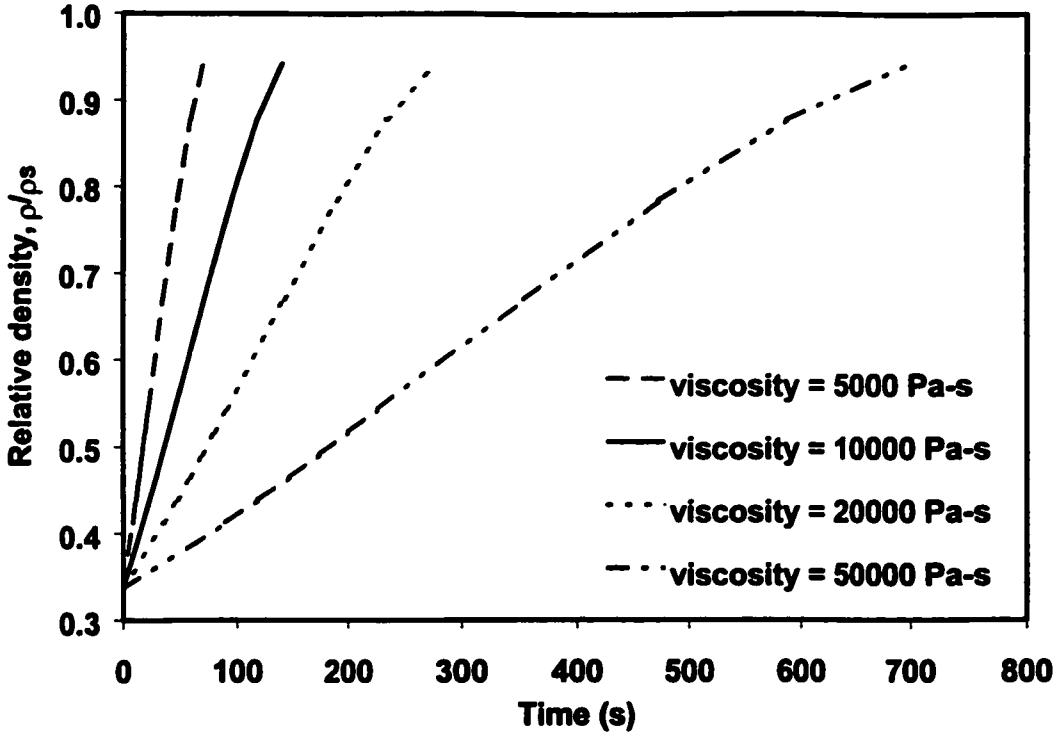

Figure 5.32: Effect of viscosity on densification curves predicted by Scherer's model (Rest of physical properties same as EVA-2, see Appendix 5.A.)

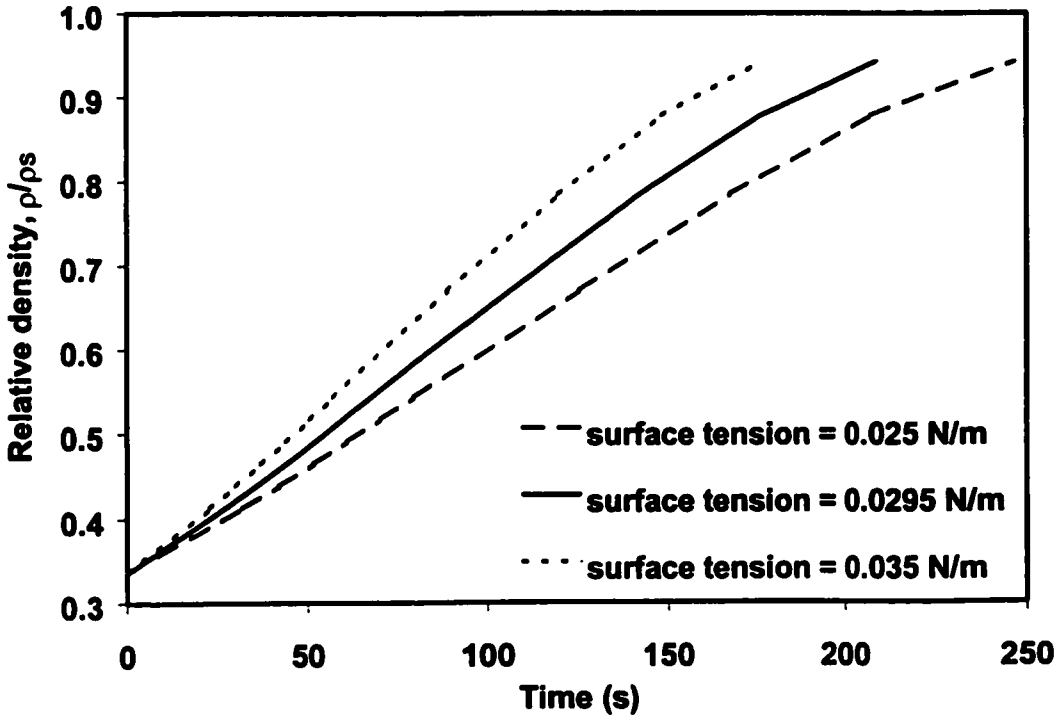

Figure 5.33: Effect of surface tension on densification curves predicted by Scherer's model (Rest of physical properties same as EVA-2. see Appendix 5.A.)

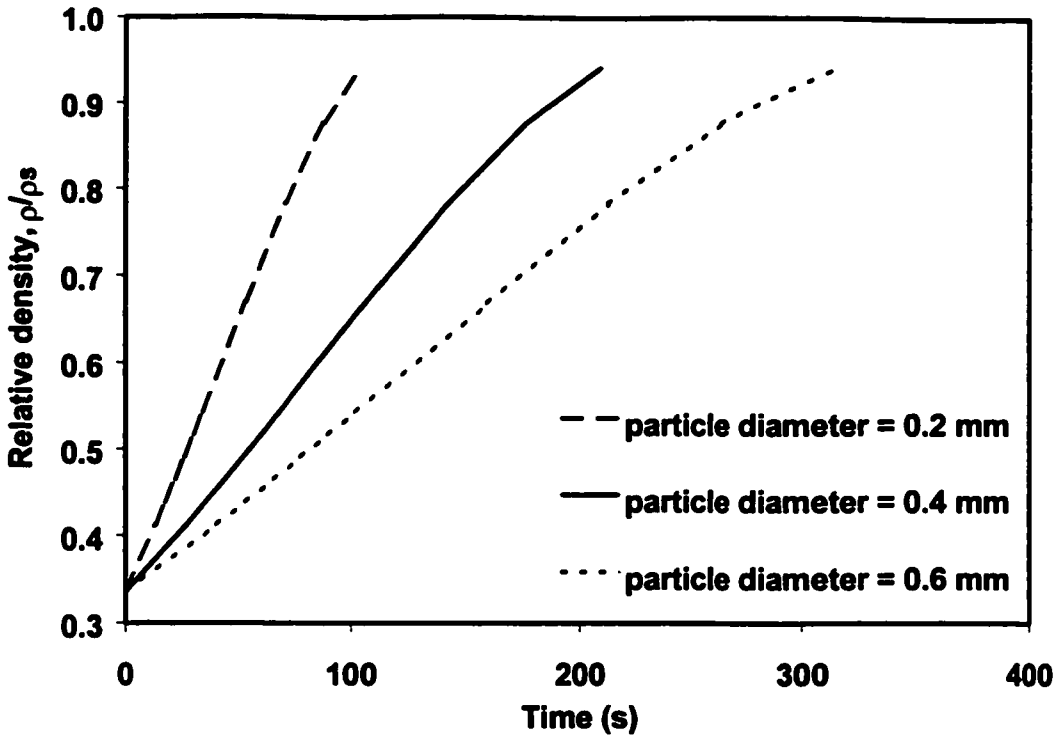

Figure 5.34: Effect of powder particle size on densification curves predicted by Scherer's model (Rest of physical properties same as EVA-2, see Appendix 5.A.)

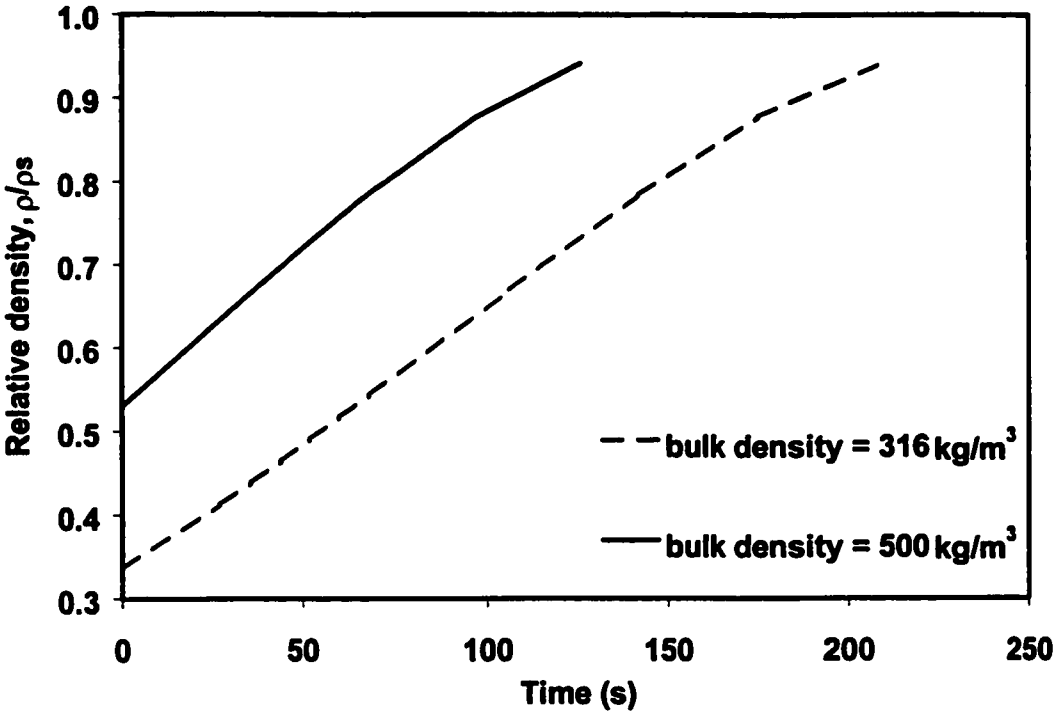

Figure 5.35: Effect of powder bulk density on densification curves predicted by Scherer's model (Rest of physical properties same as EVA-2, see Appendix 5.A.)

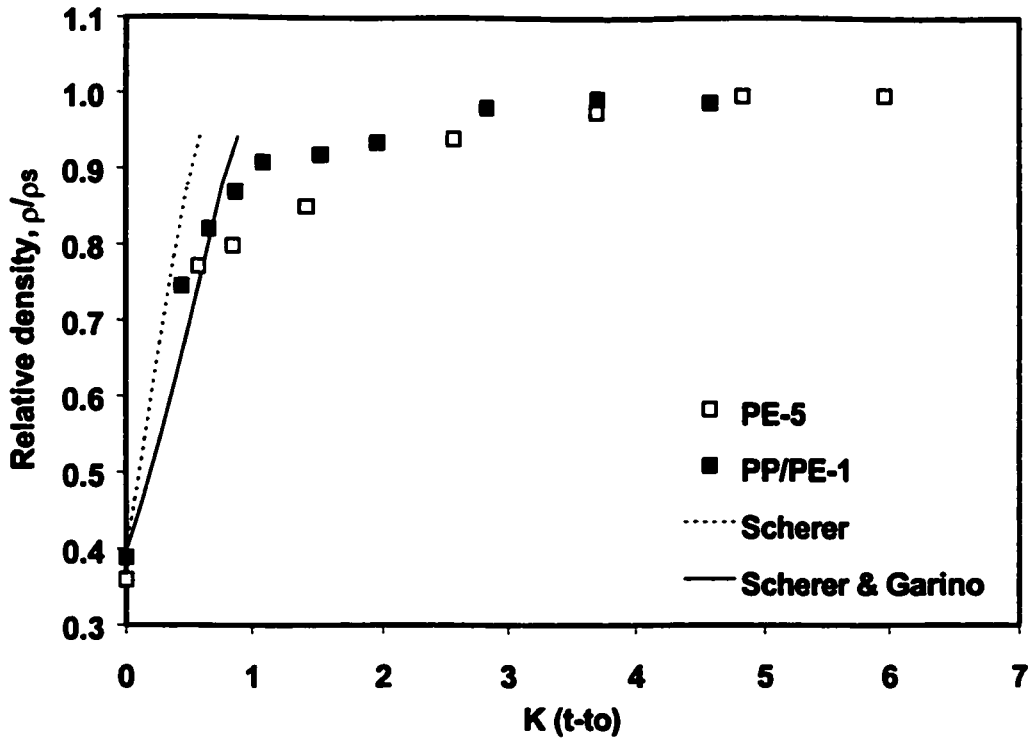

Figure 5.36: Comparison of model predictions with experimental data for polyethylene (132°C) and polypropylene (165°C)

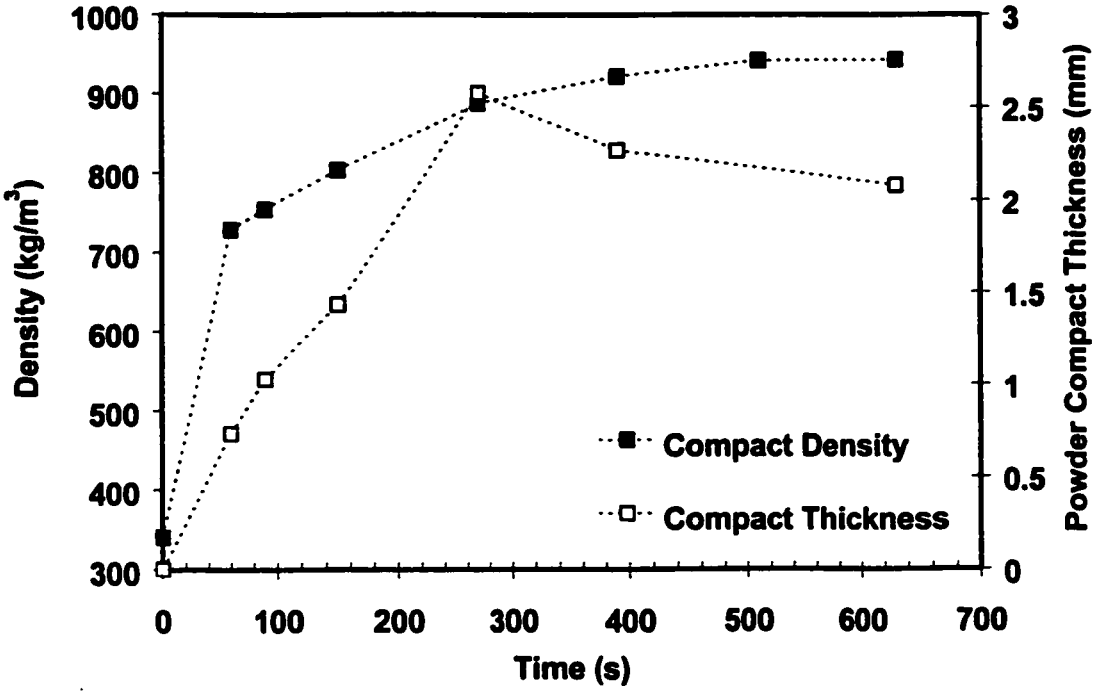

Figure 5.37: Variation of compact density and thickness as a function of time for PE-5 (132°C)

compact height increases progressively as layer after layer of powder particles adhere.

An appropriate model for this case should take the fact that the powder adheres layer by layer under consideration. This has been demonstrated for purely qualitative purposes by applying Scherer's model for distinct layers, rather than for the whole compact.

The idea is to assume that the powder compact comprises of several layers of powder particles (see also Figure 5.12). The densification of each distinct layer can be described with Scherer's model, but sintering of every layer is delayed with respect to the previous layer, because it starts to adhere later. The overall densification of the compact depends on the number of layers deposited. Once the evolution of density as a function of time for every individual layer has been calculated, the density of the whole compact is calculated as an average of the density that all layers have achieved at every time interval.

Figure 5.38 demonstrates the densification curve of PE-5 when the number of layers equals five, ten and fifteen. It has been assumed that each layer starts to adhere on the previous one after some delay time, which was taken as equal for all layers. Thus in the case of ten layers, the delay time was 27 s for all layers. The time needed for all the layers to adhere was taken as 270 s, which corresponds to the time where the compact attains its maximum height (see also Figure 5.37). The predicted curve has a saw-tooth shape, because of the discrete

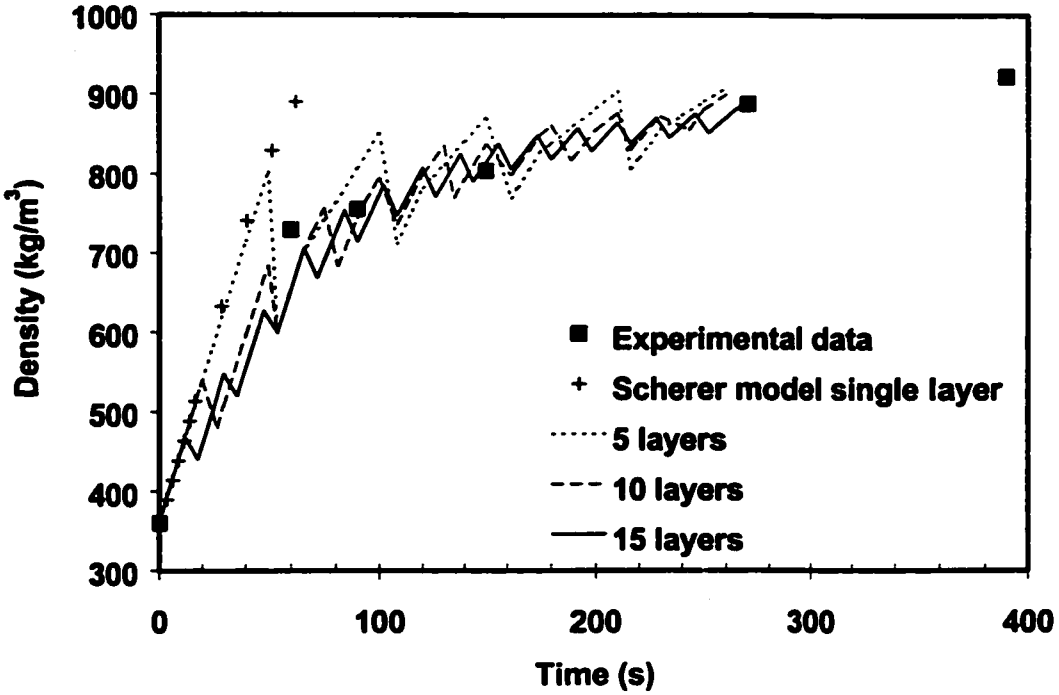

Figure 5.38: Comparison of experimental data for PE-5 with densification model for multiple layers

calculation for every layer. As the number of layers used in the calculation increased, the waviness of the prediction decreased.

The exact number of layers cannot be determined with great accuracy. However from our experimental data and microscopic observations, the powder compact described in Figure 5.38 had an initial thickness of 4 mm and the average powder particle size was 0.4 mm. Assuming that the thickness of every layer corresponds to the average particle size, it was estimated that the powder compact should consist of approximately 10 layers. Taking into account that in reality there is a particle size distribution, with some particles having smaller sizes than 0.4 mm, it is assumed that a reasonable number of layers should be between 10 and 15.

It must be noted that this is only a simple approximation, intended to elucidate the mechanism of layer deposition and densification. For an accurate calculation a detailed heat transfer analysis should be undertaken, so that the melting and deposition of each layer can be evaluated accurately.

Another interesting feature observed in Figure 5.37 is a change in slope after 300 seconds. This change has been associated with the end of layer deposition. From this point onwards, the only mechanism of densification appears to be the shrinkage of the bubbles.

5.3.4. Pore closing – The closed pores model

Since Scherer's models are only valid until the point where closed pores form, the Mackenzie and Shuttleworth (MS) model, which is appropriate for the

densification of a compact containing closed pores has been tested. According to this model densification results from the shrinkage of uniform spherical pores in a viscous matrix. The MS model leads to an equation for the sintering time necessary to reach a particular density of the compact (Mackenzie and Shuttleworth, 1949):

$$\frac{\sigma n^{1/3}}{\eta}(t-t_o)=\frac{2}{3}\left(\frac{3}{4\pi}\right)^{1/3}\int_0^{\rho/\rho_s}\frac{d(\rho/\rho_s)}{(1-\rho/\rho_s)^{2/3}(\rho/\rho_s)^{1/3}} \qquad (5\text{-}13)$$

where n is the number of pores per unit volume of solid phase which, if not known a priori, can be estimated in terms of the Scherer model from equation 5-9.

The underlying mechanism involved in all the models described above is surface tension driven flow, opposed by viscosity. The MS model, which is appropriate for relative densities above ρ/ρ_s=0.942, is frequently combined with one of Scherer's open pores model, to describe the overall densification rates of a powder compact (Orgaz-Orgaz, 1988, Scherer and Garino, 1985).

The predictions of the MS model, expressed in dimensionless form have been compared to the same experimental data as the ones shown in Figure 5.30. From Figure 5.39 it is obvious that the MS model, which considers a mechanism based on surface tension and viscosity overpredicts the data beyond the point where closed pores form. This result suggested that another mechanism may be involved in the process of pore closing. This will be the topic of Chapter 6.

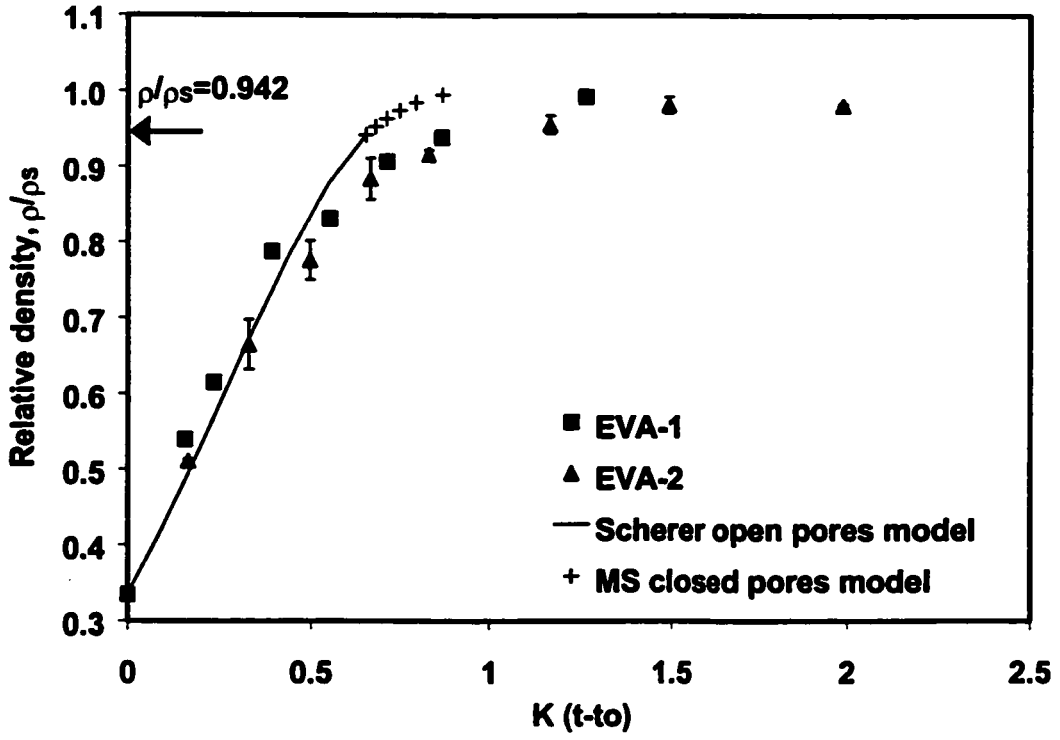

Figure 5.39: Comparison of MS closed pores model with experimental predictions for PE copolymers (105°C)

5.3.5. Estimation of bubble content and diameter

This section examines how an estimate of the size and amount of spherical bubbles, or pores formed inside polymer melts which densify as three-dimensional networks can be obtained.

It can be assumed that every pore or bubble of radius R is contained within a spherical fluid cell of radius R_{cell} (Figure 5.40). Then the whole melt consists of a number of cells, which is equal to the number of pores, N. Neglecting the mass of the gas contained within the gas bubble, compared to the mass m_p of the polymer, the polymer density can be expressed in terms of N:

$$\rho = \frac{m_p}{4/3\,\pi\,N\,R_{cell}^3} \tag{5-14}$$

The mass of the polymer can be written as:

$$m_P = \rho_S\,V_P \tag{5-15}$$

where ρ_S is the density of the fully densified polymer. (5-14) becomes

$$\rho = \frac{3\,\rho_S}{4\,\pi\,(N/V_P)\,R_{cell}^3} \tag{5-16}$$

The ratio N/V_p, which denotes the number of bubbles (or pores) per unit volume of real (bubble free) material, is the familiar quantity, n, used in Scherer's models, which is estimated from the powder properties using equation (5-9), as explained in section 5.3.1:

$$n = (1/l_o)^3(\rho_S/\rho_o) \tag{5-9}$$

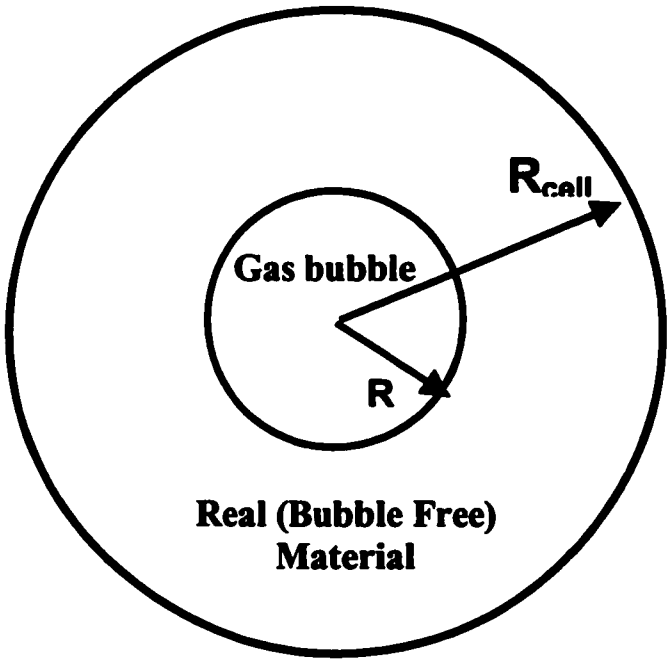

Figure 5.40: Gas bubble contained within a spherical cell of radius R_{cell}

Equation (5-16) takes the form

$$\rho = \frac{3\,\rho_S}{4\,\pi\,n\,R_{cell}^3} \tag{5-17}$$

Considering that the ratio ρ/ρ_s of the compact upon pore closing, is predicted from Scherer's model to be equal to 0.942, equation (5-17) can be used to determine the initial radius of the cell, $R_{cell,o}$.

The radius of the bubbles formed initially inside the melt, can be predicted from the cell radius R_{cell} and the density of the compact as follows. The density of the compact (represented by the cell in Figure 5.40) relative to that of the real material is:

$$\frac{\rho}{\rho_S} = \frac{V_p}{V_{cell}} = \frac{4/3\,\pi\,(R_{cell}^3 - R^3)}{4/3\,\pi\,R_{cell}^3}$$

or (5-18)

$$\frac{\rho}{\rho_S} = 1 - \left(\frac{R}{R_{cell}}\right)^3$$

Inserting $\rho / \rho_S = 0.942$ and the value of R_{cell} found from equation (5-17) into equation (5-18) can provide an estimate of the initial value of radius, R_o.

An interesting feature of this approach is that the bubble diameter and quantity are not influenced by viscosity, but only from powder characteristics. This finding is in agreement with the experimental data, which showed that for the PE copolymers the bubble size and number were relatively unaffected by viscosity values (see also Table 5.4). Table 5.7 compares predictions made by using the above approach to actual experimental data for EVA-2. It must be noted

that the predictions shown in Table 5.7. have been made by using the model of an ideal structure, assuming that the particles comprising it are monodispersed in size, whereas in reality a distribution of particle sizes exists. In addition, as will be discussed in Chapter 6, it has been shown experimentally that coalescence between neighbouring bubbles can also take place, something that cannot be accounted by the current models. In spite of the limitations of the model, it can be concluded that, although the predictions consistently overpredict the actual data, especially in terms of bubble diameter, they lie within the same order of magnitude. Thus they can provide an estimate of bubble contents and sizes if experimental data are not readily available. A detailed sample of calculations applicable for EVA-2 is given in Appendix 5.B.

Table 5.7: Comparison of predicted and actual bubble size and contents for EVA-2

	Experiment	**Prediction**
Bubble diameter (mm)	0.18 ± 0.10	0.31
No. of bubbles / mm^3 sample	3.465 ± 0.116	3.96
% Air content in melt	2.40 ± 0.11	5.8

The above analysis cannot be applied for polyethylenes and polypropylenes, because of the different densification mechanism. Sintering occurs as layer upon layer is deposited. Void spaces between particles close as the layer sinters and air is pushed away before the next layer starts to melt, thus

viscosity plays an important role because it determines the rate of sintering of every layer. In order to estimate the bubble size and numbers a detailed calculation should be made for every layer. An added difficulty is that as soon as the bubbles at the bottom layers form they start to dissolve, before the bubbles in subsequent layers have formed, therefore diffusion effects must be taken into account in the calculation.

5.4. Conclusions

In this chapter sintering and bubble formation in polymer melts have been studied and their dependence on the fundamental process of the coalescence of two particles has been established.

Densification of polymer melts during the early stages is profoundly influenced by rheology, thermal and powder properties. High melt viscosities favor low particle coalescence rates and result in the formation of more bubbles and in slower overall densification rates. Weak dependence of viscosity on temperature and presence of amorphous contents result in the formation of large amounts of bubbles in the polymer melt and are responsible for slow densification rates. It has been suggested that the densification process is characterized by a competition between melting and ease of flow of the polymer: Low melting points, combined with high viscosities at temperatures just above the melting point, result in low coalescence rates and in the subsequent entrapment of large amounts of bubbles.

A comparison of experimental data with the open pores models suggested by Scherer for the densification of three-dimensional powder compacts was made. These models, which consider the evolution of density as a function of viscosity, surface tension and powder properties, can describe successfully the trends observed for low crystallinity / low melting point polymers. A modification of Scherer's model to take into account the deposition in layers occurring in semi-crystalline polymers such as polyethylenes and polypropylenes has been suggested. It was found that these models are valid until the point where closed pores, or bubbles form.

5.5. Nomenclature for Chapter 5

d: pore dimaneter in Scherer's cubic array model, m

l: distance between centerlines of neighbouring cylinders in Scherer's cubic array model, m

l_o: initial length of cylinders in cubic array, m

L: distance between the centres of two spheres, m

Lo: initial distance between the centres of two spheres, m

m_p: mass of polymer, kg

n: number of pores/unit volume of solid phase

N: number of pores contained in the polymer melt

P: number of pores per particle in Frenkel / Scherer model

R: bubble or pore radius, m

R_{cell}: radius of spherical fluid cell containing bubble, m

t: time, s

t_o: initial time, s

T: temperature, K

V_p: volumer of bubble free polymer, m^3

x: dimensionless ratio α/l in Scherer's cubic array model

y: neck radius between two spheres, m

Greek symbols

α: particle radius or sphere radius, m

α_o: initial particle radius or sphere radius, m

ε_f: free strain rate during the deformation of an unconstrained body, s^{-1}

η: melt viscosity, Pa.s

ρ: polymer density, kg/m^3

ρ_o: initial density, or bulk density of powder compact, kg/m^3

ρ_s: density of fully densified polymer, kg/m^3

σ: surface tension, N/m

Appendix

Table 5.A: Values of physical properties applicable for EVA-2, PE-5 and PP/PE-1

Physical Property	EVA-2	PE-5	PP/PE-1
Average particle diameter (m)	$4\ 10^{-4}$	$4\ 10^{-4}$	$3.58\ 10^{-4}$
Powder bulk density, ρ_o (kg/m^3)	316	360	374
Solid density, ρ_S (kg/m^3)	942	945	900
Surface tension (N/m)	0.0295[1]	0.0293[2]	0.0217[3]
Zero shear viscosity (Pa-s)	16900[1]	5200[2]	5540[3]

[1] at 105°C
[2] at 132°C
[3] at 165°C

Appendix 5.A

Calculation of geometric parameters of cylindrical array from EVA-2 powder properties

The geometric parameters required for the construction of the cylindrical array model (see also Figure 5.30) can be calculated by combining equations 5.A-1. and 5.A-2.

$$\frac{\rho}{\rho_S} = 3\pi x^2 - 8\sqrt{2}\, x^3 \qquad (5.A\text{-}1)$$

$$x = \alpha / l \qquad (5.A\text{-}2)$$

The powder bulk density will be used in equation 5.A.1 as the initial density of the compact, ρ_o. From the data in Table 5.A.1, ρ_o/ρ_S=0.335. From equation 5.A-1,

we obtain x=0.22 and from equation 5.A-2, by substituting the average particle radius, $\alpha = 2\ 10^{-4}$m, the initial distance between the centerlines of the neighbouring cylinders is calculated to be $l_o = 9.095\ 10^{-4}$ m.

The number of closed pores / volume of solid phase can be found from equation 5.A-3:

$$n = (1 / l_o)^3 (\rho_S / \rho_o) \qquad (5.A\text{-}3)$$

or $n = 3.9584\ 10^9$ pores / m^3.

The parameter K can be obtained by using the above calculated parameters and the values of viscosity and surface tension shown in Table 5.A from equation (5.A-4):

$$K = (\sigma/\eta l_o)\ (\rho_s / \rho_o)^{1/3} \text{ or } K = (\sigma\ n^{1/3} / \eta) \qquad (5.A\text{-}4)$$

The value of K applicable for EVA-2 is $K = 0.002762\ s^{-1}$

Appendix 5.B

Estimation of bubble and cell diameter from Scherer's model

The radius, R_{cell}, of the cell surrounding the pore is given by:

$$\rho = \frac{3\ \rho_S}{4\ \pi\ n\ R_{cell}^3} \qquad (5.A\text{-}5)$$

According to Scherer's theory, upon pore closing we have ρ/ρ_S=0.942. Substitution of this value and the value of n calculated from equation (5.A-3) to equation (5.A-5) gives: $R_{cell} = 4\ 10^{-4}$ m.

Subsequently the radius of the pore can be estimated from equation (5.A-6):

$$\frac{\rho}{\rho_S} = 1 - \left(\frac{R}{R_{cell}}\right)^3 \qquad (5.A\text{-}6)$$

The result is $\underline{R=1.55\ 10^{-4}\ m}$

A summary of the results obtained by the above calculations is given in Table 5.B.

Table 5.B: Summary of results obtained by applying Scherer's cylindrical array model

Parameter	Value
Initial distance between cylinders, l_o (m)	$9.095\ 10^{-4}$
Number of closed pores / m^3 solid phase, n	$3.9584\ 10^{9}$
K (s^{-1})	0.002762
Radius of cell surrounding pore, R_{cell} (m)	$4\ 10^{-4}$
Radius of pore, R (m)	$1.55\ 10^{-4}$

Chapter 6

BUBBLE DISSOLUTION IN POLYMER MELTS

The work presented in the preceding chapter demonstrated that models, such as Scherer's model and its variations, which are based solely on surface tension and viscosity cannot describe adequately the latest stages of densification in polymer melts, which involve pore closing, or in our case bubble removal.

The objective of the current chapter is to identify the mechanisms, which control the latest stages of densification and to propose an appropriate model. The first step was to complete a fundamental study on the removal of bubbles from polymer melts and its dependence on material properties. A rigorous model, which includes all the parameters relevant to the bubble dissolution process, such as surface tension, viscosity and diffusion phenomena has been applied.

Next, the proposed model has been adjusted to allow predictions of density evolution with time and has been combined with Scherer's open pores model, in order to make possible the prediction of the whole densification process.

6.1. Theory

6.1.1. Dynamics of bubble dissolution

Although in reality the polymer melt during rotational molding contains many bubbles, a simplified approach will be implemented, which treats the dissolution of a single spherical gas bubble in an infinite polymer melt (Figure 6.1). The problem is assumed to be isothermal.

The kinematics of the problem are satisfied by the continuity equation, which for spherical geometry, uni-directional flow in the r direction, constant density, ρ and using the boundary condition that the bubble wall velocity, at $r = R$ is $U_r = dR/dt$, is simplified to (Middleman, 1977):

$$U_r = \frac{R^2 \dot{R}}{r^2} \tag{6-1}$$

The dynamics of the system are governed by the conservation of momentum in the radial direction

$$\rho\left(\frac{\partial U_r}{\partial t} + U_r \frac{\partial U_r}{\partial r}\right) = -\frac{\partial P}{\partial r} + \left[\underline{\nabla} \bullet \underline{\underline{\tau}}\right]_r$$
$$\text{where } \left[\underline{\nabla} \bullet \underline{\underline{\tau}}\right]_r = \frac{1}{r^2}\frac{\partial}{\partial r}(r^2 \tau_{rr}) - \frac{\tau_{\theta\theta} + \tau_{\varphi\varphi}}{r} \tag{6-2}$$

Since the fluid is highly viscous, the inertia terms can be neglected and equation (6-2) becomes

$$-\frac{\partial P}{\partial r} + \frac{1}{r^2}\frac{\partial}{\partial r}(r^2 \tau_{rr}) - \frac{\tau_{\theta\theta} + \tau_{\varphi\varphi}}{r} = 0 \tag{6-3}$$

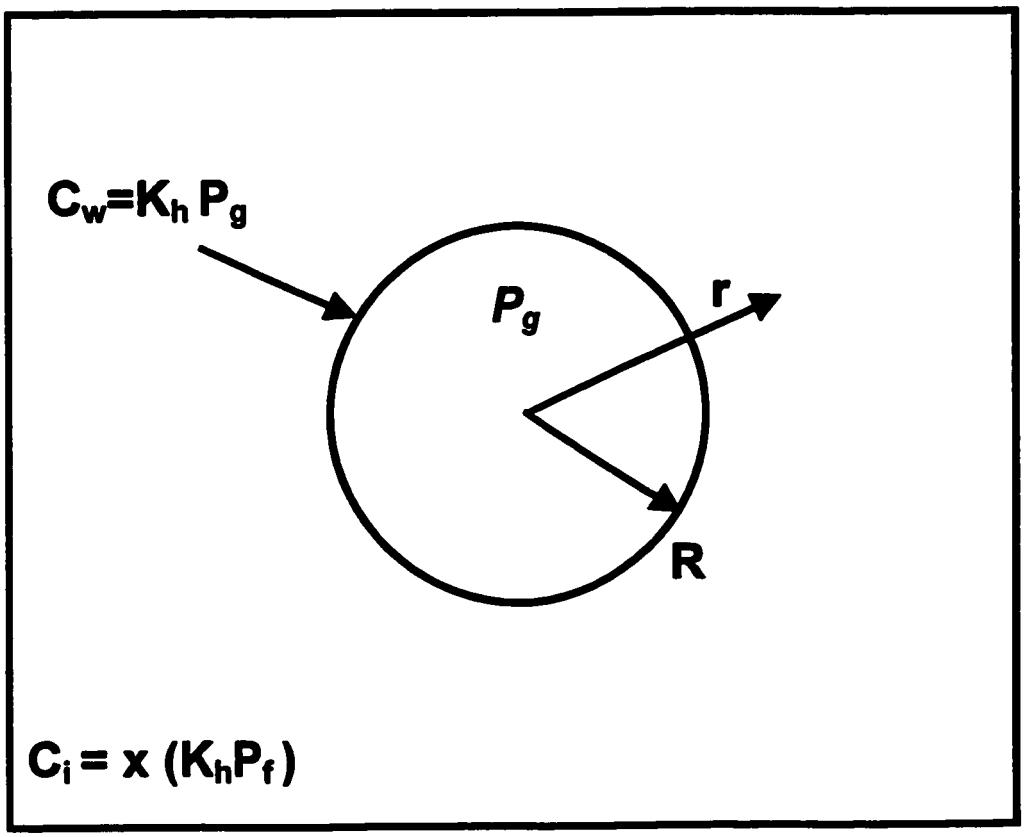

Figure 6.1: Geometry of a single spherical bubble surrounded by an infinite amount of fluid

Taking into account spherical symmetry ($\tau_{\theta\theta}=\tau_{\varphi\varphi}$), an integration from the bubble wall to infinity allows us to relate the stresses within the fluid to the gas pressure inside the bubble and the ambient pressure (Pearson and Middleman, 1977):

$$P(R) - P(\infty) + \tau_{rr}(\infty) - \tau_{rr}(R) + 2\int_R^\infty \frac{\tau_{rr} - \tau_{\theta\theta}}{r}\, dr = 0 \qquad (6\text{-}4)$$

A force balance at the bubble-liquid interface gives:

$$2\pi R\sigma + \pi R^2[P(R) - \tau_{rr}(R)]_L = \pi R^2[P_g + \tau_{rr,g}]_G \qquad (6\text{-}5)$$

Since the normal stress due to a low viscosity gas can be neglected, $\tau_{rr,g} = 0$. Equation (6-5) becomes:

$$P(R) = \tau_{rr}(R) + P_g - \frac{2\sigma}{R} \qquad (6\text{-}6)$$

where the pressure P_g is the average gas pressure within the bubble.

Substituting (6-6) into (6-4) and assuming that at $r = \infty$, $\tau_{rr} = 0$

$$P_g - P(\infty) - \frac{2\sigma}{R} + 2\int_R^\infty \frac{\tau_{rr} - \tau_{\theta\theta}}{r}\, dr = 0 \qquad (6\text{-}7)$$

For a Newtonian liquid, the stress components depend on the rate of deformation:

$$\tau_{ij} = \eta\Delta_{ij} \qquad (6\text{-}8)$$

The components of the rate of deformation tensor for uniaxial elongational flow are:

$$\Delta_{rr} = 2\frac{\partial U_r}{\partial r}$$
$$\Delta_{\theta\theta} = \Delta_{\varphi\varphi} = 2\frac{U_r}{r} \qquad (6\text{-}9)$$

Differentiation of equation (6-1) results in:

$$\frac{\partial U_r}{\partial r} = -\frac{2R^2\dot{R}}{r^3} \tag{6-10}$$

Substitution of (6-10) to (6-9) gives

$$\Delta_{rr} = -\frac{4R^2\dot{R}}{r^3}$$
$$\Delta_{\theta\theta} = \Delta_{\varphi\varphi} = \frac{2R^2\dot{R}}{r^3} \tag{6-11}$$

The normal stresses can now be calculated by using the Newtonian constitutive equation (6-8) and the rate of deformation components, given by (6-11). The result can be substituted in equation (6-7) and after rearranging and naming $P(\infty)=P_f$

$$\dot{R} = \frac{1}{4\eta}\left[(P_g - P_f)R - 2\sigma\right] \tag{6-12}$$

Equation (6-12) relates the pressure inside the bubble to the rate of dissolution of the bubble.

6.1.2. Determination of the pressure inside the bubble

In order to determine the rate of dissolution of a bubble from equation (6-12) we must have a relation for the gas pressure inside the bubble. This can be found by applying the conservation of mass principle for gas inside the bubble (Barlow and Langlois, 1962). If buildup of adsorbed gas on the bubble wall is assumed to be negligible, the rate of decrease of gas within the bubble equals the rate of diffusion of gas from the bubble across the wall, towards the liquid. The

mass balance can be written:

$$\frac{4}{3}\pi \frac{d(c_g R^3)}{dt} = (4\pi R^2)\, D \left(\frac{\partial c}{\partial r}\right)_{r=R} \tag{6-13}$$

Assuming that the gas inside the bubble is ideal, the concentration of gas within the bubble can be related to the pressure inside the bubble, $c_g = P_g/(R_g T)$:

$$\frac{d}{dt}\left(\frac{P_g}{R_g T} R^3\right) = 3 R^2 D \left(\frac{\partial c}{\partial r}\right)_{r=R} \tag{6-14}$$

The pressure inside the gas bubble can be also related to the gas concentration at the bubble-liquid interface through Henry's law:

$$c_w = K_h P_g \tag{6-15}$$

where K_h is Henry's law constant. This equation is valid for dilute solutions.

To solve equation (6-14) it is necessary to know the concentration profile in the liquid. This can be determined by solving the complete diffusion equation for the liquid surrounding the bubble (Bird et al., 1960), which for spherical coordinates can be simplified by neglecting the terms involving convective transport:

$$\frac{\partial c}{\partial t} = \frac{D}{r^2}\frac{\partial}{\partial r}\left(r^2 \frac{\partial c}{\partial r}\right) \tag{6-16}$$

Equation (6-16) can be solved subject to the following boundary and initial conditions:

$$c(r,0) = c_i, \quad r > R$$
$$\lim_{r\to\infty} c(r,t) = c_i, \quad t > 0$$
$$c(R,t) = c_w, \quad t > 0$$

The concentration of gas dissolved initially in the bulk of the polymer melt can be determined from Henry's law, if the melt is saturated with air:

$$(c_i)_{sat} = K_h P_f \qquad (6\text{-}17a)$$

In reality it is impossible to know the degree of saturation of the polymer melt, so when comparing model predictions to experimental data, it is necessary to assume that c_i will be a fraction x of $(c_i)_{sat}$:

$$c_i = x\,(c_i)_{sat} \qquad (6\text{-}17b)$$

Comparison with several experimental data, as will be demonstrated in the experimental section, showed that x lies between 0.9 and 1.

6.1.3. Numerical solution scheme and model implementation

The rate of bubble dissolution can be determined by solving simultaneously equations (6-12), (6-14) and (6-16) with the aid of (6-15) and (6-17). A numerical method, using a finite difference discretization and a forward Eulerian scheme has been implemented. A quasi-steady state approximation (solution of the steady-state equation for every time step) is used for solving the diffusion equation, following the steps shown below:

- Initially, as the powder melts and the pockets of air form, the system pressure is equal to the ambient pressure. Once the bubble is formed, the pressure inside the bubble increases slightly due to curvature, through the action of surface tension (equation 6-6). The initial pressure P_g inside the bubble can be determined from equation (6-6), by neglecting τ_{rr} (assuming there is no movement of the melt due to bubble shrinkage yet) and setting P(R) equal to

the ambient pressure. In order for the solution to begin, the initial bubble radius is substituted for R in equation (6-6) at the first time increment.

- By using the initially estimated pressure P_g inside the bubble, the air concentration at the air bubble interface, c_w, can be determined from Henry's law, equation (6-15). The initial concentration of air dissolved in the bulk of the polymer, c_i, can be also estimated from Henry's law as explained in equations 6-17(a) and (b), using the ambient pressure.
- The concentration gradient $\partial c/\partial r$ can be determined for the first time increment by solving equation (6-16).
- Equations (6-12) and (6-14) are solved simultaneously, to give the new values of P_g and R at the end of the time increment.
- Using the most recent value of P_g, the new air concentration, c_w, can be determined from equation (6-15). By using this c_w and the new bubble radius, the concentration gradient $\partial c/\partial r$ can be determined for the second time increment (eq. 6-16) and the procedure is repeated.

In order to implement the model the initial bubble diameter, ambient pressure, initial concentration of gas in the polymer melt and the physical constants of the system, such as viscosity, surface tension, diffusion coefficient and Henry's law constant are required. The concentration of air in the polymer melt is determined by curve fitting, since it is impossible to determine either theoretically or experimentally, as explained in the theory section (equations 6-17(a) and (b)).

6.1.4. Estimation of physical constants

The diffusion coefficients and Henry's law constants for air into a polyethylene melt were estimated by using data and charts published by Griskey (1995). The Lennard-Jones parameters for air, needed for using Griskey's charts were obtained from Bird et al. (1960). The temperature dependence of these parameters can be estimated by applying an Arrhenius type equation (Durrill and Griskey, 1969). For Henry's law constant we can write:

$$\ell nK_h = \ell nK_{h_o} - \frac{E_S}{R}\left(\frac{1}{T} - \frac{1}{T_o}\right) \qquad (6\text{-}18)$$

where K_{ho} represents Henry's law constant at a reference temperature T_o and E_S is the heat of solution, which can be estimated for air dissolved into a PE melt from Griskey (1995).

In a similar manner, the temperature dependence of the diffusion coefficient can be found from:

$$\ell nD = \ell nD_o - \frac{E_d}{R}\left(\frac{1}{T} - \frac{1}{T_o}\right) \qquad (6\text{-}19)$$

where D_o is the diffusion coefficient at a reference temperature T_o. Since no data are available for the activation energy E_d of air dissolved in molten PE, the activation energy for nitrogen given in (Durrill and Griskey, 1969) was used.

Furthermore, estimates of surface tension values for linear polyethylene melts were obtained from Wu (1995). The surface tension of typical polymer melts shows a linear dependency with temperature, for temperatures ranging

between 20 and 200°C:

$$\sigma = \sigma_o + (d\sigma/dT)\,(T_o - T) \qquad (6\text{-}20)$$

Wu (1995) supplies values of the slope – $(d\sigma/dT)$ for several polymers.

A summary of values of physical constants available in the literature is given in Table 6.1. These can be used in conjunction with equations (6-18), (6-19) and (6-20) to estimate values at any desired temperature.

Table 6.1: Numerical values of physical properties for polyethylene melts

Physical Property	Value	Reference
Diffusion coefficient, m^2/s (at 188.3°C)	$8.5\ 10^{-9}$	Griskey, 1995
Activation energy, kcal/mol	2.0	Durrill & Griskey, 1969
Henry's law constant, $mol/(m^3Pa)$ (at 188.3°C)	$3.75\ 10^{-5}$	Griskey, 1995
Heat of solution, kcal/mol	0.85	Griskey, 1995
Surface tension, N/m (at 20°C)	0.0357	Wu, 1995
$-(d\sigma/dT)$, N/(m °C)	$5.7\ 10^{-5}$	Wu, 1995

6.2. Results – Model predictions

6.2.1. Bubble dissolution mechanism

The application of the proposed model gives an insight to the mechanism of bubble dissolution. The concentration of air, c_w, in the polymer/air interface (bubble walls) corresponds always to saturation conditions and can be found by applying Henry's law. The concentration, c_i in the rest of the polymer melt, is usually slightly below the saturation level, as will be proven below in sections 6.2.5. and 6.3.1. This concentration difference gives rise to a driving force, which results in the diffusion of air from the bubble to the surroundings. As gas is removed from the bubble, the diameter decreases and the air pressure inside the bubble increases further. Figure 6.2 shows the change in P_g as the bubble diameter decreases, for the dissolution of a typical gas bubble of initial diameter equal to 0.25 mm in a PE melt which is close to saturated conditions (c_i=0.995 $(c_i)_{sat}$) and has viscosity η = 3000 Pa·s and surface tension σ = 0.026 N/m, at 190°C. At long times, P_g increases dramatically as $R \rightarrow 0$ (equation 6-6) and this causes an acceleration in the bubble dissolution rate. This happens because the increase in P_g inside the bubble results to an increase in c_w, as predicted by Henry's law and subsequently to an even larger concentration difference between the bubble/air interface and the polymer melt, thus accelerating diffusion.

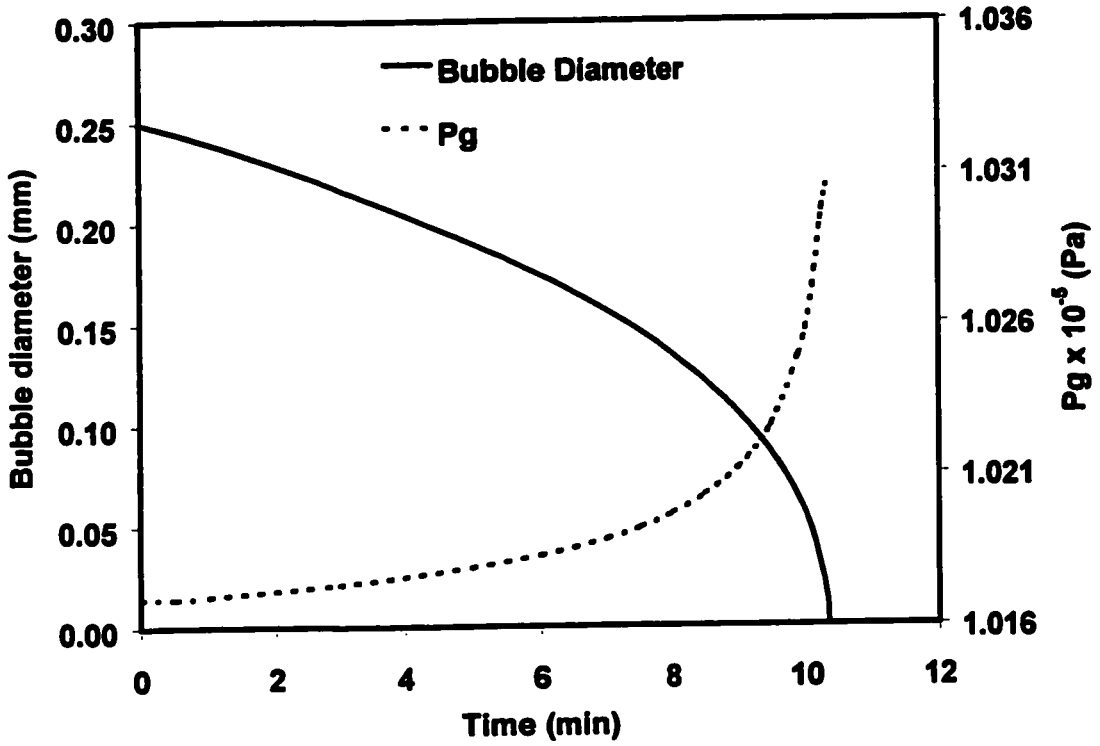

Figure 6.2: Diameter and air pressure inside the bubble versus time for the dissolution of a typical gas bubble (d_o = 0.25 mm) in a PE melt (η = 3000 Pa·s, c_i=0.995 $(c_i)_{sat}$) , 190°C.

6.2.2. Effect of viscosity

It has been speculated in the literature that melt viscosity affects bubble dissolution rate, because as melt viscosity decreases, polymer chains become shorter and diffusion of air through the melt is facilitated (Crawford and Spence, 1996). However, it has been shown that both in the case of the diffusion of gases in solid polymers (Crank and Park, 1968) and in molten polymers (Griskey, 1995) the value of the diffusion coefficient does not depend on the viscosity of the polymer but rather on the size of the gas molecule and on the monomer type and structure.

The effect of viscosity in the bubble dissolution process can be understood better by inspecting the force balance at the bubble-liquid interface (equation 6-6). As the bubble shrinks, a normal force is generated in the polymer melt, which acts on the opposite direction; that is, it opposes the movement of the bubble boundary. For a Newtonian liquid, the normal stress increases when viscosity increases (equation 6-8). Thus for higher viscosity values, the normal force opposing the movement of the bubble boundary becomes larger.

Bubble dissolution rates, for viscosity values ranging from 500 to 10000 Pa-s at 190°C, are shown in Figure 6.3. This range of viscosities was chosen because it is typical for PE rotomolding grade resins. From Figure 6.3 it can be seen that the effect of viscosity is more prominent at longer times, when bubble diameter becomes small. This can be understood by examining the relative magnitude of contribution of the terms in equation (6-6). The relative magnitudes

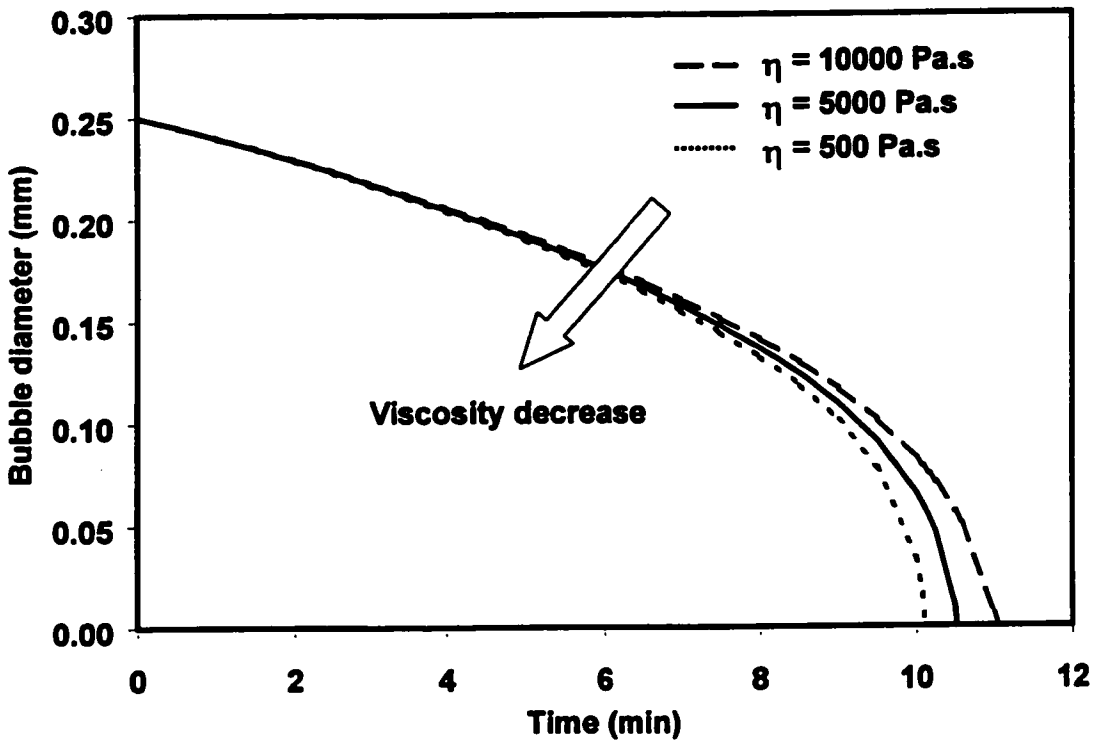

Figure 6.3: Effect of melt viscosity on bubble dissolution curves in a PE melt. (d_o = 0.25 mm, 190°C, c_i=0.995 $(c_i)_{sat}$)

of the surface tension and normal stress terms for the typical bubble dissolution case shown in Figure 6.2 are plotted in Figure 6.4. In the beginning the surface tension term is around 150 times larger than the normal stress term (which depends on viscosity). This means that at the early stages the magnitude of the normal stresses is insignificant and does not affect the result. At much longer times, as the dissolution of bubble proceeds, the surface tension term becomes only around three to four times larger, meaning that now the normal stress term (and thus the viscosity contribution) becomes significant. As the bubble diameter tends towards zero, both terms increase abruptly.

6.2.3. Effect of bulk concentration of air in the polymer melt

Another parameter, which is very important, is the bulk concentration of air in the polymer melt. Polyolefin melts, in equilibrium with the atmospheric air, contain dissolved air. The solubility of air depends on pressure and the amount of dissolved air when the polymer melt is saturated can be determined from Henry's law. The exact amount of air contained in the polymer melt in typical rotomolding conditions cannot be determined exactly, but our results show that the melt is close to the saturation conditions. However, even small levels of under-saturation result in significantly accelerated dissolution rates, due to high concentration gradients. The effect of decreasing the concentration of air inside the polymer melt is demonstrated in Figure 6.5.

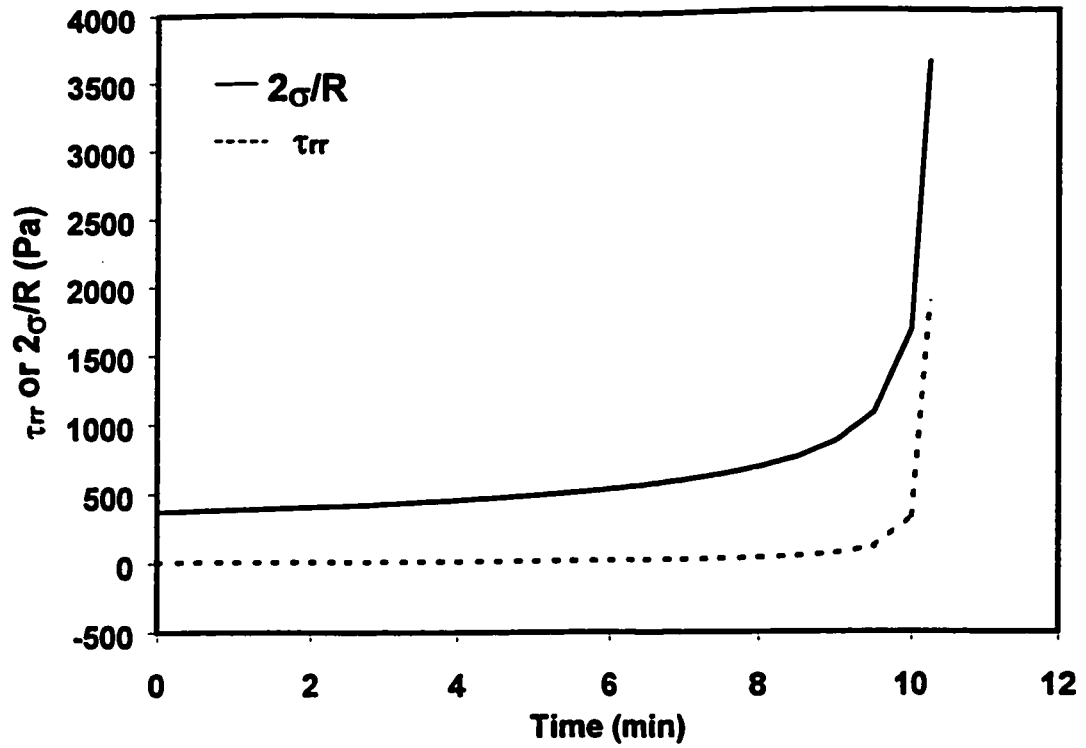

Figure 6.4: Relative magnitude of surface tension and normal stress terms as a function of time in a PE melt ($d_o = 0.25$ mm, $\eta = 3000$ Pa·s, 190°C, c_i=0.995 $(c_i)_{sat}$).

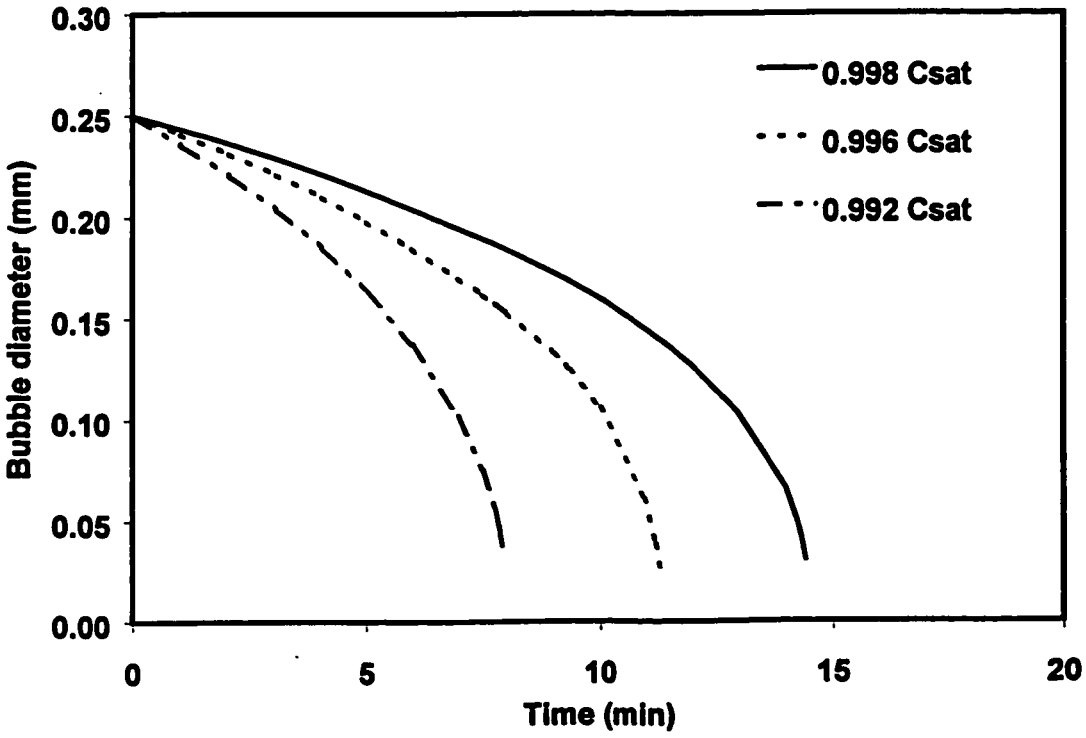

Figure 6.5: Effect of bulk concentration of air on bubble dissolution curves. ($d_o = 0.25$ mm, $\eta = 3000$ Pa·s, 190°C).

6.2.4. Effect of initial bubble size

The initial bubble diameter greatly affects the rate of bubble dissolution, as can be seen in Figure 6.6. From this it can be concluded that the initial size of the bubbles is very important for the subsequent dissolution and there is a critical initial bubble diameter above which a bubble cannot be completely dissolved for usual rotomolding cycles of up to 20-30 minutes.

6.2.5. Comparison with experimental data available in the literature

A comparison of the model predictions with data published in the literature (Spence, 1994) is presented in Figure 6.7. The published data refer to the diffusion of air in a medium density polyethylene melt (NCPE 8017 by Neste Chemicals with MFI=3.2), at a temperature of 190°C, under atmospheric pressure. The experiments had been conducted using the hot plate technique, during which a 50 g sample of powder was placed on a base plate enclosed by a cylindrical ring, complete with a glass viewing port. The glass viewing port permitted the observation and recording of bubbles as they formed and disappeared. Details of this technique can be found in the literature (Spence, 1994, Crawford and Spence, 1996 and Spence and Crawford, 1996).

The model predictions, obtained by using $c_i = 0.996\ (c_i)_{sat}$, are in reasonably good agreement with the experimental data, as demonstrated in Figure 6.7.

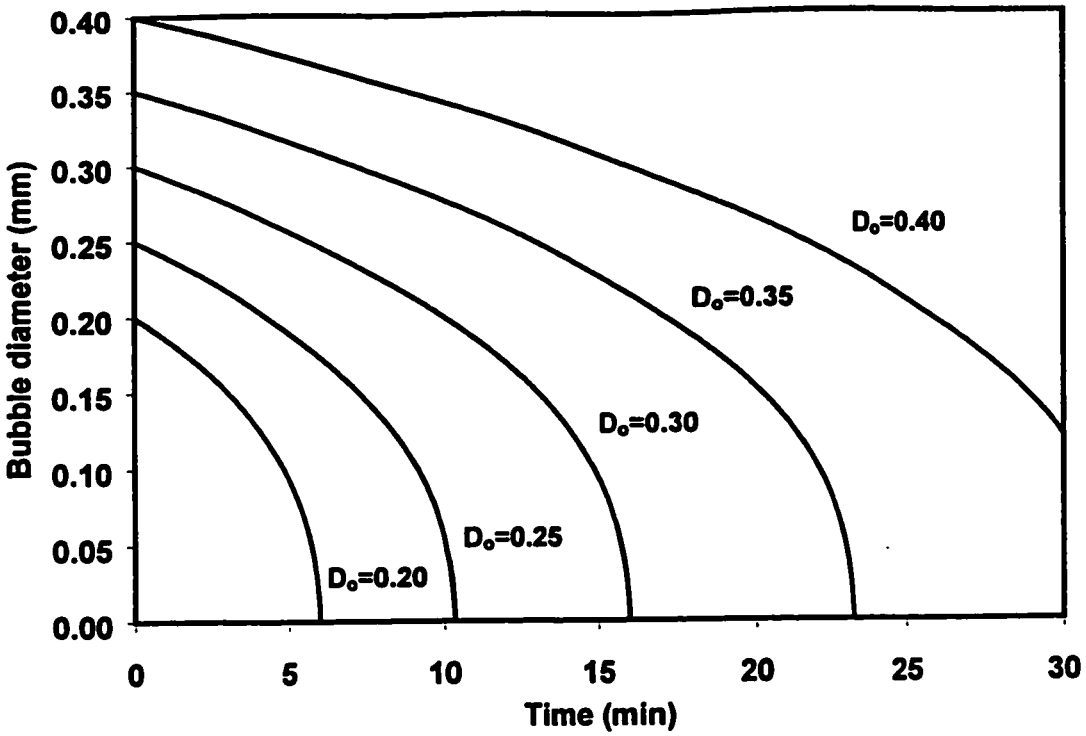

Figure 6.6: Effect of initial bubble diameter on bubble dissolution curves. (c_i=0.995 $(c_i)_{sat}$, η = 3000 Pa·s, 190°C).

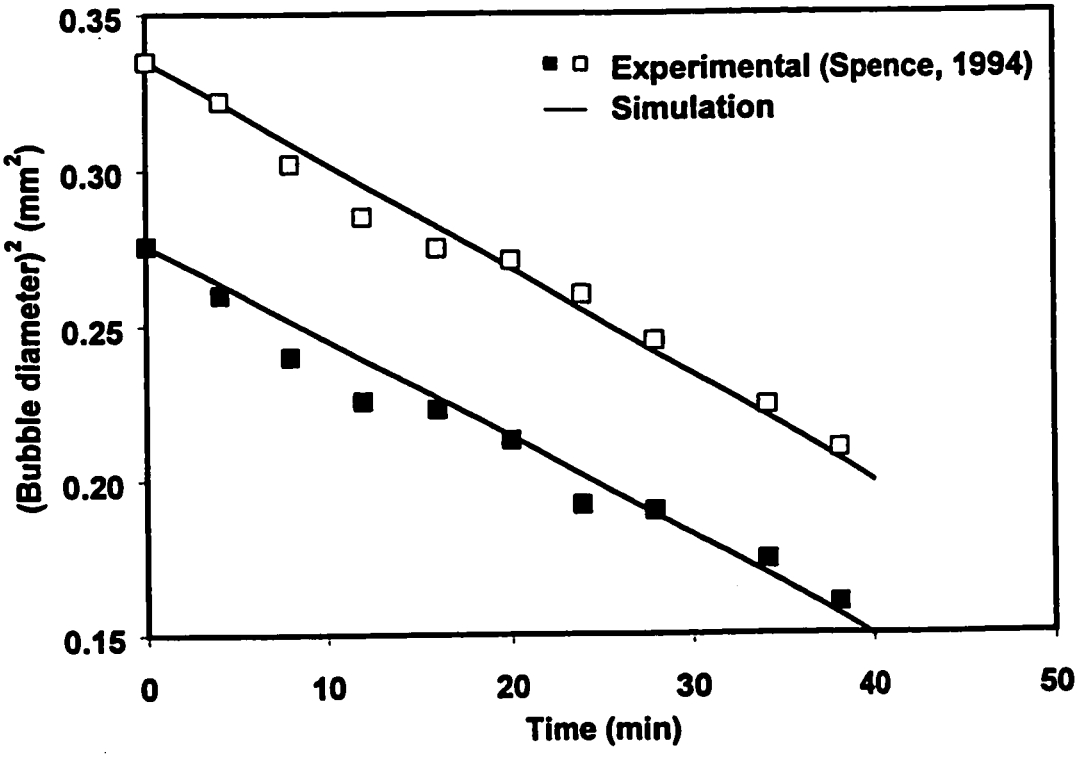

Figure 6.7: Comparison of model predictions with experimental data from Spence (1994).

6.2.6. Effect of pressure

Increasing pressure after the melt has formed, has been reported to increase bubble dissolution rates significantly, if the pressure is introduced after the polymer has melted (Spence, 1994, Spence and Crawford, 1996). The effect of pressure in bubble dissolution can be explained as follows: First, when the ambient pressure increases from P_0 to P_1, the pressure inside the bubble increases as well. This causes an immediate shrinkage of the bubble, which can be predicted by using Boyle's law (Spence, 1994, Spence and Crawford, 1995):

$$P_1 V_1 = P_0 V_0$$
$$V_1 = \frac{P_0 V_0}{P_1} \tag{6-21}$$

where 0 and 1 denote initial and final conditions respectively. For a spherical bubble:

$$V = \frac{4\pi R^3}{3} \tag{6-22}$$

Substitution of (6-22) into (6-21) gives:

$$R_1 = \sqrt[3]{\frac{P_0}{P_1} R_0^3} \tag{6-23}$$

The second effect is associated to the dependence of the driving force for dissolution on pressure. Before increasing the pressure, the already formed melt is close to saturation conditions, corresponding to P_0. When the pressure inside the bubble increases suddenly to P_1, the concentration of air, c_w, at the bubble walls increases, according to Henry's law, while the concentration of air, c_i, inside the

polymer melt remains practically unaffected. Therefore the gradient $\partial c/\partial r$, which is the driving force for diffusion increases significantly, as shown in Figure 6.8. The respective dissolution curves are shown in Figure 6.9. Figure 6.10 shows a comparison of model predictions with experimental data provided by Spence (1994), under an absolute pressure of 200 kPa (2 bar). The experimental results presented were obtained by using pressurized hot plate tests under isothermal conditions at 190°C, using a polyethylene with MFI=3.2 (NCPE 8017 by Neste Chemicals). The setup consisted of a controlled pressure line and sealed hot plate rig, which incorporated a pressure connection, thermocouple probes and a viewing window. Details of the technique can be found elsewhere (Spence, 1994, Spence and Crawford, 1995, 1996).

In light of the above, the fact that the polymer must be completely molten before pressure is introduced (Spence and Crawford, 1996) can be readily explained. If the pressure were introduced prior to the melting of the polymer, the melt would become saturated with air upon melting so there would be no increased gradient to facilitate the bubble dissolution.

6.3. Experimental

Bubble dissolution experiments were conducted by using the heating chamber described in Chapter 3. The sample cup holder was loaded with 1g of PE-2 (LLDPE with MI=5) powder and placed in the center of the heating chamber, which was kept at a constant temperature with the aid of a temperature controller.

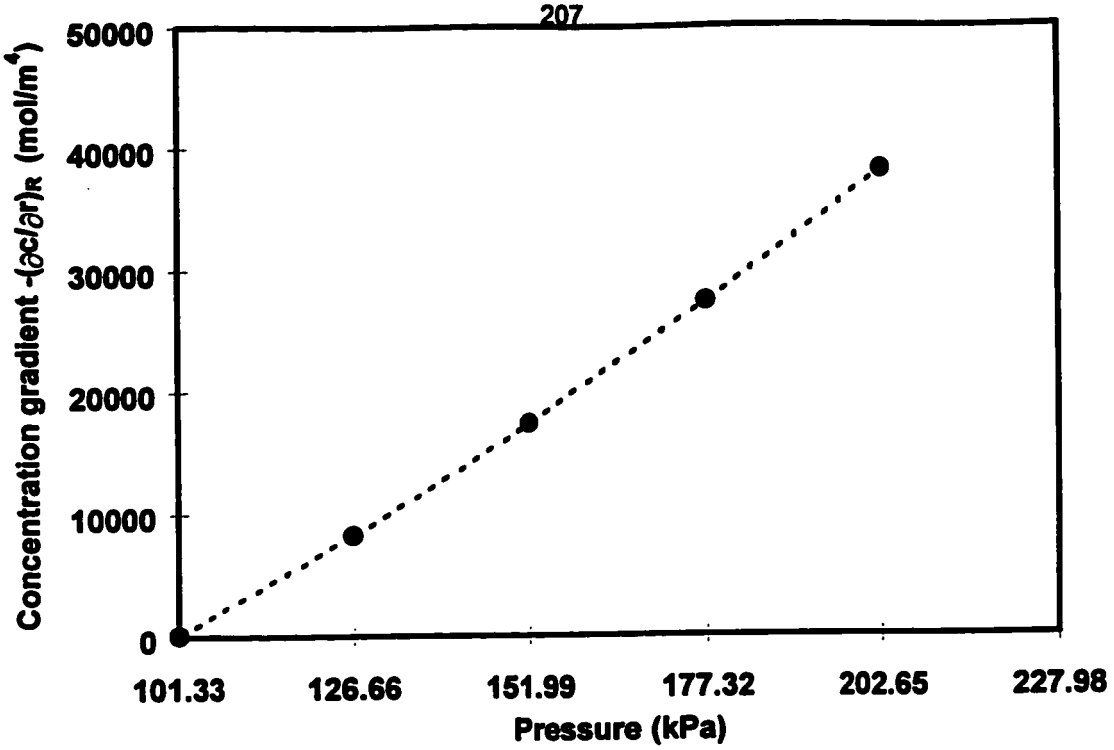

Figure 6.8: Effect of pressure on initial concentration gradient (d_o = 0.25 mm, η = 3000Pa·s, 190°C).

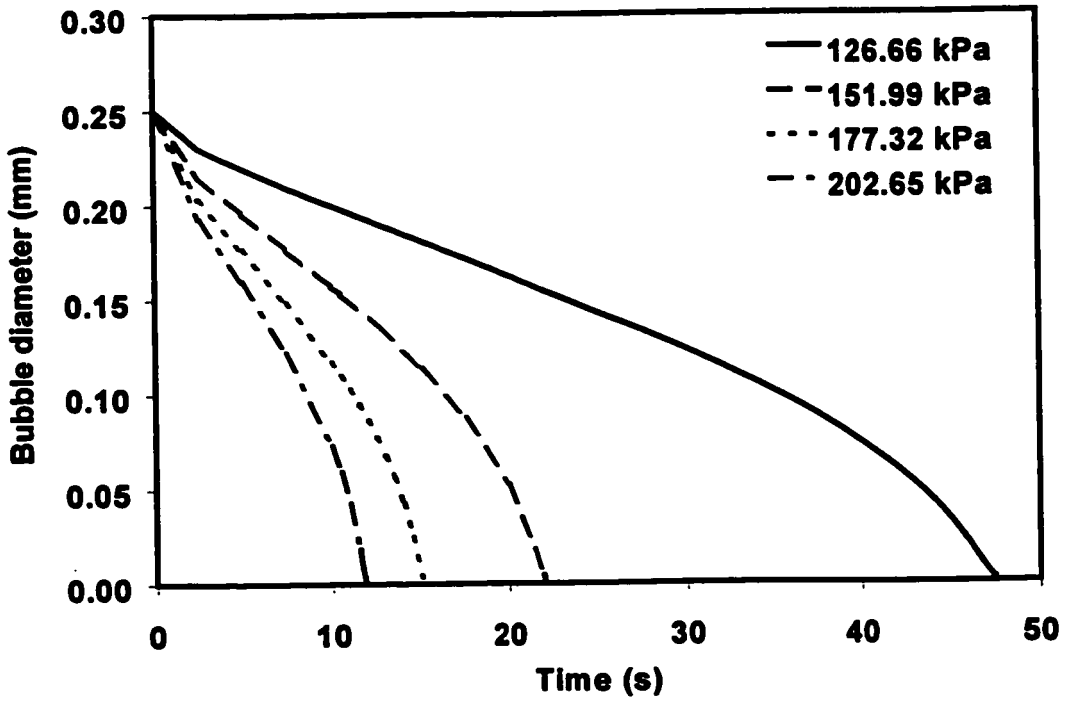

Figure 6.9: Effect of pressure on bubble dissolution curves (do = 0.25 mm, η = 3000 Pa·s, 190°C)

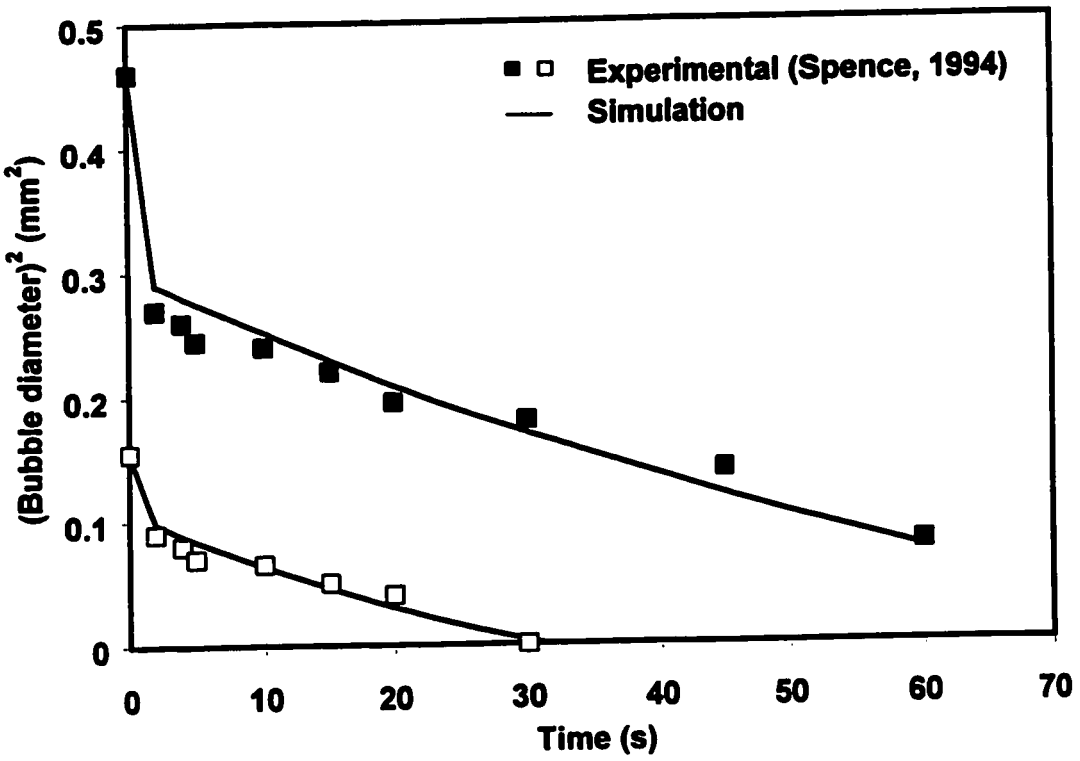

Figure 6.10: Comparison of model predictions with experimental data from Spence (1994) at increased pressure (200 kPa).

All the experiments were done isothermally at 190°C, under atmospheric pressure and the duration of the experiments was 30 min.

Several bubbles were observed as they dissolved and image analysis was performed to determine the dissolution rate. With the aid of image analysis, plots of bubble diameter as a function of time were constructed.

6.3.1. Results and comparison with model predictions

From the experimental results it was seen that there is a great variability in the behavior of the bubbles, depending on their size, their proximity to other bubbles and the overall bubble content in the polymer melt.

Some typical dissolution curves for PE-2, along with the model predictions, are shown in Figure 6.11. In Figure 6.11, time zero is considered as the time when the bubbles have formed and have assumed a spherical shape. The bubbles shown have been carefully chosen so that they are relatively isolated inside the polymer melt, to eliminate possible interaction effects. The model predictions, obtained by using $c_i = 0.95(c_i)_{sat}$, are in good agreement with the experimental data.

Bubble dissolution is considerably slower in regions with high bubble contents. Figure 6.12 compares the behavior of one of the isolated bubbles shown in Figure 6.11, with that of a bubble with similar initial diameter, which lies in a region of high bubble content. It appears that in the latter case, after the bubble forms, there is an induction period where there is very little dissolution, followed by a period during which considerable dissolution takes place. The existence of

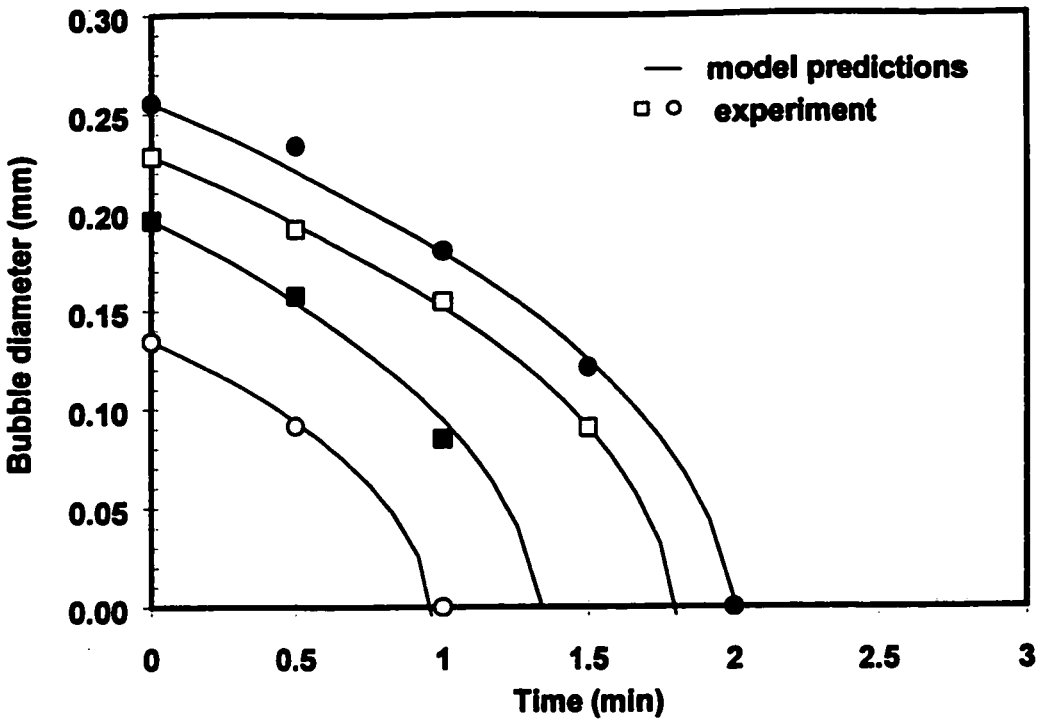

Figure 6.11: Typical bubble dissolution curves for PE-2 at 190°C

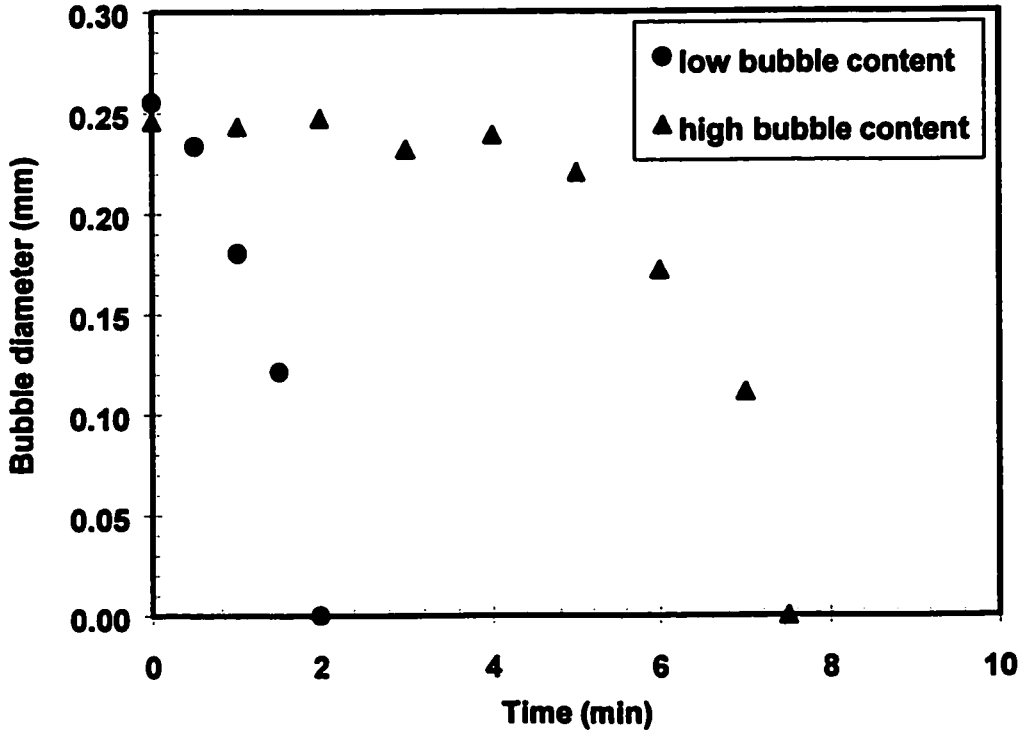

Figure 6.12: Bubble dissolution curves for low and high bubble concentrations in PE-2 at 190°C

two periods is illustrated in Figure 6.13, for the same bubble shown in Figure 6.12. The possibility that the abrupt change in slope is due to polymer degradation was examined by performing TGA on the PE-2 resin used in the bubble dissolution experiments. No evidence of degradation was found when the polymer was held at a constant temperature of 190°C for a period of 150 minutes, which is considerably longer than the duration of the experiment.

It is speculated that the initial period observed in Figure 6.13 is associated with interaction between neighbouring bubbles which can result in the transfer of air from one bubble to another. From the visual inspection of the dissolution of the bubble under consideration, it was seen that the change in the slope of the dissolution curve was associated with the disappearance of the smaller bubbles surrounding it. The point where the bubble remained eventually isolated coincides with the change of slope. This is demonstrated better in Figure 6.14, which shows the simultaneous dissolution curves of two neighbouring bubbles. Once the smaller bubble disappears, there is an obvious instantaneous increase in the diameter of the bigger bubble, which subsequently dissolves at a faster rate.

In addition, it is expected that due to the presence of lots of bubbles diffusing simultaneously the melt becomes almost saturated, thus reducing the concentration difference and the driving force for dissolution. In the case of interacting bubbles the model can be applied successfully only for the second region, which coincides with the disappearance of the surrounding bubbles, as shown in Figure 6.13. A value $c_i = 0.974\ (c_i)_{sat}$ was used to fit the second region

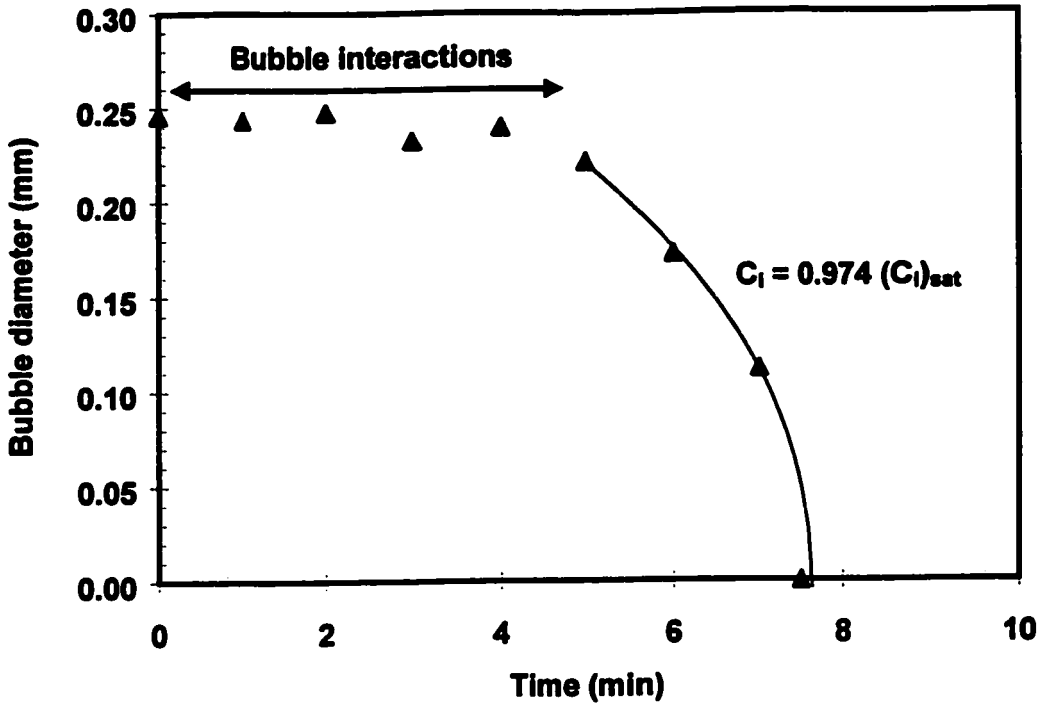

Figure 6.13: Regions observed during the dissolution of a typical air bubble in PE-2 for high bubble concentrations.

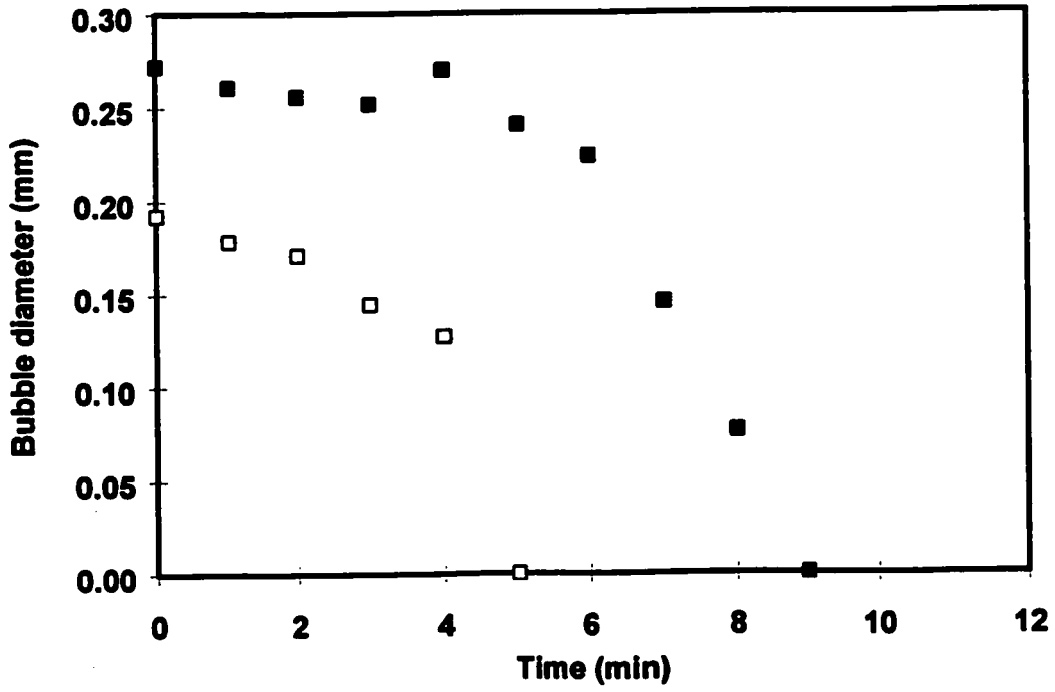

Figure 6.14: Simultaneous dissolution of two neighbouring bubbles in PE-2

in Figure 6.13.

From the above it becomes clear that high overall bubble contents in the melt result in slower bubble dissolution rates.

When the melt viscosity is higher more and larger bubbles form initially upon melting of the powder, as explained in Chapter 5. This is one of the causes for the longer times needed for complete dissolution of bubbles observed in practice.

The experimental results confirmed the importance of the initial bubble size. Small bubbles tend to dissolve quickly, while big ones may not dissolve at all during the experiment. This effect can be clearly seen in Figure 6.11 and it is consistent with model predictions.

6.4. Densification model based on diffusion

The work presented in chapter 5 demonstrated that models based solely on surface tension and viscosity cannot describe adequately the latest stages of densification in polymer melts, which involve pore closing (or bubble removal). In this chapter it was found that diffusion of air from the bubble to the polymer melt should be taken into account. The applicability of a model based on this concept has been demonstrated. After the validation of the bubble dissolution model the next task was to use this model towards making predictions of density variation as a function of time at the late stages of densification. The ultimate goal is to use these results in conjunction with the predictions of Scherer's open pores model, to build an overall densification model.

6.4.1. The cell concept

The predictions of the dissolution model are given in terms of bubble radius versus time. However, in order to derive a model describing densification, the values of radius must be converted to densities. The problem is to deduce the properties of the equivalent homogeneous material from the properties of the real material and the number and the size of the pores. Mackenzie and Shuttleworth (1949) proposed a method, which is valid when the volume of the pores is sufficiently small compared with the volume of the material. Every pore, or bubble, with radius R is surrounded by a spherical cell of the real incompressible material, of radius R_{cell} (Figure 6.15). The material outside the spherical cell (including the pores it contains) is replaced by an equivalent continuum. It is assumed that the equivalent continuum is not affected by the presence of the pore and its surrounding shell. The pressure at the outer boundary of the shell is assumed to be equal to the applied pressure to the system (ambient pressure for the present problem).

To relate the stresses within the fluid to the gas pressure inside the bubble and the applied pressure at the outer boundary of the shell, the conservation of momentum equation (equation 6-3) will now be integrated along the radial direction from the bubble surface to the outer boundary of the shell:

$$P(R) - P(R_{cell}) + \tau_{rr}(R_{cell}) - \tau_{rr}(R) + 2\int_{R}^{Rcell} \frac{\tau_{rr} - \tau_{\theta\theta}}{r}\, dr = 0 \qquad (6\text{-}24)$$

The total normal stress at the outer boundary of the shell is assumed to be

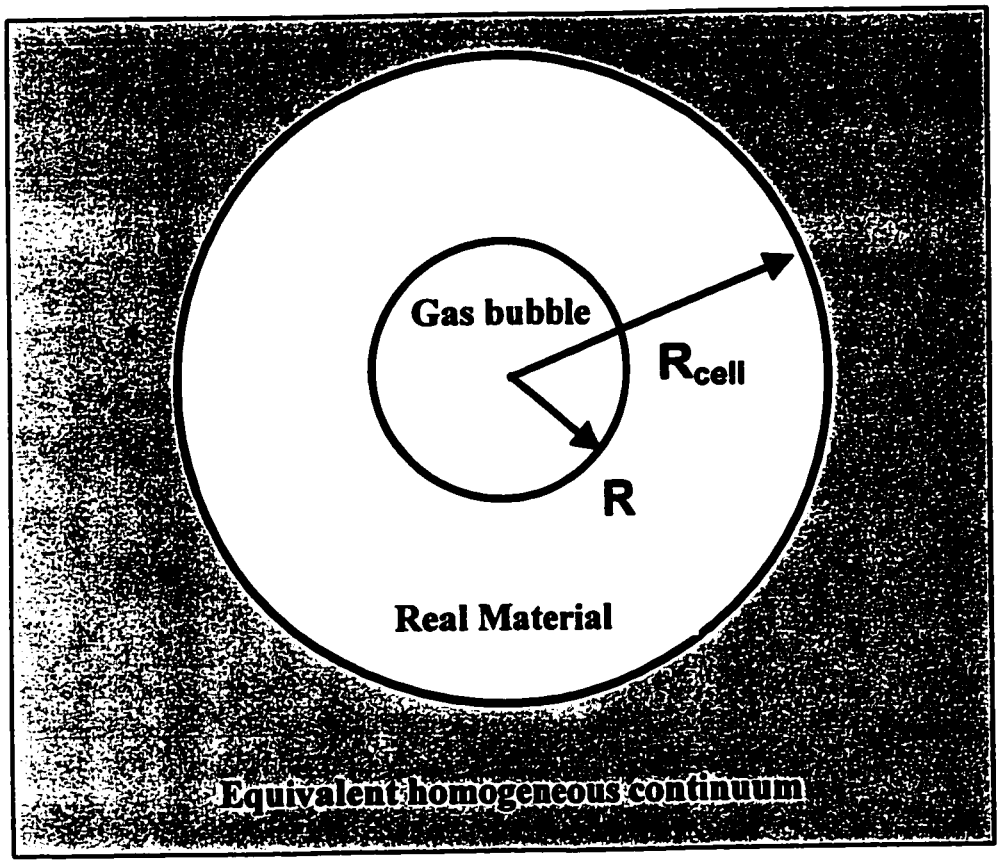

Figure 6.15: Bubble of radius R surrounded by a spherical cell of radius R_{cell}

equal to the applied (ambient pressure), P_f (Arefmanesh and Advani, 1991).

Combining equation (6-24) with the aid of the force balance at the bubble-liquid interface, (equation 6-6) gives:

$$P_g - P_f - \frac{2\sigma}{R} + 2\int_{R}^{R_{cell}} \frac{\tau_{rr} - \tau_{\theta\theta}}{r} dr = 0 \qquad (6\text{-}25)$$

Equation (6-25) is solved instead of equation (6-7) whenever the cell model is applied and a prediction of bubble radius versus time is obtained, using the procedure described in section 6.2.3.

The density ρ of the whole compact (represented by the cell in Figure 6.15) relative to the density ρ_S of the real, fully densified material can be found for every time step from:

$$\frac{\rho}{\rho_S} = \frac{V_S}{V_{cell}} = \frac{4/3\,\pi\,(R_{cell}^3 - R^3)}{4/3\,\pi\,R_{cell}^3}$$

or (6-26)

$$\frac{\rho}{\rho_S} = 1 - \left(\frac{R}{R_{cell}}\right)^3$$

The radius, R_o, of the bubbles formed initially inside the melt and the initial radius of the cell, $R_{cell,o}$, corresponding to the density ρ_o of the compact when closed pores form, can be either estimated by the methods outlined in section 5.3.3 of Chapter 5 or determined experimentally. In order to apply the bubble dissolution model, the initial bubble radius, R_o, which corresponds to t=0 is used to solve the equations for bubble dissolution. For the next time step, Δt, a new value of R(t) is found by solving the equations describing bubble dissolution.

After the value of R has been updated, a new value of $R(t)_{cell}$ must be determined. If the mass and volume of polymer within the cell (Figure 6.15) are assumed to be constant, for every time step t a new value of R_{cell} can be found from:

$$[R(t)]^3_{cell} = R^3_{cell,o} - R_o^3 + [R(t)]^3 \qquad (6\text{-}27)$$

Substitution of the values R(t) determined from the dissolution model and $R(t)_{cell}$ found from equation (6-27) into equation (6-26) results in the calculation of a new density value $\rho(t)$.

6.4.2. Comparison of model with experimental data

The applicability of the diffusion based densification model described above will be demonstrated by using the same example of the densification of a PE copolymer (EVA-2) at a temperature of 105°C, used in Chapter 5, section 5.3.4. In section 5.3.4 it was seen that the MS model for closed pores was inappropriate for the description of the densification process after the point where Scherer's models fail at ρ/ρ_S=0.942 (see also Figure 5.37). In this section the diffusion model has been used to predict the densification process beyond this point. As a first approach, the value of the initial radius, R_o, estimated in section 5.3.5 was used. From Table 5.7, it can be seen that $R_o = 1.55\ 10^{-4}$m. The radius of the cell determined from equation (5-17) was $R_{cell,o} = 4\ 10^{-4}$ m (see also Appendix 5.B).

Values of surface tension can be estimated at 105°C by using data from Wu (1995). According to Wu the value of surface tension for EVA with 17%

vinyl-acetate content is 0.0355 N/m at 20°C and $-d\sigma/dT = 6.7\ 10^{-5}$ N/(m °C). Substitution of these data into equation (6-20) gives at 105°C a value of σ = 0.0295 N/m. Unfortunately there are no data available in the literature for the diffusion coefficient and Henry's law constant for air in an EVA melt. Due to the lack of data, the values applicable for the PE melt, shown in Table 6.1 were used. These values were corrected to account for temperature using equations (6-18) and (6-19), as explained in section 6.1.4. Finally the value of zero shear viscosity of EVA-2 at 105°C is 16900 Pa-s (see also Figure 4.4). A summary of the values of the physical constants used in the simulation is given in Table 6.2.

Table 6.2: Numerical values of physical properties of EVA-2 at 105°C

Physical Property	Value
Diffusion coefficient, m^2/s	$5.26\ 10^{-9}$
Henry's law constant, $mol/(m^3Pa)$	$3.05\ 10^{-5}$
Surface tension, N/m	0.0295
Zero shear viscosity, Pa-s	16900

By inserting these values in the bubble dissolution model, the dissolution curve of a bubble of initial radius $R_o = 1.55\ 10^{-4}$ m corresponding to initial diameter d_o = 0.31 mm, was obtained as shown in Figure 6.16. The same figure shows how the relative density ρ/ρ_S of the cell surrounding the bubble varies as a

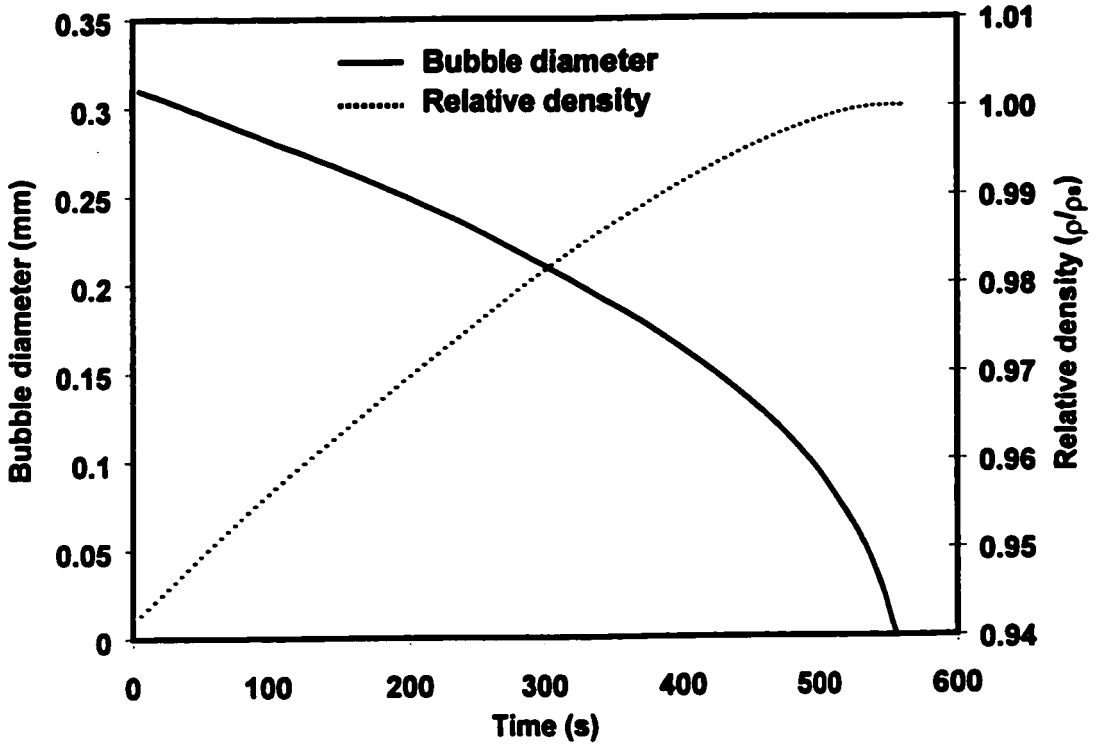

Figure 6.16: Dissolution curve and respective densification curve of cell

function of time, as the bubble dissolves.

The complete prediction of densification obtained by combining the dissolution model with Scherer's open pores model is presented in dimensionless terms in Figure 6.17.

A better fit than that shown in Figure 6.17 can be obtained by considering that Scherer's open pores model breaks down earlier than the predicted by the model point where $\rho/\rho_S=0.942$, as explained in section 5.3.3. By inspection of the experimental data for EVA-2 it was determined that in reality the formation of round bubbles and subsequently the onset of the diffusion-controlled stage begins earlier, at approximately $\rho/\rho_S=0.9$, which corresponds to t = 205 s. In addition, according to the experimental data the average diameter of the bubbles formed inside an EVA-2 melt is 0.18 mm (see also Table 5.4). Substitution of the average bubble diameter, corresponding to $R=9\ 10^{-5}$ m and the density ratio $\rho/\rho_S=0.9$ to equation (6-26) provided an estimate of $R_{cell}=1.94\ 10^{-4}$ m. By using these initial values in the dissolution model, combined with the numerical values of the parameters shown in Table 6.2, the result demonstrated in Figure 6.18 was obtained.

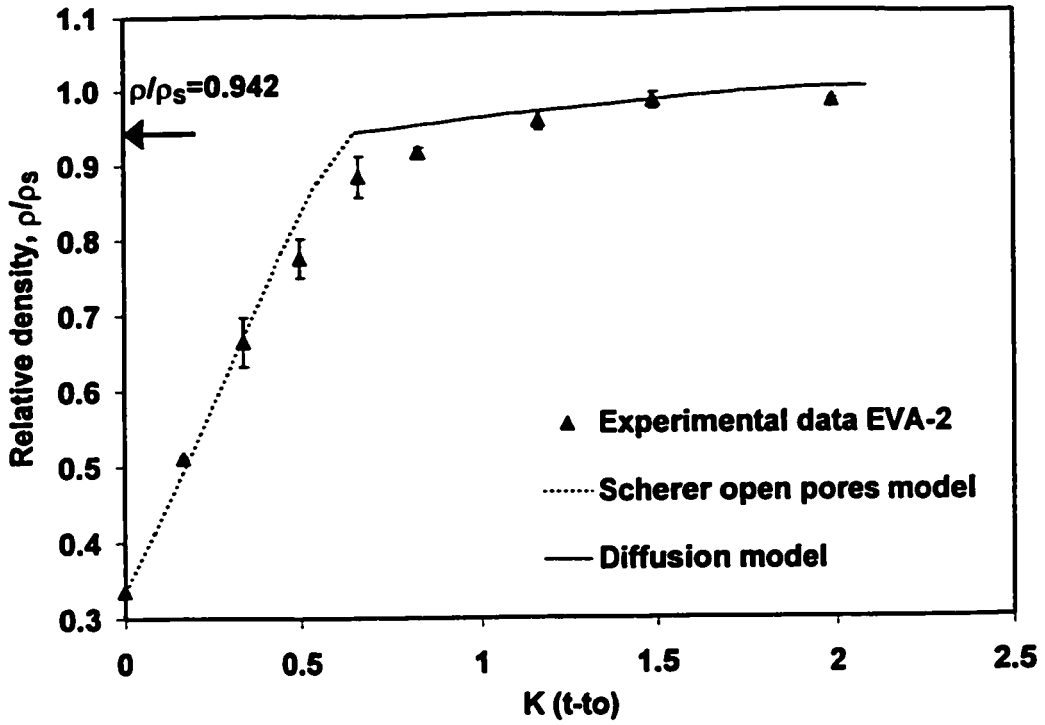

Figure 6.17: Prediction of densification in dimensionless terms by combining Scherer's open pores model and dissolution model. Data for EVA-2, at 105°C.

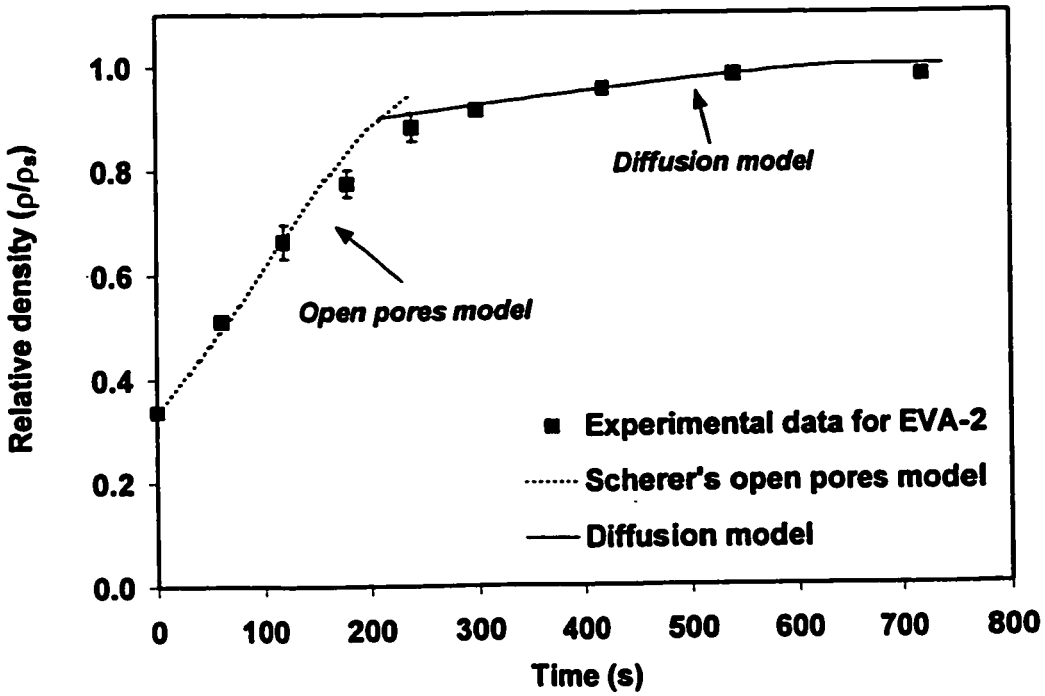

Figure 6.18: Prediction of densification by combining Scherer's open pores model and dissolution model. Data for EVA-2, at 105°C. Onset of diffusion stage and initial bubble diameter estimated based on experimental data.

6.5. Conclusions

A model which includes diffusion, surface tension and viscosity effects, has been applied, in an effort to describe bubble dissolution in polymer melts. It was concluded that the process is controlled by the diffusion of air from the bubbles to the melt. Bubble dissolution depends significantly on initial bubble size, surface tension and air concentration in the polymer melt. In addition the proposed model predicts that application of pressure after the formation of the melt results in significant acceleration of the rate of bubble dissolution.

Bubble dissolution experiments confirmed model predictions for relatively isolated bubbles. In the case of high initial bubble contents in the polymer melt, dissolution was delayed considerably and two distinct regions were observed: an initial period, where dissolution is very slow due to interactions between bubbles, followed by a fast dissolution period, associated to the disappearance of surrounding bubbles. These results reveal that one of the most important factors governing the bubble dissolution process is the bubble content initially present in the polymer melt.

The proposed model has been used successfully to make predictions of the densification process, starting from the point where closed pores form. It can be concluded that the dissolution model can be used in conjunction with Scherer's open pores model to describe the overall densification of a polymer melt.

6.6. Nomenclature for Chapter 6

c	Concentration (mol/m^3)
c_g	Concentration of gas inside bubble (mol/m^3)
c_i	Concentration of gas in bulk of polymer melt (mol/m^3)
$(c_i)_{sat}$	Saturation concentration of gas in bulk of polymer melt (mol/m^3)
c_w	Concentration of gas at bubble-liquid interface (mol/m^3)
D	Diffusion coefficient (m^2/s)
D_o	Diffusion coefficient (m^2/s) at reference temperature T_o
d_o	Initial bubble diameter (mm)
E_d	Activation energy for diffusion coefficient (J/mol)
E_S	Heat of solution (J/mol)
K_h	Henry's law constant (mol/(m^3 Pa))
K_{ho}	Henry's law constant (mol/(m^3 Pa)) at reference temperature T_o
r	Radial coordinate
R	Bubble radius (m)
R_{cell}	Radius of spherical cell surrounding bubble (m)
$\dot{R}$	Bubble shrinkage rate (m/s)
R_g	Universal gas constant (8.3143 Pa m^3 mol^{-1} K^{-1})
P	Pressure (Pa)
P_f	Pressure in bulk of polymer melt (Pa)
P_g	Gas pressure inside bubble (Pa)
t	Time (s)
T	Temperature (K)
U	Fluid velocity (m/s)
V	Bubble volume (m^3)
V_{cell}	Cell volume (m^3)
V_S	Volume of real material (m^3)

Greek symbols

Δ_{ij} ij-th components of the rate of deformation tensor (s^{-1})

η Viscosity (Pa s)

ρ Density (kg/m^3)

ρ_o Density of the compact when closed pores form (kg/m^3)

ρ_S Density of real, fully densified material (kg/m^3)

σ Surface tension (N/m)

σ_o Surface tension (N/m) at reference temperature T_o

τ_{ij} ij-th components of stress tensor (Pa)

Subscripts, superscripts

G Gas

L Liquid

Chapter 7

CONCLUSIONS, CONTRIBUTIONS AND RECOMMENDATIONS

7.1. Conclusions

A comparative study of the processing characteristics of various polymers, including polyethylene, various polyethylene copolymers, polycarbonate and polypropylene/ polyethylene copolymers revealed that polyethylene based polymers offer better toughness, while polypropylenes offer better stiffness. Introduction of comonomers can alter the properties of the original polymers favorably. However it can also result in processing difficulties, narrower processing windows and presence of bubbles in rotomolded parts. The occurrence of excessive amounts of bubbles which are hard to remove has been mostly encountered in polymers with high amorphous contents and low crystallinities. Rheological characterization suggested that these types of polymers appear to exhibit weak viscosity dependence on temperature and higher melt elasticities.

Experiments on the melting behavior of several rotational molding grade polyolefin resins demonstrated that densification of polymer melts during the early stages is profoundly influenced by rheology, thermal and powder properties. High melt viscosities favor low particle coalescence rates and result in the formation of more bubbles and in slower overall densification rates. The variation

of viscosity with temperature is of great importance as well. Especially in the case of polymers with very low crystallinity, such as ethylene based copolymers, viscosity decreases gradually starting from very high values. Because of the low melting points, the powder particles stick together very early in the process, when viscosity is very high, forming a three dimensional network. Bubbles are trapped during this period and subsequently take long times to dissolve resulting in slow densification rates. On the other hand, typical semi-crystalline polyethylene particles seem to coalesce very fast upon melting, thus forming a homogeneous melt layer by layer. It is thus suggested that the densification process is characterized by a competition between rate of melting and ease of flow of the polymer: Low melting points, combined with high viscosities at temperatures just above the melting point, result in low coalescence rates and in the subsequent entrapment of large amounts of bubbles.

It was also demonstrated that polyethylenes and polyethylene plastomers with narrow molecular weight distribution, made by metallocene catalysts may prove beneficial, because of faster sintering rates and the subsequent formation of less bubbles than polyethylenes of similar melt flow index made by conventional catalysts. In terms of rheology, these metallocene made polyethylenes display lower melt elasticities and narrower relaxation spectra, because of uniformity in the chain structure.

In the case of impact modified PP/PE copolymers with similar viscosities, the coalescence of particles was delayed and significantly higher amounts of

bubbles were formed when the resins had higher rubber contents. Rheological measurements demonstrated that increased rubber contents also result in higher melt elasticity.

Powder particle size and particle shape were seen to affect significantly the process of bubble formation, as well. The most important requirement for a relatively bubble free part seems to be the presence of regularly shaped particles.

Scherer's open pores models for the densification of three-dimensional powder compacts, which consider the evolution of density as a function of viscosity, surface tension and powder properties, can describe successfully the trends observed for low crystallinity / low melting point polymers. A modification of Scherer's model to take into account the deposition in layers occurring in semi-crystalline polymers can describe qualitatively the data for polyethylenes and polypropylenes. It was found that these models are valid until the point where closed pores, or bubbles form.

A model which includes diffusion, surface tension and viscosity effects, has been applied, in an effort to describe the final stage of bubble dissolution in polymer melts. It was concluded that the process is controlled by the diffusion of air from the bubbles to the melt. Bubble dissolution depends significantly on initial bubble size, surface tension and air concentration in the polymer melt. The application of pressure after the formation of the melt results in significant acceleration of the rate of bubble dissolution. The interaction between neighbouring bubbles, manifested as transfer of air from one bubble to another, is

also an important phenomenon when very high amounts of bubbles exist in the melt, because it results in a significant delay of the overall removal of bubbles.

The proposed model has been used successfully to make predictions of the densification process, starting from the point where closed pores form. It can be concluded that the dissolution model can be used in conjunction with Scherer's open pores model to describe the overall densification of a polymer melt.

Rheology, which is influenced by the structural characteristics of the polymers, is closely related to processing behaviour and knowledge of the rheological characteristics of the resins can contribute towards an a priori understanding of how they behave during processing. The quick rheological characterization methods suggested in this work, such as the determination of the Relaxation spectrum index (RSI) or the measurement of dynamic moduli and tanδ, can help in the estimation of the processing behavior of the polymers beforehand. In general wide relaxation spectra and higher melt elasticities have been associated to the appearance of more bubbles and longer cycle time requirements.

7.2. Summary of contributions

As part of the present research work several contributions, summarized below, were made for the first time. Nearly all of these contributions, besides their theoretical significance are also expected to have considerable practical importance in the rotomolding industry.

- A detailed evaluation of the effect of material properties and structure of polymers on the rotomolded part properties has been made.
- The important material parameters in bubble formation have been identified. The importance of temperature dependence of viscosity has been demonstrated.
- A rigorous model for the description of bubble dissolution in polymer melts has been proposed.
- The effect of increased pressure on bubble dissolution has been explained.
- The mechanisms involved in polymer densification have been elucidated and two stages were identified: The early stage is governed by viscous and surface tension forces. Diffusion is the controlling mechanism during the final stage.
- Suitable models for the overall densification process have been applied. These models can be used as a springboard for further research developments in this area, such as inclusion of temperature, pressure and viscoelastic effects.
- A methodology was proposed, which has a potential for use in the identification of suitable rotomolding resins through dynamic oscillatory rheological measurements.

7.3. Recommendations for future work

The densification models proposed in this work have been applied only for isothermal conditions, using constant values of material properties. However, since rotational molding is transient in nature, temperature profiles exist in reality

throughout the powder bed and the molten polymer, and the material passes from a solid state to a melt state. Thus the proposed densification models should be solved simultaneously with the heat transfer problem, in order to efficiently predict the effect of molding and material properties on the molding cycle and the molded part porosity.

The bubble dissolution model could be improved by taking into account the presence of several neighbouring simultaneously diffusing bubbles.

Sintering of powders which have been pre-compacted by using pressure is encountered frequently in the ceramics processing, as well as in the processing of some polymers, such as polycarbonate. It would be of interest to examine experimentally and theoretically the effect of the application of pressure in the initial stages of sintering and its potential for application on rotational molding.

On the materials front, an extensive investigation is needed on the rotomoldability of polyolefins made by metallocene catalysts. A comparison of several resins with similar viscous but different viscoelastic characteristics could clearly prove useful in the elucidation of the role of viscoelasticity. Another subject which has not received any attention until now, but could offer tremendous potential is the development of polyolefin blends suitable for rotational molding.

References

Anon. (1967), "New rotomolding material - polystyrene", Modern Plastics, 45 (10), pp. 98-99.

Anon. (1968 (a)), "Big push starts in powder rotomolding", Modern Plastics, 45 (3), pp. 64-68.

Anon. (1968 (b)), "Where's the action in ABS?", Modern Plastics, 45 (2), pp. 79-83.

Anon. (1976), "Rotomolding: in the brink of something big", Modern Plastics, 53 (9), pp. 69-71.

Anon. (1980), "Now, clear PC rotomolded parts", Modern Plastics, 57 (11), pp. 46-47.

Anon. (May 1993), "Co-Rotomolding joins Nylon and HDPE", Plastics Technology, pp. 20-23.

Anon. (1997), "Metallocene PEs could put a new spin on rotomolding", Modern Plastics 74 (2), pp. 30-33.

Arefmanesh, A. and Advani, S.G. (1991), "Diffusion-induced growth of a gas bubble in a viscoelastic fluid", Rheol. Acta, 30 (3), pp. 274-283.

Arefmanesh, A. and Advani, S.G. (1995), "Non-isothermal bubble growth in polymeric foams", Polym. Eng. Sci., 35 (3), pp. 252-260.

Barlow, E.G. and Langlois, W.E. (1962), "Diffusion of gas from a liquid into an expanding bubble", IBM J. Res. Dev., 6, pp. 329-337.

Baumgärtel, M. and Winter, H.H. (1989), "Determination of discrete relaxation and retardation time spectra from dynamic mechanical data", Rheol. Acta, 28 (6), pp. 511-519.

Baumgärtel, M. and Winter, H.H. (1992), "Interrelation between continuous and discrete relaxation time spectra", J. Non-Newtonian Fluid Mech., 44, pp. 15-36.

Baumgärtel, M., Soskey, P.R. and Winter, H.H. (1994), "Iris 5: Innovative rheological interface software", User's Manual, IRIS Development, Amherst, MA., USA.

Bawiskar, S. and White, J.L., (1995) "Simulation of heat transfer and melting in rotational molding", Int. Polym. Process., 10 (1), pp. 62-67.

Beall, G.L. (1998), "Rotational molding. Design, materials, tooling and processing", Hanser, Munich.

Bellehumeur, C.T. (1997), "Polymer sintering and its role in rotational molding", Ph.D. Thesis, McMaster University.

Bellehumeur, C.T., Bisaria, M. and Vlachopoulos, J. (1996), "An experimental study and model assessment of polymer sintering", Polym. Eng. Sci., 36 (17), pp. 2198-2207.

Bellehumeur, C.T., Kontopoulou, M. and Vlachopoulos, J. (1998), "The role of viscoelasticity in polymer sintering", Rheol. Acta ,37 (3), pp. 270-278.

Bird, R.B., Stewart, W.E. and Lightfoot, E.N. (1960), "Transport Phenomena", Wiley, New York.

Bisaria, M.K., Takács, E., Bellehumeur, C.T. and Vlachopoulos, J. (1994), "Anatomy of a rotomolding cycle", Rotation 3 (4), pp. 12-18.

Cable, M. and Evans, D.J. (1967), "Spherically symmetrical diffusion-controlled growth or dissolution of a sphere", J. Appl. Phys., 38 (7), pp. 2899-2906.

Carreau, P.J., Bousmina, M. and Ajji, A. (1994), "Rheological properties of blends: Facts and challenges" in Progress in Pacific Polymer Science 3, K.P. Ghiggino Ed., Springer-Verlag, New York, 25-40.

Chen, C.H., White, J.L. and Ohta, Y. (1990), "Mold pressurization as a method to reduce warpage in rotational molding of polyethylene", Polym. Eng. Sci., 30 (23), pp. 1523-1527.

Chung, C.I. and Lin, M.I. (1978), "Nature of melt rheological transition in a styrene-butadiene-styrene block copolymer", J. Polym. Sci.: Polym. Phys., 16, 545-553.

Cramez, M.C., Oliveira, M.J. and Crawford, R.J. (1998), "Effect of pigmentation on the microstructure and properties of rotationally moulded polyethylene", 7 (2), pp. 18-21.

Crank, J. and Park, G.S. (1968), "Diffusion in polymers", Academic Press, New York.

Crawford, R.J. (1992), "Introduction to rotational moulding" in Rotational moulding of plastics", R.J. Crawford (ed.), Wiley, New York., pp. 1-24.

Crawford, R.J. and Nugent, P.J. (1989), "Computer simulation of the rotational moulding process for plastics", Plast. Rubber Process. Appl., 11 (2), pp. 107-124.

Crawford, R.J. and Nugent, P.J. (1992a), "Impact strength of rotationally moulded polyethylene articles", Plast. Rubber Compos. Process. Appl., 17 (1), 33-41.

Crawford, R.J. and Nugent, P.J. (1992b), "A new process control system for rotational moulding", Plast. Rubber Compos. Process. Appl., 17 (1), pp. 23-31.

Crawford, R.J. and Scott, J.A. (1985), "An experimental study of heat transfer during rotational molding of plastics", Plast. Rubber Process Appl., 5, pp. 239-248.

Crawford, R.J. and Scott, J.A. (1987), "The formation and removal of gas bubbles in a rotational moulding grade of PE", Plast. Rubber Process Appl., 7 (2), pp. 85-99.

Crawford, R.J. and Spence, A.G. (1996), "The effect of processing variables on the formation and removal of bubbles in rotationally molded products", Polym. Eng. Sci., 36 (7), pp. 993-1009.

Crawford, R.J., Nugent, P.J, and Xin, W. (1991), "Prediction of optimum process conditions for rotomolded parts, Int. Polym. Process., 6 (1), pp. 56-60.

Dodge, P.T. (1999), "Polypropylene: An alternate material in rotational molding", Proc. SPE/11th Int. Conf. on Polyolefins, Houston, TX, pp. 451-463.

Doremus, R.H. (1960), "Diffusion of oxygen from contracting bubbles in molten glass", J. Amer. Ceram. Soc., 43 (12), pp. 655-661.

Durrill, P.L. and Griskey, R.G. (1969), "Diffusion and solution of gases into thermally softened or molten polymers: Part II. Relation of diffusivities and solubilities with temperature pressure and structural characteristics", AIChE J., 15 (1), pp. 106-110.

Epstein, P.S. and Plesset, M.S. (1950), "On the stability of gas bubbles in liquid-gas solutions", J. Chem. Phys., 18 (11), pp. 1505-1509.

Eshelby, J.D. (1949), discussion in paper by Shaler AJ: "Seminar on the kinetics of sintering", J. Metals 1 (12); Metals Transactions 185, p. 806.

Exner, H.E. and Petzow, G. (1975), "Shrinkage and rearrangement during sintering of glass spheres", in Sintering and Catalysis, Ed. G.C. Kuczynski, Plenum Press, NY.

Fatnes, A.M. (1999), "Benefits to be realised through process optimisation of new generation PE", Proc. ARM Spring meeting, Barcelona, Spain, pp. 81-83.

Ferry, J.D. (1980), "Viscoelastic properties of polymers", 3rd Ed., Wiley, 1980.

Fogler, H.S. and Goddard, J.D (1970), "Collapse of spherical cavities in viscoelastic fluids", Phys. Fluids, 13 (5) , pp. 1135-1141.

Foster, W.E. (1970), "Need a tough rotomolded part? Now you can rotomold polycarbonate", Plastics Technology, 16 (12), pp. 47-48.

Frenkel, J. (1945), "Viscous flow of crystalline bodies under the action of surface tension", J. Phys., 9 (5), pp. 385-391.

Gala Industries (1995), "Micropellets-An alternative rotomolding product form", Rotation, 4 (4), pp. 9-12.

Gogos, G., Olson, L.G., Liu, X. and Pasham, V.R. (1998), "New models for rotational molding of plastics", Polym. Eng. Sci., 38 (9), pp. 1387-1398.

Gogos, G., Liu, X., and Olson, L.G. (1999), "Cycle time predictions for the rotational molding process with and without mold/part separation", Polym. Eng. Sci., 39 (4), pp. 617-629.

Gouinlock, E.V. and Porter, R.S. (1977), "Linear dynamic mechanical properties of an SBS block copolymer", Polym. Eng. Sci., 17 (8) 535-543.

Grassley, W.W. (1984), "Viscoelasticity and flow in polymer melts and concentrated solutions", in Phycisal properties of polymers, Americal Chemical Society, Washington, D.C.

Greene, C.H. and Gaffney, R.F. (1959), "Apparatus for measuring the rate of absorption of a bubble in glass", J. Amer. Ceram. Soc., 42 (6), pp. 271-275.

Griskey, R.G. (1995), "Polymer Process Engineering", Chapman & Hall, New York.

Han, C.D. and Yoo, H.J. (1981), "Studies on structural foam processing. IV. Bubble growth during mold filling", Polym. Eng. Sci., 21 (9), pp. 518-533.

Harkin-Jones, E. and Crawford, R.J. (1996a), "Rotational molding of liquid plastic systems: An assessment of material moldability", Adv. Polym. Technol., 15 (1), pp. 71-100.

Harkin-Jones, E. and Crawford, R.J. (1996b), "Mechanical properties of rotationally molded Nyrim", Polym. Eng. Sci., 36 (5), pp. 615-625.

Hopper, R.W. (1984), "Coalescence of two equal cylinders: Exact results for creeping viscous plane flow driven by capillarity", J. Am. Ceram. Soc. (Communications), 67 (12), pp. C262-C264.

Hornsby, P.R. and Maxwell, A.S. (1992), "Mechanism of sintering between polypropylene beads", J. Mat. Sci., 27, pp. 2525-2533.

Jagota, A. and Dawson, P.R. (1988a), "Micromechanical modeling of powder compact – I. Unit problems for sintering and traction induced deformation", Acta Metal., 36 (9), pp. 2551-2562.

Jagota, A. and Dawson, P.R. (1988b), "Micromechanical modeling of powder compact – II. Truss formulation of discrete packings", Acta Metal., 36 (9), pp. 2563-2573.

Jagota, A. and Dawson, P.R. (1990), "Simulation of the viscous sintering of two particles", J. Am. Ceram. Soc., 73, pp. 173-177.

Jagota, A., Mikeska, K.R. and Bordia, R.K. (1990), "Isotropic constitutive model for sintering particle packings", J. Am. Ceram. Soc., 73 (8), pp. 2266-2273.

Jagota, A. and Scherer, G.W. (1993), "Viscosities and sintering rates of a two-dimensional granular composite", J. Am. Ceram. Soc. 76 (12), pp. 3123-3135.

Jagota, A. and Scherer, G.W. (1995), "Viscosities and sintering rates of composite packings of spheres", J. Am. Ceram. Soc. 78 (3), pp. 521-528.

Jog, J.P. (1993), "Solid state processing of polymers: A review", Adv. Polym. Technol., 12 (3), pp. 281-289.

Kandis, M. and Bergman, T.L. (1997), "Observation, prediction and correlation of geometric shape evolution induced by non-isothermal sintering of polymer powder", J. Heat Transfer (Transactions of the ASME), 119, pp. 824-831.

Kazatchkov, I.B., Bohnet, N., Goyal, S.K. and Hatzikiriakos, S.G. (1999), "Influence of molecular structure on the rheological and processing behavior of polyethylene resins", Polym. Eng. Sci., 39 (4), pp. 804-815.

Kelly, P.Y. (undated), "A microscopic examination of rotomoulded polyethylene", Du Pont Canada.

Khakhar, D.V., McCarthy, J.J., Shinbrot, T. and Ottino, J.M. (1997), "Transverse flow and mixing of granular materials in a rotating cylinder", Phys. Fluids, 9 (1), pp. 31-43.

Kliene, R.I. (1992), "Rotational moulding of polyethylene" in Rotational moulding of plastics, R.J. Crawford (ed.), Wiley, New York, pp. 27-55.

Kontopoulou, M. (1995), "A study of the parameters involved in the rotational molding of plastics", M.Eng. thesis, McMaster University.

Kontopoulou, M., Bisaria, M. and Vlachopoulos, J. (1997), "An experimental study of rotational molding of Polypropylene / Polyethylene copolymers", Int. Polym. Process., 12 (2), 165-173.

Kontopoulou, M., Takács, E. and Vlachopoulos, J. (1998), "Resins for rotomolding: Considering the options", Plastics Engineering, 54 (2), 29-31.

Kontopoulou, M., Takács, E. and Vlachopoulos, J. (1999), "Particle coalescence and densification in rotational molding", in Innovations in rotational molding in the year 2000 and beyond, Proc. SPE/RETEC, Strongsville OH, pp. 7-12.

Kramer, F. (1985), "Mathematical Models of Bubbles Growth and Dissolution in Glass Melts", in Gas Bubbles in Glass, International Commission on Glass, Belgium.

Kuczynski, G.C. (1949), "Study of sintering of glass", J. Appl. Phys., 20, pp. 1160-1163.

Kuczynski, G.C. and Zaplatynskyj, I. (1956), "Sintering of Glass", J. Am. Ceram. Soc., 39, pp. 349-350.

Kuczynski, G.C., Neuville, B. and Toner, H.P. (1970), "Study of sintering of polymethyl methacrylate", J. Appl. Polym. Sci., 14, pp. 2069-2077.

Lacroix, C. Aressy, M. and Carreau P.J. (1997), "Linear viscoelastic behavior of molten polymer blends: A comparative study of the Palierne and Lee and Park models", Rheol. Acta, 36, pp. 416-428.

Liu, G., Park, C.B. and Lefas, J.A. (1998), "Production of low-density LLDPE foams in rotational molding", Polym. Eng. Sci., 38 (12), pp. 1997-2009.

Liu, S.-J. (1996), "A study of the sintering behavior of polyethylene", Rotation, 5 (4), pp. 20-31.

Liu, S.-J., Chiou, Y.H. and Lin, S.T. (1996), "Study of sintering behavior of polyethylene", Proc. SPE/ANTEC, Indianapolis, pp. 1676-1680.

Liu, S.-J. and Tsai, C.-H. (1998), "An experimental study of foamed polyethylene in rotational molding", Proc. SPE/ANTEC, Atlanta, GA., pp. 1161-1165.

Long, P.K. (1989), "Polycarbonate - Do's and Don'ts", presented in ARM meeting.

Lontz, J.F. (1964), "Sintering of polymer materials", in Fundamental Phenomena in the Material Sciences, Vol. 1, Bonis and Hausner ed., Plenum Press.

Loti, D. and Howerter, R. (1999), "Rotational molding with crosslinkable metallocene-based high density polyethylene", Proc. SPE/11th Int. Conf. on Polyolefins, Houston, TX, pp. 429-438.

Mack, M. and Voigt, J. (1999), "Trends in underwater pelletizer technology: Considering new types of polyolefin resins", Proc. SPE/11th Int. Conf. On Polyolefins, Houston, TX, pp. 216-220.

Mackenzie, J. K. and Shuttleworth, R. (1949), "A phenomenological theory of sintering", Proc. Phys. Soc. (London), 62, pp. 833-852.

Macosko C.W. (1994), "Rheology principles, measurements and applications", VCH Publishers, Weinheim.

Mark, H.F. (Ed.) (1990), "Encyclopedia of Polymer Science and Engineering", Vol. 4, 2nd Ed., Wiley, New York, p. 487.

Martinez-Herrera, J.I. and Derby, J.J. (1994), "Analysis of capillary-driven viscous flows during the sintering of ceramic powders", AIChE J., 40 (11), pp. 1794-1802.

Mathot, V.B.F. (1994), "Calorimetry and thermal analysis of polymers", Hanser, New York.

Mazur, S. (1995), "Coalescence of polymer particles", in Polymer powder technology, M. Narkis and N. Rosenzweig (eds), John Wiley & Sons, New York, pp. 157-216.

Mazur, S. and Plazek, D.J. (1994), "Viscoelastic effects in the coalescence of polymer particles", Progr. Org. Coat., 24, pp. 225-236.

McCarthy, J.J., Shinbrot, T., Metcalfe, G., Wold, J.E. and Ottino, J.M. (1996), "Mixing of granular materials in slowly rotated cylinders", AIChE J., 42 (12), pp. 3351-3363.

Middleman, S. (1977), "Fundamentals of Polymer Processing", McGraw-Hill, New York.

Monrabal, B. (1994), "Crystallization analysis fractionation: A new technique for the analysis of branching distribution in polyolefins", J. App. Polym. Sci., 52, 491-499.

Monrabal, B. (1996), "CRYSTAF: Crystallization analysis fractionation. A new approach to the composition analysis of semicrystalline polymers", Macromol. Symp. 110, 81-86.

Monrabal, B. (1998), Polymer Char, Valencia Parc Tecnologic, Paterna Spain, Private communication.

Mooney, P.J. (1995), "Rotational molding: At the take-off stage of growth", Rotation 4 (3) , pp. 24-30.

Mooney, P.J. (1999), "The evolution of the rotational molding business", Proc. SPE/11th Int. Conf. on Polyolefins, Houston, TX, pp. 413-427.

Nagy, T. and White, J.L. (1996), "The effect of colorants on the properties of rotomolded polyethylene parts", Polym. Eng. Sci., 36 (7), pp. 1010-1018.

Narkis, M., Puterman, M., Boneh, H. and Kenig, S. (1982), "Rotational molding of thermosetting three-phase syntactic foams", Polym. Eng. Sci., 22 (7), pp. 417-421.

Narkis, M. (1995), "Sintering of compacted thermoplastic powders", in Polymer Powder Technology, M. Narkis and N. Rosenzweig (eds), Wiley, New York, pp. 279-298.

Nelson, J.C., Xue, S., Barlow, J.W., Beaman, J.J., Marcus, H.L. and Bourell, D.L. (1993), "Model of the selective laser sintering of bisphenol-A polycarbonate", Ind. Eng. Chem. Res., 32 (10), pp. 2305-2317.

Nugent P.J. (1990), "A study of heat transfer and process control in the rotational moulding of polymer powder, Ph.D. Thesis, The Queen's University of Belfast, UK.

Nugent, P.J. and Crawford, R.J. (1992), "Process control for rotational moulding", in Rotational moulding of plastics, R.J. Crawford (ed.), Wiley, New York, pp. 191-212.

Oliveira, M.J., Cramez, M.C. and Crawford, R.J. (1996), "Structure-properties relationships in rotationally moulded polyethylene", J. Mat. Sci., 31, pp. 2227-2240.

Olson, L.G., Gogos, G., Pasham, V., and Liu, X. (1998), "Axisymmetric finite element models of rotational molding", Proc. SPE/ANTEC, Atlanta, pp. 1116-1120.

Orgaz-Orgaz, F. (1988), "Gel to glass conversion: Densification kinetics and controlling mechanisms", J. Non-Cryst. Solids, 100, pp. 115-141.

Pantani, R., D' Amore, M. and Titomanlio, G. (1996), "Modelling of powder flow in rotational moulding", Proc. PPS 12th Annual Meeting, Sorrento, Italy, pp. 767-768.

Papanastasiou, A.C., Scriven, L.E. and Macosko, C.W. (1984), "Bubble growth and collapse in viscoelastic liquids analyzed", J. Non-Newt. Fluid Mech., 16, pp. 53-75.

Pearson, G. and Middleman, S. (1977), "Elongational flow behavior of viscoelastic liquids: Part I. Modeling of bubble collapse", AIChE J., 23 (5), pp. 715-722.

Petrucelli, F. (1992), "Rotational moulding of Nylons", in Rotational moulding of plastics, R.J. Crawford (ed.), Wiley, New York, pp. 56-93.

Pokluda, O., Bellehumeur, C.T. and Vlachopoulos, J. (1997), "A modification of Frenkel's model for sintering", AIChE J., 43, pp. 3253-3256.

Progelhof, R.C., Cellier, G. and Throne, J.L. (1982), "New technology in rotational molding: Powder densification", Proc. SPE/ANTEC, San Francisco, pp. 627-629.

Quantum (undated), "A rotomolder's guide to polypropylene".

Rabinovitz, E. and Rigbi, Z. (1985), "Rotational reaction molding of polyurethane", Plast. Rubber Process Appl., 5 (4), pp. 365-368.

Ramesh, N.S., Rasmussen, D.H. and Campbell, G.A. (1991), "Numerical and experimental studies of bubble growth during the microcellular foaming process", Polym. Eng. Sci., 31 (23), pp. 1657-1664.

Rao, M.A. and Throne, J.L. (1972), "Principles of rotational molding", Polym. Eng. Sci., 12 (4), pp. 237-264.

Readey, D.W. and Cooper, A.R. (1966), "Molecular diffusion with a moving boundary and spherical symmetry", Chem. Eng. Sci., 21, pp. 917-922.

Richardson, M.J (1984), "Thermal analysis of polymers using quantitative Differential Scanning Calorimetry", Polymer Testing, 4, pp. 101-115.

Richart, D.S. (1995), "Powder coating", in Polymer Powder Technology, M. Narkis and N. Rosenzweig (eds), Wiley, New York, pp. 219-277.

Rosenzweig, N. and Narkis, M. (1981), "Sintering rheology of amorphous polymers", Polym. Eng. Sci., 21 (17), pp. 1167-1170.

Rosenzweig, N. and Narkis, M. (1995), in "Polymer Powder Technology", M. Narkis and N. Rosenzweig (eds), Wiley, New York, pp. 1-4.

Scherer, G. W. (1977), "Sintering of low-density glasses: I. Theory", J. Am. Ceram. Soc., 60 (5-6), pp. 236-239.

Scherer, G. W. (1984), "Viscous sintering of a bimodal pore-size distribution", J. Am. Ceram. Soc., 67 (11), pp. 709-715.

Scherer, G.W. (1979), "Sintering inhomogeneous glasses: Application to optical waveguides", J. Non-Cryst. Solids, 34, pp. 239-256.

Scherer, G.W. (1991), "Cell models for viscous sintering", J. Am. Ceram. Soc., 74 (7), pp. 1523-31.

Scherer, G.W. and Bachman, D.L. (1977), "Sintering of low-density glasses: II. Experimental study", J. Am. Ceram. Soc., 60 (5-6), pp. 239-243.

Scherer, G. W. and Garino, T. (1985), "Viscous sintering on a rigid substrate", J. Am. Ceram. Soc., 68 (4), pp. 216-220.

Scott, J.A. (1986), "A study of the effect of process variables on the properties of rotationally moulded plastic articles", Ph.D. Thesis, Queen's University of Belfast.

Sloane, D. (1997), "The measurement of the interfacial tension between polymer melts", Undergraduate thesis, McMaster University, April 1997.

Spence, A.G. (1994), "Analysis of bubble formation and removal in rotationally moulded products", Ph.D. Thesis, The Queen's University of Belfast, UK.

Spence, A.G. and Crawford, R.J. (1995), "Simulated bubble removal under pressurised rotational moulding conditions", Rotation, 4, pp. 17-23.

Spence, A.G. and Crawford, R.J. (1996), "Removal of pinholes and bubbles from rotationally moulded products", Proc. Instn. Mech. Engrs., 210 (B6), pp. 521-533.

Street, J.R. (1968), "The rheology of phase growth in elastic liquids", Trans. Soc. Rheol. 12 (1), pp. 103-131.

Strong, A.B. and Kinghorn, K.B. (1998), "Development of ABS resins for use in rotational molding", ARM materials committee and Bringham Young University.

Sugimoto, M., Masubuchi, Y., Takimoto, J. and Koyama, K. (1999), "Dynamic viscoelasticity and uniaxial behavior of high-melt-strength polypropylene melts", Proc. PPS 15th Annual Meeting, The Netherlands.

Sun, D. and Crawford, R.J. (1993a), "Computer simulation of rotational moulding heat transfer processes", Plast. Rubber Compos. Process. Appl., 19 (1), pp. 47-53.

Sun, D. and Crawford, R.J. (1993b), "Analysis of the effects of internal heating and cooling during the rotational molding of plastics", Polym. Eng. Sci., 33 (3), pp. 132-139.

Tadmor, Z. and Gogos, C.G. (1979), "Principles of polymer processing", Wiley, NewYork.

Takács, E., Bellehumeur, C.T. and Vlachopoulos, J. (1996), "Differences in rotomoldability of polyethylene micropellets and powders", Rotation, 5 (3), pp. 17-24.

Tanaka, A. (Jan. 1974), "Rotational molding of ABS resin", Japan Plastics, pp. 16-21.

Techakijkajorn, J., Frederick, W.J. and Tran, H.N. (1999), "Sintering and densification of recovery boiler deposits: Laboratory data and a rate model", J. Pulp Paper Sci., 25 (3), pp. 73-80.

Throne, J.L. (1972), "Some factors influencing cooling rates of rotational molding parts", Polym. Eng. Sci., 12, pp. 335-339.

Throne, J.L. (1976), "Rotational molding heat transfer – An update", Polym. Eng. Sci., 16 (4), pp. 257-264.

Throne, J.L. (1979), "Rotational molding", in Plastics Process Engineering, Marcel Dekker.

Throne, J.L. (1995), "Rotational molding" in Polymer Powder Technology, M. Narkis and N. Rosenzweig (eds.), Wiley, New York.

Throne, J.L. and Sohn, M.S. (1989a), "Characterization of rotational molding grade polyethylene powders", Adv. Polym. Technol., 9 (3), pp. 181-192.

Throne, J.L. and Sohn, M.S. (1989b), "Structure-property considerations for rotationally moulded polyethylenes", Adv. Polym. Technol., 9 (3), pp. 193-209.

Thummler, F. and Thomma, W. (1967), "The sintering process", Metall. Reviews, 12, pp. 69-108.

Van de Vorst, G.A.L. (1994), "Modelling and numerical simulation of viscous sintering", Ph.D. Thesis, Eindhoven University of Technology, The Netherlands.

Vick, L.W. and Kander, R.G. (1997), "Ambient temperature compaction of polycarbonate powder", Polym. Eng. Sci., 37 (1), pp. 120-127.

Vick, L.W. and Kander, R.G. (1998a), "Hot compaction and consolidation of polycarbonate powder", Polym. Eng. Sci., 38 (11), pp. 1824-1837.

Vick, L.W. and Kander, R.G. (1998b), "Pressureless sintering of polycarbonate powder compacted at ambient temperature", Polym. Eng. Sci., 38 (12), pp. 1985-1996.

Vlachopoulos, J., Bellehumeur, C.T. and Kontopoulou, M. (1996), "The role of rheology in rotomolding", Proc. 12th Int. Congr. Rheol., Quebec City, pp. 696-697.

Wasserman, S.H. (1997), "Characterizing the melt relaxation behavior of metallocene polyethylenes", Proc. SPE/ANTEC, pp. 1129-1133.

White, J.L., Bawiskar, S. and Nagy, T. (undated), "Rotational molding of ABS resins", University of Akron, Akron, Ohio.

Wu, S. (1995), "Polymer Interface and Adhesion", Marcel Dekker, New York.

Xu, L. (1994), "Rotational moulding of thick wall products", Ph.D. Thesis, The Queen's University of Belfast, UK.

Xu, L. and Crawford, R.J. (1993), "Analysis of the formation and removal of gas bubbles in rotationally moulded thermoplastics", J. Mat. Sci., 28, pp. 2067-2074.

Xu, L. and Crawford, R.J. (1994), "Computer simulation of the rotational moulding process", Plast. Rubber Compos. Process. Appl., 21 (5), pp. 257-273.

Xu, L. and Crawford, R.J. (1997), "The development of the computer simulation program for the rotomolding process". Proc. SPE/ANTEC, Toronto, pp. 3205-3209.

Zana, E. and Leal, L.G. (1975), "Dissolution of a stationary gas bubble in a quiescent viscoelastic fluid", Ind. Eng. Chem. Fundam., 14 (3), pp. 175-182.